NAVAL FACILITIES ENGINEERING SERVICE CENTER
Port Hueneme, California 93043-4328

Technical Report TR-2036-SHR

DEVELOPMENT OF A PLASTICITY BOND MODEL FOR REINFORCED CONCRETE - THEORY AND VALIDATION FOR MONOTONIC APPLICATIONS

by

James V. Cox

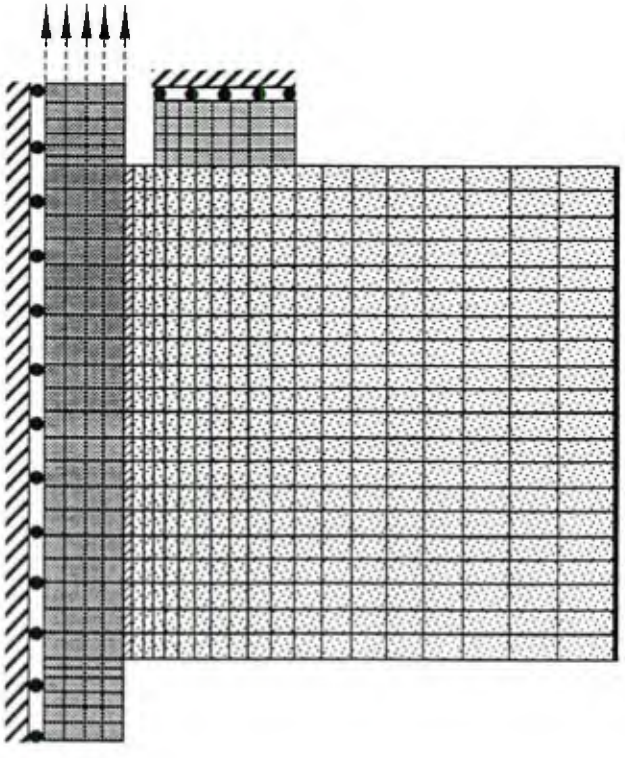

December 1994

Sponsored by
Office of Naval Research
Arlington, VA 22217-5000

REPORT DOCUMENTATION PAGE

Form Approved OMB No. 0704-018

1. AGENCY USE ONLY *(Leave blank)*	2. REPORT DATE	3. REPORT TYPE AND DATES COVERED
	December 1994	Final; Sep 89 through Sep 94

4. TITLE AND SUBTITLE
DEVELOPMENT OF A PLASTICITY BOND MODEL FOR REINFORCED CONCRETE - THEORY AND VALIDATION FOR MONOTONIC APPLICATIONS

5. FUNDING NUMBERS
PE - 61153N
WU - DN66342

6. AUTHOR(S)
James V. Cox
Department of Civil Engineering, Johns Hopkins University
3400 N. Charles Street, Baltimore, MD 21218-2686

7. PERFORMING ORGANIZATION NAME(S) AND ADDRESSE(S)
Naval Facilities Engineering Service Center
560 Center Drive
Port Hueneme, CA 93043-4328

8. PERFORMING ORGANIZATION REPORT NUMBER
TR-2036-SHR

9. SPONSORING/MONITORING AGENCY NAME(S) AND ADDRESSES
Office of Naval Research
800 Quincy Street
Arlington, VA 22217-5000

10. SPONSORING/MONITORING AGENCY REPORT NUMBER

11. SUPPLEMENTARY NOTES
See companion report CR94.001, NFESC, March 1994

12a. DISTRIBUTION/AVAILABILITY STATEMENT
Approved for public release; distribution unlimited.

12b. DISTRIBUTION CODE

13. ABSTRACT *(Maximum 200 words)*

Reinforced concrete modeling requires models for the constituent materials, concrete and steel, and for their interaction which is called bond. This study's objective is to develop and validate a monotonic bond model that, at least qualitatively, reflects the micromechanics and yet has potential application in the numerical analysis of structures or their components. A plasticity bond model is derived from simplified analyses of selected experimental results. This model relates local slip and radial dilation to bond stress and radial confinement stress. It represents the response of a finite-thickness region around the bar called the bond zone. The resulting model only requires knowledge of two fundamental properties of the concrete and two geometric properties of the reinforcement, and yet is able to reproduce the results of six independent experimental studies with acceptable accuracy.

14. SUBJECT TERMS
Reinforced concrete, bond model, plasticity, anchor pullout, monotonic loading, constitutive model, finite elements

15. NUMBER OF PAGES
308

16. PRICE CODE

17. SECURITY CLASSIFICATION OF REPORT	18. SECURITY CLASSIFICATION OF THIS PAGE	19. SECURITY CLASSIFICATION OF ABSTRACT	
Unclassified	Unclassified	Unclassified	UL

Abstract

Reinforced concrete modeling requires models for the constituent materials, concrete and steel, and for their interaction (bond). While constituent material models have received much attention, bond models have advanced less rapidly. Many of the early bond models related average bond stress to slip and were derived from curve fits to an isolated data set; thus, they lacked generality and were only applicable to specimens with stress histories similar to the "original experiments." More recent efforts have included micromechanical models of bond behavior, that explicitly represent the bar surface geometry, and phenomenological models that represent the mechanical interaction of the bar and concrete in a homogenized sense.

This study's objective is to develop and validate a monotonic bond model that, at least qualitatively, reflects the micromechanics and yet has potential application in the numerical analysis of structures or their components. To meet this objective a phenomenological bond model is developed that is applicable to a large range of slip. A key premise is that the model must include the radial response near the bar to achieve a measure of generality and to represent the mechanical interaction between the ribs and adjacent concrete.

A plasticity bond model is derived from simplified analyses of selected experimental results. This model relates local slip and radial dilation to bond stress and radial confinement stress. It represents the response of a finite-thickness region around the bar – the *bond zone*. The forms of the yield surface, evolution laws and flow rule qualitatively reflect the mechanics of bond. The model development, associated mechanics, and experimental basis are discussed for each component of the model. The stability of the plasticity model, and its implementation are also discussed.

The resulting model only requires two fundamental properties of the concrete and two geometric properties of the reinforcement, and yet is able to reproduce the results of six independent experimental studies with acceptable accuracy. Many aspects of bond response are predicted well, including: initial bond stiffness, bond strength, change of ductility with confinement stress, friction response and splitting. The two-dimensional plasticity bond model has a measure of generality.

Acknowledgements

I thank Professor Leonard Herrmann, my chairman, for his support and encouragement. He has been my teacher, mentor and one of my best friends. I thank Professors Karl Romstad and Yannis Dafalias for serving on my committee. Their comments, suggestions and genuine interest in my work are greatly appreciated.

I thank each of the committee members for timely reviews, as I pushed the limits on the submission date. I'm sure there are significant papers that are not adequately referenced, and there are many improvements I would like to make. However, next week I become a professor, so it is time to stop.

To the regents of the University of California, to whom I have written many checks, I thank you for writing one check to me, a Regents Fellowship during the time of this study.

I am indebted to the Office of Naval Research, and the Naval Civil Engineering Laboratory (NCEL) for providing financial support for this study. Many individuals in the management of NCEL were very supportive of my graduate efforts, especially: Dr. Bob Storer, Bill Armstrong, and Bob Odello. I am particularly indebted, to my senior colleague and friend, Dr. Ted Shugar, the project engineer for this work. He too has been a teacher, mentor and a dear friend. For thirteen years, we worked together on projects that were challenging and fun. I would also like to thank my colleagues Joe Holland, Javier Malvar and George Warren. They all challenged me technically, pushed me to write, and supported me and my family during this process.

Table of Contents

Page

Chapter 1

Introduction

Reinforced concrete is one of the most cost effective and widely used construction materials for both civilian and military infrastructure. Yet the behavior of structures composed of this composite material is difficult to accurately predict. One only needs to reflect on the structural failures associated with the Loma Prieta and Northridge earthquakes to realize the magnitude of the problem faced by structural engineers. Having resided close enough to be shaken by both of these quakes, my interest in structural modeling is more than academic. Many technical and social issues receive increased attention after these types of events. On the technical side, among the issues emphasized by structural engineers are the difficulty in predicting 1) representative ground motions, 2) the extent of soil-structure interaction, and 3) material behavior in the structure. In addition, advanced finite element analysis (FEA) techniques which are purported to have the potential to "solve" many of the technical issues see limited application in the civil engineering design environment; they are often deemed to be cost prohibitive. Nonetheless, these techniques are valuable in obtaining a better understanding of structures (*e.g.*, in examining a basis for design and investigating failures) and in analyzing special structures for which engineering codes do not apply. The combination of advanced numerical algorithms, powerful workstations, CAD integrated graphic pre- and post-processors, and graphic user interfaces are allowing FEA technology to be applied to an increasing number of design problems.

This study addresses the technical issue of reinforced concrete behavior. While there has been much work in the development of models for the constituent materials (concrete and

steel), development of models for their interaction has progressed at a slower rate. The initial motivation for this study came from an informal review of a basic research project titled "Structural Modeling" in 1988.* Professor Tom Hughes (1988) indicated in his plate and shell element work a "general solution" to the bond problem was a key missing link. Professor Leonard Herrmann indicated he had come to the same conclusion in his work with Dr. Joseph Jung (1989). This review was the seed for a project on bond modeling.† Other elements of this project were reported in Chang (1992), McMichael (1993), and Herrmann and Cox (1994).

The motivation for bond modeling is multifold. By design, bars are used to reinforce concrete (a brittle matrix) to both prevent and bridge cracks. As such, bond behavior is important in predicting the nature of localized failures and the amount of energy dissipated. Structural models that totally disregard the effects of bond typically fail to predict localized cracking. In many environments (*e.g.*, marine and salted highways), the size of cracking also affects the longevity of the structure. While bond often influences local behavior, this local behavior can have global ramifications. The corresponding stiffness deterioration increases the period of vibration, decreases the energy dissipation capacity, and can result in a significant redistribution of internal forces (see *e.g.*, Filippou *et al.* [1983]). Bertero (1979) found the hysteretic behavior of reinforced concrete structures, subjected to severe seismic excitation, is strongly dependent upon bond.

Bond has been modeled at several scales. Figure 1-1 presents three scales of modeling with geometrically descriptive names. The relative scales are reflected in the discretization of a typical FEA mesh. *Rib-scale* analyses require the ribs (also called deformations and lugs) on the bars to be explicitly discretized. Among the difficulties in modeling bond at

---

* An Office of Naval Research funded project at the Naval Civil Engineering Laboratory.

† Admittedly, this conclusion has been reached by many individuals in the community (see *e.g.*, ASCE [1982]).

this scale is that the scale is significantly smaller than the "unit cell for concrete;" that is, much of the aggregate is larger than the rib so the homogeneous concrete assumption is extremely idealistic. In addition, rib-scale bond models will be no better than the concrete model's ability to model fracture and crushing failures. While analyses at this scale have not provided a "general analysis capability," they have provided much insight to the micromechanics of bond – especially in the early response. Thus, they are sometimes referred to as *micromechanical models*. To model bond for large slips at the rib-scale would be numerically challenging since damaged material can change state (*i.e.*, become a powder) and be deposited on the rib face or in cracks. Interesting examples of rib-scale analyses include the studies of Hungspreug (1981), Reinhardt *et al.* (1984), Ozbolt and Eligehausen (1992a,b), Yao (1992), and Wang (1993).

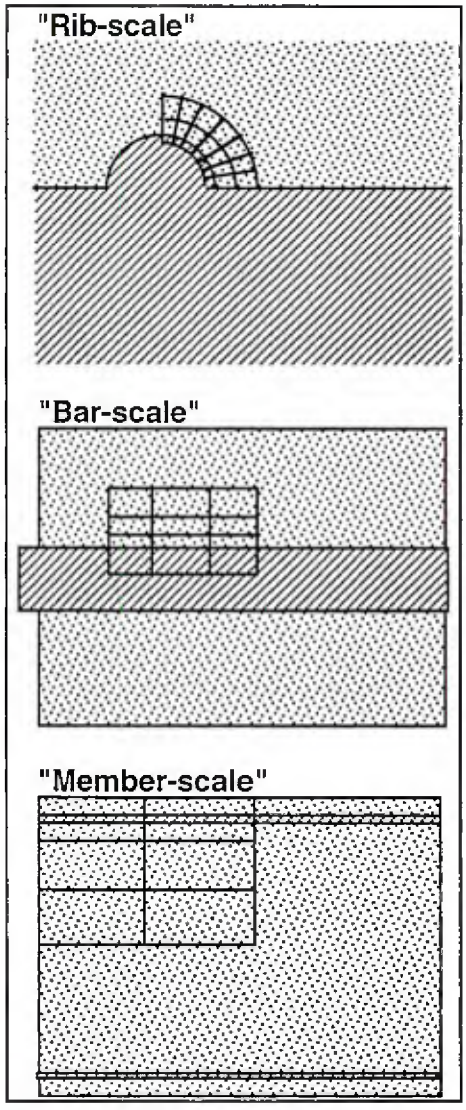

Figure 1-1 Scales of bond analysis.

At the other extreme, the *member-scale*, either a structural component or complete structure is modeled; this requires a careful selection of the discretization and element types. The reinforcing might be modeled using a *discrete*, *embedded* or *smeared* approach (see *e.g.*, ASCE [1982]). In the discrete approach, the reinforcement is modeled using truss-like elements. In an embedded approach, the reinforcing elements do not necessarily pass

though mesh nodes, and their deformation is constrained to be "like"* that of the elements they intersect. The anisotropy of the composite is determined directly by the analysis program with no burden on the user to define unit cells and to homogenize the problem. In a smeared approach, the analyst (possibly with the aid of a preprocessor) determines the anisotropic properties of a unit cell, essentially smearing the effect of the reinforcement.

Typically at the member-scale the reinforcement has been treated as a one-dimensional element, and bond laws have been limited to single-stress models. The discrete reinforcement model is the easiest to implement, but the reinforcement schedule controls the geometry of the mesh. The embedded reinforcement model is simpler to use, but usually it does not accurately account for high gradients near the bars or the associated bond behavior; this reinforcement model is often used when the anisotropy is important and the reinforcement pattern is irregular.

The intermediate scale shown is the *bar-scale*. At this scale the bar and concrete are treated as continuums, and the mechanical interaction of the ribs is homogenized and modeled as an interface phenomenon. Clearly, rib-scale analyses (see *e.g.*, Hungspreug [1981]) and experiments (see *e.g.*, Gerstle and Ingraffe [1990]) indicate that the perceived bond response is not limited to the "interface;" that is, transverse cracking caused by the mechanical interaction is not constrained to an infinitesimally thin region but rather extends within a finite region around the bar (see *e.g.*, Lutz and Gergely [1967]).

These three scales reflect the trilemma one faces in many modeling problems. The practical problems are orders of magnitude larger than the scale at which the "basic mechanics" occur, and a phenomenological model is a compromise between the two "extremes."

---

* Some implementations of embedded elements are not displacement compatible. For example, consider a 4-node, bilinear element which intersects a reinforcing bar that does not coincide with an isoparametric coordinate line. If the reinforcing bar's strain is determined solely from the interpolated displacements at the element's edges, it will be incompatible. The reinforcing bar will exhibit a linear variation in displacement while the embedding element will exhibit a quadratic variation along the same line.

1.1 Objective

The objective of this study is to develop and validate a bond model which, at least qualitatively, reflects the micromechanics and yet has potential application in the numerical analysis of structures or their components. While the model need not be micromechanical, its formulation and application should yield additional insight to the mechanics of bond. The model should require only one calibration for standard steel bars and be capable of reproducing (with an accuracy comparable to experimental scatter) bond tests results from several independent research groups.

1.2 Scope

This study was limited to the development of a monotonic bond model applicable to problems where the stress state near the bar can be approximated as an axisymmetric state (*e.g.*, problems which include large doweling forces will not be considered). A follow-up study generalized this model to cyclic loading (Herrmann and Cox [1994]). The model has initially been applied to standard steel reinforcing bars. It has potential application to steel bars with nonstandard rib patterns, epoxy coated bars and to fiber reinforced plastic bars; however, all of these would at least require recalibration. This study did not have an experimental component, but a set of NCEL (Naval Civil Engineering Laboratory) experiments provided important data for the model development. The calibration and validation problems considered herein were conducted by six independent research groups. All of the experiments considered used very different specimens, but they were all pull-out specimens of normal strength concrete.

1.3 Approach

To fulfill the objectives of this study, a bar-scale model* was developed to represent the interaction between concrete and a steel reinforcing bar. Thus, this model is inherently phenomenological in nature since the mechanical interaction of the ribs is implicitly homogenized at this scale. Some have argued that a better understanding of the mechanics of bond can only be attained by explicitly modeling the micromechanics. To quote Professor Dafalias (from his plasticity course): "Truth is relative to the scale a phenomenon is examined." This statement is consistent with the philosophy adopted for this study. The phenomenological model should **NOT** be a "black box" obtained from mindless curve fits, but rather it should represent the effect of the corresponding physical mechanisms. The emphasis of the model development is to gain a more fundamental understanding of the mechanics of bond while attaining a model that has a measure of general applicability. Validation of a model is never complete, and thus a better understanding of the associated mechanics is more likely to result in its appropriate application.

The mechanical interaction between the steel bars and concrete is very difficult to quantify. There are many inherent difficulties with studying this problem; including, 1) bond behavior is comprised of several mechanisms, and 2) the combined response of these mechanisms is difficult to measure. For a bar-scale model, experimental data that give the "local response" are desired but are inherently illusive. There have been many attempts to measure the local response. Some researchers have focused on local measurements of bar and concrete strains (see *e.g.*, Nilson [1972]). Others have designed small specimens and assume local values can be obtained from averages of global measurements (*e.g.*, end slip and bar force).

---

* Though it might be considered a misnomer, the bond model will sometimes be referred to as a "constitutive law." Because it does not serve as a general model for a constituent material, some would prefer to think of it as a "structural model."

Both types of measurements have well-known strengths and weaknesses. Local measurements are inherently difficult to obtain accurately, especially considering that bond stress is obtained from derivatives of the bar strain data. Global measurements while exhibiting less scatter provide less information. To use global measurements experimentalists design specimens with small embedment lengths to justify the assumption of uniform bond stress distribution. If a specimen is too small, the very mechanisms one wishes to measure can be disturbed (*e.g.*, by inhibiting transverse cracking that would occur in a larger specimen). If a specimen is too large, the global responses are not an accurate measure of local bond behavior; in a sense the specimen acts as a filter hiding some of the information. It's very analogous to Heisenberg's uncertainty principle of physics and equally frustrating.

Many researchers have shown collections of bond stress versus slip curves which show a great variation. A premise of this study is that these variations are principally due to differences in concrete properties, steel bar geometries, specimen configurations, and experimental scatter, and that the first three factors can be accounted for by modeling the bond specimen. Since the bond model represents the mechanical interaction between the concrete and steel bar, it is likely to have physical parameters that represent the concrete strength and bar geometry.

The model development was an iterative process which progressed as: 1) form hypotheses on the nature of bond from the experimental data, 2) model these hypotheses in a phenomenological model, 3) predict the behavior of published experiments, and 4) claim a validation or iterate again. Because bond response cannot be directly examined, simplifying assumptions were made to extract information from experimental data that would allow the initial formulation of a general bond model. To facilitate the early iterations in the development process, simplified specimen models were incorporated. Additional information on these simplified models is presented in Herrmann and Cox

(1994). In this study, I refer to these simplified models as *point models*; this name reflects that these models are discrete since all spacial approximations are included in their formulation (*i.e.*, simple analytical approximations of the specimen response are used).

Other specimen models were of one and two spacial dimensions. Chang (1992) demonstrates one-dimensional models that approximate the radial behavior of the specimen without an explicit discretization of this dimension. For this study, the use of two-dimensional FEA specimen models is limited to validation problems. The idealistic approach of modeling many specimens in detail (*e.g.*, two-dimensional FEA models) and attempting to extract constitutive information from the predicted results is very time consuming. The point models helped alleviate this problem.

An incremental plasticity framework was adopted in this study for the bond model development. Motivating experimental results and an overview of the theory will be presented in the next chapter. To obtain a general model, a measure of the normal stress and radial dilation were incorporated in the formulation. This is not the first model to incorporate these variables in the formulation. However, it appears to be the only model that with their inclusion has successfully estimated the response of multiple bond tests without recalibration. With radial dilation and normal stress incorporated in the model, there is the potential to capture both pull-out and splitting failures in bond specimens. Tepfers and Olsson (1992) emphasize the importance of the latter in stating that "most bond failures are splitting failures."

One of the key aspects of the objective was that the model must have potential application in the numerical analysis of structures or their components. The "bar-scale" is a scale of compromise, and the application of a bond model derived at this scale to structural problems will be a challenge – except for the smallest of structural components. As you examine the form and behavior of the plasticity bond model, it will be apparent that even with the homogenization the scale of the ribs "is still present." Since bond behavior is

mainly attributed to the mechanical interaction of the ribs with the concrete this is not a surprise. It could present a significant numerical burden because integration of the bond law could require significantly smaller time steps (for accuracy) than that required for the overall structural response.

At the member-scale, the size of the elements was characterized as being large relative to the diameter of the bar. Another related numerical challenge in implementing the model at this larger scale is that high gradients near the bar must be accounted for so that the bond model receives "good input." De Groot *et al.* (1981) appear to have been the first to apply a bond model at the member-scale that incorporated normal stress and radial dilation in the formulation. Their approach treats the combined bond model-reinforcement in a discrete manner. In this current project, McMichael and Herrmann (McMichael, 1993) developed a smeared reinforcement model for reinforced concrete which incorporates relative slip and dilation as primary nodal variables. Their analysis of the unit cell uses a thick-walled cylinder approximation of the material near the bar to model the local gradients. The point models used in Herrmann and Cox (1994) implemented the partly cracked elastic model of Tepfers (1979). Fracture mechanics models (see *e.g.*, Rosati and Schumm [1992]) should also be considered in future efforts to model the concrete response near the bar. Use of these "local models" to "connect" the bond model to a relatively coarse mesh might help alleviate the "problem of scale." Without continued efforts in this area, application of bar-scale models will be very limited.

1.4 Background

In providing background for this study, it is not my goal to review every significant bond paper ever written. The bibliography lists many studies which will not be discussed in this work. The following references contain collections of bond papers or state-of-the-art reviews on the subject: Hungspreug (1981), ASCE (1982), and CEB (1992). The most

recent reference, for the International Conference of Bond in Concrete, contains overview papers on this work and on most of the experimental studies used for the model development and validation.

This section is divided into subsections which provide background on the mechanics of bond, parameters which affect bond, one-dimensional bond models, and two-dimensional bar-scale models.

Overview of the Mechanics of Bond for Monotonic Loading

This subsection presents a brief overview of the mechanics of bond, principally to establish some terminology that is essential to the description of previous work; additional detail will be provided in the model development chapters – Chapters 3 through 5. For additional detail on the mechanics of bond consider the classic papers of Rehm (1961) and Lutz and Gergely (1967), and the detailed review of Hungspreug (1981).

Figure 1.4-1 schematically illustrates the response of concrete in the region near a ribbed-bar. For plain bars (without ribs), "adhesion" and friction are the main contributing mechanisms of bond. The apparent "adhesion" has contributions from chemical bonding and the effect of shrinkage stresses that develop during curing. For ribbed-bars, these mechanisms are secondary (by design) to the mechanical interaction of the ribs with the surrounding concrete.

Adhesion breaks down relatively early in the bond response. After the breakdown of adhesion the bond force is transferred by friction and the mechanical interaction of the ribs with the adjacent concrete. With increasing bar force, the mechanical interaction dominates the transfer of force.

At this point in the loading, clearly the transfer of bond force is concentrated near the rib faces and the use of the term "bond stress" implies an average force per unit area.* With this concentration of bearing force, increased loading will begin to fail the adjacent concrete in two ways: the crushing of concrete adjacent to the contact area of the ribs and transverse cracking (typically cone-shaped cracks – also called secondary cracking) initiating from the ribs. Different researchers often emphasize one "mode of failure" over the other. For example, Gerstle and Ingraffea (1990) questioned the traditional concept of bond slip by experimentally focusing on the fracture response of clear resin, bond specimens. In a subsequent discussion of the paper, Gambarova and Giuriani indicated "the assumption that secondary microcracking is the dominant mechanism contributing to bond slip is unrealistic, though useful for its straightforwardness." They claimed that concrete crushing becomes the dominant factor even for very small slip values.

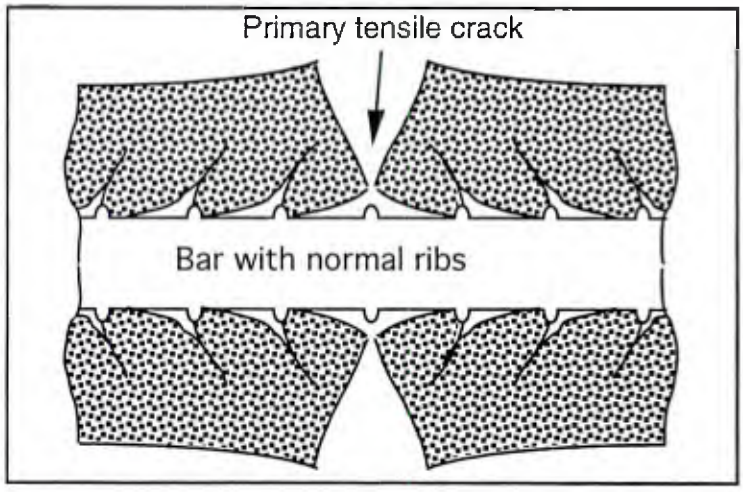

Figure 1.4-1 Mechanical interaction of ribs with concrete – bearing and transverse cracking (after Goto [1971]).

It seems that for a given specimen the dominant slip mechanism would be dependent upon the stress state in the concrete near the rib. In subsequent chapters, the explanation of the bond model is based more upon the crushing mechanism, but transverse cracking is also an important mechanism. Many researchers have explained their models in terms of

* This homogenization is discussed in more detail in Chapter 3.

transverse cracking alone. With stable propagation of transverse cracks, the concrete near the bar appears to form *inclined struts* (see Figure 1.4-1) which are sometimes referred to as *compression cones* or *prisms* when idealized without friction (De Groot *et al.* [1981]). The bond stiffness is then characterized by the stiffness of these inclined struts.

As the loading progresses, radial splitting forces can develop. In terms of transverse cracking, this is explained by a rotation (about the θ-axis) of the comb-like inclined struts which produces a larger radial component of contact force. In terms of crushing, this is explained by the deposition of crushed concrete on the face of the rib which increases the effective contact angle (between the rib and concrete) thus increasing the radial component of the contact force. The net effect is the same; without adequate constraint, a splitting failure can occur.

The softening response, characteristic of a bond slip behavior, is often explained in terms of a progressive shear failure of the concrete between the ribs. Crushing of increasingly damaged material might also produce a softening response. Under very low confinement stress, geometric changes in the contact between the rib and concrete can contribute to softening as well (as discussed in Chapters 3 and 4).

Parameters Affecting Bond

This section will briefly present many parameters that have been attributed with affecting bond behavior. The discussion of experimental studies will be limited, but many other studies, though not reviewed here, are listed in Tables 1.4-1 and -2 by the bond parameter(s) that were studied. A check mark or arrow in a column indicates the given parameter was studied or at least discussed by the authors; the converse does not necessarily hold. The check mark indicates a "first-hand reference," whereas an arrow implies the reference was inferred in statements made by another author. The "Analytical model parameter" column of the tables indicate studies that either investigated the effect of a

parameter with a micromechanical model, incorporated the parameter in a phenomenological model, or at least quantified the effect of the parameter on bond strength. These tables are undoubtedly incomplete* but were a convenient reference list early in the study.

Most bond tests provide data that are more useful for design than for the development of a local bond model. Typical bond specimens are of the pull-out and tensile types, the former being representative of anchorage conditions and the latter being representative of the tensile region in a flexural member. Many of these tests were designed to study the influence on bond behavior of parameters that I refer to as *design parameters.* These parameters are useful in design, but are not appropriate for a bar-scale bond model. For member-scale bond models which are one-dimensional in form, the local state of the adjacent concrete cannot be "sensed" by the bond model and thus design parameters are necessary to account for variations in response within a member. Models that include design parameters can be difficult to apply in analyses. For example, if the embedment distance within a pull-out specimen is found to affect the local bond response, how does one incorporate this as a design parameter? If a crack develops near a joint, at each point along adjacent bars the bond model must "be told" its distance from this crack – difficult information to communicate within the architecture of a general FEA system. Conversely, a bar-scale model inherently has the potential to receive information about the local state of the material for which the embedment distance variable was indirectly accounting for.

Table 1.4-1 lists several design parameters and some related references. This classification is somewhat subjective. For example, Shima *et al.* (1987) claim that the bar strain gives an indication of the state of transverse cracking near the bar and thus of the material state.

---

* In particular the individual papers of the latest International Conference on Bond (CEB [1992]) are not included.

There are many other bond parameters which might be directly included in a bar-scale model. They are considered to be more "basic" in the sense that their "proper" inclusion in a model can produce more general predictive capabilities. Table 1.4-2 lists these parameters, key bond responses (*e.g.*, transverse cracking), and some related references. Additional parameters are listed in Hungsprueg (1981).

Table 1.4-1 Bond design parameter references.

Parameter/Researcher(s)	Experimental parameter	Analytical model parameter
Bar spacing		
Chamberlin (1952)	←	
Ferguson *et al.* (1954)	←	
Untrauer and Warren (1977)	←	
Goto and Otsuka (1979)	←	
Kemp and Wilhelm (1979)	✓	
Morita and Kaku (1979)	✓	
Skorobogatov and Edwards (1979)	←	
Eligenhausen *et al.* (1983)	✓	
Bar strain		
Edwards and Yannopoulos (1979)	✓	
Shima *et al.* (1987)	✓	✓
Casting position, vibration and revibration		
Menzel (1939,1941)	←	
Rehm (1957)	←	
Rehm (1961)	←	
Edwards and Yannopoulos (1979)	✓	
Eligenhausen *et al.* (1983)	✓	
Dohaney (1985)	←	
Mehlhorn and Keuser (1985)		✓
Altowaiji *et al.* (1986)	←	
Cover thickness		
Ferguson and Thompson (1962,65)	←	
Houde (1973)	←	
Tepfers (1973)	←	
Orangun *et al.* (1977)		←
Edwards and Yannopoulos (1979)	✓	
Eligehausen (1979)	←	
Kemp and Wilhelm (1979)	✓	
Mirza and Houde (1979)	✓	✓
Morita and Kaku (1979)	←	
Tepfers (1979)	✓	✓
Confining rebar		
Abrams (1913)	←	
Ferguson *et al* (1954)	←	
Ferguson and Thompson (1962, 1965)	←	
Robinson (1965)	←	
Lutz and Gergely (1967)	✓	
Morita and Kaku (1973)		←
Tepfers (1973)	←	
Orangun *et al.* (1977)		←
Untrauer and Warren (1977)	←	
Eligehausen (1979)	←	
Kemp and Wilhelm (1979)	✓	
Morita and Kaku (1979)	✓	
Viwathanatepa *et al.* (1979)		←
Eligenhausen *et al.* (1983)	✓	
Giuriani *et al.* (1991)	←	

Table 1.4-1 continued

Parameter/Researcher(s)	Experimental parameter	Analytical model parameter
End distance		
Nilson (1968)		✓
Perry and Jundi (1969)	✓	
Wahla (1970)	←	
Tanner (with Nilson ,1971)	←	←
Nilson (1972)	✓	
Dörr (1978)	←	
Edwards and Yannopoulos (1979)	✓	
Mirza and Houde (1979)	✓	
Shipman and Gerstle (1979)		✓
Viwathanatepa *et al.* (1979)	←	
Cowel *et al.* (1982b)	←	
Shima *et al.* (1987)	✓	
Splitting-crack opening		
Gambarova, Rosati and Zasso (1989)	✓	✓
Modena *et al.* (1989)	✓	

Table 1.4-2 "Basic" bond parameter and response references.

Parameter or response/Researcher(s)	Experimental parameter	Analytical model parameter
Adhesion		
Taylor and Broms (1964)	←	
Tassios (1979)	←	
Eligenhausen *et al.* (1983)	✓	
Aggregate type		
Richart and Jensen (1931)	←	
Tilantera and Rechardt (1977)	←	
Mehlhorn and Keuser (1985)		✓
Robins and Austin (1986)	←	
Bar rib pattern		
Abrams (1913,1925)	←	
Wastein and Seese (1945)	←	
Clark (1946)	←	
Rehm (1957)	←	
Rehm (1961)	←	←
Lutz, Gergeley, and Winter (1967)	←	
Wilhelm *et al.* (1971)	←	
Hansen and Hawkins (1973)	←	
Martin (1973)	←	
Kemp *et al.* (1977)	←	
Rehm and Eligehausen (1979)	✓	
Eligehausen (1979)	←	
Goto and Otsuka (1979)	←	
Hawkins and Lin (1979)	←	
Losberg and Olsson (1979)	✓	
Morita and Kaku (1979)	✓	
Rehm and Eligehausen (1979)	✓	
Soretz and Holzenbeim (1979)	✓	
Eligenhausen *et al.* (1983)	✓	✓
Mehlhorn and Keuser (1985)		✓
Balaazs (1986)	←	
Darwin and Graham (1993)	✓	
Bar surface quality		
Menzel (1939)	←	
Johnston and Cox (1940)	←	
Kemp *et al.* (1968)	←	
Bar diameter		
Rehm (1957)	←	
Martin (1973)	←	
Morita and Kaku (1973)	✓	
Mirza and Houde (1979)	✓	
Rehm and Eligenhausen (1979)	✓	
Eligenhausen *et al.* (1983)	✓	✓
Ueda *et al.* (1986)		←
Soroushian and Choi (1989)	←	

Table 1.4-2 continued.

Parameter or response/Researcher(s)	Experimental parameter	Analytical model parameter
Bond or transverse cracks		
Lutz (1970)		←
Goto (1971)	←	
Martin (1973)		←
Ma *et al.* (1976)		←
Yannopoulos (1976)		←
Bertero and Popov (1977)	←	
Tassios (1979)	←	
Viwathanatepa *et al.* (1979)		←
Eligenhausen *et al.* (1983)	✓	
Concrete compressive strength		
Abrams (1913)	←	
Richart and Jensen (1931)	←	
Davis *et al.* (1938)	←	
Gilkey *et al* (1940)	←	
Rehm (1957)	←	←
Rehm (1961)	←	
Mathey and Watstein (1961)	←	
Ferguson and Thompson (1962)	←	
Untrauer and Henry (1965)	✓	✓
Perry and Jundi (1969)	✓	
Tanner (with Nilson, 1971)	←	←
Nilson (1972)	✓	
Houde (1973)	←	
Martin (1973)	←	
Hawkins and Lin (1979)	←	
Orangun *et al.* (1977)		←
Mirza and Houde (1979)	✓	✓
Vos and Reinhardt (1982)	←	
Reinhardt *et al.* (1984)		✓
Eligenhausen *et al.* (1983)	←	←
Ueda *et al.* (1986)		←
Concrete tensile strength		
Dörr (1980)	←	
Hungspreug (1981)	←	
Reinhardt *et al.* (1984)		✓
"Bond zone" dilation		
De Groot *et al.* (1981)		✓
Malvar (1991)	✓	
Dowel interaction		
Gergely (1969)	←	
Sharma (1969)	←	
Houde (1973)	←	
Jimenez *et al.* (1979)	✓	
Kemp and Wilhelm (1979)	✓	
Morita and Kaku (1979)	✓	
Mainz *et al.* (1992)		✓

Table 1.4-2 continued.

Parameter or response/Researcher(s)	Experimental parameter	Analytical model parameter
Frictional bond resistance		
Morita and Kaku (1973)	✓	✓
Viwathanatepa *et al.* (1979)	←	←
Shipman & Gerstle (1979)		✓
Tassios (1979)	←	←
Cowel *et al.* (1982)	←	
Eligenhausen *et al.* (1983)	✓	
Load direction		
Morita and Kaku (1973)	✓	✓
Viwathanatepa *et al.* (1979)		←
Eligenhausen *et al.* (1983)	✓	✓
Load history		
1) Quasi-static		
a) cyclic tension		
Muhlenbruch (1945 & 1948)	←	
Singh, Gerstle, and Tulin (1965)	←	
Bresler and Bertero (1968)	✓	
Perry and Jundi (1969)	✓	
Rehm and Eligenhausen (1977)	←	
Dörr (1978)	✓	
Rehm and Eligenhausen (1979)	✓	
Cowell *et al.* (1982)	←	←
Eligenhausen *et al.* (1983)	✓	✓
b) reversed		
Ismail and Jirsa (1972)	✓	
Morita and Kaku (1973)	✓	✓
Hassen and Hawkins (1973)	←	
Rehm and Eligenhausen (1977)	←	
Hawkins and Lin (1979)	←	
Morita and Kaku (1979)	✓	
Rehm and Eligenhausen (1979)	✓	
Shipman & Girstle (1979)		✓
Tassois (1979a,b)		←
Viwathanatepa *et al.* (1979)	←	
Hungspreug (1981)	✓	✓
Cowel *et al.* (1982)	←	
Hawkins *et al.* (1982)	←	
Eligenhausen *et al.* (1983)	✓	✓
Popov (1984)		←
Shah and Chung (1986)	←	
2) Dynamic		
Perry and Jundi (1969)	✓	
RILEM (1986)	←	
Shah and Chung (1986)	←	

Table 1.4-2 continued.

Parameter or response/Researcher(s)	Experimental parameter	Analytical model parameter
Loading rate		
Vos and Reinhardt (1982)	←	
Eligenhausen *et al.* (1983)	✓	✓
Vos (1983)	←	←
Reinhardt *et al.* (1984)		✓
Shah and Chung (1986)	←	
Temperature		
Diederichs and Schneider (1981)	←	
Morley and Royles (1983)	←	
Shih *et al.* (1986)	←	
Shih *et al.* (1988)	←	
Transverse or confining pressure		
Leonhardt (1957)	←	
Untrauer & Henry (1965)	✓	✓
Dörr (1978)	✓	
Tassois (1979)	←	
Viwathanatepa *et al.* (1979)		←
Dörr (1980)	←	←
Hungspreug (1981)	✓	✓
Cowel *et al.* (1982)	←	
Navaratnarajah (1982)	←	
Robins and Standish (1982)	←	
Eligenhausen *et al.* (1983)	✓	✓
Vos (1983)	←	←
Reinhardt *et al.* (1984)		✓
Mehlhorn and Keuser (1985)		←
Shirai and Sato (1985)	✓	✓
Robins and Austin (1986)	←	
Navaratnarajah and Speare (1987)	✓	
Gambarova *et al.* (1989)	✓	
Modena *et al.* (1989)	✓	
Giuriani *et al.* (1991)	←	
Malvar (1991)	✓	

The particular area of experimentation that is of interest in this study is the effect of confinement stress on bond behavior. Hungspreug (1981) gave an extensive review of confinement effects in general (*i.e.*, transverse pressure, cover thickness, and secondary reinforcement effects). A more recent overview of many experimental works that focus on confinement stress is given in Malvar (1992a,b).

Leonhardt (1957) appears to have been the first to consider the effect of confinement stress on bond. Untrauer and Henry (1965)* investigated the effect on bond of pressure applied to opposing sides of 6-inch cube specimens. Several other experimental studies on the effect of confinement stress on bond followed (see *e.g.*, Table 1.4-2). Some specimens were cylindrical with applied radial tractions, and others were cube-shaped with normal tractions applied to two opposite faces. Both pull-out and tensile specimens have been investigated.

While the early studies recognized the importance of confinement stress, the conjugate kinematic quantity (radial dilation) was not indirectly measured until the works of Modena *et al.* (1989) and Malvar (1991); the former measured a crack opening, and the latter measured the change in specimen circumference. Both quantities (confinement stress and radial dilation) are necessary to formulate a "general model," otherwise the contribution to the normal stress due to the wedging action of the ribs cannot be accounted for, and splitting failures cannot be predicted.

Unfortunately, prescription of a compressive traction boundary condition does not directly give information on the confinement stress near the bar. For validation, where the test is

* This study is historically ironic. In 1965 Professor Untrauer was the major professor of Dr. Shugar (the NCEL project engineer for the project that encompasses the bond modeling work), and until 1964 Professor Henry was on leave from NCEL to pursue graduate studies. Bond was the topic of his research – a study also funded by NCEL.

treated as an initial-boundary value problem this is not a problem, but for model development there were few tests that were directly useful.

The experimental works of Malvar (1991), Gambarova *et al.* (1989), Eligehausen *et al.* (1983), Rehm and Eligehausen (1979), Shima *et al.* (1987), and Tepfers and Olsson (1992) were considered in this study. The first three were examined during the model development. Of these, the first two give the most useful data for developing a model that includes both radial dilation and confinement stress. The specimens of Malvar (1991) and Gambarova *et al.* (1989) are pull-out specimens with small embedment lengths. Both studies assume the embedment length is sufficiently small that the response along the bar is uniform. In addition to global measurements of bond stress and slip, both studies include a measure of radial dilation and normal stress. Details on each of these experiments will be presented in the following chapters on model development, calibration, and validation.

One-Dimensional Bond Models

The experimental studies are an essential basis of the model development, but the emphasis of this study is the development and validation of a bar-scale model. As such, some additional background on the evolution of bond models is important for perspective. A recent ACI report on bond under cyclic loads (ACI [1991]) presents an extensive list of references on bond models. This subsection presents some early bond models that were essentially one-dimensional in nature (*i.e.*, they relate bond stress to slip). The next section presents some two-dimensional models where the normal stress and/or radial dilation are incorporated in the model.

Rehm (1957) proposed a "basic law of bond." The rib bearing stress divided by the compressive strength was expressed as a power law of the end slip. This relationship was obtained from the results of single-rib tests, and thus was considered to have a local nature.

His tests showed the bearing stress at the rib could be an order of magnitude larger than the uniaxial compressive strength.

Ngo and Scordelis (1967) presented the first study on the FEA of reinforced concrete. Their model of a reinforced concrete beam treated the steel bars as a row of plane stress triangle elements connected to the adjacent concrete via nodal link elements. All of the materials, including those associated with bond, were assumed to be linear. The normal and tangential link element components were assumed to be uncoupled. The authors studied the distribution of stresses in the concrete, steel, and bond elements for various assumed crack patterns (*i.e.*, the analyses were linear). By modern standards the beam models were simple, yet this study was effective at examining both the potential and difficulties in FEA modeling of reinforced concrete.

Nilson (1968) presented a nonlinear FEA of an eccentric tensile member. Like the previous researchers, the reinforcement was treated as a continuum in a state of plane stress and was connected to the adjacent concrete with link elements. Nilson suggested that an alternative approach would be "to create a boundary layer of special elements concentric to the bar and immediately adjacent to it." These two approaches, the link elements of which are simply discrete from the onset, typify bond elements used in bar-scale analyses. The "boundary layer of special elements" generally consists of interface elements. The analysis incorporated an orthotropic nonlinear elastic law for the concrete and a discrete cracking algorithm which modified the nodal connectivity.

Nilson's bond law (*i.e.*, used for the tangent component of the link element) expressed the bond stress as a cubic polynomial of the slip up to the ultimate bond stress. Beyond this point the behavior was assumed to be position dependent. Link elements within one bar diameter of a crack were assumed to drop to zero bond stress, and those further from cracks were assumed to maintain the ultimate bond stress. The polynomial was fit to the

experimental data of Bresler and Bertero (1966). Despite the subsequent use of this law in the literature, the author had disclaimed any generality.

After each advance of the crack (*i.e.*, change of the mesh connectivity) the entire model was completely unloaded and reloaded. As with the previous model by Ngo and Scordelis (1967), this model was a research tool designed to provide insight to the behavior of reinforced concrete. Nilson indicated the complexity and importance of accurate bond modeling; he suggested the experimental data were insufficient "to establish a fundamental bond law."

Nilson (1971) presented piecewise linear approximations to Tanner's (1971) tensile tests which accounted for end distance and compressive strength of the concrete. The model's dependence in the end distance was linear. The predicted bond stress varied as the square root of the compressive strength which could be considered to be a measure of the tensile strength of the concrete.

Houde (1973) tested 62 tensile specimens and 32 beam end specimens. The tensile specimens used three bar sizes, #4, #6 and #8. Based on the results from the tensile tests and six beam end specimens (using #8 bars), he expressed bond stress as a fourth order polynomial of the slip. In contrast to Nilson's (1971) findings, Houde did not find the bond response to be position dependent; the maximum bond stress was attained at all locations for slips in the range $[10 \times 10^{-4}, 12 \times 10^{-4}]$ inches. Some of his work is summarized in Mirza and Houde (1979).

All of these models (ASCE [1982]) were considered to be limited to small slips prior to splitting. The models were essentially assumed to be nonlinear elastic; the subtle exception is the dependence of Nilson's models on end distance (*i.e.*, the bond model response was dependent upon the cracking response of adjacent concrete).

Dörr (1978) fit cubic polynomials to his local bond stress versus slip measurements too. He fit different polynomials for each level of confinement stress, but did not directly include normal stress in a more general model.

The starting point for the development of a cyclic model is a monotonic model. Extension of the model developed in this study to cyclic loading is presented in Herrmann and Cox (1994). Cyclic bond models will not be reviewed in detail; but their monotonic response is relevant to this study. The graph of bond stress versus slip during monotonic loading is often referred to as the *monotonic envelope* (see *e.g.*, Eligenhausen *et al.*, 1983). The references listed in Table 1.4-2 and the "general references" listed at the beginning of this section provide additional background on cyclic models. Among the well-known cyclic bond models are those of Morita and Kaku (1973), Tassios (1979), Viwathanatepa *et al.* (1979), Shipman and Gerstle (1979), and Eligenhausen *et al.* (1983).

Morita and Kaku (1973) presented the first analytical bond-slip model for cyclic loading. They extended a bilinear bond stress-slip relationship for monotonic loading to a piecewise-linear model for reversed loading cycles. Tassios (1979) presented another piecewise-linear model of which the monotonic envelope was comprised of six line segments and thus the softening portion of the response (characteristic of large slips) was included. Viwathanatepa *et al.* (1979) proposed another model which used four line segments to approximate the monotonic envelope. They identified distinct bond behavior regions in a beam column joint: unconfined concrete in tension, confined concrete, and unconfined concrete in compression for which they attributed different monotonic envelopes.

Shipman and Gerstle (1979) combined the work of Nilson (1971), Singh, Gerstle and Tulin (1973), and Morita and Kaku (1973) to develop another cyclic bond model. The ascending response of the monotonic envelope was defined by the polynomial relationship of Nilson (1971).

Ciampi *et al.* (1981) and Eligenhausen *et al.* (1983) developed a cyclic model from a very extensive set of experiments with a specimen designed to model the confined state in a beam-column joint. The monotonic envelope consisted or four parts: 1) a power curve ascending segment, 2) a flat plateau, 3) a linear descending segment, and 4) a flat friction segment. The effects of many parameters (like concrete compressive strength) were incorporated by scaling the monotonic envelope. In addition, the monotonic envelope is "continuously" modified to reflect progressive damage in the concrete adjacent to the bar. Modifications of this model were proposed by Filippou *et al.* (1983a,1983b).

Yankelevsky *et al.* (1992) proposed a model based on the experimental works of Viwathanatepa *et al.* (1979) and Eligehausen *et al.* (1983). This model additively combined three continuous component functions to obtain a smooth response for a given direction of loading. Each component of the model was associated with a major resistance component and were named as: 1) steel-concrete bond component, 2) cyclic friction component, and 3) virgin friction component.

Each of the cyclic models discussed above reflects progressively more experimentally observed behavior. All of the models discussed above are one-dimensional in nature (*i.e.*, they relate bond stress to slip). Some analysts (see *e.g.*, Eligehausen *et al.*, 1983) adjust the monotonic envelope to account for the external transverse pressure, but the pressure developed due to the wedging action of the ribs is not explicitly included. Thus, there is no potential for the models to predict a splitting failure; pull-out failure is assumed *a priori*. While there is no claim of generality, they are relatively simple to implement at the "member scale" using a discrete reinforcement model and have been incorporated in the analysis of many structural components.

These models were usually implemented as the tangential constitutive relationship for a nodal link or interface element (see *e.g.*, ASCE [1982]). The normal constitutive

relationship (*i.e.*, relating normal stress and radial dilation) at the member-scale was assumed to model the doweling response of the reinforcement.

Two-Dimensional Bar-Scale Models

The models which are most closely related to the one developed in this study incorporate normal stress and radial dilation in the formulation at the bar-scale; that is, these components are associated with the mechanical interaction of the ribs. To model this interaction the normal and tangential components must be coupled, and thus they will be referred to as *two-dimensional models*. As previously mentioned, one benefit of bar-scale models is the potential to predict splitting failures.

Many two-dimensional models have been based upon very mechanical representations of the wedging action. They attempt to explicitly model the response of the inclined compression struts. A few of these models are briefly reviewed below.

De Groot *et al.* (1981) developed a two-dimensional model which included two components in parallel (*i.e.*, they experienced the same slip). The first component represented the behavior of a plane bar, and the second component represented the response of the inclined struts. The first component was modeled as elastic perfectly plastic. The elastic portion was attributed to the local elastic response of the concrete. The perfectly plastic response began at a defined value of slip. In refining the model, this slip value was expressed as a quadratic function of the normal stress at the bar (assuming a compressive normal stress) .

In the second component of this model, the inclined struts were idealized as cone-shaped "prisms" with no frictional interaction. The shear and normal stresses were related to incremental slips and radial displacements by simple considerations of the equilibrium and kinematics of the inclined strut (similar to Appendix A of Herrmann and Cox [1994]). These relations are fully defined given the angle, length, and stiffness of the strut.

The authors developed novel, combined bond-reinforcement models applicable to axisymmetric and three-dimensional problems. Validation problems were conducted using both tensile (axisymmetric and three-dimensional) and "beam-end" (three-dimensional) specimens. The concrete was represented by an elastoplastic Mohr-Coulomb model with two tension cut-off criteria. The analyses exhibited relatively good agreement with the experiments in predicting bar strains. Qualitatively, specimen cracking was predicted well but localized cracking was broadly distributed in the analysis. The validation examples were limited to small slips. It appears the formulation would not correctly estimate the response for large slips (typical of pull-out failures) since the wedging effect of the inclined struts was not history dependent. The incorporation of a softening response in the bond model might have contributed to more localized cracking in the specimen.

Morita and Fujii (1985) implemented "combined link elements" which included both a standard *slip link* (with tangential and normal "springs") and a *wedge link* with inclined springs.* The links were connected in series (*i.e.*, they saw the same force). A piecewise linear, cyclic bond law (Morita and Kaku [1973]) related the tangent force and corresponding relative displacement in the slip link; the monotonic portion was bilinear. Each spring in the wedge link: 1) was inclined at 45 degrees, 2) behaved elasticly in compression, and 3) carried no tension.

Zhiming *et al.* (1992) presented an "inclined strut model." They relate the bond stiffness to the stiffness of the inclined strut by defining the direction of the force transferred by the strut. The direction of this force is estimated from observed angles of inclined cracks and the coefficient of friction. The bond stiffness was obtained from the derivative of a bond stress-slip formula based on numerous experiments; it was the product of a fourth order

* According to De Groot *et al.* (1981), Van Mier (1978) had previously incorporated inclined springs to model the wedging action of the ribs.

polynomial in slip, the concrete splitting strength, a function of the cover thickness, and a function of the position along the bar. The last two functions include "design parameters" that will not be necessary in more general bar-scale models (*i.e.*, when the model is affected by the state of the specimen).

The remaining mechanical model was developed by Mainz *et al.* (1992). In contrast to the slip and wedge (*i.e.*, inclined nodal link elements with one-dimensional laws) links in series, the authors use two sets of interface elements. Inclined interface elements (at 30 degrees relative to the axis) model the wedging action of the ribs, and interface elements with "normal orientation" model the effect of the cylindrical surface between the ribs.

In the tangent-normal coordinate system of each interface element, the constitutive relations were uncoupled (*i.e.*, were one-dimensional). The normal relation of the inclined interface elements was nonlinear elastic; the normal stress initially increased with normal displacement and then decreased. This relationship contained three adapting parameters that were determined for each study. Very high stiffnesses (apparently constant) were selected for each of the other constitutive relations, but apparently there was no stiffness without contact (*i.e.*, when the relative normal displacement was positive).

The authors successfully modeled several sets of bond tests with excellent accuracy. They included examples where the specimen was modeled with three-dimensional finite elements without assuming an axisymmetric state near the bar. All of the examples presented only extended to the ultimate bond stress. The authors indicated that determining the adapting parameters was difficult. Through these parameters they were able to account for variations in concrete strength, bar diameter, rib pattern, bar position within the specimen, and external transverse pressure. While the accuracy was excellent, it appears the adapting parameters were recalibrated for each study. Additionally, the explicit use of inclined interface elements does not appear easy to extend to cyclic applications.

All of these models gave some of the qualitative behavior of the mechanical interaction and could produce splitting failures in a specimen. Each study effectively demonstrated the potential of using a bar-scale model to investigate the response of a structural component or test specimen.

Mehlhorn and Keuser (1985) presented a two-dimensional model where the bond stress divided by the concrete strength was expressed as a cubic function of the slip up to the ultimate bond strength; the model behaved as perfect plasticity under continued monotonic loading. The slip was nondimensionalized by the slip at ultimate bond strength which was defined to be a linear function of the normal stress at the bar; this produced a more "ductile" response with higher confinement stresses as observed experimentally. The cubic bond stress function included four factors that account for 1) aggregate size, concrete consistency and casting position, 2) rib geometry, 3) normal stress and radial dilation, and 4) bar strain and orientation of transverse cracks.

While the model does include normal stress and radial dilation, they only serve to modify the one-dimensional bond stress function. Based upon the experimental results of Dörr (1978), the scaling factor increases with compressive normal stress with a positive curvature (*i.e.*, it is nonconvex when the scale factor is interpreted as a measure of bond stress). The influence of radial dilation was designed to account for radial tension in the bond zone. When the radial dilation is equal to the rib height the scale factor is zero, and when the radial dilation is zero the scale factor is one. Apparently the only constraint on radial dilation is that it must be nonnegative. This bar-scale model attempts to introduce the contribution of many parameters, but it does not account for the wedging action of the ribs.

All of these models have obvious strengths, but they do not fulfill the objective of this project; they all lack in one of the following areas: 1) application to large slips, 2) extendibility to cyclic loading, 3) accurate radial response

(important for splitting crack predictions), or 4) requirement of a single calibration (for standard bars).

1.5 Nomenclature

In this section nomenclature is presented which is used throughout the text. In particular, model calibration parameters are referenced to the points in the text where they are defined. Most of the nomenclature presented is also defined "locally" within the text. Nomenclature that is defined and used locally is not listed below.

The rank of a quantity is usually reflected in its nomenclature as follows: scalars are italicized, vectors are underlined, and matrices are bold-faced. Standard indicial notation is used to express some tensor relations.

Greek Symbols

α_e — A factor in the exponent of the yield criteria's "exponential criterion." It is introduced in Equation (3.3-1a) and has a calibrated value of 0.27.

α_p — The exponent of the yield criteria's "power criterion" component. It is introduced in Equation (3.3-1b) and has a calibrated value of 0.40.

β — A parameter for the kinematic softening function. It is introduced in Equation (3.4-4) and calibrated to a value of approximately 2.7.

$\underline{\delta}$ — The vector (physical and algebraic) of relative displacements between the inner and outer surfaces of the bond zone. The superscripts "e" and "p" are used to denote $\underline{\delta}$'s elastic and plastic components, respectively. See Section 3.1.

δ_n — The average, relative normal displacement of the bond zone over a unit cell -- one component of $\underline{\delta}$. When it is positive it is referred to as the *radial dilation*; when it is negative it is referred to as the *radial contraction*.

δ_t — Slip -- the average, relative tangential displacement of the bond zone over a unit cell. It is one component of $\underline{\delta}$.

λ The loading index -- it is positive if and only if plastic deformation is occurring. It is a function of the state variables ($\underline{Q}$ and $\underline{h}$) and the stress rates ($\dot{\underline{Q}}$).

σ The normal stress -- the average normal stress over a cycle of the bar's rib pattern. It is defined in Equation (3.1-2).

$\hat{\sigma}$ The kinematic softening function. It is initially referenced in Equations (3.3-1) and later defined in Equation (3.3-4).

$\hat{\sigma}_0$ The initial value of the kinematic softening function (*i.e.*, at zero damage). It is referenced in Equations (3.3-4) and calibrated to a value of 2.25.

τ The bond stress -- the average shear stress over a cycle of the bar's rib pattern. It is defined in Equation (3.1-2).

τ_{max} The maximum bond stress -- also referred to as the *bond strength.*

ϕ The yield function -- it is a function of the state variables ($\underline{Q}$ and $\underline{h}$). Reference Inequality (2.2-1) and Equations (2.2-2) and (3.3-2).

Ψ Complementary energy function -- a potential function for elastic strains. It can be expressed in terms of generalized stresses and internal variables to incorporate elastoplastic coupling effects. Reference Section 2.4.

Latin Symbols

{a} A set of five parameters for C that affect the isotropic hardening. They are introduced in Equation (3.3-6), and calibration values are given in Table 3.3-1.

{b} A set of five parameters for C that principally affect the isotropic softening. They are introduced in Equation (3.3-6), and calibration values are given in Table 3.3-1.

C The isotropic hardening and softening function. It is introduced in Equation (3.3-2), and its specific form is defined in Equation (3.3-6).

C_∞ A parameter of the function C that uniformly changes the range of the function (*i.e.*, an additive constant). It is introduced in Equation (3.3-6), and the calibration value is listed in Table 3.3-1.

d The bond zone damage -- the only internal variable of the model. It is defined in Equation (3.2-3) as the plastic slip divided by the rib spacing.

(d_0, d_1) The interval for which weighting function, W_e, changes from 0 to 1. The interval's limits are introduced in Equation (3.3-3) and calibrated to be 0.38 and 0.53, respectively.

d_2	The damage value at which kinematic softening is complete. It is introduced in Equation (3.3-4) and calibrated to a value of 0.1.
$\mathbf{D}$	The elastoplastic moduli. Reference Section 2.5.
$\mathbf{D}^e$	The elastic moduli. Reference Equation (2.4-3a) and Chapter 5.
D_b	Diameter of the core of the bar.
expFunc	A "standard function" used in the development of the bond model; it has an exponential function in its form. It is defined in Equation (3.3-5a).
E_c	The elastic modulus of concrete. In this study, the value is estimated by Equation (B-2).
g	The *rate of dilation* -- more accurately it is the rate of plastic radial dilation with respect to plastic slip. This is the second component of $\underline{R}^p$, and is a function of both d and σ. It is introduced in Equations (4-1), and its calculation is fully defined by Algorithm 4.3-1.
$g_{min\infty}$	A parameter defining the radial contraction stage of g. The calibration value is given in Table 4.3-4.
$\{h_1,...,h_5\}$	Parameters defining the radial contraction stage of g. Their calibration values are given in Table 4.3-4.
h_n	The n^{th} element of the set of internal variables. These variables characterize the structure of the material.
$H()$	Heaviside step function.
$\{i_1,i_2,i_3\}$	Parameters which define a portion of the dilation function in scaled-space, g_s. The calibration values are listed in Table 4.3-3.
K^p	The plastic modulus -- it is positive during hardening. Reference Equation (2.2-8).
$\underline{q}$	Vector of generalized strains. Reference Sections 2.2 and 2.3 and Equations (3.1-1) and (3.1-2).
$\underline{q}^e$	Vector of generalized elastic strains. Reference Equation (2.3-1) and Section 2.4.
$\underline{q}^p$	Vector of generalized plastic strains. Reference Equations (2.3-2), (4.1-1), and Chapter 4.
$\underline{Q}$	Vector of generalized stresses.
ratFunc	A "standard function" used in the development of the bond model that can take the form of a rational function. It is defined in Equation (3.3-5b).

$\underline{R}^p$ Direction of incremental plastic deformation. Reference Equation (2.3-2) and Chapter 4.

s_r Spacing of the ribs along the bar (*i.e.*, the interval of the rib or deformation pattern).

W^p Total plastic work, defined in Equation (2.2-3).

W_e The weighting function between the power and exponential components of the yield surface. It is introduced in Equation (3.3-2) and later defined in Equation (3.3-3).

$\{Z_1, Z_2, Z_3\}$ Zeroes of the function g. It is initially defined in Figure 4.3-1. The calibration values are $\{0.35_{\text{scaled}}, 0.48, 0.8\}$ where the subscript on the first value indicates it is defined in scaled space.

Miscellaneous Symbols

C^1 Denotes a function has continuous first derivatives.

$\underline{\nabla}_Q$ Gradient operator with respect to the generalized stress components.

Unique Terminology

bar-scale ~ the scale of analysis characterized by a phenomenological bond model (*i.e.*, the mechanical interaction of the ribs is homogenized). See Figure 1-1.

bond strength ~ the maximum or ultimate bond stress.

bond stress ~ the generalized shear stress defined in Section 3.1. This is τ of Equation (3.1-2).

bond stresses ~ the generalized shear and normal stresses, $\underline{Q}$, defined in Section 3.1.

bond zone ~ a concrete region adjacent to the bar which is damaged by the mechanical interaction between the steel bar and concrete. The crushing and transverse cracking associated with bond occur within this zone. Longitudinal cracks may extend beyond this zone. Reference Figure 3.3-1.

confinement stress ~ an average compressive normal stress at the surface of the bar. The average is taken over the length of a unit cell which contains one cycle of the rib pattern. This is $-\sigma$ of Equation (3.1-2).

geometric dilation ~ dilation of the bond zone due to the rigid body interaction (*i.e.*, assuming the existence of several splitting cracks and loss of adhesion) between the inclined rib face and adjacent concrete.

interface assumption ~ the assumption that the response of the bond zone can be adequately characterized as an interface phenomenon. Reference Equation (3.1-2).

longitudinal crack ~ a crack that is idealized as occurring in a θ-coordinate plane. Once the crack has reached the outer boundary of the specimen, it is more appropriately referred to as a splitting crack.

micromechanics ~ the mechanics of bond associated with adhesion, friction, and the mechanical interaction of the ribs and adjacent concrete. In the context of this work, it is synonymous with *rib-scale mechanics*. The use of the term micromechanics to describe the scale of the bond mechanisms is not uncommon (see *e.g.*, Gerstle and Ingraffea [1990]); however, some object to its use based on the actual size of the ribs and bond zone. From a relative size point-of-view, the ribs are orders of magnitude smaller than the characteristic dimensions of the structure, so the term is adopted here for brevity.

member-scale ~ the scale of analysis where the bar diameter is orders of magnitude smaller than the characteristic size of the problem. The effect of the steel reinforcement is typically smeared at this scale. See Figure 1-1.

rib-scale ~ the scale of analysis characterized by explicit modeling of the rib geometry, Models of this scale are also referred to as micromechanical models. See Figure 1-1.

splitting crack ~ a crack that is idealized as occurring in a θ-coordinate plane. These cracks are also referred to as longitudinal cracks. Unless the crack has reached the outer boundary of the specimen, "longitudinal crack" is preferred; "splitting crack" is often loosely used in this case, and reflects the potential of the crack to split the specimen.

transverse crack ~ a "cone shaped" crack initiating at the ribs due to the mechanical interaction between the rib and adjacent concrete. They are also called bond cracks.

Chapter 2

Incremental Plasticity Theory – An Overview

This chapter provides some background information on incremental plasticity theory. The first section examines why elastoplasticity would appear to provide a good framework for the description of bond. The four subsequent sections overview the general form of an elastoplastic model indicating some of the simplifying assumptions on which the bond model is currently based. The remaining section addresses the uniqueness and stability of solutions to boundary-initial value problems that incorporate elastoplasticity constitutive laws.

2.1 Motivation For Using Elastoplasticity

Just as researchers have applied numerous classes of constitutive models to plain concrete, it's likely the same will occur with the modeling of bond. Each class of constitutive models has its own strengths, weaknesses and "evangelistic followers." It would be mathematically pleasing to claim that the theory of elastoplasticity uniquely provides the only valid approach to bond, but this is not the case. The choice of using elastoplasticity is based upon 1) experimental results that exhibit classical elastoplastic behavior, 2) extendibility of a "monotonic model" to a "cyclic model" by using a multiple branch yield surface and modifying the evolution laws (see Herrmann and Cox [1994]), and 3) the potential of extracting the characterization from a database of existing bond tests.

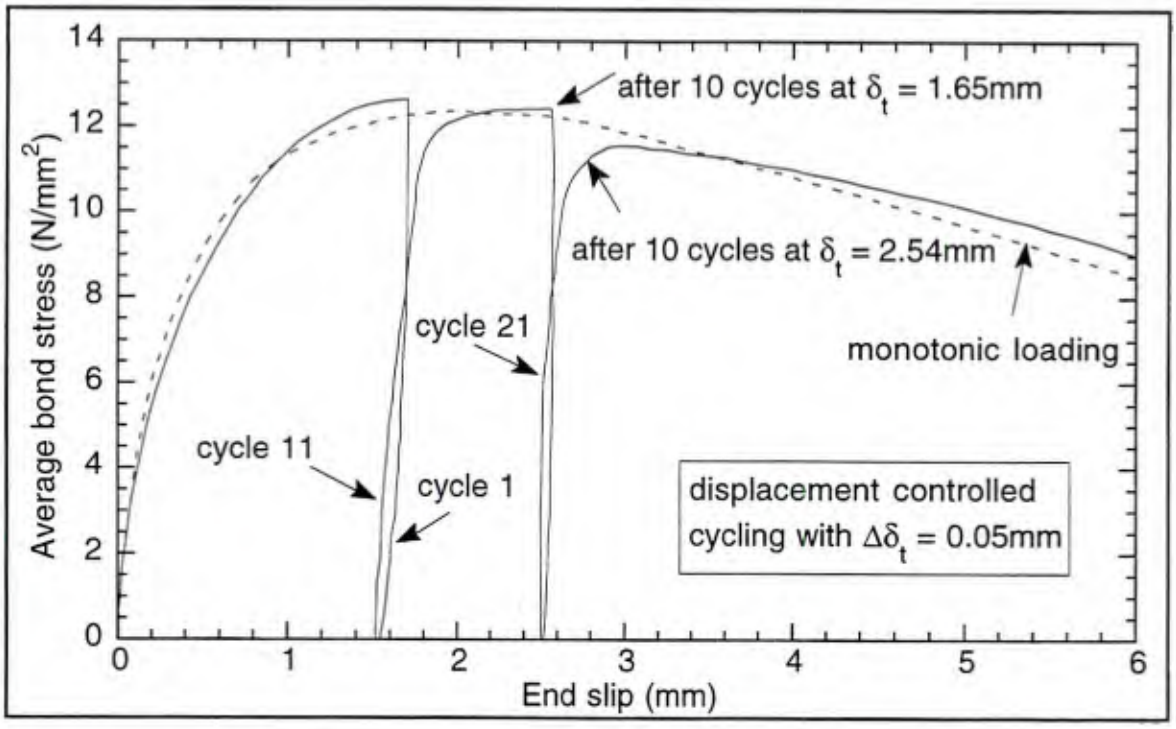

Figure 2.1-1 Bond stress–slip relationship including two series of low intensity cyclic loadings at prescribed slips (from Eligehausen *et al.* [1983], Figure 4.37).

Figure 2.1-1 shows classical elastoplastic behavior in a bond test by Eligehausen, Popov and Bertero (1983). Though this test includes ten low intensity cyclic loadings (change in slip equal to 0.05 mm) at the two designated slips, the behavior of interest is the corresponding unloading and reloading responses. It is not apparent from the response where permanent deformation is first induced, but the elastic unloading and reloading exhibits the motivation for an elastoplastic model. Most bond models incorporate a single stress component in their formulation and thus the reloading is viewed as a return to the *monotonic envelope* in τ-δ_t space (see *e.g.*, Eligehausen *et al.* [1983]).

Figure 2.1-2 shows the response of another test in the study by Eligehausen, Popov and Bertero (1983) where the cyclic loading is more substantial and centered about the initial position (zero slip). This figure explicitly presents typical cyclic bond response. The elastic unloading is followed by a plastic deformation with very little reversal of bond stress

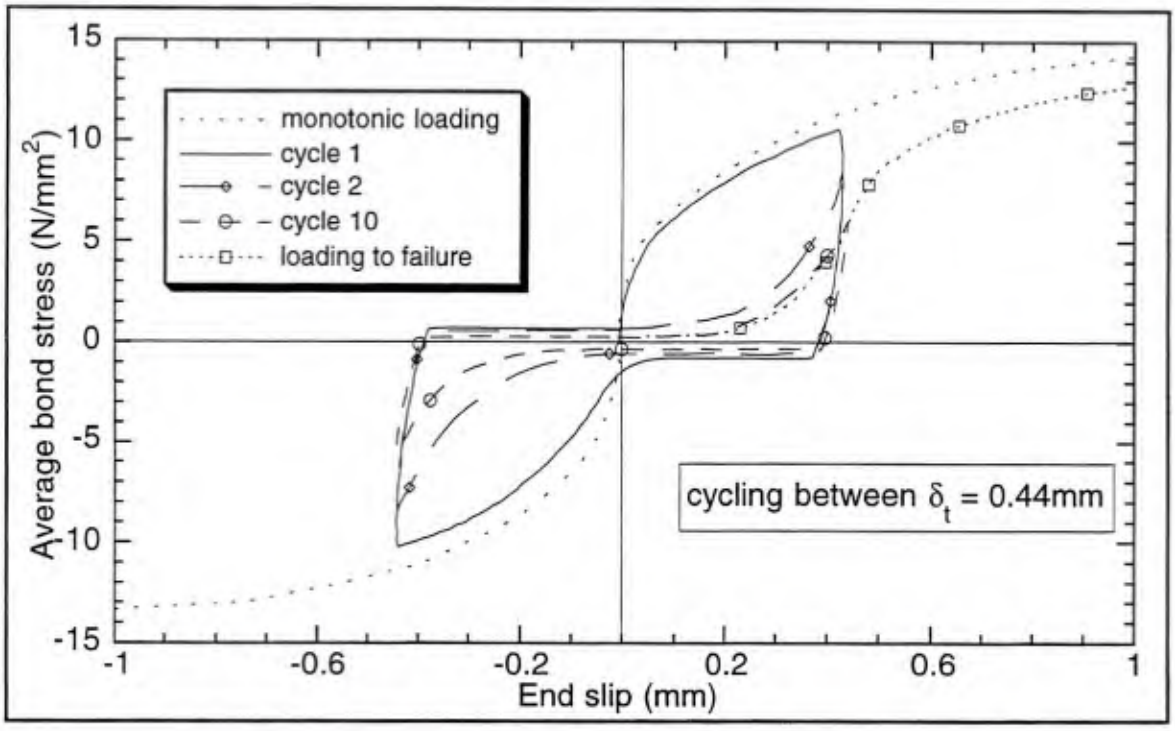

Figure 2.1-2 Bond stress–slip relationship including a small number of cyclic loading about zero slip. (from Eligehausen *et al.* [1983], Figure 4.25a).

– essentially a frictional behavior. The obvious contribution of a friction mechanism in the cyclic response further motivates the use of an elastoplastic model since the behavior of many interfaces has been modeled with Coulomb's law. Though not within the scope of this study, the potential for representing this friction-compaction phase in cyclic loading by modifying the hardening/softening law is apparent. For details on the subsequent cyclic bond model developed in this study see Herrmann and Cox (1994).

The mechanisms associated with the plastic behavior in bond are fundamentally different from those associated with metal plasticity. In metal plasticity the behavior is characterized by the movement of dislocations. Usually the local structure of the material and thus the elastic properties are not strongly affected by the motion of these dislocations. In modeling bond, one can assume that the local structure of the concrete near the contact, rib face does not significantly change (as suggested by the similar elastic responses shown in Figure 2.1-1). However if one considers all of the material near the rib (*i.e.*, include the material that

has already been significantly damaged by the rib), there is significant change in the local structure to the extent that a completely different mechanism now dominates the behavior in reverse loading (as suggested by Figure 2.1-2). In metal plasticity the Bauschinger effect has been explained by the pileup of dislocations, but otherwise the response in reverse loading does not significantly change; the same mechanisms prevail because the local structure of the material remains essentially unchanged.

2.2 Yield Surface

In classical incremental plasticity theory it is assumed that for some set of stress states a material behaves in an elastic manner such that stress and strain are uniquely related. Let's define a set of *generalized* stresses and strains that will be represented in vector form as $\underline{Q}$ and $\underline{q}$ respectively.*

The first component of the model description is a quantitative definition of the stress states for which elasticity alone governs the behavior. In general, this set of stress states changes with plastic deformation; physically this means that the state of the material is defined not by the stresses alone, so some measure of the internal structure must be included.† The change in the internal structure is characterized by a set of *internal variables*, $\{h_n\}$. The *state variables* are then defined as the union of the *external variables*, in this case stresses, and the internal variables. For a given internal structure – set of internal variables – the stress states for which elastic behavior is eminent with a change in stress satisfy the relationship

---

* These stresses and strains are generalized in the sense that they may not actually be tensor quantities. In this context "vector form" indicates the use of linear algebra notation, not that the generalized stresses and strains are vector quantities in the physical sense. For brevity the modifier "generalized" will be dropped in the remaining discussion.

† In this study the internal state is measured locally – at a point.

$$\phi(\underline{Q},\underline{h}) < 0 \tag{2.2-1}$$

This open set of stress states is often referred to as the *elastic region*.

Elastic unloading can occur with equality in the above expression as well; however, when

$$\phi(\underline{Q},\underline{h}) = 0, \tag{2.2-2}$$

there exist stress increments which will result in permanent deformation. Equation (2.2-2) is thus referred to as the *yield criterion*. In stress space (or more generally, external variable space) Equation (2.2-2) has the interpretation of a surface (or hypersurface if the dimension of the stress space exceeds three). This surface is the boundary of the elastic region and is referred to as the *yield surface*. The combination of Equations (2.2-1) and (2.2-2) represents a constraint in stress space on the response of the material since by definition all valid stress states must lie on or within the yield surface. Continued yielding thus requires the stress state to remain on the yield surface, which is commonly referred to as the *consistency condition*.

Except for the case of perfect plasticity where plastic deformations occur without a change in the internal structure, consistency requires a change in the internal variables to accommodate changes in stress during yielding. Assume that the rate constitutive equations for the internal variables – *evolution laws* – are of the form

$$\dot{h}_i = \langle \lambda \rangle \overline{h}_i \tag{2.2-3}$$

where λ is the *loading index* which will be a natural result of the consistency condition in the following development. The loading index is positive for plastic loading and thus the Macaulay bracket notation implies Equation (2.2-3) is only nonzero for this case (*i.e.*, the internal variables only change with plastic loading). Each evolution law, $\overline{h}_i$, is a function of the state variables. Evolution laws are often expressed as functions of the rates of two alternative variables: *accumulated plastic strain* or *plastic work,* which can be defined as

$$\bar{q}^p = \int \|\dot{\underline{q}}^p\| dt \tag{2.2-4}$$

and

$$W^p = \int \langle \underline{Q}, \dot{\underline{q}}^p \rangle dt \tag{2.2-5}$$

respectively.* ||.|| denotes a vector norm; <.,.> denotes an inner product – which is just the Euclidean inner product when $\underline{Q}$ and $\underline{q}$ are *conjugate* (*i.e.,* work conjugate). Evolution laws incorporating the former are referred to as *strain hardening* laws, while those incorporating the latter are referred to as *work hardening* laws.

The enforcement of consistency during loading, that is

$$\dot{\phi}(\underline{Q}, \underline{h}) = 0 \tag{2.2-6}$$

implies that the loading index is defined as

$$\lambda = \frac{1}{K^p} \frac{\partial \phi}{\partial Q_i} \dot{Q}_i \tag{2.2-7}$$

where the plastic modulus, K^p is given by

$$K^p = -\frac{\partial \phi}{\partial h_i} \bar{h}_i \quad . \tag{2.2-8}$$

In the recent text on plasticity theory by Lubliner (1990), he presents rate independent plasticity as the limiting case of classical viscoplasticity where the viscosity approaches zero. Clearly the constraint in stress space of plasticity theory is achieved in this limit. This will be further addressed in Chapter 6.

---

* Alternatively, instead of using a measure of the total plastic strain, measures of the dilatational or distortional components of the plastic strain are also used.

2.3 Flow Rule

Let's assume that the strain rates are decomposed in the common additive form as

$$\dot{\underline{q}} = \dot{\underline{q}}^e + \dot{\underline{q}}^p. \tag{2.3-1}$$

The plastic strain rate relationship should be written in a form similar to Equation (2.2-3) since the plastic strains are associated with the evolution of the internal variables. Thus the plastic strain rates are given by

$$\dot{\underline{q}}^p = \langle \lambda \rangle \underline{R}^p. \tag{2.3-2}$$

The vector $\underline{R}^p$ depends upon the state variables and defines the direction of plastic deformation. Though it is a misnomer except for the case of perfect plasticity, it is often referred to as the *flow rule*. When $\underline{R}^p$ is in the direction of the gradient of ϕ, the flow rule is referred to as an *associative flow rule* (associated with the normal to the yield surface). Materials with associative flow rules are also said to satisfy the *normality rule*, and are sometimes referred to as *standard materials*. Though the assumption of an associative flow rule is quite common in material modeling, we will see in a later section that the generalization to a nonassociative flow rule is regretfully necessary in the modeling of bond. This is not surprising since friction is a component mechanism of bond. Materials which exhibit high sensitivity to pressure and relatively small volume changes are often called *frictional materials*.

For the assumed form of the evolution laws (Equation 2.2-3) and flow rule (Equation 2.3-2), the loading index relationship (Equation 2.2-7) implies these relationships are homogeneous of order one in the stress rates. This means if the stress rates change by a factor p, so do the rates of change of the internal variables and plastic strains (*i.e.*, this form gives rate independent behavior).

Prager (1949) formulated four postulates for the mathematical theory of plasticity. One condition was irreversibility which requires a positive rate of entropy production. This condition follows from the second law of thermodynamics and requires the plastic work to be positive. However, modern plasticity laws for metals incorporate the concept of residual or back stresses (which are physically explained as being due to the build-up of dislocations). Back stresses can produce inverse plastic deformation during unloading. Physically, there is a release of energy from the material that was stored during previous inelastic response and thus the inelastic work is negative. For brittle materials such as concrete there is no analogous behavior. The change of state of brittle materials is characterized by increased microcracking, so in the context of the bond model the plastic work must always be nonnegative as postulated by Prager. Thus even with a nonassociative flow rule there are constraints on the direction of the plastic strain increments. This thermodynamic constraint is addressed in more detail in Chapter 4.

2.4 Elasticity

Now only the elastic relations remain to be defined. For some materials plastic deformation directly affects the elastic behavior. That is, the plastic deformation changes the structure of the material in such a way that it changes the subsequent elastic response. This *elastoplastic coupling* has been observed by several researchers (see *e.g.*, Rehm [1957] and Lutz and Gergely [1967]) working on bond so the added generality will be presented here though it will later be omitted in the current version of the bond model. For this discussion assume the existence of a complementary energy function $\Psi(\underline{Q},\underline{h})$ where the coupling comes from the inclusion of the internal variables. With the existence of this function the elastic strains can be expressed as

$$q_i^e = \frac{\partial \Psi}{\partial Q_i} \tag{2.4-1}$$

The elastic strain rates are then obtained from the chain rule and can be written in indicial form as

$$\dot{q}_i^e = \frac{\partial^2 \Psi}{\partial Q_i \partial Q_j} \dot{Q}_j + \frac{\partial^2 \Psi}{\partial Q_i \partial h_n} \dot{h}_n \quad . \tag{2.4-2}$$

Using matrix notation this can be written more compactly as

$$\underline{\dot{q}}^e = \mathbf{D}^{e-1} \underline{\dot{Q}} + \langle \lambda \rangle \underline{R}^c \tag{2.4-3a}$$

where

$$\mathbf{D}^e = \left[\frac{\partial^2 \Psi}{\partial Q_i \partial Q_j} \right]^{-1} \quad \text{and} \quad \underline{R}^c = \left[\frac{\partial^2 \Psi}{\partial Q_i \partial h_j} \right] \underline{\bar{h}} \quad . \tag{2.4-3b,c}$$

Consider the right-hand side of Equation (2.4-3a). The first product gives an incrementally reversible strain rate ($\underline{\dot{q}}^r$); this is the only term that would exist if the complementary energy was a function of the stress state alone. The second product represents the strain rates due to the elastoplastic coupling which are not reversible ($\underline{\dot{q}}^c$).

2.5 Elastoplastic Moduli

With all of the above constitutive relations, let's now determine the theoretical relationship between the stress and total strain rates. We start by using the definition of the reversible strain rate (given above) which implies

$$\underline{\dot{Q}} = \mathbf{D}^e \underline{\dot{q}}^r . \tag{2.5-1}$$

Equations (2.3-1), (2.3-2) and (2.4-3) allow this to be written as

$$\underline{\dot{Q}} = \mathbf{D}^e \underline{\dot{q}} - \langle \lambda \rangle \mathbf{D}^e (\underline{R}^p + \underline{R}^c). \tag{2.5-2}$$

The loading index is still expressed in terms of the stress rates, Equation (2.2-7); it must be expressed in terms of the strain rates to obtain an explicit relationship for the stress rates. To obtain an expression for the loading index in terms of the strain rates consider the form of Equation (2.2-7). By assuming plastic loading, taking the inner product of both sides of Equation (2.5-2) with $\underline{\nabla}_Q\phi$ and solving for λ, we obtain

$$\lambda = \frac{1}{K^p + \underline{\nabla}_Q\phi\,(\underline{R}^p+\underline{R}^c)}\,\underline{\nabla}_Q\phi\;\mathbf{D}^e\,\dot{\underline{q}}. \tag{2.5-3}$$

Substituting this back into Equation (2.5-2) gives the relationship between the stress and total strain rates as

$$\dot{\underline{Q}} = \left(\mathbf{D}^e - \frac{H(\lambda)}{K^p + \underline{\nabla}_Q\phi\,(\underline{R}^p+\underline{R}^c)}\,\mathbf{D}^e(\underline{R}^p+\underline{R}^c)\underline{\nabla}_Q\phi\;\mathbf{D}^e\right)\dot{\underline{q}} \tag{2.5-4}$$

where $H(\lambda)$ denotes the Heaviside step function operating on the loading index. The matrix within the parenthesis contains the incremental tangent stiffness moduli, which in the absence of plasticity simply reduces to the elastic moduli. When plasticity is present, it subtracts a rank one matrix from $\mathbf{D}^e$. Since $\mathbf{D}^e$ was derived from a potential function in the above development, continuity of Ψ implies it is symmetric. Thus the elastoplastic tangent stiffness matrix is symmetric if and only if the rank one matrix subtracted from $\mathbf{D}^e$ is symmetric, and this rank one matrix is symmetric if $\underline{\nabla}_Q\phi$ is proportional to $\underline{R}^p+\underline{R}^c$. This implies that in the absence of elastoplastic coupling $\mathbf{D}$ is symmetric if and only if the flow rule is associative.

Many nonlinear finite element analyses use the Newton-Raphson method to solve the global system of nonlinear equations. For a given material state, Equation (2.5-4) can be used as an estimate to the tangent constitutive matrix needed to determine the Jacobian matrix for the Newton-Raphson method. The motivation for using the Newton-Raphson method is its quadratic convergence which occurs for many problems when "in the

neighborhood of the solution." Using the above tangent constitutive relationship in the calculation of the Jacobian will not necessarily yield the coveted quadratic convergence. Simo and Taylor (1985) derived *algorithmically consistent elastoplastic moduli* that may be used to guarantee quadratic convergence.

With the pertinent equations of elastoplasticity presented, it would be highly desirable to be able to make definitive statements about the "nature of the solutions" obtained with their use – specifically in the areas of solution existence, uniqueness and stability. Though desirable, the scope of this study does not fully address these important topics. The following section presents an overview on the topics of uniqueness and stability with emphasis on materials with nonassociative flow rules.

2.6 Uniqueness and Stability

In elastic solids uniqueness and stability are closely related ; the relationship in plastic solids is looser but important (Hill [1958]). The following subsections address these topics separately.

Both uniqueness and stability address the mathematical nature of a solution to a boundary-initial value problem. Certainly one hopes the nature of this solution reflects the physical behavior of the actual system. Since uniqueness and stability are attributes of the entire solution, they are affected by each component of the boundary-initial value problem; the emphasis here is upon the effect of elastoplastic constitutive relationships on these attributes. That is, what constraints are there on elastoplastic material laws in order to satisfy necessary and sufficient conditions for uniqueness and stability.* These conditions

---

* These conditions for stability comprise the topic of *material stability*. By definition it is local in nature since material stability does not necessarily imply system stability and visa versa; the constitutive law is

have given rise to several material classifications which will be discussed in an *aside* within the next subsection.

Uniqueness*

For a body made of a linear elastic material subjected to small displacements and deformations, the classical uniqueness theorem of Kirchoff indicates that the stress solution for a given loading is unique and that the corresponding displacement solution is unique if the external constraints are sufficient to prevent rigid body motion. The key to the proof of this theorem is the positive definiteness of the elastic moduli (see *e.g.,* Sokolnikoff [1956]).

For a nonlinear elastic material the same arguments can be used to prove uniqueness of the infinitesimal increments. Uniqueness of the incremental solution then implies uniqueness of the global solution. The proof of uniqueness for this class of materials requires the tangent elastic moduli to be positive definite.

For bodies composed of elastoplastic materials, uniqueness theorems have been proven for certain classes of materials. With the absence of unloading, certainly no distinction can be made between an elastoplastic body and a nonlinear elastic body; thus the arguments mentioned above for nonlinear elastic bodies are valid here as well.

Melan (1938) showed that uniqueness of the incremental solution can be proven for work-hardening materials with an associative flow rule when unloading has occurred provided the hypothesis of infinitesimal strains is valid.† Sufficient conditions for uniqueness are

footnote continued from previous page
just one component of the boundary-initial value problem. However, a propagation of material instability can lead to instability of the system.

* Much of the material in this section is an overview of the discussion given by Lubliner (1990).

† Hill (1958) claims to have given a more rigorous and general proof in his 1950 paper.

the positive definiteness of the elastic moduli ($\mathbf{D}^e$) and the positiveness of the plastic modulus (K^p). In the work hardening limit of perfect plasticity, the stress field is unique but not the strain field.

When a nonassociative flow rule is employed, positive definite elastic moduli and a positive plastic modulus are not sufficient conditions for uniqueness. Mroz (1963) derived an alternative sufficient condition for this case that requires the plastic modulus to be bounded below by a critical value; he showed that Drucker's postulate (presented in the next subsection) – which materials with nonassociative flow rules inherently violate – though known to be sufficient is not a necessary condition for uniqueness. Raniecki (1979) presented a critical value in a different form.*

In applying the bond law, the sufficient conditions presented by Mroz (1963) and Raniecki (1979) are only applicable in the early part of the loading since the plastic modulus does not even remain positive (see Chapter 7).

Stability

In subjects ranging from mathematics to mental health, a "system" is referred to as *stable* if small changes to the input of the system produce correspondingly small changes to its output. An instability in a material model is undesirable if it is merely a mathematical quirk; however, if this instability reflects a physical instability in the material then it is a desirable attribute – despite the protests of the numerical analysts.

Many definitions of stability (see *e.g.,* Drucker [1964]) have been proposed to characterize the mathematical behavior of plasticity models,* some of which will be considered in this

---

* For the case of an associative flow rule, the critical value becomes zero reducing to the sufficient condition previously discussed.

* To the extent that Hill (1958) referred to the literature as "a confused literature."

section; essentially, the differences in the definitions correspond to different interpretations of the meaning of "small changes" with respect to both the input and output of the system. This section will consider 1) Drucker's definitions of a stable material for which a small change in the input (a stress increment) is produced by an external agency, 2) Mandel's (1964) definition of a stable material – being capable of propagating a small perturbation in the form of waves, and 3) an instability of finite excursion recently analyzed by Drucker and Li (1992).

In early papers on material stability, Drucker (1950, 1951) defined a restricted class of work-hardening materials by generalizing the characteristics of uniaxial stress-strain curves; by his definition these materials were stable. Lubliner (1990) presents a summary of Drucker's early work upon which the following is based.

Consider the second order terms $d\sigma d\varepsilon$ *and* $d\sigma d\varepsilon^p$. These terms have the units of work per volume and Drucker interpreted them as:

> "if a unit volume of an elastic-plastic specimen under uniaxial stress is initially at stress σ and plastic strain ε^p, and if an *external agency* slowly applies an incremental load resulting in a stress increment $d\sigma$ and subsequently slowly removes it, then $d\sigma d\varepsilon = d\sigma(d\varepsilon^e+d\varepsilon^p)$ is the work (actually twice the work) performed by the external agency in the course of incremental loading, and $d\sigma d\varepsilon^p$ is the work performed in the course of the cycle consisting of the application and removal of the incremental stress."

Drucker defined a material to be a work-hardening (or "stable") plastic material if: 1) the work during incremental loading was positive, and 2) the work done in the cycle is nonnegative – known in the literature as *Drucker's postulate*. Drucker generalized the definition to three-dimensional states of stress and strain as

$$d\sigma_{ij}d\varepsilon_{ij}>0 \quad \text{and} \quad d\sigma_{ij}d\varepsilon^p_{ij}\geq 0. \tag{2.6-1a,b}$$

The external agent is assumed to be independent of whatever caused the current load and, by definition, precludes perfect plasticity and softening – both of which are unstable under

stress control. The later inequality,* known simply as *Drucker's inequality*, can be seen to hold for perfectly plastic materials as well. Satisfaction of Drucker's inequality implies satisfaction of Inequality (2.6-1a) by the positive definiteness of the tangent elastic moduli.

Aside on Material Classification

Drucker's postulate implies a first order inequality given by

$$\left(\sigma_{ij}-\sigma_{ij}^{*}\right)\dot{\varepsilon}_{ij}^{p}\geq 0 \qquad (2.6\text{-}2)$$

where σ^* represents an initial stress in the closure of the elastic region (*i.e.*, it can be in the elastic region or on its boundary – the yield surface) but not in the neighborhood† of σ. The stress path produced by the external agency is assumed to consist of an elastic response between σ^* and σ, followed by a small stress increment $d\sigma$ that produces an incremental plastic strain of $d\varepsilon^p$, and finally an elastic unloading back to σ^*. Neglecting second order terms, Drucker's postulate implies the work per unit volume done by the external agency is nonzero as indicated in Inequality (2.6-2).

* This is often expressed in rate form.

† In this context the length of the vector $\sigma_{ij}-\sigma_{ij}^{*}$ in stress space must be much larger than the length of $d\sigma$.

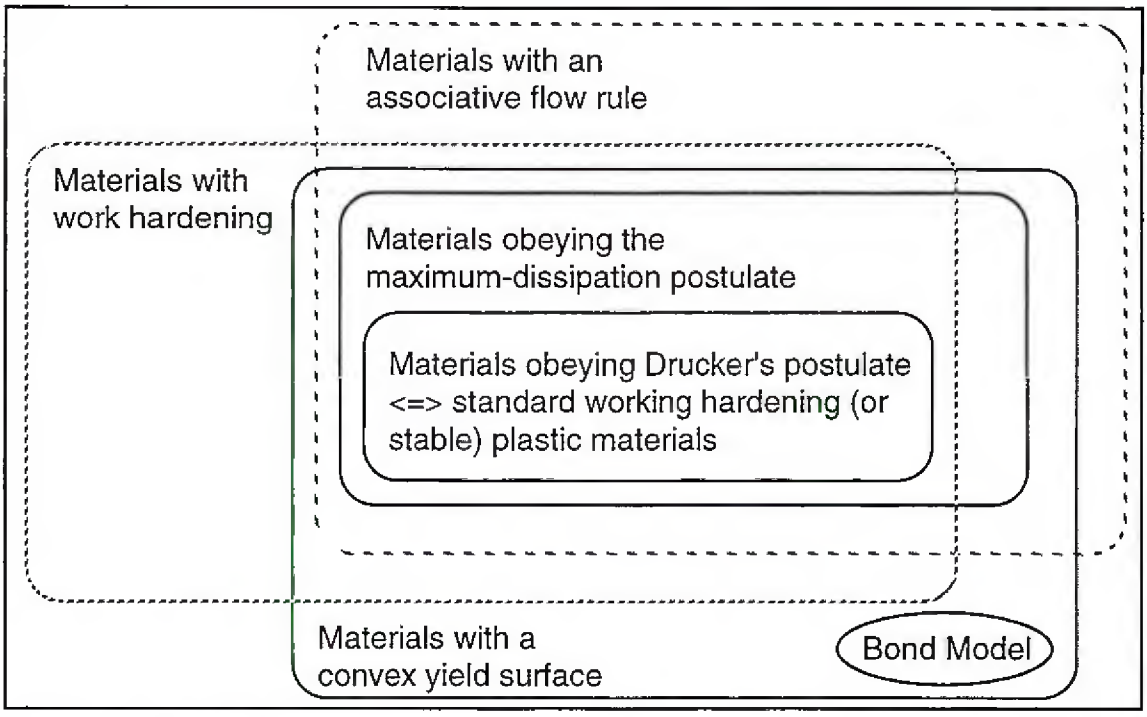

Figure 2.6-1 Bond model relative to subsets of rate independent plasticity laws.

Another interpretation of Inequality (2.6-2) comes from the definition of *plastic dissipation* given as

$$D_p(\dot{\varepsilon}^p, \underline{h}) = \sigma_{ij}\dot{\varepsilon}^p_{ij}. \tag{2.6-3}$$

Thus the inequality is also referred to as the "*principle of maximum plastic dissipation*," because it implies that σ gives the maximum *plastic dissipation* over all the stress states in the closure of the elastic region for the given increment in plastic strain.

Using relatively simple geometric arguments one can show that Inequality (2.6-2) implies 1) the material has an associative flow rule, and 2) the yield surface is convex. Figure 2.6-1 shows these implications and the relationship of the bond model to various "classes" of rate independent plasticity laws. In particular note that since the bond law is nonassociative it does not satisfy either the maximum-dissipation postulate or Drucker's postulate.

Table 2.6-1 Stability criteria.

	Monotonic Load	Load Cycle
Infinitesimal Magnitude External Agency	$d\sigma_{ij}d\varepsilon_{ij}>0$ (2.6-4a)	$d\sigma_{ij}d\varepsilon_{ij}^{p}>0$ (2.6-4b)
Finite Magnitude External Agency	$\int_{0}^{\Delta\varepsilon_{ij}}\left(\sigma_{ij}-\sigma_{ij}^{*}\right)d\varepsilon_{ij}>0$ (2.6-5a)	$\int_{0}^{\Delta\varepsilon_{ij}^{r}}\left(\sigma_{ij}-\sigma_{ij}^{*}\right)d\varepsilon_{ij}^{p}>0$ (2.6-5b)

In a later paper, Drucker (1964) sought to clarify the postulate of stability; he perceived that the meaning and purpose of the postulate had become blurred. In this study he presented four criteria of stability that can be used to define different degrees of stability. The four criteria (given in Table 2.6-1) involved permutations of external agencies that were 1) of infinitesimal and finite magnitude, and 2) applied as monotonic and cyclic loads. He presented the criteria first for the system and then deduced the material criteria simply by considering a unit block of material in a homogenous state. In the case of the cyclic load (*i.e.*, application and removal of external forces), $\Delta\varepsilon_{ij}^{r}$ represents the residual strain that remains after the removal of the external agency.

Except for the strict inequality in Inequality (2.6-4b), Inequalities (2.6-4) are the same as Inequalities (2.6-1) – Drucker's postulate. Materials that satisfy Inequalities (2.6-4) and (2.6-5) are referred to as *stable in the small* and *stable in the large*, respectively. In particular materials that satisfy Inequality (2.6-4a) are said to be *stable in the small in the forward sense*, and materials that satisfy Inequality (2.6-5a) are said to be *stable in the large in the forward sense*.

In Chapter 7 we will numerically examine stability in the small in the forward sense for a few distinct loading cases. Note that this definition of stability is equivalent with the positive definiteness of the elastoplastic moduli (**D**). For models with nonassociative flow rules, one can equivalently examine the positive definiteness of the symmetric component

of $\mathbf{D}$ (*i.e.*, $\mathbf{D}>0 \Leftrightarrow \mathbf{D}^s>0$ where $\mathbf{D}^s \equiv (\mathbf{D}+\mathbf{D}^T)/2$). Since $\mathbf{D}^s$ is symmetric by definition, its spectrum is real and thus stability is easily examined via it smallest eigenvalue (Runesson and Mroz [1988]).

Drucker (1964) emphasized that these isothermal mechanical stability criteria are not laws of nature but rather are criteria for material classification. Because they use the concept of work, they are often referred to as quasi-thermodynamic. The second law of thermodynamics guarantees that the total work done (*i.e.*, not just that done by the external agency) in a cycle is positive if plastic deformation occurs in the domain.

Drucker and Li (1992, 1993) also define sufficient conditions for material instability (emphasizing materials with nonassociative flow rules). For a material with a nonassociative flow rule there exists a continuous path in stress space for which

$$\dot{\sigma}_{ij}\dot{\varepsilon}^{p}_{ij}<0. \tag{2.6-6}$$

This so-called *wedge path*, as illustrated in Figure 2.6-2, has been the subject of many studies on stability (see *e.g.*, Lade, Nelson and Ito [1987], Lade and Pradel [1990], Pradel and Lade [1990], Lade and Yamamuro [1993], and Drucker and Li [1992, 1993]). The set of directions for which Inequality (2.6-6) holds is sometimes referred to as the *wedge region.*[*]

If the elastic response (where $\dot{\sigma}_{ij}\dot{\varepsilon}^{e}_{ij}>0$) is small relative to the inelastic response for each point on the path, then

$$\dot{\sigma}_{ij}\dot{\varepsilon}_{ij}<0, \tag{2.6-7}$$

which he defines as *instability in the small in the forward sense*. There exists a similar path for which

---

[*] It was initially defined by Mroz (1963) when addressing uniqueness. In his proof, stress paths in this region produced the greatest lower bonds on the plastic modulus necessary to ensure uniqueness. As usual, stability and uniqueness problems accompany one another.

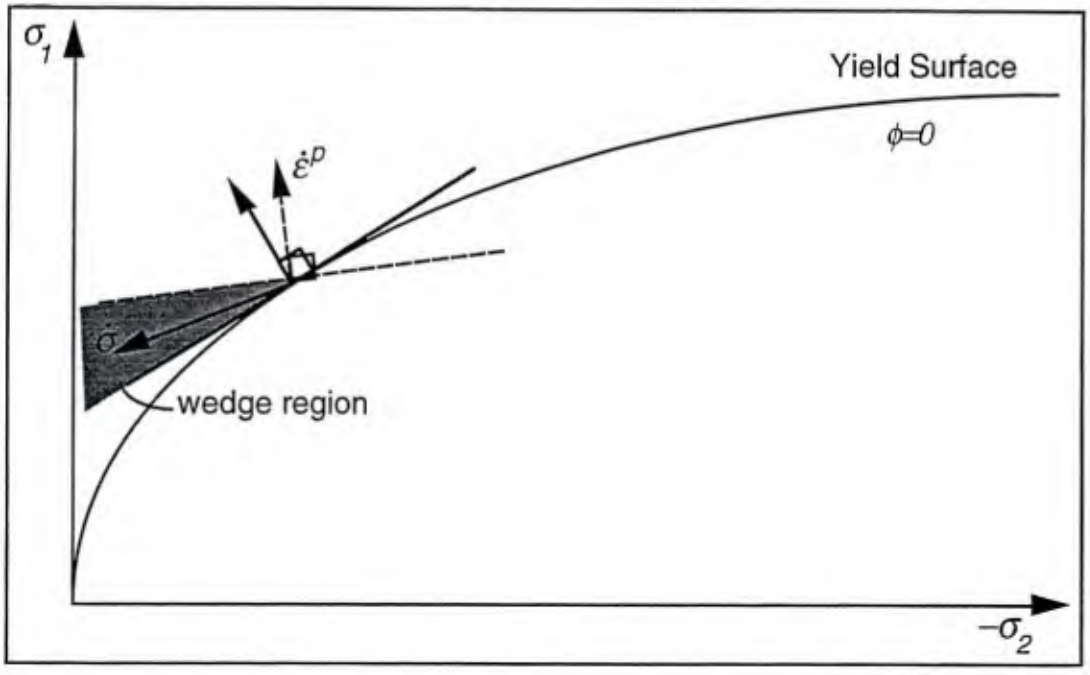

Figure 2.6-2 Wedge region with nonassociative flow rule (the case shown resembles the bond law).

$$\left(\sigma_{ij}-\sigma_{ij}^{*}\right)\dot{\varepsilon}_{ij}^{p}<0, \tag{2.6-8}$$

and thus for relatively small elastic* response

$$\left(\sigma_{ij}-\sigma_{ij}^{*}\right)\dot{\varepsilon}_{ij}<0 \tag{2.6-9}$$

along the entire path – *instability in the large in the forward sense.* This last inequality implies that the work per unit volume done by the initial state of stress (σ_{ij}^{*}) exceeds the energy stored elastically and the energy stored irreversibly in the unit volume. Thus if perturbed in a manner to begin this path, the system would begin to gain kinetic energy. (See *e.g.*, Drucker and Li [1992] for further discussion.)

The early work of Hill (1958) gives additional insight to stability in the forward sense; it is the virtual-displacement analog to Drucker's development. He considers the increase in the internal energy less the work by external forces for a system subjected to an arbitrary

---

* This is related to the observation by Rice (1976) that elasticity mitigates the tendency toward localization.

virtual displacement (large displacements and deformations permissible) from a state of equilibrium followed by an infinitesimal displacement. The derived sufficiency condition is the "system equivalent" of stability in the large in the forward sense. In the limit of an infinitesimal virtual displacement, the definition for stability in the small in the forward sense is attained. Hill's approach (Bishop and Hill [1951] and Hill [1958]) is often referred to as being based upon a maximum work postulate (see *e.g.,* Lade and Pradel [1990]).

Mandel (1964) showed that Drucker's Inequality (2.6-1b) was a sufficient but not a necessary condition for material stability. Drucker (1964) indicated: "They (Inequalities [2.6-4] and [2.6-5]) provide a sufficient condition for stability. Whether they are *necessary* is a matter of opinion on the meaning of stability." In the literature on stability, the phrase "sufficient condition" often appears to be used in a relative sense – meaning that satisfying the condition guarantees that the particular definition of stability will be met. When the phrase is used in this sense it does not imply that instability in the model cannot occur; one must assure that every possible instability will not occur (*i.e.*, satisfy the necessary conditions for each potential instability) to have a sufficient condition for material stability; Needleman (1979) discusses this added complexity for nonassociative materials.

The bond model presented in this study behaves as a *frictional material,* and stability of frictional materials remains an area of controversy. Frictional materials have been of particular interest because they exhibit localization. Explanations of this behavior were given first by Mandel (1964) and later by Rudnicki and Rice (1975). Their analyses showed that, in the absence of normality, localization can occur even during hardening conditions.

Mandel (1964) defined a stable material as being capable of propagating a small perturbation in the form of waves. He showed that a material can propagate a wave in the direction $\underline{m}$ if and only if the second order tensor **A** defined by

$$A_{jk}(\underline{m}) = m_i D_{ijkl} m_l \qquad (2.6\text{-}10)$$

is positive definite. This type of instability is referred to as a *shear band bifurcation.* Drucker and Li (1993) classify it as a *Shanley type of instability of path.* Since this defines only one possible instability, it is necessary but not a sufficient condition for material stability. Satisfaction of Drucker's inequality implies the above defined stability of path (see Appendix A).

Leroy and Ortiz (1989) (in development of a finite element analysis of strain localization) present a concise analysis giving the above necessary and sufficient condition for shear band bifurcation. The analysis is limited to small deformations and thermally decoupled, rate-independent material behavior. First, they present Maxwell's compatibility conditions which restrict the jump in velocity gradients across a plane of discontinuity to the tensor product of 1) the relative velocity of neighboring points on opposite sides of the plane (given by the direction $\underline{m}$ of Equation [2.6-10]) and 2) the normal vector to the plane. From this relationship they can express the jump in strain rates across the plane of discontinuity. Then adopting Hill's procedure (1958), they combine the incremental stress-strain relations and the requirement of traction continuity across the plane of discontinuity to establish a necessary condition for localization. When the condition is met, the solution gives possible planes of strain discontinuity and the corresponding directions of relative displacement – alternatives to continued homogeneous deformation.

In the context of the bond model, the orientation of the localization is assumed *a priori* to occur in the bond zone, and traction continuity is satisfied in the implementation.* The softening behavior, though often considered to be structural or geometrical in nature, is

---

* As discussed in Appendix G, for the interface elements the tractions vary as 1/r, so that force equilibrium is satisfied in the absence of hoop stresses.

reflected in the bond model response; thus as previously mentioned, some might prefer to classify the bond model as a "structural model" rather than a "constitutive model."

In contrast to a shear band of fixed orientation, Drucker and Li (1992) examined analytically a triaxial test response using a Mohr-Coulomb model with a nonassociative flow rule where $\|\varepsilon^e\| >> \|\varepsilon^p\|$. They found that as soon as the model entered the plastic range, the configuration was in a state of unstable equilibrium; that is, a small permissible perturbation of velocity would produce either a finite or an unlimited change in geometry for fixed external loads. The instability was of finite excursion and had the form of a single shear band with an orientation that rotated with the unstable acceleration. They referred to this as a "genuine instability of configuration" and indicated that a model that is stable in the small in the forward sense (Inequality [2.6-4a]) exhibits stability of configuration. Thus a material that is stable in the small in the forward sense will not exhibit any of the instabilities discussed above.

This analysis addressed the claim by Lade, Nelson and Ito (1987) (also see Lade and Pradel [1990], and Pradel and Lade [1990]) that Drucker's postulate (and thus stability in the small in the forward sense) is not applicable to "materials with nonassociative flow rules." Their claim was based on a set of very interesting experiments, where they attempted to continuously load triaxial sand specimens along wedge paths (see Figure 2.6-2). The stable response of these specimens has been the subject of some debate (see *e.g.*, the corresponding discussions of Drucker [1989] and Runesson and Sture [1989]).

Irregardless of the actual material behavior, Drucker and Li (1992) determined an inherent instability exists in any material model with 1) a nonassociative flow rule, and 2) relatively small elastic strains; correspondence of this mathematical instability with actual material instability is a different issue. This study only addresses the stability of the bond model. I am not aware of any bond experiments that address "wedge stress paths."

The bond model uses a nonassociative flow rule and thus, by the definitions of Drucker and Li (1992), during hardening it is potentially unstable in the small in the forward sense. This potential instability is examined numerically in Chapter 7. For the finite set of stress paths considered, the second order elastic work term is sufficient to ensure stability in the small in the forward sense. Even if this instability is found to occur, it is not necessarily a divergent instability and (as noted earlier) material stability does not imply instability in the system – merely its potential for existence; boundary conditions can inhibit instability in the system.

The next three chapters address the individual components (*e.g.*, flow rule) of the elastoplastic model. The discussion of each model component will relate hypotheses on the micromechanics of the bond phenomena to the component's phenomenological form and present supporting experimental data. Experimental evidence does not fully support the hypotheses on the micromechanics, and thus they have a speculative nature in some instances; nonetheless, they are very important because it is only a better understanding of the mechanics that reveals weaknesses in the model and motivates its subsequent improvement. Limited discussions on the evolution of the model are included to provide greater insight into the model's current form.

Chapter 3

Yield Criterion

This chapter describes the development of the yield criterion for an elastoplastic bond model applicable to monotonic loading. As described in the introductory chapter, bond (as most phenomena) can be modeled at various scales. The model developed here is for a bar-scale analysis.

In Section 2.2 a set of generalized stresses and strains were abstractly defined and subsequently used to present an overview of the theory of plasticity. The first step in the model development is to define the set of *generalized* stresses and strains employed in developing the bond model; this is presented in the first section of the chapter. The second section presents the analysis of experimental data (and simplifying assumptions) that lead to the current form of the yield criterion. The last section of this chapter presents the model's yield criterion – the yield surface and its evolution. Discussion of the corresponding mechanics is interspersed in these last two sections.

3.1 Generalized Stresses and Strains

The mechanical interaction of the reinforcement's ribs with the surrounding concrete results in a very complex behavior "near the bar" that includes fracture, crushing and friction. Analogous to a boundary layer in fluid mechanics, a region near the bar is defined that will

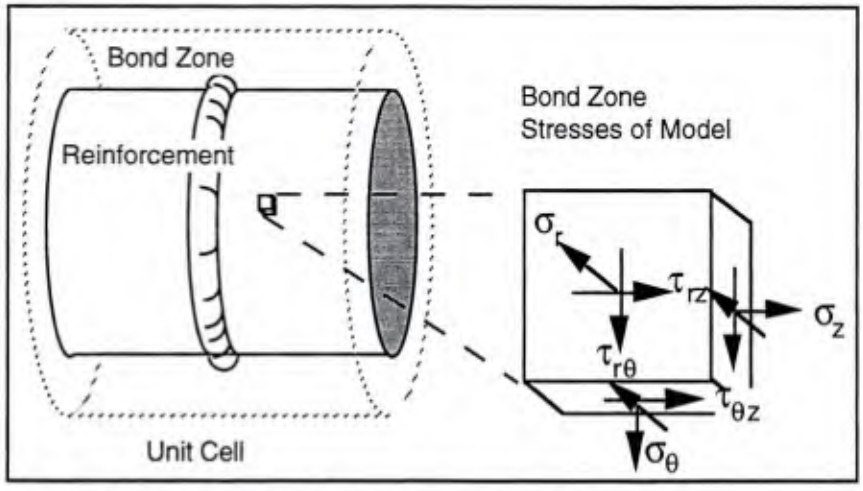

Figure 3.1-1. Generalized stresses on a unit cell.

be referred to as the *bond zone*.* In an average sense, the bond model provides a continuum mechanics description of the bond zone behavior for a *unit cell*. This unit cell represents the length of bar that contains one cycle of the rib pattern; this is illustrated, for a bar with ribs normal to the bar axis, in Figure 3.1-1. While the bond zone is conceived as a region containing the main mechanisms of bond, the effects of the mechanical interaction are not constrained to this region. For example, longitudinal cracks caused by the mechanical interaction can propagate to the surface of the concrete thus causing a splitting failure. Researchers have suggested different radii for the bond zone. For example, Gambarova *et al.* (1989) experimentally determined that the microcracking extended the thickness of the maximum aggregate size.

Consider a local cylindrical coordinate system where the z-axis corresponds to the axis of the reinforcement. The generalized stresses and strains are then defined as:

$$\underline{Q}^T = (\tau_{rz} \;\; \sigma_r \;\; \tau_{r\theta};\; \sigma_z \;\; \sigma_\theta \;\; \tau_{\theta z}) \text{ and } \underline{q}^T = \left(\frac{\delta_z}{D_b} \;\; \frac{\delta_r}{D_b} \;\; \frac{\delta_\theta}{D_b};\; \varepsilon_z \;\; \varepsilon_\theta \;\; \gamma_{\theta z} \right). \qquad (3.1\text{-}1)$$

* In previous reports on this study (Cox and Herrmann [1992a & b]), we referred to this region as the *process zone*. De Groot, Kusters and Monnier (1981) referred to this region as the bond-slip layer.

where the δs denote relative displacements, in the designated local coordinate direction, of a point on the outside of the bond zone relative to a point on the inside of the bond zone differing only in their r coordinate (*i.e.*, along a radial line in the undeformed state), and D_b denotes the diameter of the reinforcement. Though these are not a unique measure of strain, the particular form of the first three generalized strains has effectively incorporated the diameter of the bar for a variety of tests (see Chapter 7). Shima, Chou and Okamura (1987) normalized their definition of slip in this manner for their uniaxial model and referenced the earlier works of Morita an Fujii (1985) and Yamoa, Chou and Niwa (1984). A possible justification for this strain measure is discussed at the end of this section.

The stresses and strains are partitioned to separate the typical interface components from the additional components necessary to define the state of stress and deformation in a solid. The first three stresses must be interpreted as components of the traction between the bar and the concrete to be conjugate to the corresponding deformations. The remaining three stress and strain components are included rather symbolically to emphasize simplifying assumptions that will be made. The complex surface geometry of the bar and the corresponding mechanisms of bond are smeared along the unit cell. Thus: 1) the stresses are assumed to be continuous and "statically equivalent" to the true stresses over a unit cell, and 2) the strains are assumed to be continuous and in an average sense "kinematically equivalent" to the true deformations over the length of a unit cell.

The size of the bond zone is such that it is generally not valid to assume the bond phenomena are constrained to an interface surface. Gerstle and Ingraffea (1990) emphasize this by suggesting that "bond slip may not exist in the sense in which it has been previously described in the literature." This is also suggested by many rib-scale analyses that reflect the importance of transverse cracking in bond (see *e.g.*, Hungspreug [1981], and Keuser and Mehlhorn [1987]). Since the objective of this work is to develop a model that can be used for member-scale analyses, the model must be kept as simple as possible. In

addition, there are insufficient data to effectively develop a bar-scale model that explicitly considers the three-dimensional stress state in the bond zone; constituent material tests can better measure and control individual stress or strain components than bond tests. Thus the initial models have been developed retaining only the interface traction components and corresponding deformations.* Furthermore an axisymmetric state of stress and deformation is assumed. The generalized stresses and strains are then simplified to

$$\underline{Q}^T = (\tau \;\; \sigma) \text{ and } \underline{q}^T = \frac{1}{D_b}(\delta_t \;\; \delta_n) \tag{3.1-2}$$

where only the first two components of Equations (3.1-1) are retained and a simple tangent-normal coordinate system is adopted.

These assumptions are made with the realization that as validation efforts progress the need to increase the dimensionality of the model may become apparent. In particular, neither tensile or prestressed specimens have been considered. In these types of specimens σ_z is likely to have a strong effect on the transverse cracking mechanism associated with bond. In addition, the assumption of an axisymmetric state needs further examination in many cases (*e.g.,* when significant doweling forces are present).

In concluding this section, let's consider again the form of the strain measure used in Equation (3.1-2). A possible justification for the strain measure follows from considering the tangent force (F) transmitted by a bond zone of length L. Let τ denote the average bond stress over this length. The force transmitted can then be written as

$$F = L\pi D_b \tau. \tag{3.1-3}$$

---

* This is sometimes referred to as *the interface assumption* in subsequent sections. For brevity, the negative of the normal stress (*i.e.*, $-\sigma$) will be referred to as the *confinement stress*. A volumetric measure of confinement stress (as used by geotechnical engineers – the source of this terminology) might be used in later versions of the model which relax the interface assumption.

After adhesion has broken down, initially most of the transfer of force between the concrete and bar can be attributed to the mechanical interaction of the ribs with the concrete. For clarity assume that the ribs are normal to the axis of the bar and that f_r denotes the force per unit length of the rib transmitted from the bar to the concrete. The total force transmitted from the bar to the concrete can be expressed as

$$F = \frac{L}{s_r}\pi D_b f_r \tag{3.1-4}$$

where L/s_r gives the number of ribs per length L. Equating Equations (3.1-3) and (3.1-4) gives the somewhat obvious result

$$\tau = \frac{f_r}{s_r}. \tag{3.1-5}$$

For a fixed value of τ, the force per unit length of rib is proportional to the rib spacing. Furthermore, for standard bars the rib spacing is nearly proportional to the bar diameter; thus for standard bars the force per unit length of rib is nearly proportional to the bar diameter. Since f_r might be considered responsible for the local elastic deformation, crushing and the opening of transverse cracks (*i.e.*, several of the mechanisms of deformation), the use of D_b in the strain measure is not devoid of a rational basis.*

Since the strains are simply the relative displacements nondimensionalized by the bar diameter, they are defined independent of the bond zone thickness. This definition introduces a potential mesh (bond zone thickness) dependency, in application it does not occur in this study; the main reasons for this are a simple concrete model is used for the specimens, and the finite thickness interface element is integrated at the surface of the bar. An example and additional discussion of this issue are presented in Chapter 7.

---

* Admittedly this argument is simplistic in nature. The rib heights are also nearly proportional to D_b, so it is not clear that an increase in D_b increases the "contact stresses." The effect of not including the bond zone thickness in the definition of the generalized strains will be addressed in Chapter 7.

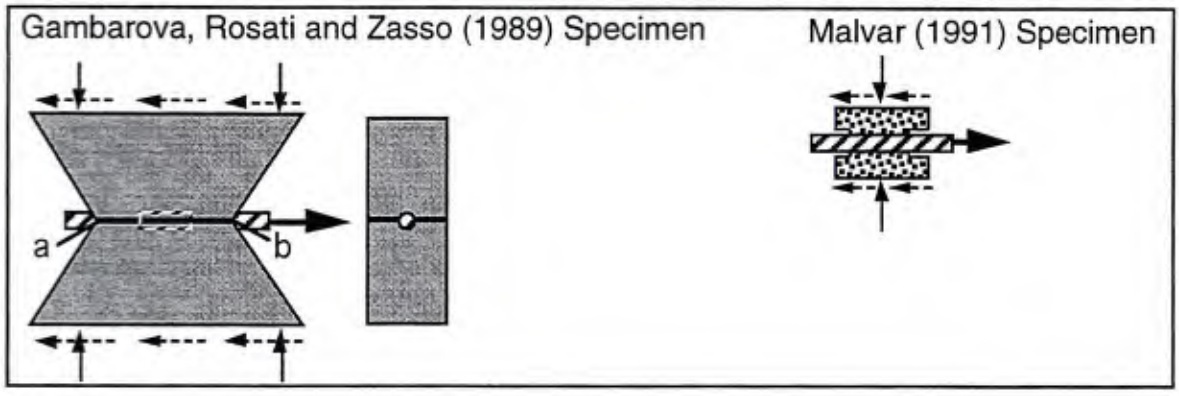

Figure 3.2-1 Schematic of the experimental specimens considered in the preliminary model development.

3.2 Experimental Data

In this section experimental data that can potentially be used to develop bond yield criteria are discussed. Simplifying assumptions that allow yield surface data to be extracted directly from the experimental results are also discussed.

Most bond experiments give some measure of τ and δ_t, but few experiments are designed to provide any measure of σ and δ_n. The experimental works of Gambarova, Rosati and Zasso (1989) and Malvar (1991) are exceptions; they give some measure of all the generalized stresses and strains of Equations (3.1-2) and thus served as an experimental basis for the early development efforts. Both specimens are shown schematically (to scale) in Figure 3.2-1.* Solid arrows represent applied forces while the dashed arrows represent reaction forces.

The experiments of Gambarova *et al.* (1989) consisted of three phases – A, B and C. All the specimens and loadings had a somewhat two-dimensional nature. A phase C specimen

* Additional details are given in Tables 7.1-1 and 7.1-2.

is shown in Figure 3.2-1. The specimen of phase B had a rectangular bar and was designed to investigate the extent of microcracking due to bond. The specimens of phases A and C differed principally in the specimen thickness; the smaller thickness phase A specimens developed in-plane splitting cracks. Thus our use of their experimental data is limited to phase C. The specimens were fabricated with a "splitting crack" through the width of the specimen. The crack opening was monitored by mechanical gauges near the points labeled "a" and "b" shown in Figure 3.2-1. A series of four tests was performed where the crack opening was manually controlled by confinement forces at the top and bottom of the specimen to maintain constant openings of 0, 0.1, 0.2 and 0.3 mm within a tolerance of 0.01 mm. The confinement forces applied to maintain the constant crack openings give a measure of σ, and the crack opening gives a measure of δ_n. Assuming both the traction components are uniformly distributed over the surface of the bar, with respect to z and θ, they can be determined from equilibrium in terms of the bar force (F) and confinement forces (N) as:

$$\tau = \frac{F}{\pi D_b L} \quad \text{and} \quad \sigma = \frac{N}{D_b L} \tag{3.2-1}$$

where L denotes the embedment length. Certainly the assumption of a uniform traction distribution is a first order approximation to a very complicated distribution that undoubtedly is a function of the crack opening. This is considered in more detail in Herrmann and Cox [1994].

The experiments of Malvar (1991) "reverse the boundary conditions," controlling the applied radial traction and measuring the change in circumference of the specimen. Unlike the tests of Gambarova *et al.* (1989), the specimen is axisymmetric and thus higher normal stresses can be applied. The reported confinement stress for these tests represents the normal traction component at the bar-concrete interface assuming the specimen carries no hoop stress (*i.e.*, assuming a sufficient number of splitting cracks are open). Four series

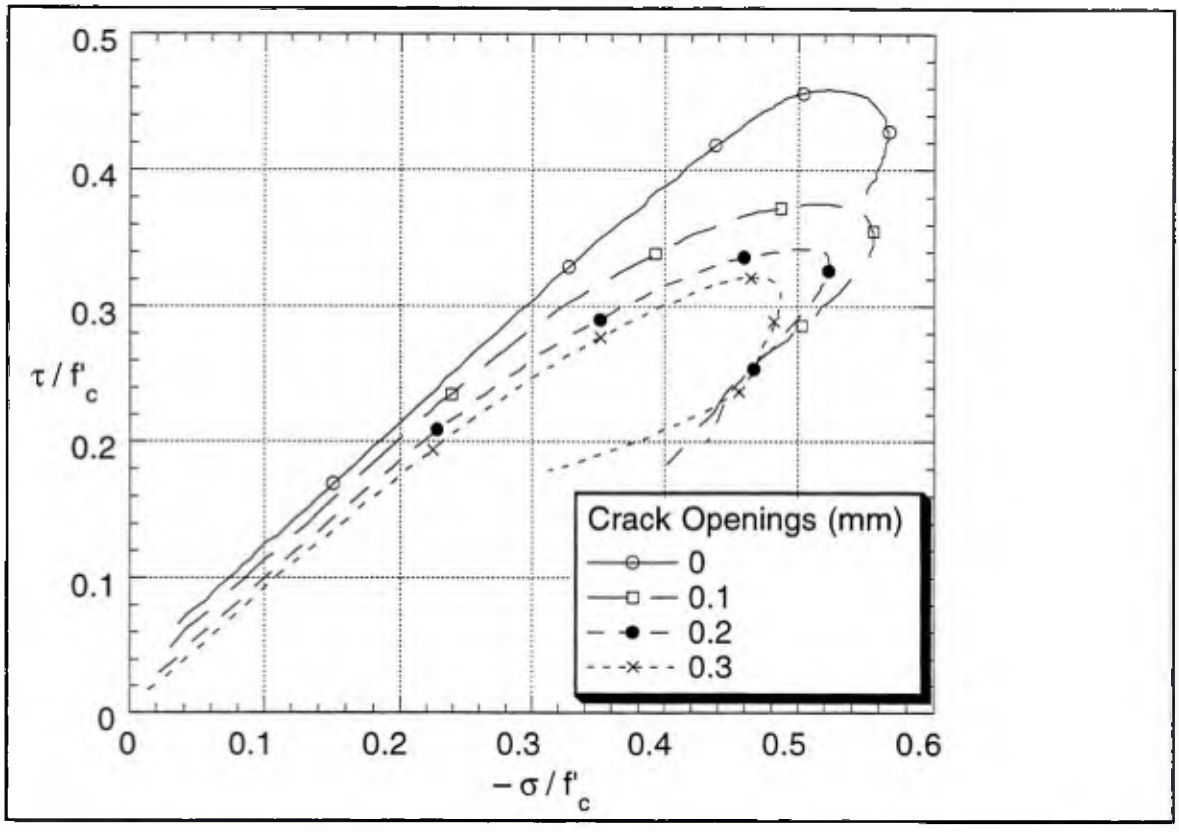

Figure 3.2-2 Stress paths for the phase C tests of Gambarova, Rosati and Zasso (1989).

of tests were performed of which the last series is not published. Series one was preliminary and consisted of three tests, σ = 500, 1000 and 2000 psi, with virgin specimens. The second and third series of tests attempted to show the variation in the bond stress-slip relationship with various confinement stresses (σ = 500, 1500, 2500, 3500, and 4500 psi). In these tests the specimens were loaded to splitting then unloaded prior to measuring the bond stress-slip relationship during reloading. The principal difference between the last two series was the deformation pattern on the bar. The fourth series of test specimens had fabricated splitting cracks. They gave significantly different results and are only referenced in a later section on the elastic moduli.

The initial development of the yield surface focused on the phase C data of Gambarova *et al.* (1989). Figure 3.2-2 shows the stress paths of their tests for various crack openings. The shape of the curves suggests that a Coulomb surface with some form of hardening and

subsequent softening might yield a good model. So consistent with the overall goal for simplicity, the initial form of the model had a Coulomb yield surface. While this model could be calibrated to match a given set of experimental results very accurately, it could not be validated for a series of different tests using a common calibration. Stress path data represent a sequence of points in stress space for a corresponding sequence of internal states of the material, whereas a yield surface represents a locus of points in stress space that share a common internal state. So although these stress paths tempt one to use a Coulomb surface, they do not imply a Coulomb surface is valid – not even for the early part of the response. As will be discussed later, the deviation of the yield surface from a Coulomb surface is in part due to the interface assumption used in the bond model.

The tests of Malvar (1991) were performed at various levels of σ,* thus if a simple measure of the internal state of the material is assumed, these data can be readily used to interpret the form of the yield surface and its evolution. Figures 3.2-3 and -4 show the bond stress versus slip curves for test series 2 and 3, respectively. Each test was performed only once, so the only measure of scatter is the consistency in the response trends with increasing $-\sigma$. Note that at the scale shown the initial elastic response appears to differ with the two rib geometries but not significantly with σ. From an initial evaluation of the data of Malvar (1991), Gambarova *et al.* (1989) and Eligehausen *et al.* (1983), D^e_{11} of Equation (2.4-3) was assumed to be $0.04E_c$. The loading history of the specimens (after the initial cracking phase) was such that the external confinement stress was already applied when the bond stress and slip were both zero, but the normal stress at the bar surface did not reach its maximum until the splitting cracks were reopened. Even though we do not exactly know the normal stress history (at the bar), if we assume that $\mathbf{D}^e$ is very diagonally dominant

* The assumption of σ representing the generalized stress at the bar surface will be critiqued.

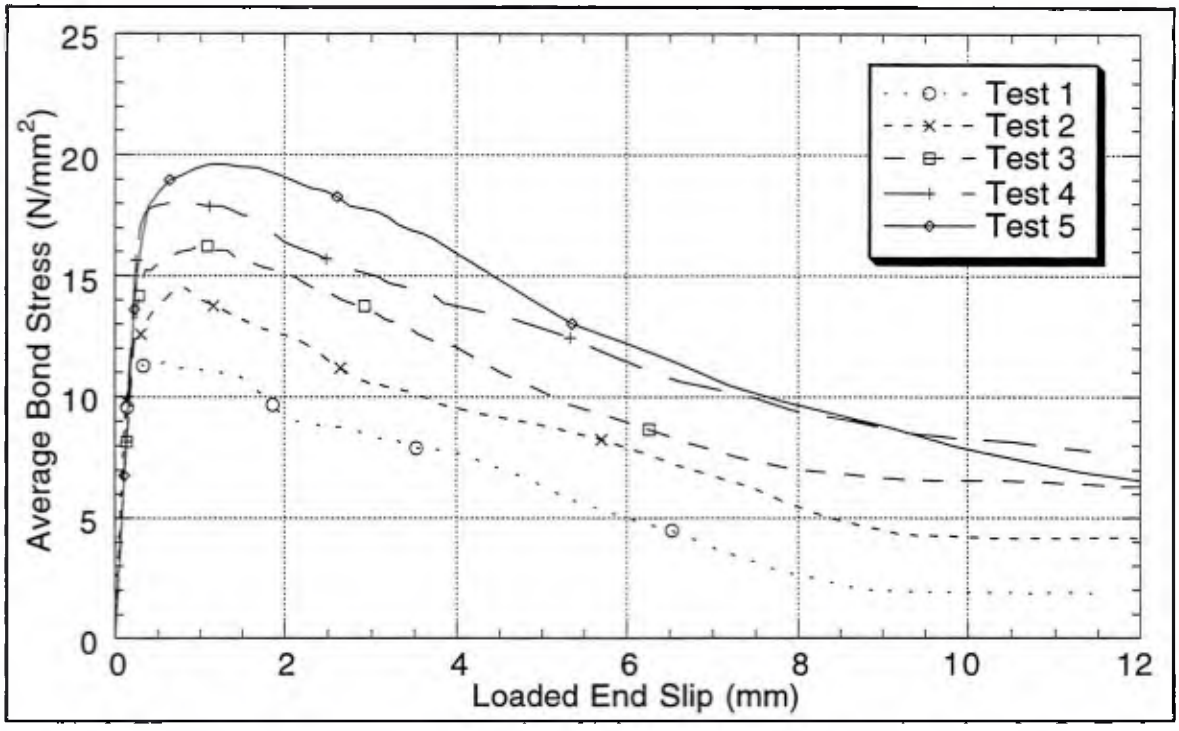

Figure 3.2-3 Bond stress versus slip results of Malvar (1991) series 2 tests. The values of $-\sigma$ for tests 1-5 were 500, 1500, 2500, 3500, 4500 psi or 3.45, 10.3, 17.2, 24.1, 31.0 N/mm^2, respectively.

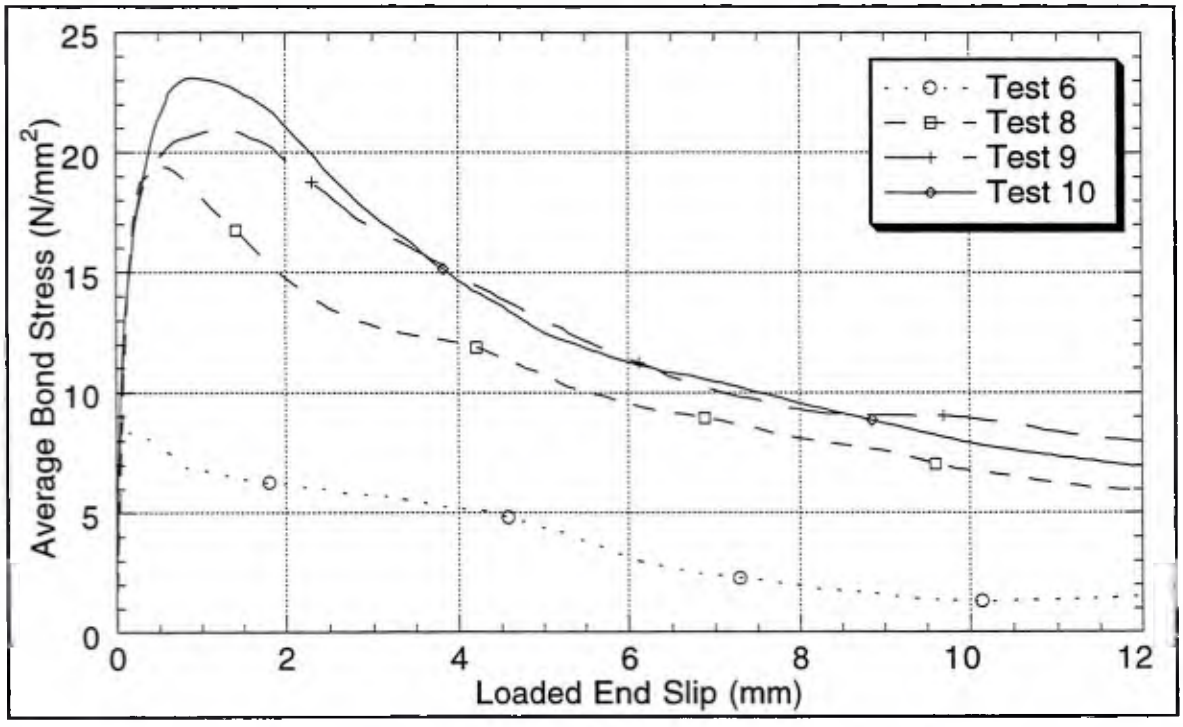

Figure 3.2-4 Bond stress versus slip results of Malvar (1991) series 3 tests. The values of $-\sigma$ for tests 6, 8, 9 and 10 were 500, 2500, 3500, 4500 psi or 3.45, 17.2, 24.1, 31.0 N/mm^2, respectively.

Table 3.2-1 Residual slip values (in mm) remaining after the initial splitting phase of the Malvar (1991) series 2 and 3 tests.

	Test 1	Test 2	Test 3	Test 4	Test 5	Test 6	Test 8	Test 9	Test 10
$q_1^p D_b$	0.18	0.10	0.20	0.24	0.17	0.054	0.057	0.064	0.10

(*i.e.,* almost diagonal) and that elastoplastic coupling is not significant in this context, then we can easily approximate the plastic slip (q_1^p) as a function of τ from Equation (2.4.3a) as

$$q_1^p = q_1 - \frac{\tau}{D_{11}^e} + q_1^{p\,0} \tag{3.2-2}$$

where $q_1^{p\,0}$ is the plastic slip which occurred during the initial splitting phase of the loading. The initial slip values are given in Table 3.2-1.

With these assumptions the relationship between bond stress and plastic slip can be obtained for each test. Figures 3.2-5 and -6 show bond stress versus plastic slip for the series 2 and 3 tests. The bars of series 3, which have ribs normal to the axis of the bar: 1) exhibit a higher elastic modulus (resulting in an initial negative slope in Figure 3.2-6), 2) require less plastic slip to split the specimen, and 3) generally attain higher bond stresses. Despite these differences, initially I will not attempt to account for differences in the rib geometry except for the length of the unit cell – the *rib spacing*, s_r.

Intuitively it seems that once the slip progresses the length of a unit cell, the concrete between the ribs has failed by a combination of crushing and mode two fracture or has been wedged radially outward due to the action of the ribs; thus only frictional behavior should remain. Experimentally many have observed this behavior (see *e.g.,* Eligehausen *et al.* [1983]). Eligehausen *et al.* (1983) introduce a *damage factor*, d, that determines the size of the monotonic envelope in their model; this damage factor is a function of the total energy dissipated by the bond mechanisms less half of the energy dissipated by friction (which is

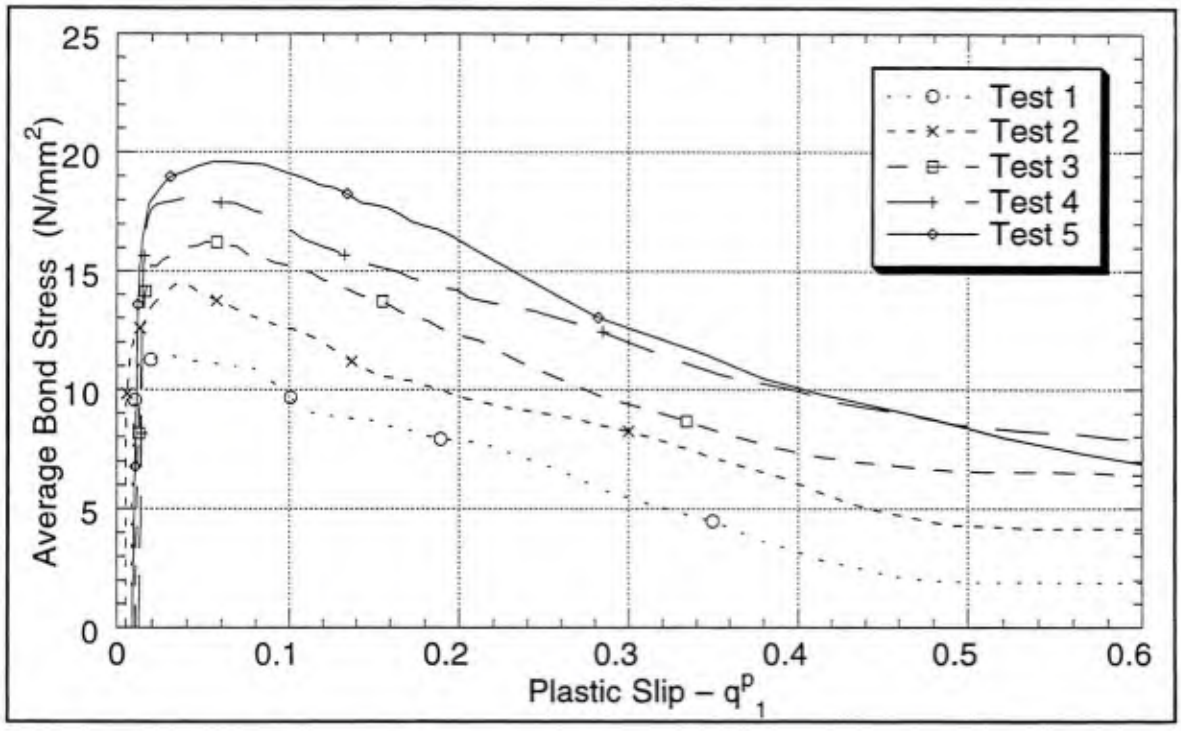

Figure 3.2-5 Bond stress versus plastic slip results of Malvar (1991) series 2 tests. The values of $-\sigma$ for tests 1-5 were 500, 1500, 2500, 3500, 4500 psi or 3.45, 10.3, 17.2, 24.1, 31.0 N/mm^2, respectively.

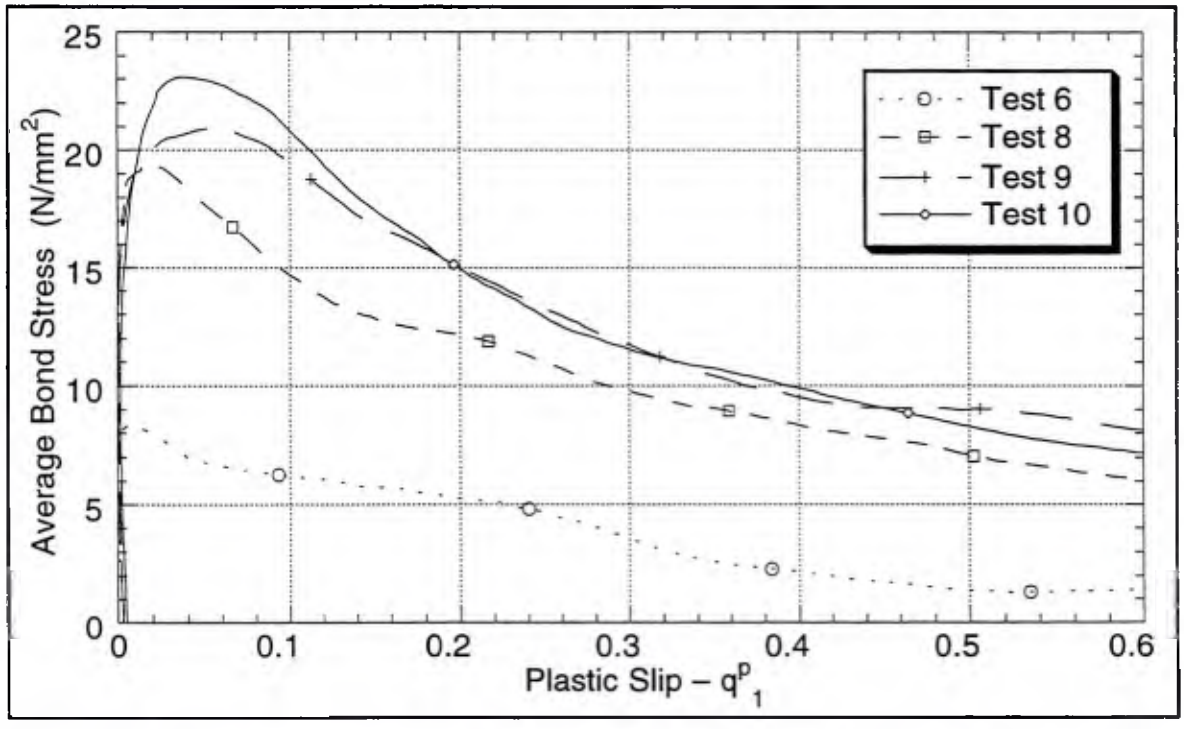

Figure 3.2-6 Bond stress versus plastic slip results of Malvar (1991) series 3 tests. The values of $-\sigma$ for tests 6, 8, 9 and 10 were 500, 2500, 3500, 4500 psi or 3.45, 17.2, 24.1, 31.0 N/mm^2, respectively.

assumed to be dissipated as heat). This suggests a work hardening law might be useful for a plasticity model.* Alternatively let's assume that strain hardening, Equation (2.2-4), is appropriate and that the radial dilation is insignificant compared to the slip;† essentially $\|.\|_\infty$ is used as the measure of the plastic strain. Furthermore let's assume (as suggested above) that plastic slip beyond s_r causes no further evolution of the yield surface. The bond zone *damage* is then defined as

$$d = min(\frac{\delta_t^p}{s_r}, 1) \tag{3.2-3}$$

where $\delta_t^p = q_1^p D_b$. Though the term *damage* is used both in this study and in that of Eligehausen, *et al.* (1983), the definition and application of the quantity differ. While use of this term suggests a measure of the physical damage of the bond zone, it is not intended to suggest that the concepts of damage mechanics are being applied in the modeling.

By Equation (3.2-3) q_1^p and d are linearly related. Thus for a given q_1^p, Figures 3.2-5 and -6 give points in stress space that have the same internal state (*i.e.*, value of d). Actually, σ at the bar surface is not known accurately because the specimen can carry hoop stress at two stages: 1) initially until the wedging action of the ribs opens the existing splitting cracks, and 2) near the end of the test when the cracks may have closed. For now assume σ reaches the bar.

Assuming that 1) the experimental scatter is greater than the effect of the different s_r in the two test series and 2) d alone is sufficient to characterize the internal state of the material, then Figures 3.2-7 through -14 present loci of points on the yield surface at various stages

---

* Early versions of the model presented here incorporated work hardening laws. They displayed no obvious advantages so the theme of simplicity prevailed.

† This assumption is made to simplify the data reduction rather than to comply with any basic principle. This will obviously not be sufficient for cyclic loading.

of evolution. These figures also show the bond model's yield surface (as a solid curve) for the same stages of evolution. The overall scatter of the data is greater for smaller values of damage – where the fracture mechanisms play a more significant role. The stresses are nondimensionalized by f_t, a measure of the tensile strength (as obtained by Equation B-1).

The plastic initiation surface (Figure 3.2-7) contains the most subjective data. The values for zero confinement stress were obtained from two uncracked specimens of series 1 and 2. Obviously the confinement stress did not remain zero at the surface of the bar; these points reflect a "thick bond zone interpretation" of the data. There is an inherent problem in defining the confinement stress with a thick bond zone since the bond model does not include the hoop stress, yet this stress component contributes to equilibrium in the r-direction. With the hoop stress ignored, one can take σ at either the inner or outer surface of the bond zone and obtain σ at the other surface from equilibrium in the r-direction. This suggests a 1/r variation in σ which only provides a good model when several splitting cracks exist and are open. A "small bond zone interpretation" of the tests with zero confinement would shift the points to the right (*i.e.*, σ would be compressive). Most of the remaining data points* are for specimens that were presplit so their $-\sigma$ values overestimate the actual values until the splitting cracks have opened. Defining the initial yield points for the tests is very subjective. Though one could use an "off-set rule" to appear less subjective, I have simply estimated the yield points assuming them equal to the apparent proportional limits.

The intersect of the model's curve with the horizontal axis is obtained from the solution of a thick-walled cylinder subjected to a tensile traction on the outer surface. The magnitude of the traction necessary to produce $\sigma_\theta=f_t$ at the inner surface of a thick-walled cylinder model of the Malvar specimen is approximately $2.25f_t$. In this latter case σ is determined by

---

* The exceptions are the preliminary tests of series 1.

including the effect of the hoop stresses, yet the value given is the projected value at the bar as if σ_θ does not exist; these inconsistencies reflect the difficulties in using the "thick bond zone interpretation" of the data. If we relate this intersection with the splitting capacity of the bond zone, then obviously it depends on the bond zone thickness we attribute to the model. In later validation problems the bond zone is modeled as being very thin, and stress states with tensile confinement stresses are not encountered. For more general application, one might want to modify the yield surface to have an insignificant intersect while still maintaining its same shape for compressive confinement stresses; this could be attained by including a factor in the current model that resembles a continuous approximation to a Heaviside function operating on $-\sigma/f_t$ (*e.g.*, $[1-\exp(\omega\sigma/f_t)]H(\omega\sigma/f_t)$ where $\omega>>1$).

Figure 3.4-8 shows the locus of points corresponding to τ_{max}. The σ=0 points are not shown since they fail in splitting.* Also note that for high confinement stresses, the bond stresses attained by the series 3 bars are greater than those of the first two series.

For the remaining states considered, the bond stresses gradually decrease until frictional behavior dominates the response. In this transition the data do not suggest that the surfaces are holomorphic. As the plastic slip increases, the data suggest that the yield surface might flatten for high confinement stresses; that is, for high confinement stress values the slope starts positive (with respect to $-\sigma/f_t$) and transitions to be nonpositive. Fortunately all of the data suggest that a convex yield surface is appropriate.

---

* This will be discussed in more detail when the form of the isotropic and kinematic hardening/softening laws are presented.

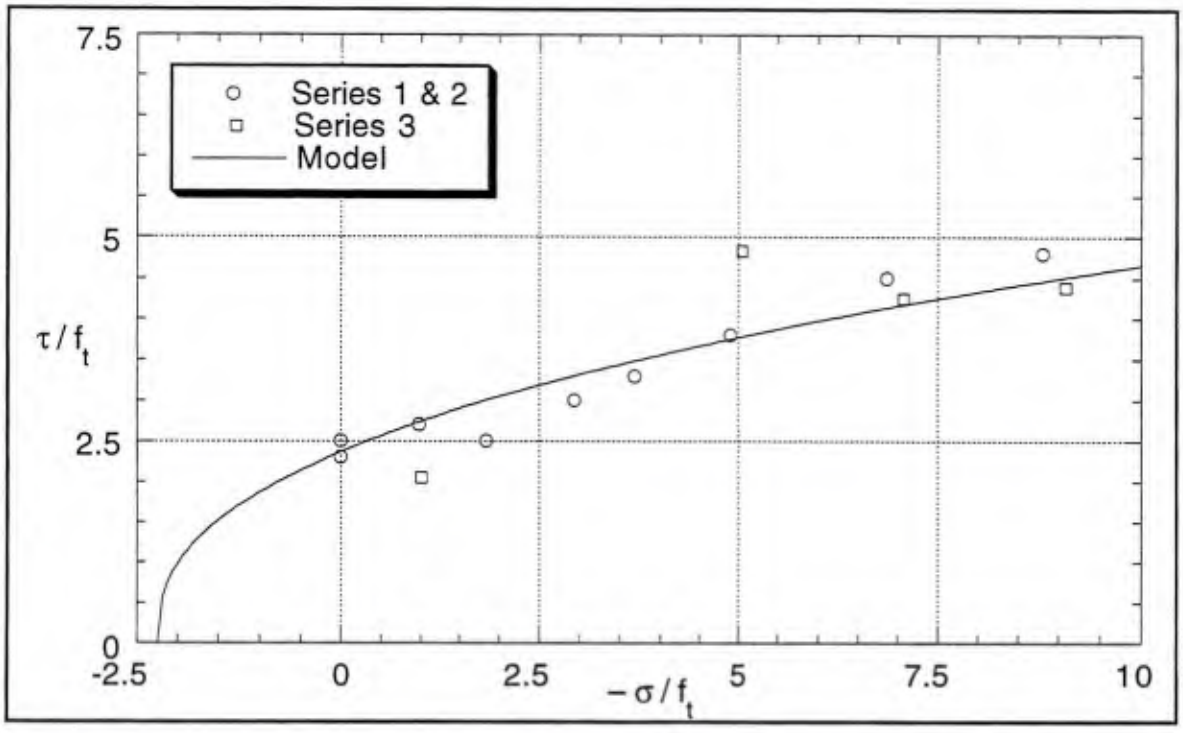

Figure 3.2-7 Yield surface data (for initiation) extracted from the results of Malvar (1991).

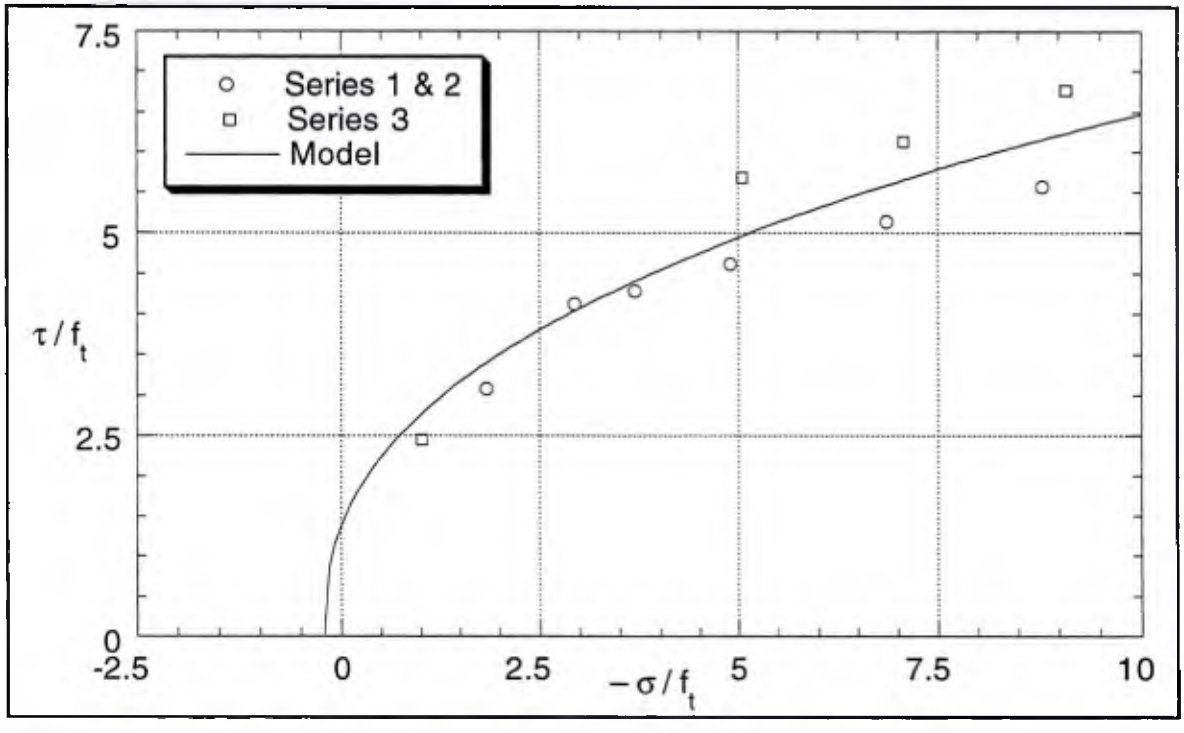

Figure 3.2-8 Yield surface data (for τ_{max}) extracted from the results of Malvar (1991).

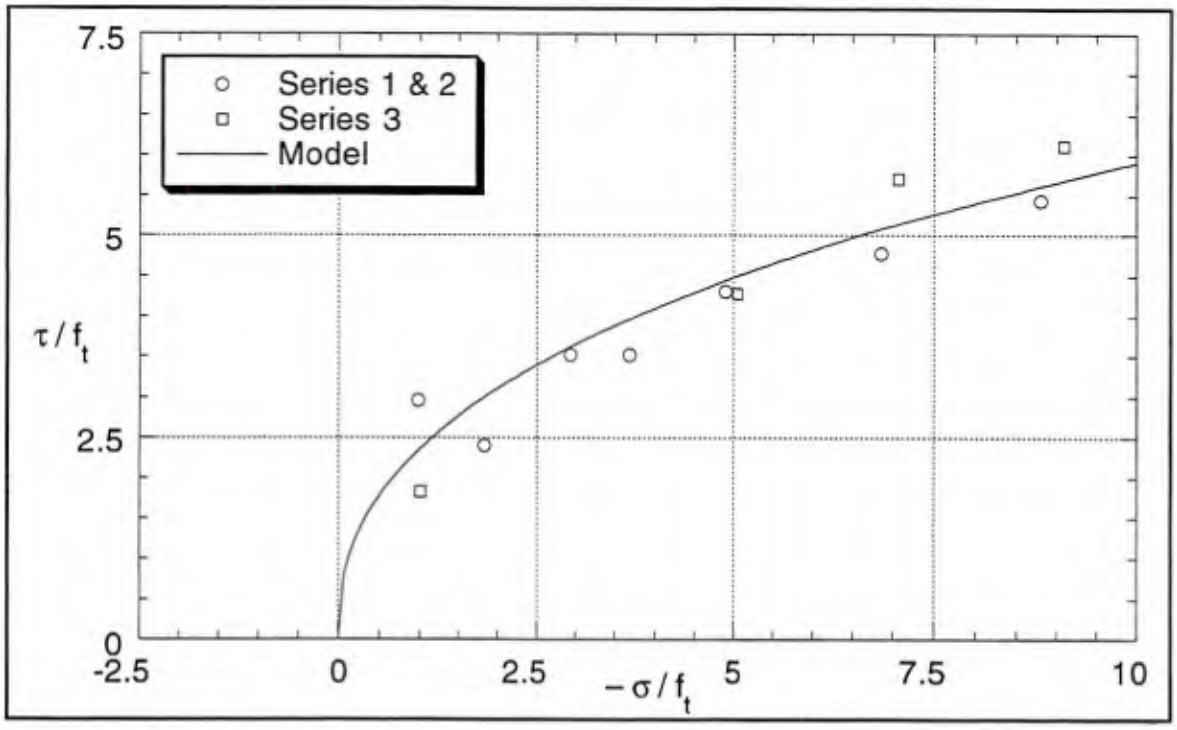

Figure 3.2-9 Yield surface data (for $q_1^p = 0.1$) extracted from the results of Malvar (1991).

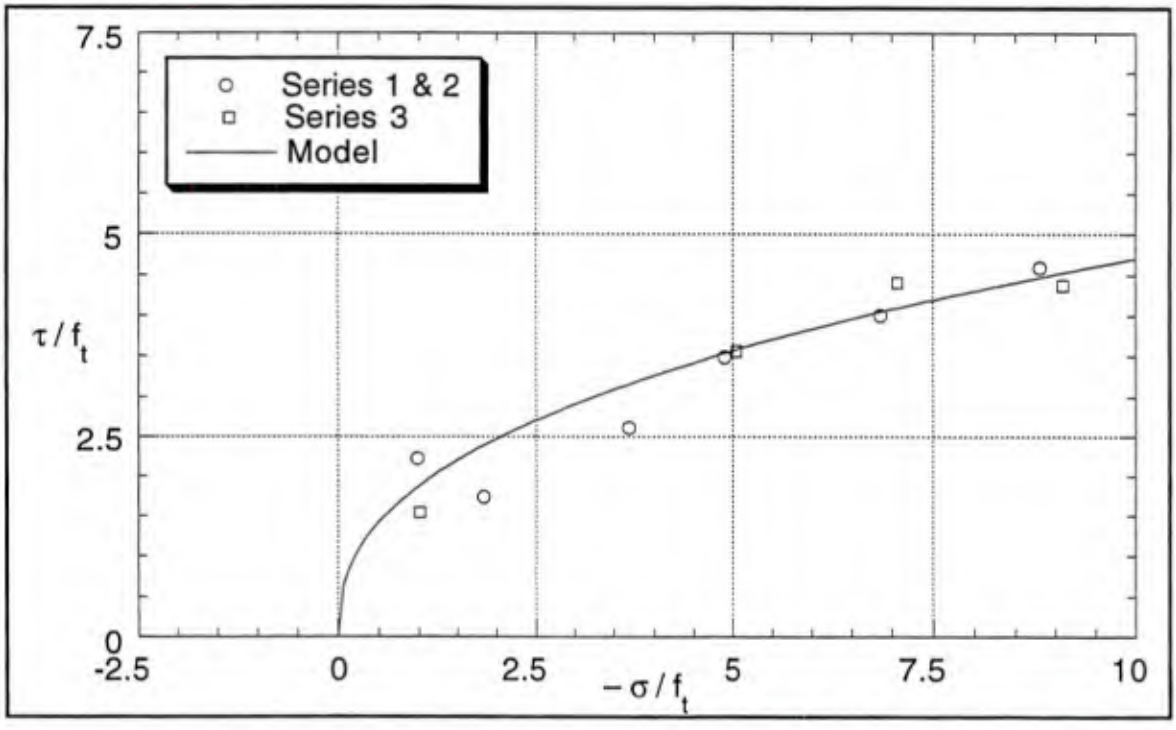

Figure 3.2-10 Yield surface data (for $q_1^p = 0.2$) extracted from the results of Malvar (1991).

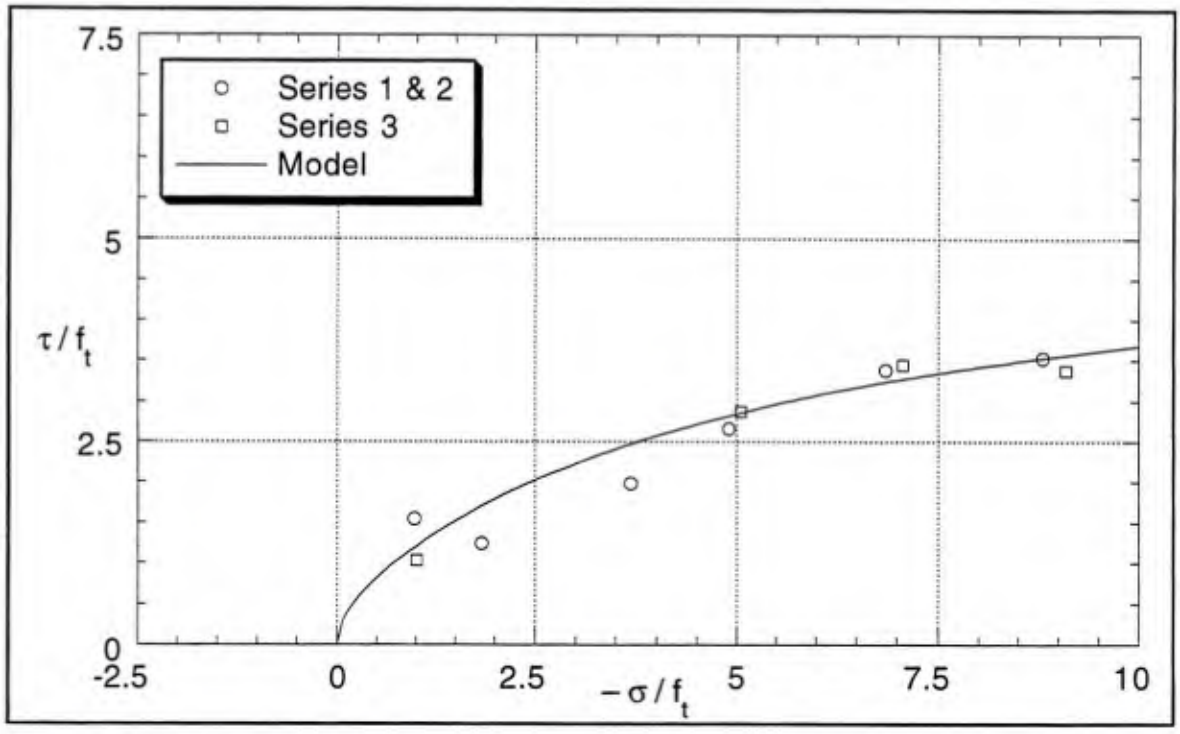

Figure 3.2-11 Yield surface data (for $q_1^p = 0.3$) extracted from the results of Malvar (1991).

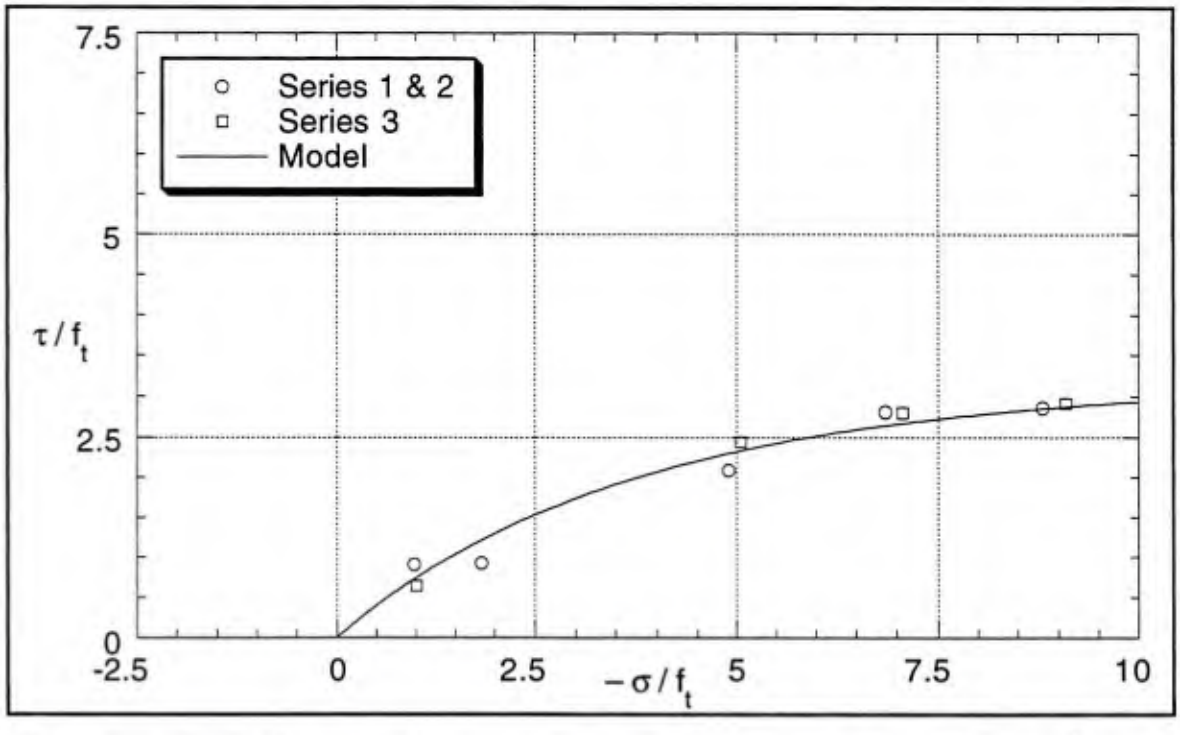

Figure 3.2-12 Yield surface data (for $q_1^p = 0.4$) extracted from the results of Malvar (1991).

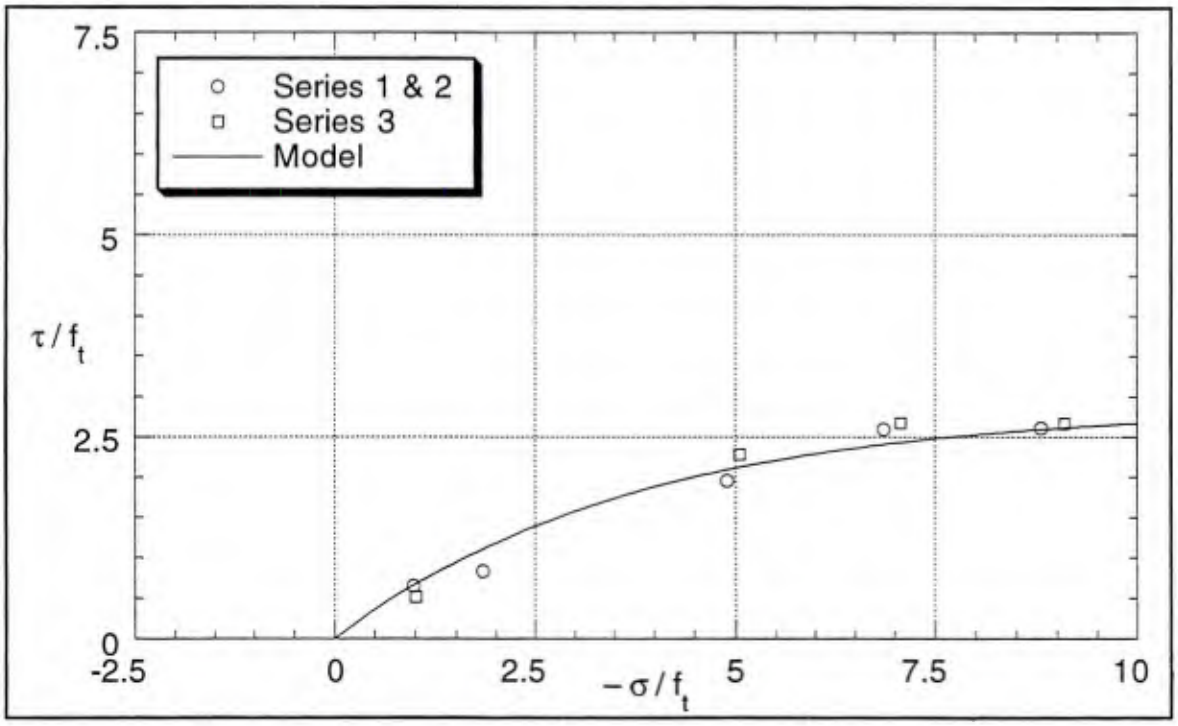

Figure 3.2-13 Yield surface data (for q_1^p = 0.45) extracted from the results of Malvar (1991).

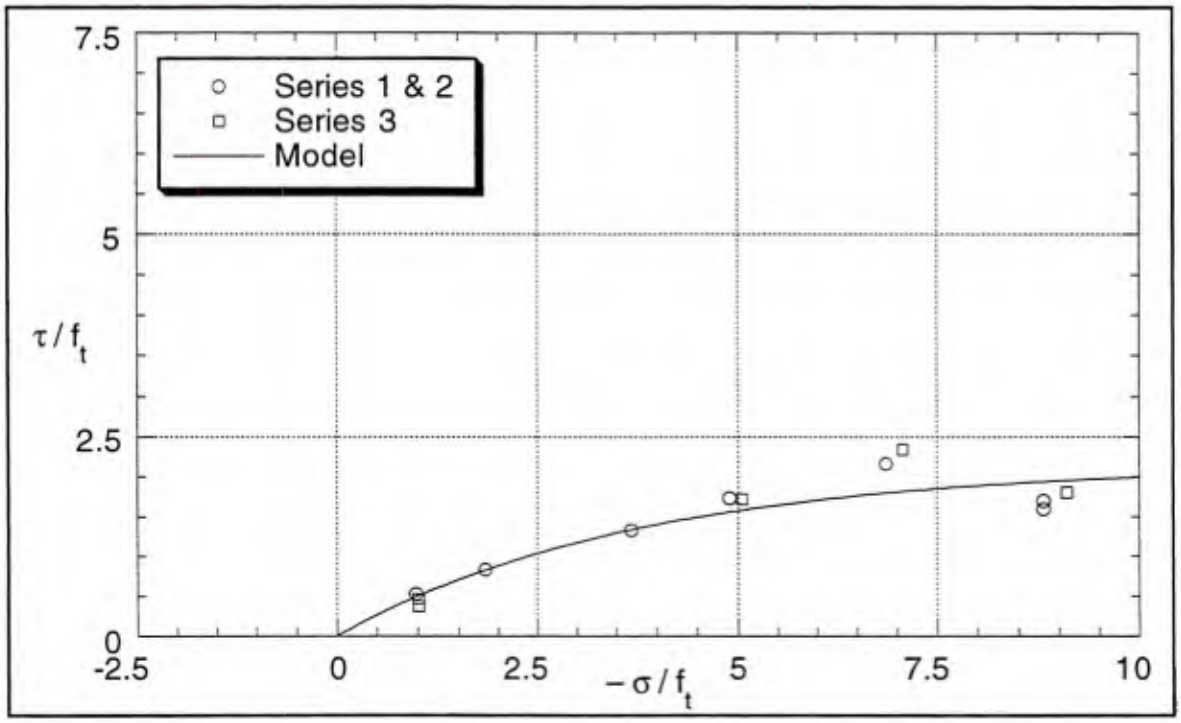

Figure 3.2-14 Yield surface data (for friction) extracted from the results of Malvar (1991).

3.3 Yield Surface Model

Many different analytical forms of yield criteria were considered. The data clearly show that the linear form of the Coulomb criterion is not accurate over a large range of confinement stresses. Most of the yield criteria considered could be expressed as linear combinations of the following two criteria (the "exponential criterion" and "power criterion," respectively)

$$\left|\frac{\tau}{f_t}\right| = C_e(d)\left[1 - e^{-\alpha_e\left(-\sigma/f_t + \hat{\alpha}(d)\right)}\right] \tag{3.3-1a}$$

$$\left|\frac{\tau}{f_t}\right| = C_p(d)\left|\frac{-\sigma}{f_t} + \hat{\alpha}(d)\right|^{\alpha_p} \operatorname{sgn}\left(\frac{-\sigma}{f_t} + \hat{\alpha}(d)\right) \tag{3.3-1b}$$

where

C_p, $C_e \in C^1[0,1]$ ~ isotropic hardening and softening functions,

$\hat{\sigma} \in C^1[0,1]$ ~ kinematic softening function, and

α_e and α_p ~ calibration parameters.

Consistent with the assumptions made in extracting the yield surface data, these hardening and softening functions are expressed in terms of the damage parameter alone.

The stresses are nondimensionalized by a measure of the tensile strength of the concrete. Researchers have scaled the stresses by the compressive strength or various powers thereof; in some cases the function gives an approximation of the tensile strength (*e.g.*, Equation B-1).

The exponential criterion, Equation (3.3-1a), can be calibrated to produce a reasonable representation of the experimental data for large values of damage (d>0.5, see *e.g.*, Figures 3.2-13 and -14). Note that the data for large d suggest a function: 1) with a finite initial (*i.e.*, for small -σ) slope, and 2) that asymptotically approaches a constant value. This asymptotic nature has been reported by many researchers (see *e.g.*, Robins and Standish [1982]). For the case of large d and small confinement stress, Coulomb's criterion can be

interpreted as a Taylor series approximation (retaining only the linear term) to this criterion. Physically this implies that friction is the sole mechanism only at relatively low confinement stresses. For higher confinement stress, the effective coefficient of friction is less. This reduction in the effective coefficient of friction can be attributed to a component of stress that has been omitted in this version of the model – the hoop stress. (This will be discussed further in the section addressing the flow rule.)

The exponential criterion can also be calibrated to give a good representation of the data for smaller values of damage, but to do so requires the kinematic softening to occur very slowly. In addition, the apparent form of the kinematic softening is relatively difficult to express analytically. The kinematic softening will be associated with two mechanisms: 1) the propagation of splitting cracks, and 2) the geometric effect of the rib wedging under the concrete reducing the effective angle at the rib interface.* For the latter mechanism the nonzero intersect has no physical meaning.† Both mechanisms are expected to produce a rapid decrease in bond stress under low confinement stress. For the kinematic hardening function to reflect this requires a rapid translation of the yield surface. To rapidly translate a surface that still models the data well over the entire range of σ values implies the surface has a relatively high initial slope that subsequently reduces with increasing $-\sigma$ – thus the motivation for the power criterion, Equation (3.3-1b).

The power criterion, Equation (3.3-1b), can be calibrated to produce a reasonable representation of the experimental data for small values of damage (d<0.4, see *e.g.*, Figures 3.2-7 and -8); it models the data well in this range because it has the desired shape characteristics mentioned in the previous paragraph (for α_p<1). Note that for α_p equal to

---

* This geometric effect will be referred to as *geometric dilation* in subsequent discussions.

† As previously suggested, one could alleviate this problem by multiplying the right-hand side by a function that has a value of unity over most of its domain but rapidly drops to zero for a small tensile confinement stress.

one the criterion reduces to Coulomb's criterion. Though the power criterion models the data well for small d, it does not model the data well for large d. Its infinite initial slope (an asset at small d) causes an over prediction of the bond stress at low confinement stress for large d.

In this application of plasticity it's not surprising that one form of the yield surface does not model the data well over the full range of damage. For relatively small values of damage the plastic behavior is attributed mostly to crushing and the opening of transverse cracks. For relatively large values of damage friction becomes an important component of the plastic behavior. I associate the change in the form of the yield surface data with this progressive change in the dominant failure mechanism. As such the following model for the yield criterion transitions from a power criterion to an exponential criterion as plastic loading progresses. The yield criterion is given as

$$\left|\frac{\tau}{f_t}\right| = C(d)\left\{W_e(d)\left[1 - e^{-\alpha_e\left(-\sigma/f_t + \hat{\alpha}(d)\right)}\right] + M\left(1 - W_e(d)\right)\left|\frac{-\sigma}{f_t} + \hat{\alpha}(d)\right|^{\alpha_p} \operatorname{sgn}\left(\frac{-\sigma}{f_t} + \hat{\alpha}(d)\right)\right\} \tag{3.3-2}$$

where

$W_e \in C^1[0,1]$ ~ weighting function between the power and exponential components

and M ~ a calibration constant.

To exploit the strengths of each criterion, the weighting function should start with a value of zero and then transition to a value of one.* Choosing a simple cubic function for the transition gives W_e as:

---

* Note that W_e is actually the weight function for the exponential component – thus its subscript. To more explicitly indicate its purpose I will often refer to it as the *transition function*.

$$W_e(d) = \begin{cases} 0, & d \in [0,d_0] \\ 3\left(\dfrac{d-d_0}{d_1-d_0}\right)^2 - 2\left(\dfrac{d-d_0}{d_1-d_0}\right)^3, & d \in (d_0,d_1) \\ 1, & d \in [d_1,1] \end{cases} \tag{3.3-3}$$

where the interval (d_0,d_1) is obtained by calibration. For the current calibration (d_0,d_1) = (0.38, 0.53).

While a smoother function could be selected, the effect of the transition has been minimized by calibrating the exponential and power components of the yield criterion to be in good agreement in the interval (d_0,d_1). In this interval, the largest disparity occurs for small confinement stresses since the two components have such different initial slopes. In the calibration results of Chapter 7, the transition between the two components of the yield surface is only apparent for a confinement stress of 500 psi (3.45 N/mm^2).

As was previously mentioned, the kinematic softening function is associated with mechanisms that occur very rapidly. As such this function is intended to reflect the brittle nature of the bond mechanisms that dominate under low confinement stress. The following simple form has been selected for kinematic softening:

$$\hat{\sigma}(d) = \begin{cases} \hat{\sigma}_0\left(\dfrac{d_2-d}{d_2}\right)^{\beta}, & d \in [0,d_2) \\ 0, & d \in [d_2,1] \end{cases} \tag{3.3-4}$$

where

d_2 ~ the damage value at which kinematic softening stops,

β ~ a calibration constant typically greater than 1, and

$\hat{\sigma}_0$ ~ the intersect of the yield surface with the σ/f_t-axis when d=0.

To determine a reasonable value for d_2, consider a very simplified model of the wedging action of the ribs that only addresses *geometric dilation* (*i.e.*, neglecting local deformations and assuming the rib face and adjacent concrete interact as a rigid contact problem).

Assume that the face of the rib has the shape of a 90-degree arc and that the maximum radial expansion of the bond zone occurs when the *point* of contact between the concrete and the rib is at the top of the arc-shaped face. For this model the ability of the rib to transmit transverse force would reach a minimum when the slip is equal to the rib height (*i.e.*, when the normal to the contact surface reaches 90 degrees); thus a reasonable value for d_2 would be the ratio of the rib height to the rib spacing (h_r/s_r). For typical steel reinforcement, the ratio of the rib height to the rib spacing is $O(1/10)$. So for this initial development, d_2 is taken to be 0.1.

Two parameters must still be set to fully define the kinematic softening. As previously discussed, $\hat{\sigma}_0$ is set to 2.25. For the proposed form of the kinematic softening function, $C^1(0,1)$ is only maintained when $\beta>1$. In the initial development β was assumed to have a nominal value of 2.7. This was obtained by fitting the general yield criterion of Equation (3.3-2) to the experimental data for the maximum bond stress,* Figure 3.2-8. The experimental data suggest that the maximum bond stresses occur at an average value of d=0.0575. In fitting the surface to the experimental data at this state, $\hat{\sigma}(0.0575)=0.02$ is obtained. Solving Equation (3.3-4) for β then gives $\beta \approx 2.7$.

One phenomenon that the kinematic softening function allows the model to reproduce is the variation in the slip at which maximum bond stress occurs. Figures 3.2-3 and -4 reflect an increase in the slip at which τ_{max} occurs with an increase in $-\sigma$. Figures 3.2-5 and -6 indicate that much of the shift in the maximum bond stresses can be attributed to the elastic component of slip, but this is not the only factor. Despite the above use of an average

---

* It is actually a misnomer to refer to the yield surface at any state as being the surface at which the maximum bond stresses occur unless: 1) kinematic softening does not exist, and 2) the confining stress is constant. Figure 3.2-8 was referred to as the surface for which τ_{max} occurred; more accurately this is the state at which the isotropic hardening attains its maximum. As discussed in the next paragraph, one of the advantages of including the kinematic hardening is that it allows a variation in the damage at which τ_{max} occurs for different confinement stresses while retaining a simple definition of damage.

damage value to determine β, it is apparent from Figures 3.2-5 and -6 that the damage value for τ_{max} increases with increased confinement stress. The bond behavior appears less brittle as the confinement stress increases. The interaction of the kinematic softening and isotropic hardening can produce the same behavior. Another important factor in this behavior can be the change in confinement stress (*i.e.*, the bond stress can increase even during isotropic softening if $-\sigma$ is increasing).

As previously discussed, the power and exponential forms of the yield criterion, Equations (3.3-1), provide reasonable models for small and large values of damage, respectively. The transition interval defined in Equation (3.3-3) was easily determined while calibrating the isotropic hardening/softening function. Each criterion was fit to the experimental data over the full range of damage. Analogous to tuning a cross-over circuit in a stereo speaker to optimize the use of the drivers, the damage interval of (0.38,0.53) was selected for transition. That is, 0.38 was selected as the lower bound of "reasonable results" for the exponential criterion, and 0.53 was selected as the upper bound of "reasonable results" for the power criterion. Though one could apply relatively sophisticated nonlinear least squares procedures to obtain values for α_e, α_p, M, and $C(d)$ for various internal states, a simpler approach was taken in this study. The quantities α_e and α_p were assumed to be constants (0.27 and 0.4, respectively) subjectively selected based on linear least square fits (with respect to $C(d)$) of the functions to the experimental data over the applicable ranges of damage. The parameter M was assigned the value of 1.38; this parameter scales the power component so that a single isotropic hardening/softening function can be used instead of requiring the inclusion of both C_e and C_p of Equations (3.3-1). Linear least square fits of the model to the experimental data (given in Figures 3.2-7 through -14) yield values of $C(d)$ as shown in Figure 3.3-1.

Note that the values of plastic slip at which pure frictional behavior begins (Figures 3.2-5 and -6) are somewhat subjective and certainly not equal. Thus, in Figure 3.3-1 a range of

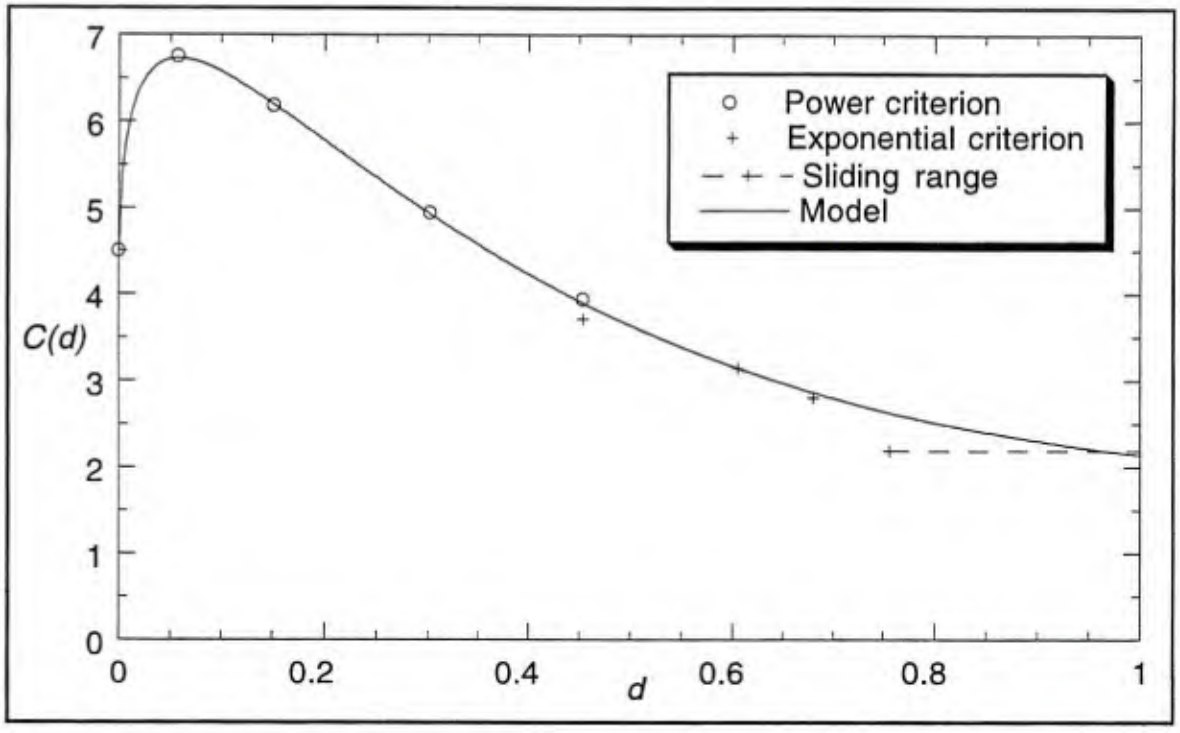

Figure 3.3-1 Isotropic hardening/softening function compared to values obtained by fitting power and exponential yield surfaces to experimental data.

damage is given for this "sliding behavior." However, with the simple definition of damage adopted in this study, pure frictional behavior occurs at a unique value of d (and thus of q_1^p also) that is independent of σ.

The hardening portion of C occurs over a relatively small range of damage. It can be attributed to two possible mechanisms – crushing and fracture. Crushing could cause compaction of a somewhat porous concrete near the rib-contact region. The results of a simple rib-scale analysis given in Figure 3.3-2 reflect the concentration of stress that would be expected near the face of a rib. This simplified analysis treated the steel and concrete as homogeneous, linear, isotropic elastic materials. Contact friction elements were used at the material interface, but prestress due to shrinkage which develops during curing was not included. The rib is idealized as having the cross section of half a circle when in actuality it is relatively flat on its top surface with inclined faces. As the relatively porous concrete in

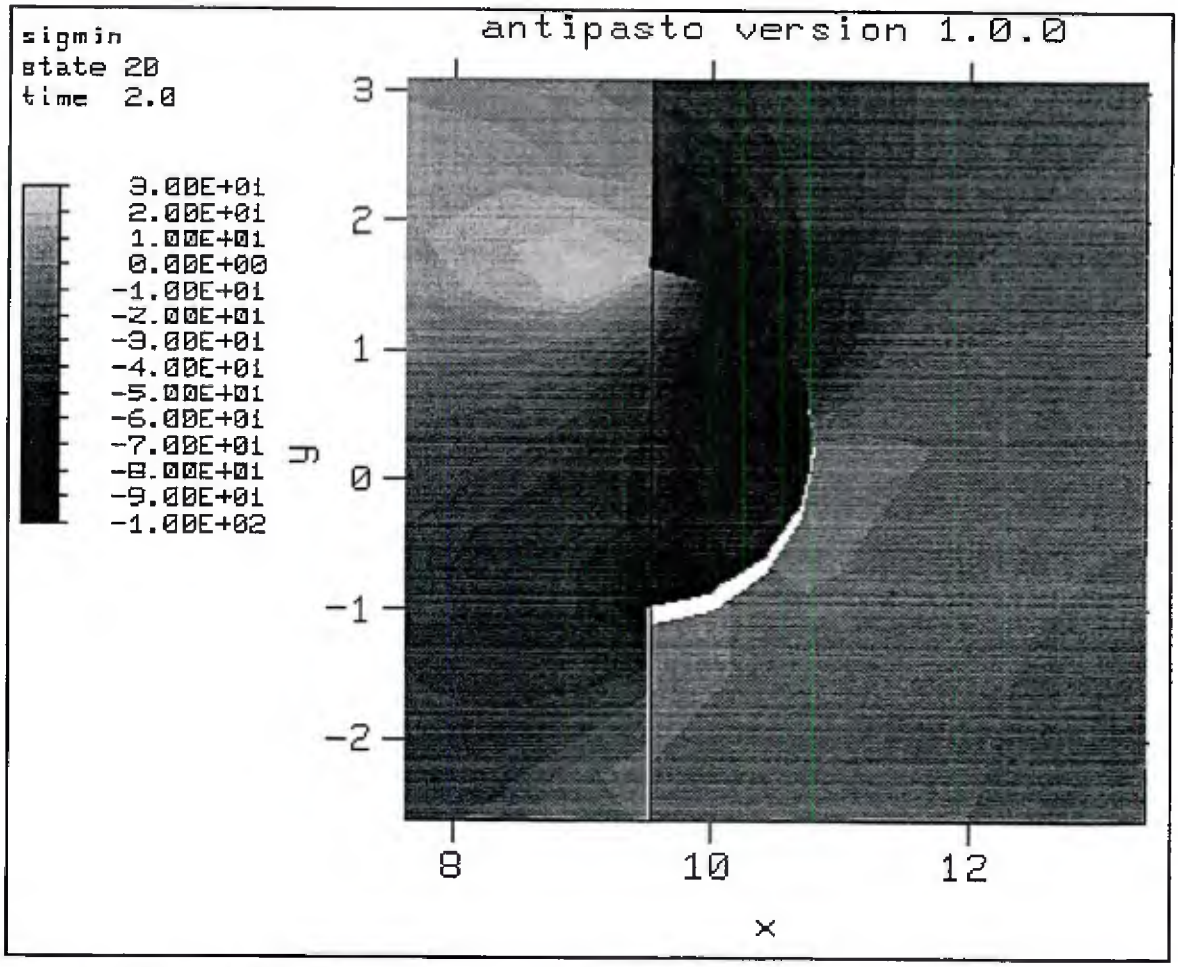

Figure 3.3-2 Minimum principle stress near the face of a rib.

front of the rib crushes, it in effect increases the contact region with the remaining porous concrete thus increasing the force necessary to produce additional crushing. This is consistent with observations of elastoplastic coupling that indicate an initial increase in elastic properties with plastic deformation (see *e.g.*, Rehm [1957] and Lutz and Gergely [1967]).

Alternatively one might attribute the hardening to stable crack growth. Assuming the transverse cracks are axisymmetric, the area associated with an infinitesimal increase in crack length increases linearly with radius. Thus one would expect progressively more energy to be required for a unit propagation of the transverse crack. Though this is not

consistent with the elastoplastic coupling cited in the previous paragraph, it still might be a significant contributing mechanism for some states of stress.

For low confinement stresses the effects of isotropic hardening should be less significant since the stresses near the face of the rib are reduced. The ribs tend to wedge under the concrete (geometric dilation) rather than induce extensive crushing or propagate transverse cracks. It is the previously mentioned "interaction" of the isotropic hardening and kinematic softening that produces this more brittle behavior at low confinement stresses.

As one would expect, relative to the rib spacing the isotropic hardening is short-lived. The dominant behavior is that the force necessary to produce plastic slip progressively reduces with plastic slip – softening. The mechanisms include crushing, fracture and friction; the latter of which dominates "in the end." The progression of this failure is discussed in more detail in the following chapter addressing the flow rule.

In the implementation of the bond law, two *standard functions* were included for possible use in development of both the hardening laws and flow rule. These functions are given as

$$expFunc(\theta_2,\theta_3,\theta_4,\theta_5,x) = \frac{\theta_2 + \theta_3}{\theta_2 + \theta_3 e^{\theta_4 x^{\theta_5}}} \tag{3.3-5a}$$

and

$$ratFunc(\theta_2,\theta_3,\theta_4,x) = \frac{\theta_2}{\theta_2 + \theta_3 x^{\theta_4}} \tag{3.3-5b}$$

where θ_2, θ_3, θ_4 and θ_5 are calibration constants. These functions are defined to have a unit value at x equal to zero. For the calibration represented in Figure 2.4-15, C is defined in terms of the standard exponential function as:

$$C(d) = -a_1 expFunc(a_2,a_3,a_4,a_5,d) + b_1 expFunc(b_2,b_3,b_4,b_5,d) + C_\infty \tag{3.3-6}$$

where C_∞, {a} and {b} are given in Table 3.3-1 below.

Table 3.3-1 Calibration constants for C.

C_∞	a_1	a_2	a_3	a_4	a_5	b_1	b_2	b_3	b_4	b_5
1.7	3.3	0	1	10	0.6	6	0	1	2.6	1.2

With these calibration constants Equation (3.3-6) can be simplified to

$$C(d) = -3.3\exp\left(-10d^{3/5}\right)+6\exp\left(-2.6d^{6/5}\right)+1.7. \tag{3.3-7}$$

Note that $C \in C^1(0,1)$ and as such has a much cleaner form for numerical implementation than the C^0 monotonic envelopes that are currently used in most bond models. The definition of d, Equation (3.2-3), however does imply that C has a slope discontinuity with respect to plastic slip at d=1.

All of the calibration constants for C would typically be chosen as nonnegative. Defining $a_5<1$ and $b_5>1$ implies C^1 of the bond slip relationship as follows:

$$\begin{aligned} a_5<1 \wedge b_5>1 &\Rightarrow \lim_{d\to 0^+} \frac{dC(d)}{dd} = +\infty \\ &\Rightarrow \frac{d\phi}{dd} \to +\infty \\ &\Rightarrow K^p \to +\infty \\ &\Rightarrow \mathbf{D} \to \mathbf{D}^e \\ &\Rightarrow \underline{Q} \in C^1(\underline{q}) \end{aligned} \tag{3.3-8}$$

The general form of C given by Equation (3.3-7) is simpler to calibrate than it might first appear. Assuming the first term has a relatively large a_4 value, it principally affects the hardening portion of the function since it tends to zero rapidly with increasing d. Thus when calibrating, one can fit the last two terms to the softening data, and then fit the total function – adjusting only the first term – to the hardening data.

Figure 3.3-3 shows both "hardening functions" and the transition function with the values of damage aligned between the plots. This figure illustrates that isotropic hardening and

kinematic softening nearly occur over the same range of damage values. It is also apparent that by the time the yield surface attains its exponential shape (*i.e.*, W_e=1) further change in *C(d)* is relatively small which is consistent with friction being the dominant mechanism at this point. The reduction in *C(d)* that does occur can be attributed, in part, to a reduction in the effective coefficient of friction as the damaged interface is "smoothed."

With the calibration of the yield criterion complete, Figure 3.3-4 shows the yield surface at several states of internal damage reflecting its evolution. The geometric effect of each

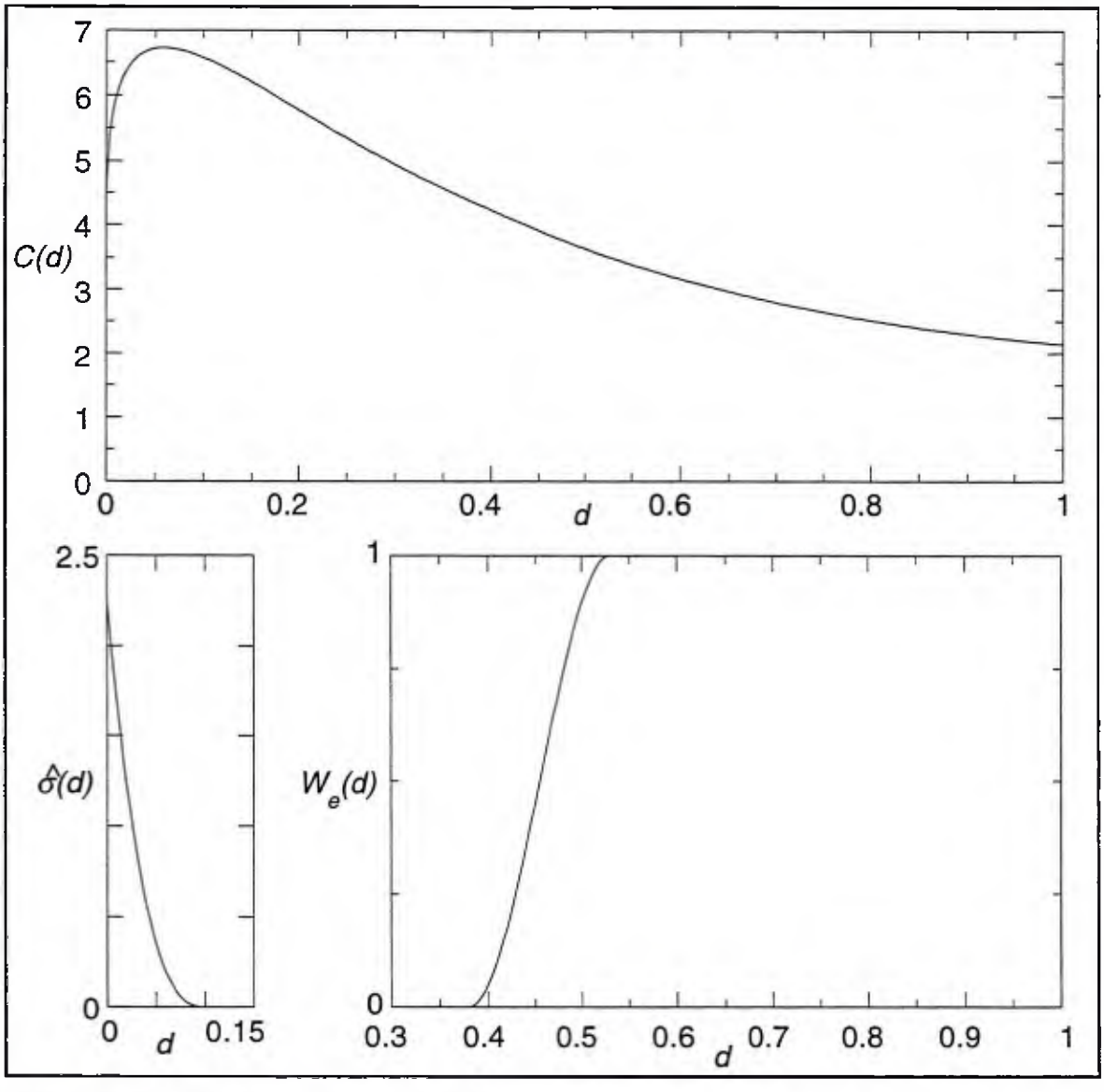

Figure 3.3-3 "Hardening" and transition functions.

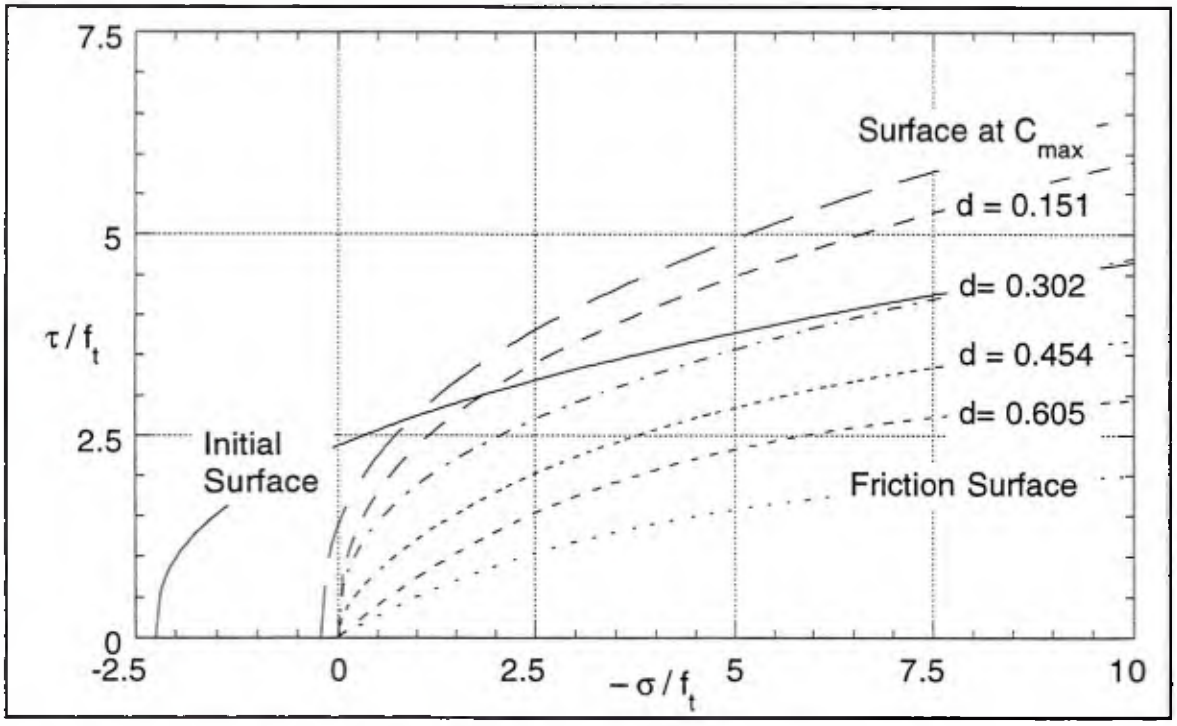

Figure 3.3-4 Yield surface evolution.

component function of the yield criterion is readily apparent: $\hat{\sigma}$ rapidly translates the yield surface to the origin, C "expands" (during hardening) then partially "contracts" (during softening) the surface to a final size for friction, and W_e transitions the shape of the surface from the power form to the exponential form which is most apparent in the initial slope of the surface.

For values of $-\sigma$ less than approximately f_t the bond stress at initial yielding exceeds the bond stress when C is a maximum; this implies that for a fixed confinement stress in this range, the maximum bond stress is attained prior to the maximum expansion of the yield surface. Thus as the confinement stress decreases the maximum bond stress is attained with less plastic slip, and the maximum bond stress decreases; *i.e.*, the model exhibits a more brittle behavior. This aspect of the model and the variation in normal stress during the loading history cause the slip at which maximum bond stress occurs to vary.

The general shape of the yield surfaces in Figure 3.3-4 are reminiscent of the curved meridians often used to define failure surfaces for concrete in principal stress space (see *e.g.*, Chen [1982]). In particular the curved meridians are adopted over straight meridians when the first invariant of stress – proportional to the distance along the hydrostatic axis – is expected to be relatively high. This is analogous to our previous observation that a Coulomb surface can be interpreted as an approximation to the bond model's yield surface for low confinement stresses. The similarity between the bond model yield surface and the meridians of concrete failure surfaces suggests that additional stress components could be added by generalizing the measures of distortional and dilatational stresses. However, one would not expect that a concrete failure surface in principal stress space could be directly adopted because: 1) the bond model includes a phenomenological characterization of the concrete's mechanical interaction with the ribs, and 2) the measures of distortional and dilatational stress must account for the orientation of the bar.

While considering the incorporation of additional stress components, let's take another look at the current stress components used in the yield criterion. In the earlier development, the generalized stresses and strains were reduced to two components each. As defined the generalized stresses and strains reference a coordinate system associated with the orientation of the bar; so by definition their components are scalars that are invariant with rigid body rotations.

The objectivity of the constitutive law can be established in a more formal manner that may be useful in future development efforts. Figure 3.3-5 shows a reinforcement bar with an arbitrary orientation given by the angle γ. The directions tangent and normal to the top surface of the bar are represented by $\mathbf{t}$ and $\mathbf{n}$, respectively.

Cauchy's law gives the tractions on this surface of the bar as $\sigma \cdot \mathbf{n}$. Now σ and τ can be obtained by taking the inner product of the traction vector with $\mathbf{n}$ and $\mathbf{t}$, respectively as

$$\sigma = \mathbf{n} \cdot \sigma \cdot \mathbf{n} \quad \text{and} \quad \tau = \mathbf{t} \cdot \sigma \cdot \mathbf{n} \ . \tag{3.3-9a,b}$$

In this form the yield criterion can be expressed in terms of the stress tensor defined in an arbitrary coordinate system where the directionality of the bar surface element and slip direction are characterized by **n** and **t**, respectively. The objectivity of the yield criterion is simply established by showing that ϕ is an isotropic function of its arguments; for the form of the yield criterion given by the substitution of Equations (3.3-9) into Equation (3.3-2) this merely requires $\mathbf{n}\cdot\sigma\cdot\mathbf{n}$ and $\mathbf{t}\cdot\sigma\cdot\mathbf{n}$ to be admissible mixed invariants. Among the admissible mixed invariants are

$$\mathbf{v}_1\cdot\mathbf{A}\cdot\mathbf{v}_1 \quad \text{and} \quad \mathbf{v}_2\cdot\mathbf{A}\cdot\mathbf{v}_1 \tag{3.4-10}$$

where $\mathbf{v}_1$ and $\mathbf{v}_2$ are vectors and **A** is a symmetric tensor. These are exactly the forms of $\mathbf{n}\cdot\sigma\cdot\mathbf{n}$ and $\mathbf{t}\cdot\sigma\cdot\mathbf{n}$ thus formally establishing the obvious – that the adoption of the local coordinate system is equivalent to introducing directional internal variables (**n** and **t**) and that each of the stress components in this local coordinate system corresponds to a mixed invariant between the stress tensor and the directional internal variables. To add stress components to the model, one could consider other admissible invariants that provide a generalized measure of distortion and dilation.

With the description of the yield criterion complete, the next chapter discusses the model's flow rule. If the model had an associative flow rule, the direction of plastic strain rates would now be known. However, careful examination of experimental data suggests that simplification cannot be made.

Chapter 4

Flow Rule

This chapter describes the development of the flow rule for an elastoplastic bond model applicable to monotonic loading. As discussed in Section 2.2 the flow rule defines the evolution of plastic strains. Though the assumption of an associative flow rule is quite common in material models, the data analyzed in this section indicate that a nonassociative flow rule is regretfully necessary in modeling bond at the bar-scale. As Equation (2.5-4) suggests, this will lead to the burden of a nonsymmetric tangent stiffness matrix. In addition, material stability during hardening could be sacrificed. These liabilities of a nonassociative flow rule cause some critics to denounce any material law that adopts the rule. Unfortunately to take this stance, in the context of interface models, also requires one to abandon classical Coulomb friction as well. One advantage to "uncoupling the yield criteria and flow rule" in the initial development, is that refinements to each component have only a secondary influence on the behavior associated with the other component. For example, a change in the yield criterion does not necessarily imply a change in the plastic strain directions. Admittedly this is a simplification, for it is expected that radial dilation (as with granular materials) is associated with the material softening. In the last section we will see that during this radial dilation, the yield criterion and flow rule must jointly satisfy the second law of thermodynamics.

As with the development of the yield criterion, the experimental works of Gambarova, Rosati and Zasso (1989) and Malvar (1991) serve as the experimental basis for the development of the flow rule. Since the tests of Gambarova *et al.* (1989) control the crack

opening, the normal stress history varies considerably with time. Thus in the initial development based on the results from this data set, the flow rule was modeled without any direct dependence on the confinement stress; Section 4.4 shows this was not a valid model.

In subsequent development efforts focusing on the data of Malvar (1991), I developed the flow rule presented in this section. It directly incorporates the effect of confinement stress in a form that is consistent with observed experimental results. Unfortunately the experimental data are sparse, and radial dilation, even in the tests of Malvar (1991), is difficult to measure accurately. As such, the flow rule presented in this section is probably the weakest component of the model; qualitatively though (as will be shown in Chapter 7) it gives very reasonable results for overall response and for the induction of splitting cracks in the adjacent concrete.

The following sections sequentially discuss 1) the reduction of the experimental results to obtain data directly usable to model the flow rule, 2) the mechanics associated with the experimental form of the flow rule data, 3) the flow rule model, and 4) a thermodynamic constraint on radial dilation.

4.1 Data Reduction

Figures 4.1-1 and -2 present the radial dilation data of Malvar's (1991) series 2 and 3 tests. These plots clearly reflect a decrease in radial dilation with increased confinement stress. While the increase in bond stress with increased confinement stress was very consistent from test to test (Figures 3.2-3 and 3.2-4) the radial dilation data show some variation; for example, the radial dilations of tests 1 and 8 were less than those of tests 2 and 9, respectively.

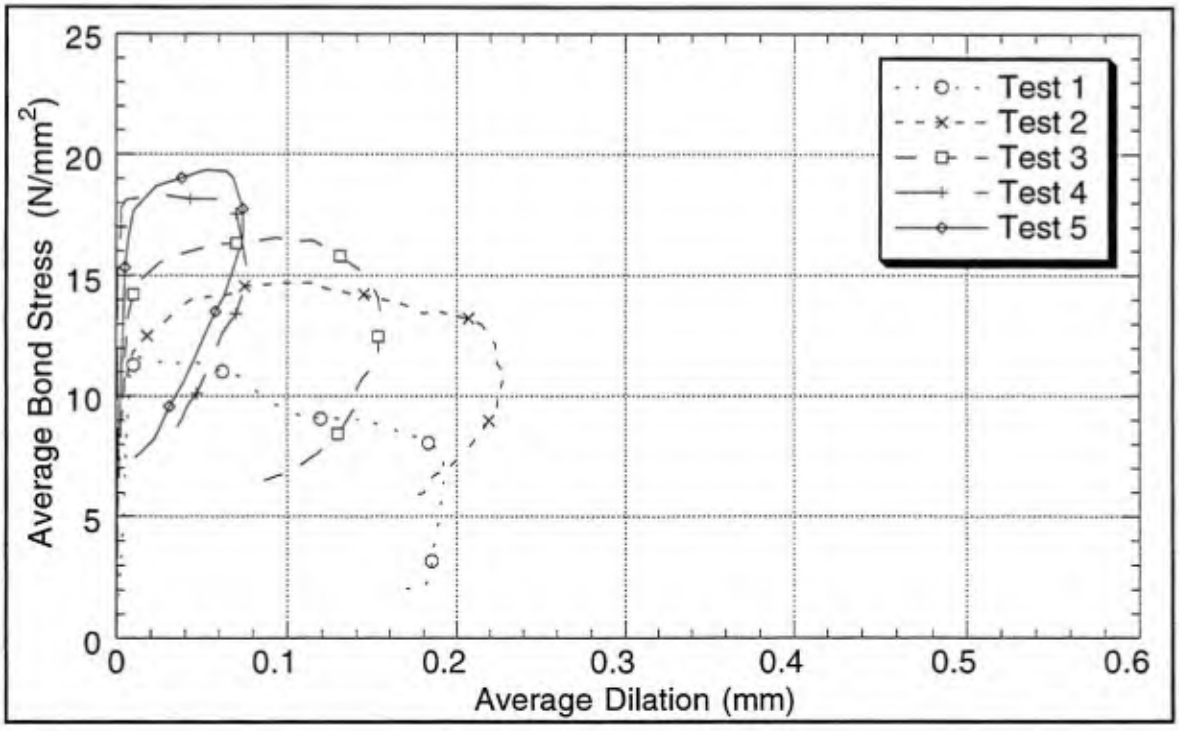

Figure 4.1-1 Bond stress versus average radial dilation results of Malvar (1991) series 2 tests. The values of $-\sigma$ for tests 1-5 were 500, 1500, 2500, 3500, 4500 psi or 3.45, 10.3, 17.2, 24.1, 31.0 N/mm^2, respectively.

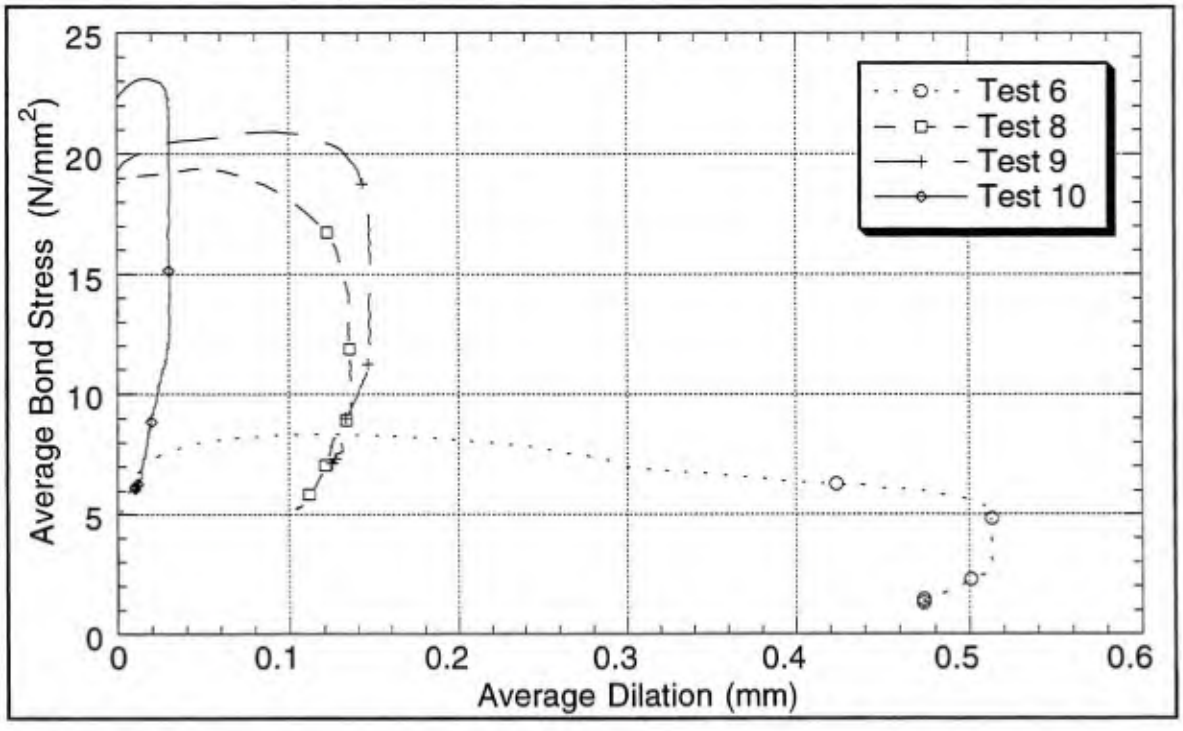

Figure 4.1-2 Bond stress versus average radial dilation results of Malvar (1991) series 3 tests. The values of $-\sigma$ for tests 6, 8, 9 and 10 were 500, 2500, 3500, 4500 psi or 3.45, 17.2, 24.1, 31.0 N/mm^2, respectively.

The difference in the shapes of the graphs between the two series of tests indicates that the rib geometry affects the radial dilation response. Certainly at the rib-scale, one would expect the crushing and transverse cracking behavior to vary with the rib geometry.

Various forms have also been considered for the flow rule. They have all been of the general form

$$\{\dot{q}^p\} = \langle\lambda\rangle \begin{Bmatrix} \operatorname{sgn}(\tau) \\ g \end{Bmatrix}, \tag{4.1-1a}$$

thus the direction of plastic strain defined in Equation (2.3-2) is given by

$$\{R^p\} = \begin{Bmatrix} \operatorname{sgn}(\tau) \\ g \end{Bmatrix}. \tag{4.1-1b}$$

Since the first term of the plastic strain vector is normalized, the function g represents the slope of the vector with respect to the plastic slip direction. Unlike the functions associated with the yield surface, the flow rule always has an incremental form.

The direction of plastic strain is often expressed in terms of an elastoplastic potential. In this case Equation (4.1-1b) then becomes

$$\{R^p\} = \left\{\frac{\partial \psi}{\partial Q_i}\right\} \tag{4.1-2a}$$

where

$$\psi(d,Q) = |\tau| + \int_{\sigma^0}^{\sigma} g(\hat{\sigma},d)\,d\hat{\sigma}. \tag{4.1-2b}$$

The interpretation of g as the slope of the plastic strain vector suggests that the experimental data of Malvar (1991) might be analyzed to determine a model for g. Consistent with the assumptions made in obtaining the yield surface, I assume for the flow rule that: 1) g is only dependent upon the confinement stress and *damage,* as defined by Equation (3.2-3); 2) q_f^p can be accurately estimated from Equation (3.2-2); 3) the $-\sigma$ value reported by Malvar

(1991) is the normal stress at the bar; and 4) the radial elastic contraction due to the applied confinement stress is not significant.

While these assumptions allow a model for g to be more readily obtained from the experimental data, they also impose limitations on the resulting model. Assumption (1) implies that a history characterized by plastic slip followed by an increase in confinement stress will not result in plastic contraction during this latter phase of loading; this is not a realistic response. One would expect the increase in confinement stress to cause additional local crushing near the rib (especially for relatively low initial confinement stresses), thus producing a plastic contraction.* Assumption (3), as discussed in the previous chapter, implies a thick bond zone interpretation of the data which has inherent limitations when σ_θ is not included in the model. Assumption (4) implies either a thick bond zone interpretation of the data or that D_{22}^e is very large. The validity of these last assumptions will be discussed in Chapter 7 when the model is applied with a small bond zone interpretation to the Malvar specimens.

The data acquisition system used by Malvar (1991) was upgraded between test series 2 and 3. The recorded data of the first two series of tests consisted of plotter data as digitized for Figures 3.2-3 and 4.1-1. The data of the last two test series were digitally recorded. Thus the relationship between the components of plastic strain is only directly available for the latter series of tests.†

---

* The model can produce additional plastic deformation, but plastic radial contraction cannot be directly caused by the increase in confinement stress. Plastic deformation (slip and dilation) might occur because the relative magnitudes of the terms in $\mathbf{D}^{-1}$ (see Figure 7.1-20) could cause plastic slip.

† One could correlate the plastic slip and radial dilation for the series 2 tests via the common values of average bond stress, but derivatives of coarse data (to obtain the plastic strain directions) are poor.

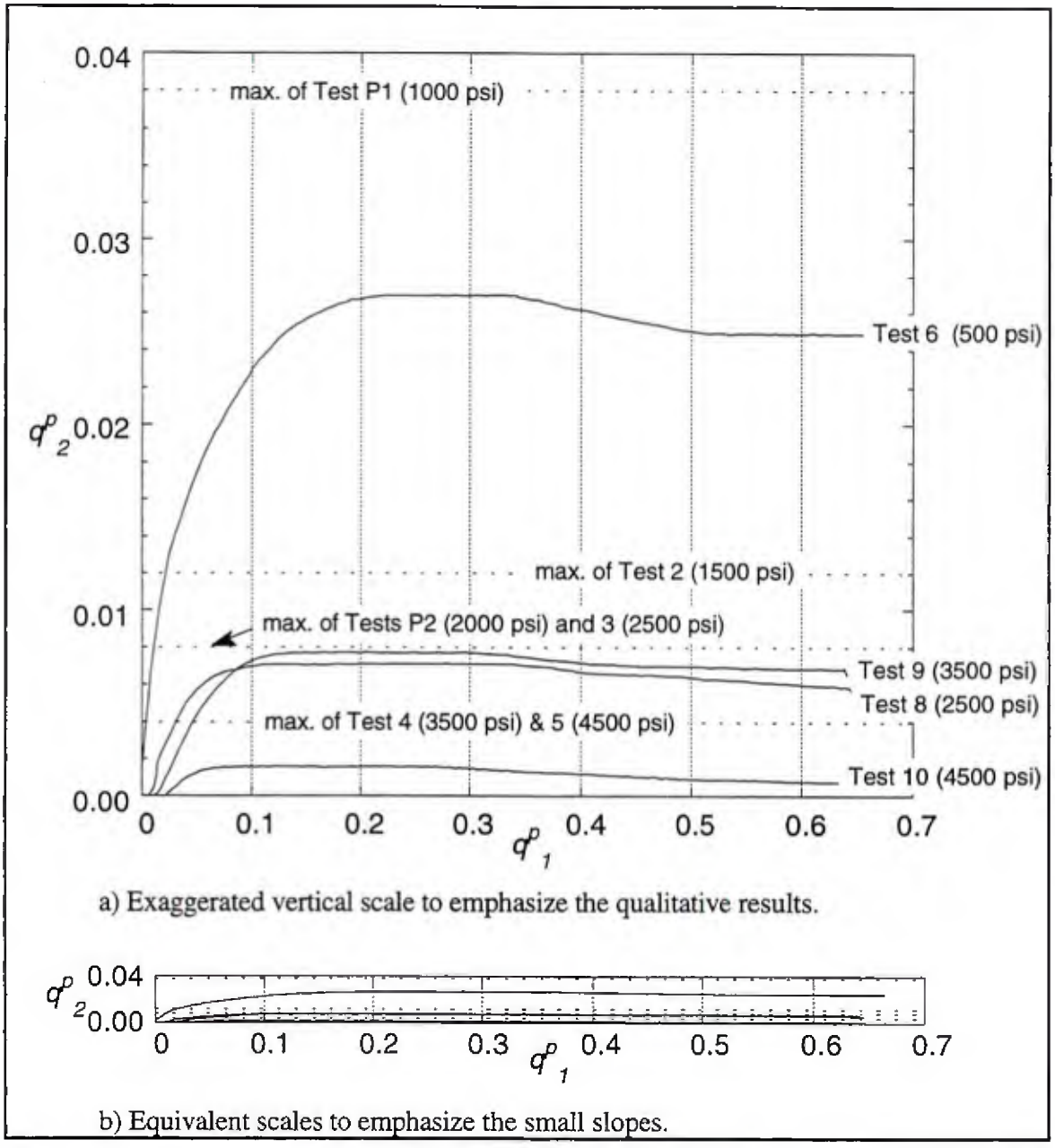

Figure 4.1-3 Plastic radial dilation versus plastic slip deduced from the series 3 tests of Malvar (1991).

Figure 4.1-3 presents plastic radial dilation (actually the total with assumption 4) versus plastic slip for test series 3. In addition, the maximum radial dilations for the series 1 and 2 tests are shown. Note that the slopes (values of g) of the graphs shown in Figure 4.1-3b are close to zero over the full range of plastic slip. The only slopes that deviate noticeably

from the horizontal occur at very small plastic slips. The positive slopes denote radial dilation while the negative slopes denote radial contraction of the bond zone.

As noted earlier, the radial dilations given by tests 8 and 9 do not follow the trend of reduced radial dilation with increased $-\sigma$. Comparison with the maximum results of the series 1 and 2 tests suggests that test 8 is more representative of the trends in the data than test 9; without sufficient data to examine the experimental scatter this is a subjective call.

From these graphs it is obvious that adoption of an associative flow rule is futile. For relatively small values of plastic slip, the slopes of the graphs increase with decreasing confinement stress ($-\sigma$); this trend is consistent with the normal to the yield surface having a larger component in the σ–direction with decreasing $-\sigma$. Any correlation stops here. For plastic slips near 0.2, slopes are approximately zero for all levels of confinement stress which suggests a horizontal yield surface (*i.e.*, the bond stress does not depend upon the confinement stress). For plastic slips near 0.4, the slopes are negative and increase in magnitude with decreasing $-\sigma$; this implies the shape of the yield surface is such that larger elastic bond stresses can be attained by reducing the confinement stress. Not only is this contrary to intuition and experimental data, it also implies the yield surface is nonconvex. Conversely if one assumes the model's yield surface is reasonable, an associative flow rule implies the bond zone continually dilates which is contrary to the experimental data given above.

To obtain plots of g from the data shown in Figure 4.1-3, the derivative of each graph as a function of plastic slip must be estimated from the experimental data. Initially a three-point, unevenly-spaced, finite difference scheme was used; even small variations in the experimental data produced large variations in the derivative estimates with this approach. As an alternative, a least squares approach was tried where a line was fit to three or five points, and then the slope (g) was associated with the plastic slip of the middle point. The

five-point least squares approach gave a smoother curve which fell within the scatter of both three-point methods and thus was adopted for the data reduction results shown below.

Figures 4.1-4 present the experimental graphs of g for the series 3 tests. Since g was obtained from dq_2^p/dq_1^p, the fundamental theorem of calculus implies that the area under the positive part of a curve is proportional to the maximum radial dilation and the area under the negative portion of a curve is proportional to the subsequent radial contraction.

Consider the following trends in the experimental data which will be incorporated in the model function for g:

1. The graph of g passes through the origin. This is not apparent in test 6 principally because the five-point least squares calculation would require many data points over a very small range of slip to capture this.
2. The ascending portion of the graph (prior to $g(d)_{max}$) is fairly straight.
3. The damage interval over which contraction occurs is not strongly dependent upon the level of confinement stress.

<u>For increasing $-\sigma$</u>:

4. The d at which $g(d)$ is a maximum increases.
5. $g(d)_{max}$ decreases.
6. The d at which $g(d)=0$ decreases.
7. The amount of radial dilation decreases.
8. The subsequent amount of radial contraction decreases.

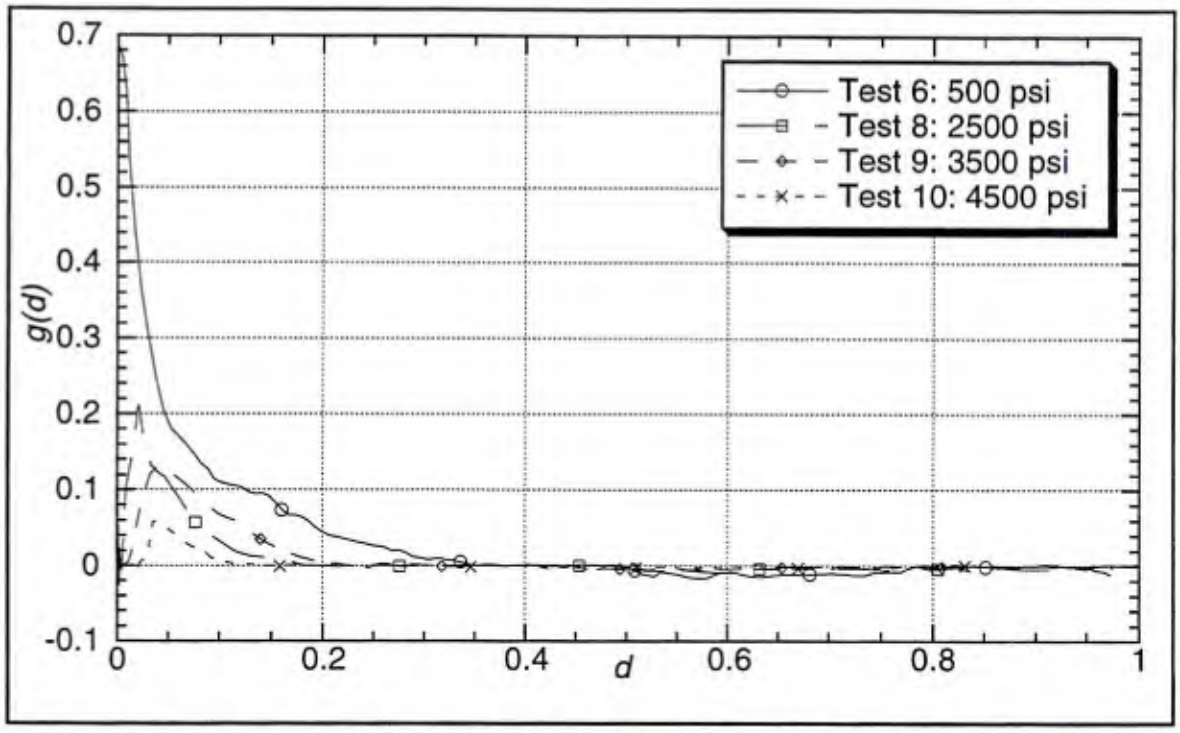

Figure 4.1-4a *g(d)* versus *d* deduced from the series 3 data of Malvar (1991).

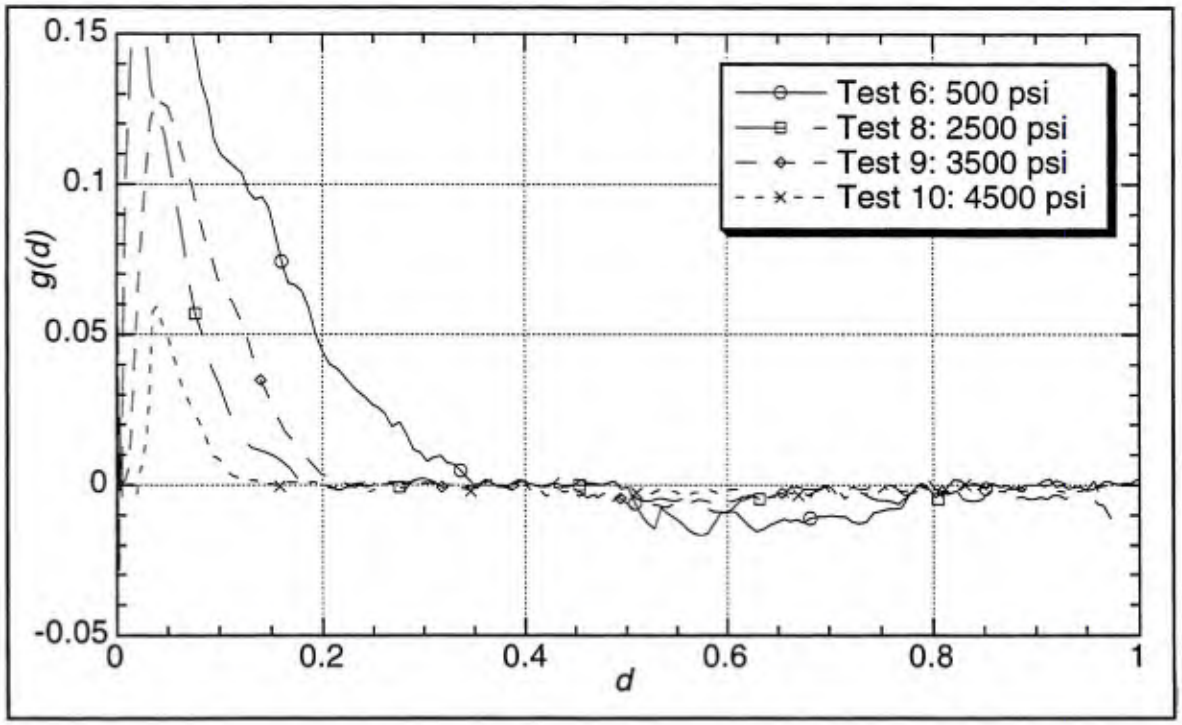

Figure 4.1-4b *g(d)* versus *d* deduced from the series 3 data of Malvar (1991) – a closer look.

4.2 Mechanics

In the previous chapter some of the mechanics associated with the yield surface were discussed. While the yield surface and flow rule are not directly coupled (*i.e.*, via an associative flow rule), the mechanics they represent are one in the same; as such, the discussion of the mechanics associated with the yield surface was inherently incomplete until the kinematics of the bond zone could be addressed. As previously mentioned, the following discussion presents hypotheses that are consistent with the experimental data. In this discussion the focus is upon crushing, but transverse cracking contributes to the behavior as well.

Figure 4.2-1 shows four distinct stages that can be associated with the flow rule. The first stage, the radial dilation stage, corresponds to the range of d for which g is positive. During this stage the yield surface experiences kinematic softening and isotropic hardening followed by isotropic softening. The isotropic hardening is associated with two possible mechanisms: the crushing of relatively porous concrete in front of the ribs increasing the "effective area of contact" and the stable propagation of transverse cracks. Both of these mechanisms are schematically shown in the figure, but their relative contributions are dependent upon the stress history. The off-diagonal terms of the elastic moduli (discussed in the next chapter) appear to be very small. This implies that until plastic deformation occurs the wedging action of the ribs is not significant. As porous material near the face of the rib crushes, some of it compacts on the face of the rib (Lutz and Gergely [1967]) and the "effective angle of contact" between the rib face and intact concrete increases. It appears that this initial build-up of the wedging action corresponds to the initial ascending portion of the graphs of g shown in Figures 4.1-4. Though this portion of g is nearly linear, for larger values of $-\sigma$ there is a short initial interval where g remains zero; this

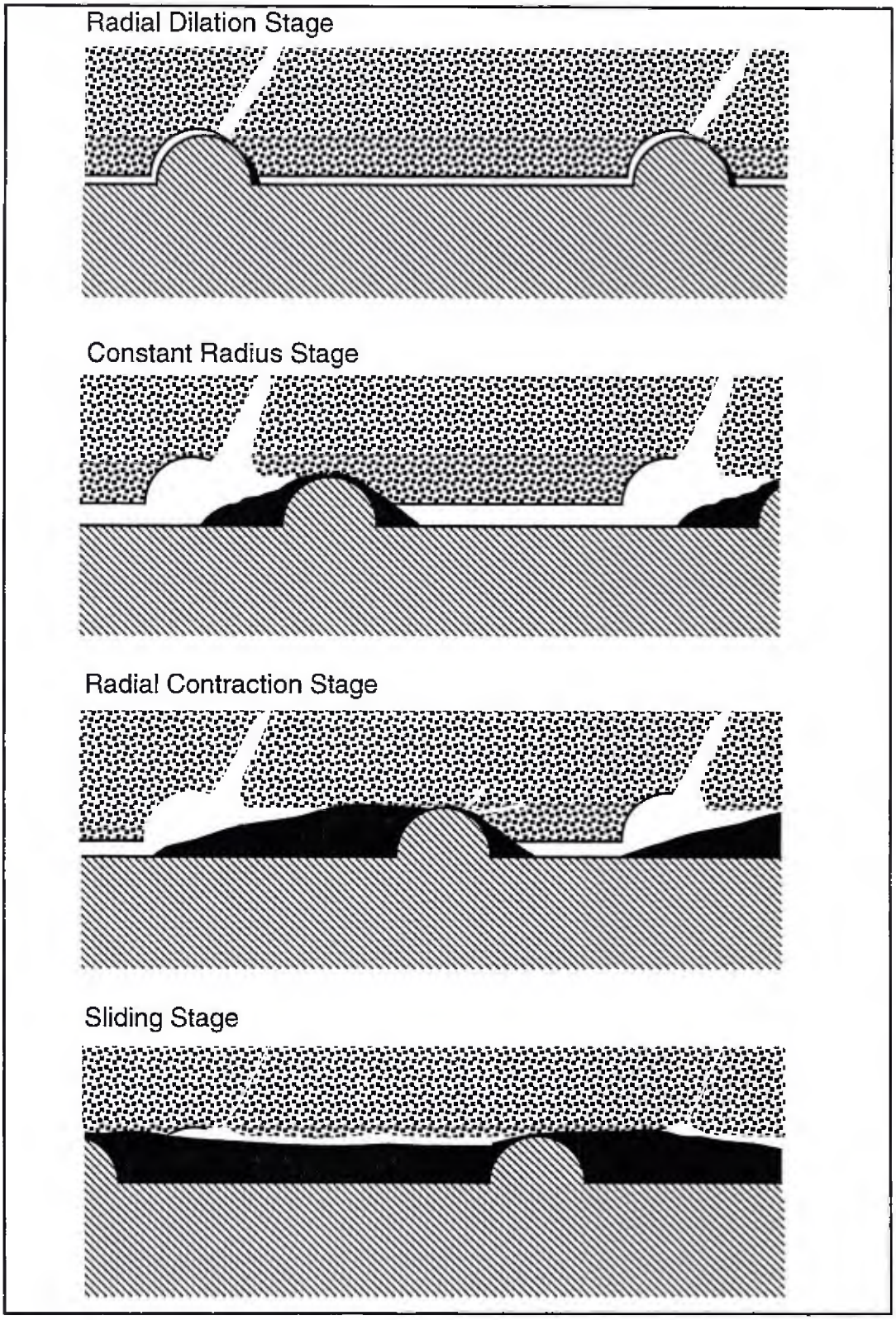

Figure 4.2-1 Stages of behavior associated with the flow rule.

suggests that for higher confinement stresses more material must be crushed before the wedging action is sufficient to produce radial dilation.

Due to the presence of hoop stress, the variation of the confinement stress in Malvar's tests makes this portion of g difficult to interpret for a thin bond zone. The data only give the shape of g for a constant confinement stress with a thick bond zone interpretation (*i.e.*, as Malvar's test assuming a thick bond zone).

Figures 3.2-6 and 4.1-4 (recalling the relationship between values of q_1^p and d) indicate that the rate of dilation (g) is a maximum at about 70 percent of the damage at which the maximum bond stress (τ_{max}) occurs. That is, "trend 4" is consistent with the shift in maximum bond stress (discussed in the previous chapter) with increased confinement. The "effective angle and area of contact" are assumed to increase with the crushing of the relatively porous concrete near the rib. The resulting radial dilation tends to increase the effective angle of contact but reduce the effective area of contact. The interplay of these two mechanisms results in a maximum bond stress and the subsequent behavior is unstable "under stress control." Even though many experiments are under displacement control globally, at the local level – at the rib-scale – there is a likely instability associated with the partial release in the elastic strain energy stored in the adjacent concrete and bar. In stress space this manifests itself as a shrinking of the yield surface.

Figure 4.1-2 indicates that dilation continues into the softening regime which corresponds to the remaining positive area (for $d>d_{gmax}$ where $g(d_{gmax})$=max $g(d)$) under the graphs of g. This dilation is probably occurring with relatively little crushing (*i.e.*, primarily *geometric dilation* as described in the simple contact model of the previous chapter).

Trend 5 follows from the above argument. Under low confinement stress less crushing occurs prior to radial dilation, therefore the effective angle of contact is lower during the *geometric dilation*. Since the normal to the rib face has a larger component along the axis

of the bar (the converse holds for the tangent to the rib face), a unit slip produces more radial dilation.

This continued dilation into the softening regime increases with a decrease in the confinement stress – trend 6. From an energy point of view this trend is easy to understand: the higher the confinement stress – the more energy that is required to dilate the bond zone. Assuming the contact area decreases with dilation, the rib would tend to wedge under the adjacent concrete until it required less energy to crush the material. Thus the amount of radial dilation would typically decrease with an increase in confinement stress – trend 7.

During this radial dilation stage, the propagation of splitting (longitudinal) cracks is expected. This is depicted in Figure 4.2-2a for the Malvar specimens. From a thin bond zone viewpoint these splitting cracks are occurring in the adjacent concrete but do affect the confinement stress in the bond zone. The specimens of series 2 through 4 are presplit so during the test there is crack opening rather than crack propagation. As discussed in the previous section, until the cracks are completely open the full confinement stress does not reach the bar.

For the rib geometry used in test series 3, the next stage of behavior is characterized as producing additional crushing with no change in radial dilation. This stage is depicted in Figure 4.2-1 as the "constant radius stage." This corresponds to the horizontal section of the graphs in Figure 4.1-2. In contrast, Figure 4.1-1 shows that the bars of test series 2 which have inclined ribs do not exhibit this behavior. One would expect some variation in the micromechanics with different rib patterns.

During this second stage the longitudinal cracks are open in the Malvar specimens as depicted in Figure 4.2-2b. In general the "constant radius stage" is not associated with open splitting cracks. In a few of the validation problems of Chapter 7, the radial dilation

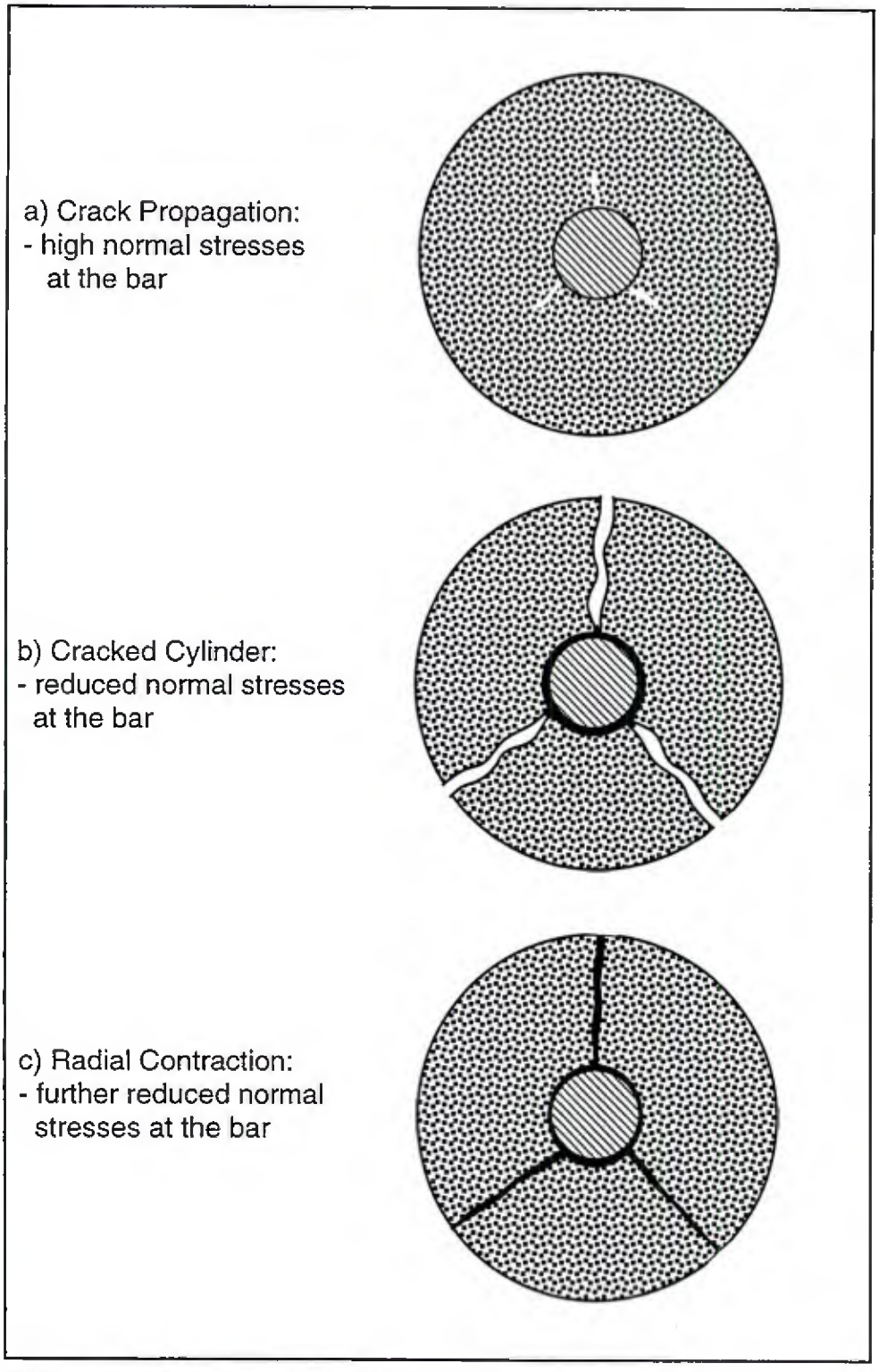

Figure 4.2-2 Relationship of splitting (longitudinal) cracks to $-\sigma$.

of the bond model will induce longitudinal cracking, but yet the cracks remain stable and do not propagate to the surface of the specimen.

While no change in radius occurs during this stage, softening continues. Three possible contributions to the softening are: 1) the material between the ribs has experienced significant microcracking during the earlier loading which continues to coalesce during this stage; 2) since the rib progressively crushes additional material there is less material, which is already damaged, to maintain the force being transmitted by the rib; and 3) with this crushing the encountered material is in a less confined state.

Another possible explanation is that much of the material between the ribs has sheared off (*i.e.*, mode two cracking) but continues to interlock (as a small scale aggregate interlock behavior) with the adjacent material. As slip increases, the surfaces smooth thus reducing the effective coefficient of friction and the corresponding bond stress.

Now let's consider possible explanations of the radial contraction. As the rib nears the cavity left by the adjacent rib, any remaining intact material between the ribs is probably sheared off. If this occurs along an inclined shear plane, it would be one source of the radial contraction. Another source could be the complete failure and subsequent deposition of damaged material into the cavity left by the adjacent rib (keyway). Therefore the amount of the contraction would depend upon the size of the cavity and the amount of damaged material. These two factors are inversely related; the amount of damaged material would increase and the relative keyway size would decrease with an increase in the fixed confinement stress.

In reality the confinement stress does not remain constant during a test history, so a measure of the plastic work might better reflect the amount of contraction that could take place. A functional form of g that depends only on d (as defined here) and σ cannot correctly handle large variations in σ. For example, the confining stress might be relatively

high during the radial dilation but yet allow enough dilation to fail the adjacent cover in splitting. The confinement stress would then decrease and the subsequent contraction would be over predicted.

The real significance of the contraction actually is manifested in the shape of the yield surface. Material damaged by the mechanical interaction can easily be deposited in two places: 1) in the keyway (as just discussed), and 2) in the longitudinal crack openings. The latter is of more importance when the cracks have opened significantly. In addition, with significant microcracking the material in the bond zone would tend to dilate. With contraction this dilated material and the crushed material that has been forced into the longitudinal cracks can impose a new constraint on the kinematics; it can carry compressive hoop stress without contracting to its original radius. The net effect is the material near the bar (as schematically shown in Figure 4.2-2c) can act as a thick-walled cylinder and partially isolate the bar from the outside confinement stress. The rate of radial contraction subsequently reduces to zero and the asymptotic shape of the yield surface reflects this isolation. For relatively small values of confinement stress, this effect is not as significant (or might not even occur) and thus the Coulomb surface (a Taylor series approximation to the model's yield criterion) appears adequate.

Another mechanism that could contribute to the contraction of the bond zone is compaction of the damaged "debris." Angular debris formed earlier in the loading might be crushed and rounded so that it could pack more densely.

With the radial contraction complete the "sliding stage" begins (Figure 4.2-1). The mechanism of friction now governs the interface between the bar and the concrete. The *effective coefficient of friction* (*i.e.*, secant line to a point on the yield surface) varies with the level of confinement stress. Though this reduction in the effective coefficient of friction has been previously observed (see *e.g.*, Robins and Standish [1982]), I have not found an explanation of the mechanisms that cause it. This mechanism again indicates the need to

consider the bond phenomena as occurring within a bond zone rather than as occurring on an interface. The interface assumption simplifies the initial model, but also imposes some limitations on the stress history. Whether these limitations significantly limit the scope of application of the model will be partially examined in Chapter 7.

Since under low confinement stress much of the dilation is attributed to geometric dilation, one would expect that if the slip exceeds the lug spacing dilation could occur again. This behavior seems like an unnecessary detail to include for most applications, and thus is not incorporated in the model.

The above description of the micromechanics is admittedly an interpretation of data which was obtained via many simplifying assumptions. Nonetheless, the interpretation: 1) is consistent with observations made by many researchers, 2) is consistent with the state of damage found in the specimens of Malvar (1991), 3) provides insight to potential limitations of the model, and 4) explains the variation in the effective coefficient of friction.

4.3 Model

This section describes the initial model for the function g. In the earlier discussion of the data reduction I noted that test 9 was not consistent with the other results, so for the model development only the results of tests 6, 8 and 10 were used. The graphs given in Figures 4.1-4 are assumed to give g for values of constant σ, thus the graph of g will be a surface. Assuming graphs for constant stress are similar in shape, the model curve shown in Figure 4.3-1 is adopted. Table 4.3-1 gives corresponding values of d and $g(d)^*$ for the three tests.

---

* The notation $g(d)$ is adopted for brevity. In actuality g is a function of both σ and d. More explicitly $g(d)=g(\sigma,d)|_{\sigma=constant}$.

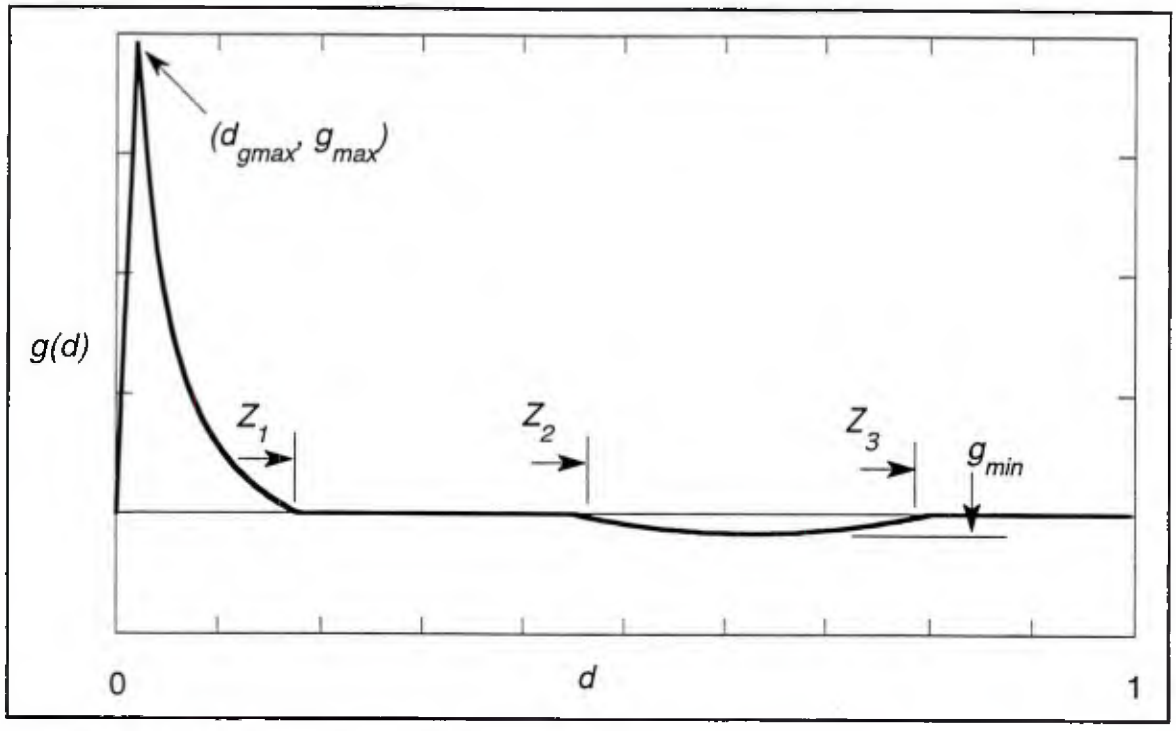

Figure 4.3-1 Model graph of $g(d)$ versus d.

Table 4.3-1 d and $g(d)$ values of tests 6, 8 and 10.

	Test 6	**Test 8**	**Test 10**
d_{gmax}	~0.0012	0.021	0.039
g_{max}	0.69	0.21	0.060
Z_1	0.35	0.18	0.14
Z_2	0.50	0.49	0.4
Z_3	0.82	>1	0.79
g_{min}	–0.018	–0.0095	–0.006

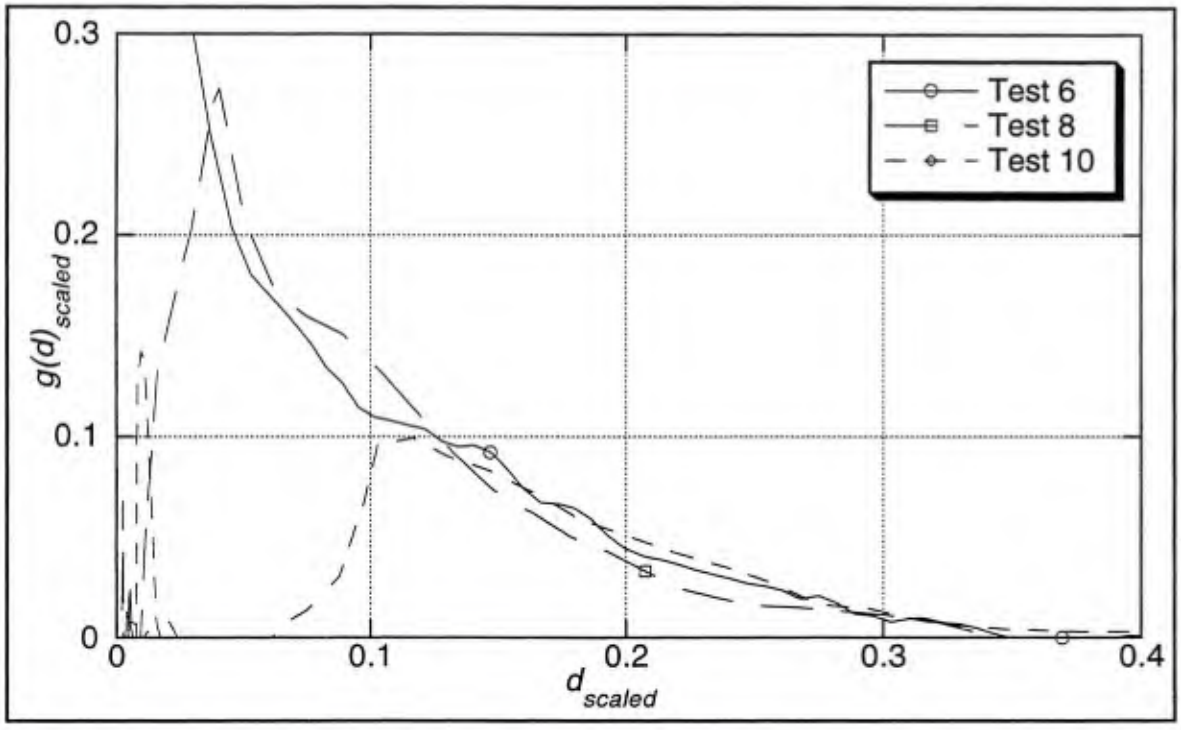

Figure 4.3-2 Scaling of $g(d)$ versus d, for the radial dilation stage, to a common curve.

Table 4.3-2 Scaling factors for the radial dilation stage.

	Test 6	**Test 8**	**Test 10**
H_{scale} **(domain)**	1	1.92	2.97
V_{scale} **(range)**	1	1.29	1.67

First consider the dilatational portion of g. Let's assume that the descending part of the curves might be represented by a common function of σ and d. As a simple means to represent this functional dependence, let's attempt to scale the descending parts of tests 8 and 10 to coincide with test 6. A domain or horizontal scale factor (H_{scale}) is used to align Z_1 for the tests and then a range or vertical scale factor (V_{scale}) is used to match the range of the curves. The results are given in Figure 4.3-2 and Table 4.3-2.

Now assuming that the above scale factors are functions of σ/f_t, alone, these results are simply fit to model functions that reflect this dependence. Figure 4.3-3 shows the

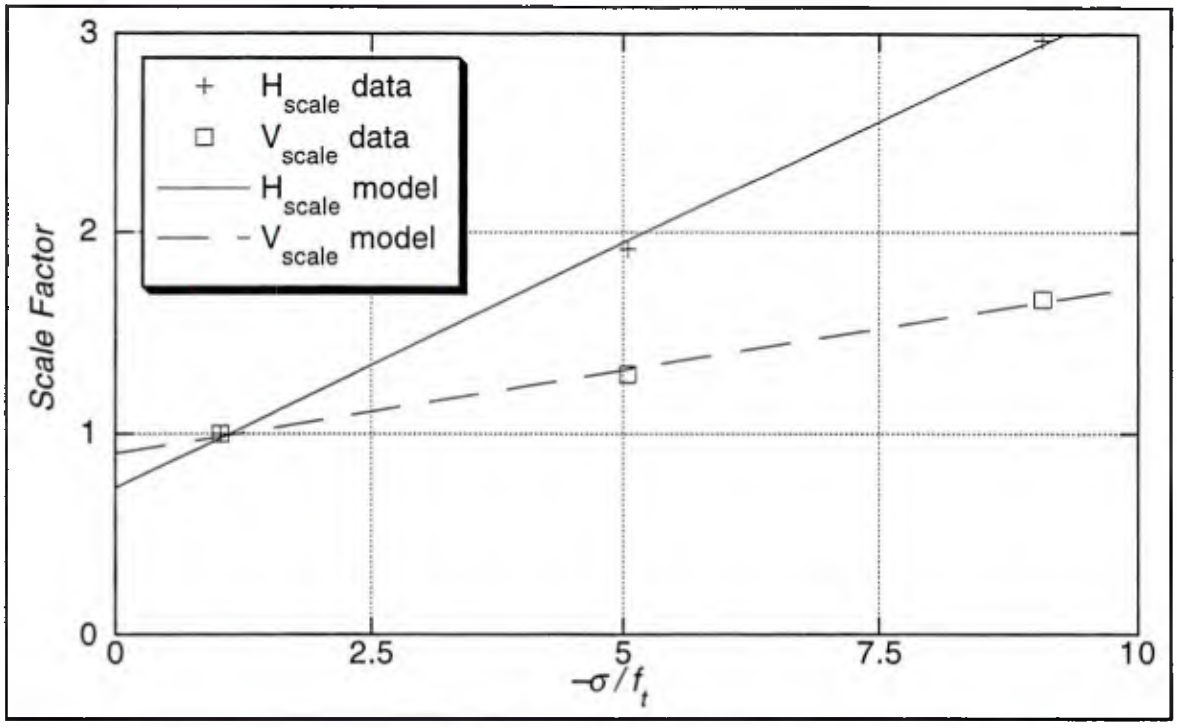

Figure 4.3-3 Least squares fit of line segments to H_{scale} and V_{scale} experimental data.

experimental data and the model line segments obtained by least squares fits. The corresponding formulas for the scale factors are given as:

$$H_{scale} = 0.73 + 0.244\left(\frac{-\sigma}{f_t}\right) \tag{4.3-1a}$$

and

$$V_{scale} = 0.90 + 0.0830\left(\frac{-\sigma}{f_t}\right). \tag{4.3-1b}$$

For brevity, let g, d, and Z_1 in the "scaled-space" be denoted as g_s, d_s, and Z_{1s}, respectively. The first zero of g (Z_1) is assumed to have a constant value in "scaled-space" of 0.35. Now a model function is fit to this descending curve assuming the dependence upon σ is captured via the linear varying, scaling factors. For expediency, the standard functions defined by Equations (3.3-5) are adopted. For the initial calibration the curve is modeled in the following form

$$g_s(d_s) = i_1\ [ratFunc(i_2,i_3,i_4,d_s) - ratFunc(i_2,i_3,i_4,Z_{1s})] \tag{4.3-2a}$$

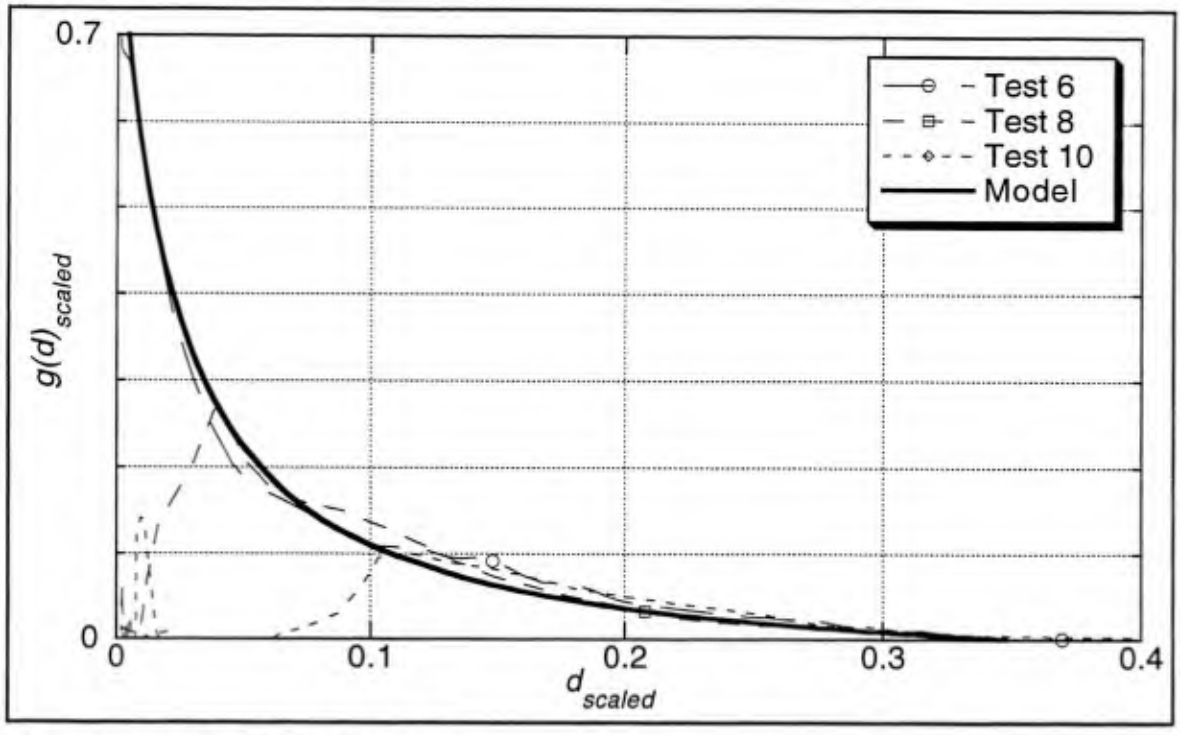

Figure 4.3-4 Model function for g_s.

Table 4.3-3 Calibration parameters defining g_s.

i_1	i_2	i_3	i_4	Z_{1s}
0.9091	1.1	50	1	0.35

where the calibration parameters were selected as given in Table 4.3-3 above.

For the selected calibration constants, g_s can be written approximately as

$$g_s(d_s) = \frac{1}{1.1+50d_s} - \frac{1}{18.6}. \qquad (4.3\text{-}2b)$$

Figure 4.3-4 compares the model function to the experimental data in the "scaled-space." For the dilatational portion of g only the ascending part of the curves remains to be constructed. For a fixed confinement stress this part of the curve is assumed to be a line passing through the origin, and thus given Equation (4.3-2) the value of d_{gmax} will fully define it. The value of d_{gmax} also appears to vary linearly for the three tests; Figure 4.3-5

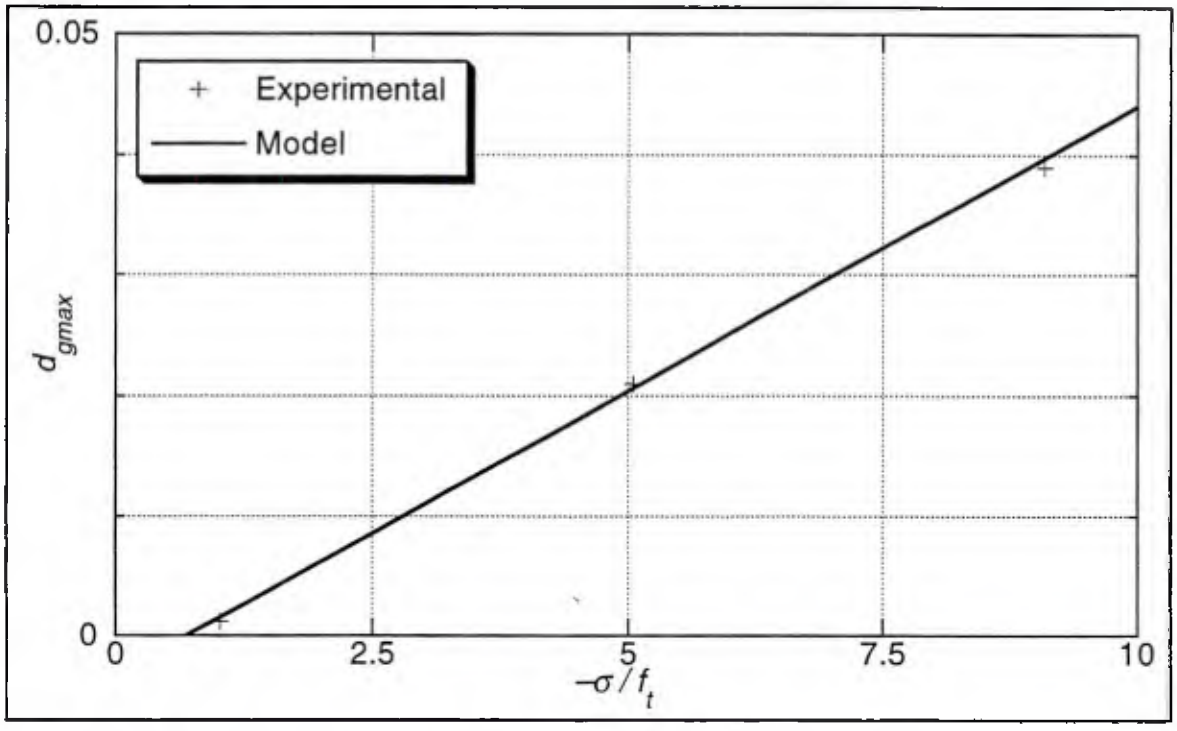

Figure 4.3-5 Least squares fit of line segment to d_{gmax} experimental data.

shows the experimental data and model function obtained by a least squares fit. The corresponding formula for d_{gmax} is given by

$$d_{gmax} = \max\left\{0, -0.00328 + 0.00473\left(\frac{-\sigma}{f_t}\right)\right\}. \tag{4.3-3}$$

A detail not included in the initial implementation of g is that Equations (4.3-1a) and (4.3-3) allow d_{gmax} to exceed Z_1. The two quantities are equal at $-\sigma/f_t \approx 16.4$ which means, in its current form, Equation (4.3-3) allows the flow rule to loose continuity at very high values of confinement stress. This can be corrected by defining a upper bound on d_{gmax} of Z_1. When this bound is attained no radial dilation occurs.

To complete the model we must define 1) the two remaining zeros of $g - Z_2$ and Z_3, 2) the minimum value of $g - g_{min}$, and 3) the model function for the radial contraction stage. The data for the contraction stage show significant scatter (see Figure 4.1-4b) compared to the magnitude of the values. Thus a simple model will be chosen for this stage and then

evaluated on its ability to reproduce experimental results for radial contraction. With this perspective, Z_2 and Z_3 are taken as the constants 0.48* and 0.8, respectively. The curve for g during the radial contraction stage is modeled with the quadratic function

$$g(d) = g_{min}\left[1-\left(\frac{2d-Z_2-Z_3}{Z_3-Z_2}\right)^2\right] \quad \text{for } d\in(Z_2,Z_3) \tag{4.3-4}$$

where g_{min} is a function of the confinement stress. The value of g_{min} for each confinement stress was obtained graphically from enlargements of Figure 4.1-4b. Probably a better approach would be to obtain the total radial contraction from Figure 4.1-2 and then set g_{min} to match this value (*i.e.*, so it has the correct area).

Figures 4.3-6 shows the experimental values of g_{min} for their respective confinement stresses and the corresponding model curve. This initial model curve was fit to the experimental data including the results of test 9 (not shown here).

Again for expediency the standard functions defined by Equations (3.3-5) are used. In particular, for this calibration I used the exponential function

$$g_{min}(\sigma) = g_{min\infty}-h_1 expFunc(h_2,h_3,h_4,h_5,-\sigma/f_t) \tag{4.3-5a}$$

where the calibration constants are given in Table 4.3-4 below.†

Table 4.3-4 Calibration constants for g_{min}.

h_1	h_2	h_3	h_4	h_5	$g_{min\infty}$
0.015	1	1	0.72	0.8	–0.006

* Originally Z_2 was taken to be 0.45 (as shown in Figures 4.3-7 and -8). For very low confinement stresses this resulted in $Z_1>Z_2$ and thus a discontinuity in g. The revision in the calibration, which is used in all subsequent work, enforces $Z_1\le Z_2$.

† The exponential function was used when the data of test 9 was included which suggested an asymptotic behavior for $g_{min}(\sigma)$. Excluding this data, one might consider a line segment with an upper bound of zero to be a simpler and adequate model curve.

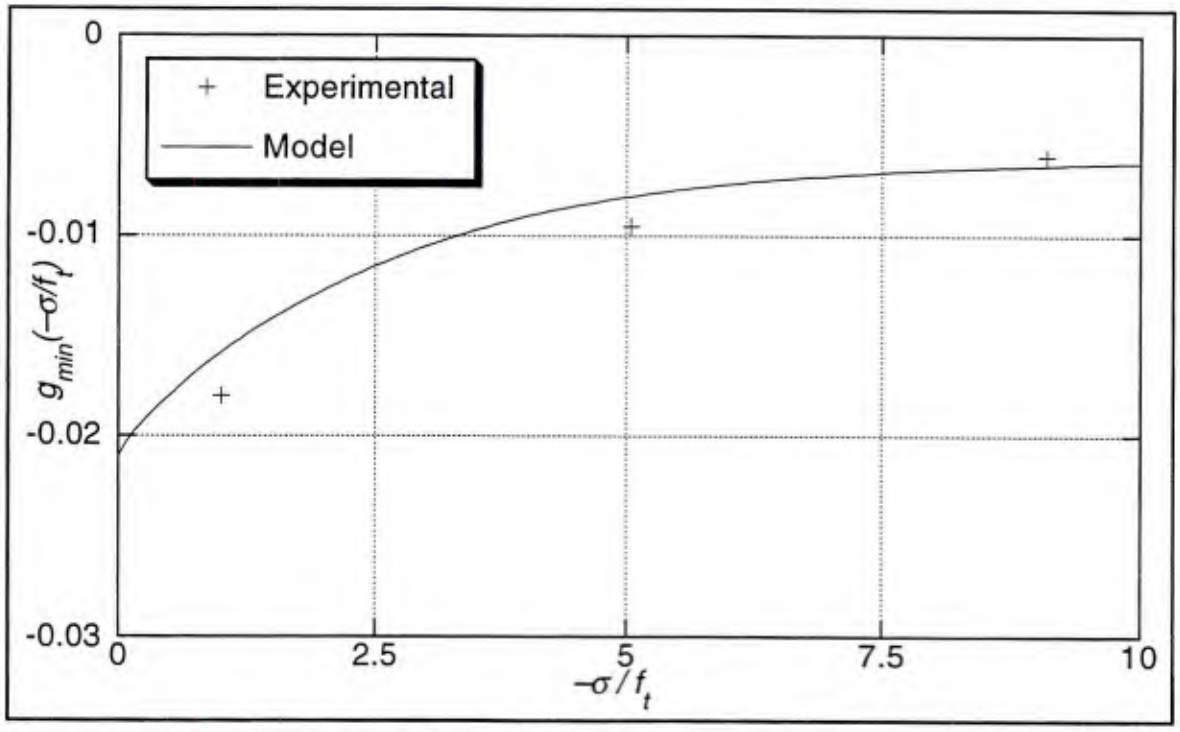

Figure 4.3-6 g_{min} experimental data and model function.

For the given calibration constants, this formula simplifies to

$$g_{min}(\sigma) = -0.006 - \frac{0.03}{1+\exp\left(0.72\left(\frac{-\sigma}{f_t}\right)^{0.8}\right)}. \qquad (4.3\text{-}5b)$$

The model of g for a fixed σ is graphically rather simple, but including the dependence of the confinement stress complicates the model significantly. Fortunately many of the model parameters appear to vary linearly with confinement stress, but these observations are based upon very little data; in contrast to the yield surface data we are limited to three tests in this case. The fit of the model to the experimental data is shown in Figure 4.3-7. Every previously noted trend in the data is captured by the model. Figure 4.3-8 shows the graph of the model function for g. The fact that it can even be shown as a graph implies a limited history dependence in the model. For a given bond test, a particular material point in the bond zone experiences a σ-d history that appears as a curve in σ-d space. The area of the surface bounded by this curve and $g(\sigma,d)$ is proportional to the radial dilation for a given

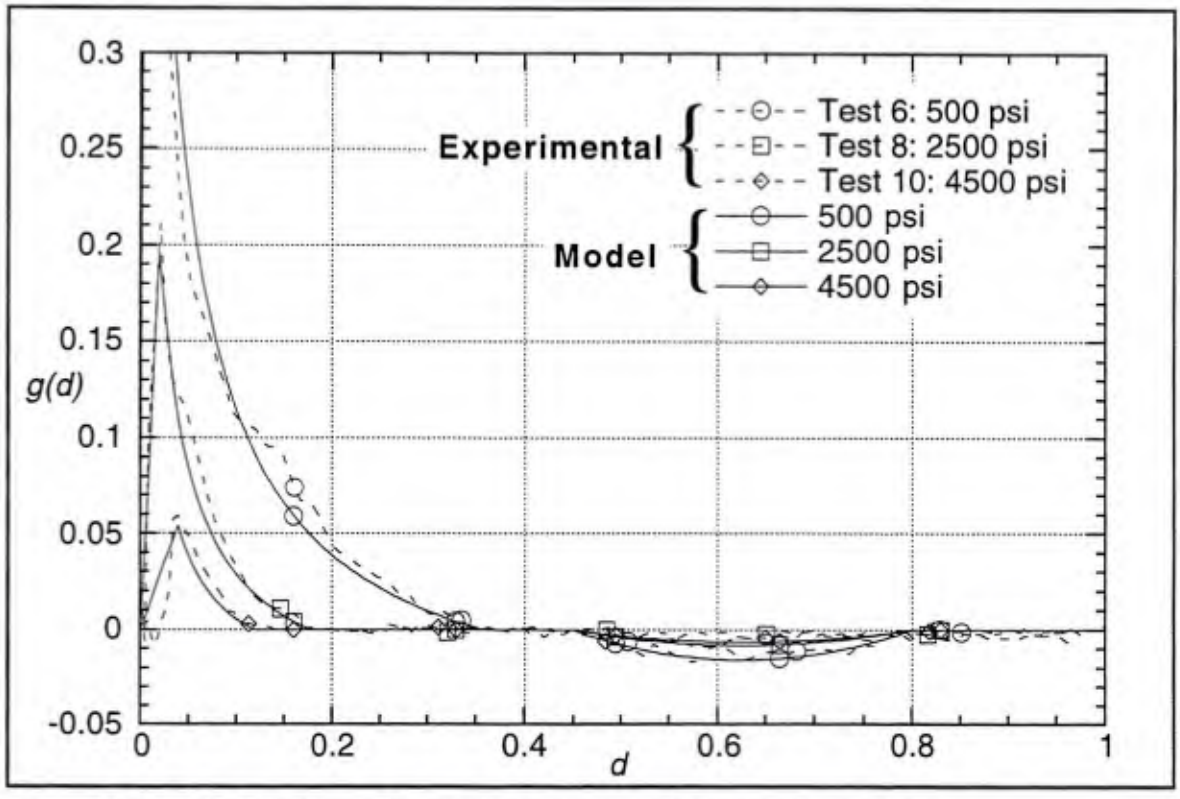

Figure 4.3-7 Model's flow rule function g, compared to experimental data.

state. The general reduction of $g(\sigma,d)$ with increasing confinement stress is an important quality. The mechanics of this trend were previously discussed, but its necessity for the model was not. For a bar in "well confined concrete" the elastic component of the bond model will cause an increase in the confinement stress with radial dilation which in turn reduces subsequent radial dilation. If the trend were reversed the model would predict uncontrolled growth in both confinement stress and radial dilation; in the next section you will see there are stress paths that violate the second law of thermodynamics even if g is simply independent of the confinement stress.

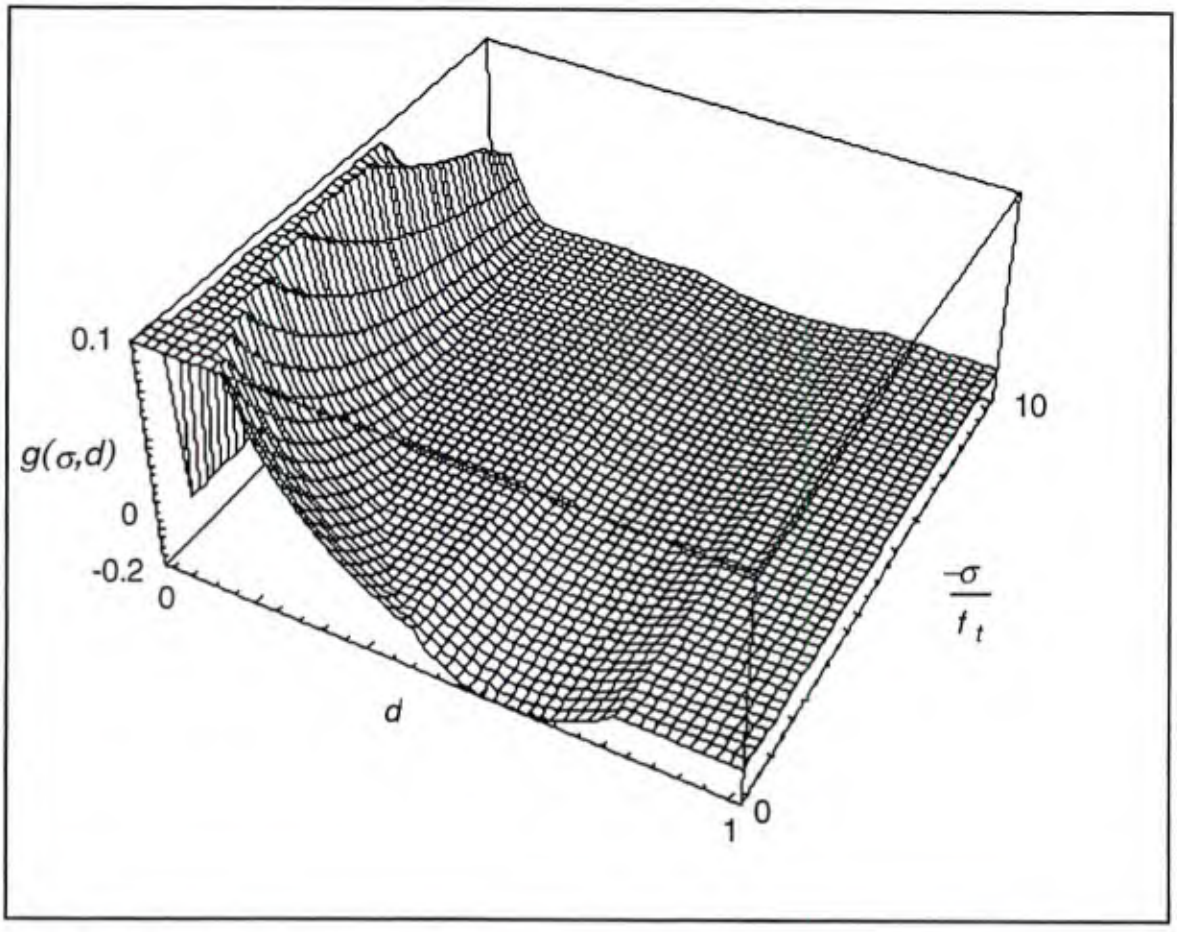

Figure 4.3-8 Graph of g for $g(\sigma,d) \in [-0.02,0.1]$.

To summarize the model, the algorithm for determining g for given values of σ and d is presented below in Algorithm (4.3-1). The algorithm is calibration independent except for the forms of the standard functions, Equations (3.3-5), used in Equations (4.3-2) and (4.3-5) which are set during the calibration. The pseudo-code used to describe the algorithm has a Pascal dialect; the symbols (* and *) are delimiters for comments which would have no corresponding executable statements in a computer language.

Algorithm 4.3-1 Calculation of $g(\sigma,d)$.

Calculate H_{scale} by formula (4.3-1a)
Calculate V_{scale} by formula (4.3-1b)
Calculate d_s by: $d_s := d\, H_{scale}$
Calculate Z_1 by $Z_1 := Z_{1s}/H_{scale}$
Calculate d_{gmax} by formula (4.3-3)
IF $d \in [0, d_{gmax}]$ THEN
    (* This is the ascending curve of the radial dilation stage. *)
    Calculate g_s by formula (4.3-2) letting $d_s := d_{gmax} H_{scale}$
    Calculate g_{max} by: $g_{max} := \dfrac{g_s}{V_{scale}}$
    Calculate g by: $g := \dfrac{d}{d_{gmax}} g_{max}$
ELSIF $d \in (d_{gmax}, Z_1)$ THEN
    (* This is the descending curve of the radial dilation stage. *)
    Calculate g_s by formula (4.3-2)
    Calculate g by: $g := \dfrac{g_s}{V_{scale}}$.
ELSIF $d \in [Z_1, Z_2]$ THEN
    (* This is the constant radius stage. *)
    Set g:= 0
ELSIF $d \in (Z_2, Z_3)$ THEN
    (* This is the radial contraction stage. *)
    Calculate g_{min} by formula (4.3-5)
    Calculate g by formula (4.3-4)
ELSE
    (* This is the sliding stage. *)
    Set g:= 0
END

4.4 Thermodynamic Constraint on Radial Dilation

The flow rule and yield criterion have been presented as essentially being uncoupled, but thermodynamics constrains the combination. As discussed in Section 2.3, the change of state of brittle materials like concrete requires the incremental plastic work to be nonnegative for an arbitrary loading cycle. This is not a trivial constraint on the bond law since it has plastic dilation in the presence of compressive confinement stress; in fact, one can set calibration constants to violate this constraint. Appendix C shows in detail that for the calibration presented in this and the previous chapter, the incremental plastic work is

always positive for the bond law. This section focuses on the interpretation of this constraint in the context of the bond law.

As previously noted, the generalized stresses and strains are conjugate within a positive multiplicative constant; thus the plastic work is nonnegative if and only if $\underline{Q}^T\dot{\underline{q}}^p \geq 0$. By Equations (3.1-2) and (4.1-1a), this implies

$$\langle\lambda\rangle[\mathrm{sgn}(\tau)\tau + g\sigma] \geq 0 \tag{4.4-1}$$

which simplifies to

$$|\tau| + g\sigma \geq 0. \tag{4.4-2}$$

This inequality gives a general constraint that any calibration of the bond law must satisfy. To be complete we must consider both cases where the product $g\sigma$ would be negative: 1) compressive confinement stress with radial dilation, and 2) tensile confinement stress with radial contraction. The first case is considered in detail in Appendix C. The second case suggests that the current form of the flow rule does not adequately consider tensile confinement stress since Equation (4.3-5b) is not defined in this case. However, since radial contraction occurs after the kinematic softening (for the current calibration), the second case cannot occur (*i.e.*, the yield surface prevents tensile stresses by this time).

Now consider the first case – a compressive confinement stress. Inequality (4.4-2) constrains the extent of radial dilation that can occur as

$$g \leq \frac{|\tau|}{-\sigma}. \tag{4.4-3}$$

For brevity the term bounding g (in this case $-|\tau|/\sigma$) will be referred to as the *dilation bound*. Though not explicitly shown, both g and τ are functions of d and σ; so this inequality must hold for all consistent combinations of (d,τ,σ). For the current calibration, the analysis can be simplified by eliminating the dependence on damage; while Equation

(4.4-3) represents a necessary condition for a valid bond law, the development in Appendix C presents simpler sufficient conditions that are calibration dependent.

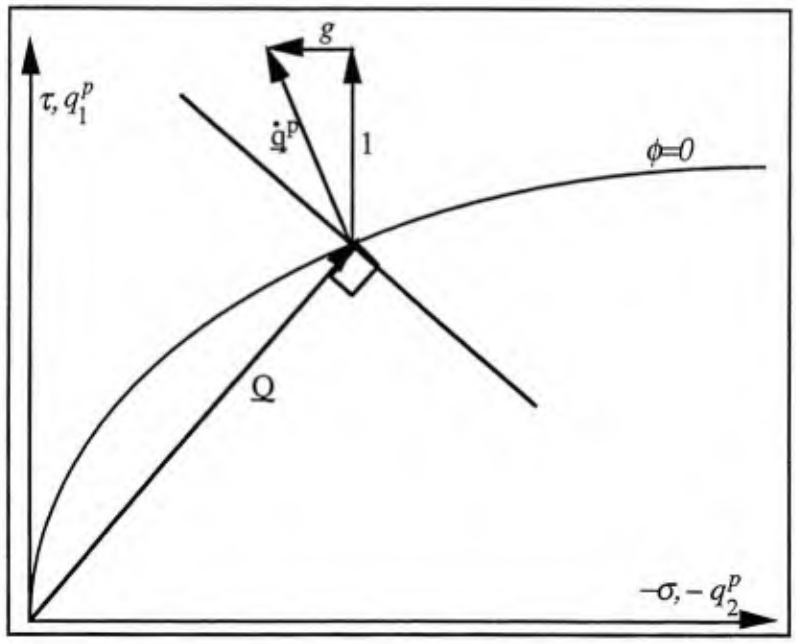

Figure 4.4-1 Graphical interpretation of non-negative incremental plastic work.

The initial motivation for the flow rule's dependency upon the confinement stress was experimental, but Inequality (4.4-3) indicates this dependency is theoretically essential for many strictly convex yield surfaces. This is illustrated in Figure 4.4-1. Geometrically non-negative plastic work is equivalent to saying the projection of the plastic strain increment onto the stress vector must be positive (as Inequalities [4.4-1] and [4.4-2]). Alternatively, the angle of the strain increment (relative to the vertical axis) must be less than the angle of the secant to the yield surface (as Inequality [4.4-3]).

For strictly convex yield surfaces where the secant angles asymptotically approach zero for increasing confinement stress, the rate of dilation must be confinement stress dependent to prevent the potential of negative incremental plastic work. This is apparent from Figure 4.4-1. Assume g is independent of σ, and has the direction shown in the figure for plastic loading. By increasing the confinement stress and bond stress to form a path coincident with the yield surface (*i.e.*, fully elastic and thus with no change of internal state), a stress state can be attained where the projection of $\underline{\dot{q}}^p$ onto $\underline{Q}$ is negative. This might occur at such a large value of confinement stress, that one could argue that for realistic stress levels

the constrain is satisfied. While this may be true, the intermediate stress states obtained by nonlinear equation solvers do not necessarily remain within practical bounds, and a fictitious energy source could introduce significant numerical problems.

There are convex and strictly convex yield surfaces that will always yield nonnegative incremental plastic work without confinement stress dependency. The simplest of examples is the Coulomb surface. Even with cohesion, the secant to the surface only asymptotically approaches having a slope equal to the coefficient of friction; thus, if the radial dilation is less than or equal to that given by an associative flow rule the incremental plastic work will always be positive. For this case confinement stress dependence is only necessary when the dilation is to exceed that predicted by an associative flow rule. A simple example of a strictly convex surface is the positive branch of a hyperbola where the Coulomb surface serves as the asymptote. Again dilations less than or equal to that given by the normal to the Coulomb surface require no normal stress dependence. In either case isotropic softening could reduce the dilation bound for a given internal state without requiring confinement stress dependency.

To summarize, the composite form of g (Algorithm 4.3-1) is somewhat complicated, but so are the mechanisms it must represent. Despite its complicated form, the corresponding algorithm is relatively straightforward. The analysis of the Malvar test series provided qualitative data which could be used to develop a model. The major trends in the data were explained in terms of proposed mechanisms and are reflected in the model's behavior. The second law of thermodynamics does constrain the calibration of the model, and the current calibration satisfies this constraint. The remaining question is, "is the functional dependence of g upon σ and d general enough to reproduce other bond tests?" This question is addressed later in the results of Chapter 7.

Chapter 5

Elastic Moduli

This chapter presents the last component of the model – the elastic law. A simple model has been used for the elastic component of bond; except for a small variation that reflects the underlying contact problem (between the ribs and the adjacent concrete), the elastic response is assumed to be linear. This is obviously a simplification. The first section addresses the mechanics and general form of the elastic moduli, and the last section addresses how these idealized moduli were obtained from experimental data.

5.1 Mechanics and Model

I previously suggested that isotropic hardening of the yield surface could be due to a compaction of relatively porous concrete near the rib face and that this was consistent with observed elastoplastic coupling (see *e.g.*, Lutz and Gergely [1967]). In this case the plastic deformation actually improves the elastic properties. As plastic slip progresses, one would expect the damage of the material, due to extensive microcracking, to degrade the elastic properties. In the limit, as the slip becomes very large, one expects the off-diagonal terms* of $\mathbf{D}^e$ to go to zero and the diagonal terms to be significantly reduced. Yet to introduce elastoplastic coupling complicates the model, and very little experimental datum is available

* The off-diagonal terms provide the coupling between the tangent and normal components of generalized stress and strain. This is shown explicitly in Equation (5.1-2).

to quantify this generalization; thus in this version of the model, elastoplastic coupling will not be included.

While elastoplastic coupling will be ignored, the underlying contact problem still affects the form of the elastic law. Chemical adhesion has been found to break down at relatively low stresses. Lutz and Gergely (1967) suggested that representative adhesion values can be obtained from tests of nonreactive aggregate with mortar; Taylor and Broms (1964) obtained shear strengths of 280 to 600 psi, while Hsu and Slate (1963) obtained tensile strengths of 190 to 240 psi. The apparent adhesion value would be dependent upon the shrinkage stresses and many other factors, but still let's assume that the breakdown of adhesion occurs with negligible plastic deformation. With the loss of adhesion, one would expect the bearing of the ribs against the adjacent concrete to produce some wedging action even prior to crushing. This is apparent even in the simplified analysis results of Figure 3.3-2 where the concrete and steel have separated on all but the bearing face. This view of the micromechanics is reflected in some early forms of the elastic law. Different Cauchy and Green elasticity laws were considered. An example of a Cauchy-elastic law is given by

$$\begin{aligned} \tau &= \overline{D}^e_{11} q^e_1 - \overline{D}^e_{12} T_{12}(q^e_1) q^e_2 \\ \sigma &= \overline{D}^e_{22} q^e_2 - \overline{D}^e_{21} T_{21}(q^e_1) q^e_1 \end{aligned} \tag{5.1-1}$$

where T_{12} and T_{21} are qualitatively like "shifted members of a Heaviside sequence" as illustrated in Figure 5.1-1.

The "incremental elastic moduli" are then given by

$$\mathbf{D}^e = \begin{bmatrix} \overline{D}^e_{11} - \overline{D}^e_{12} \dfrac{\partial T_{12}}{\partial q^e_1}(q^e_1) q^e_2 & -\overline{D}^e_{12} T_{12}(q^e_1) \\ -\overline{D}^e_{21} \left\{ \dfrac{\partial T_{21}}{\partial q^e_1}(q^e_1) q^e_1 + T_{21}(q^e_1) \right\} & \overline{D}^e_{22} \end{bmatrix}. \tag{5.1-2}$$

By proper choices of $\overline{D}^e_{12}, \overline{D}^e_{21}, T_{12}$ and T_{21} one can obtain symmetry in the above moduli, however reciprocity is not a requirement initially. That is, assuming no adhesion when $q^e_1=0$ an increment in q^e_1 might produce an increment in σ but an increment in q^e_2 would not

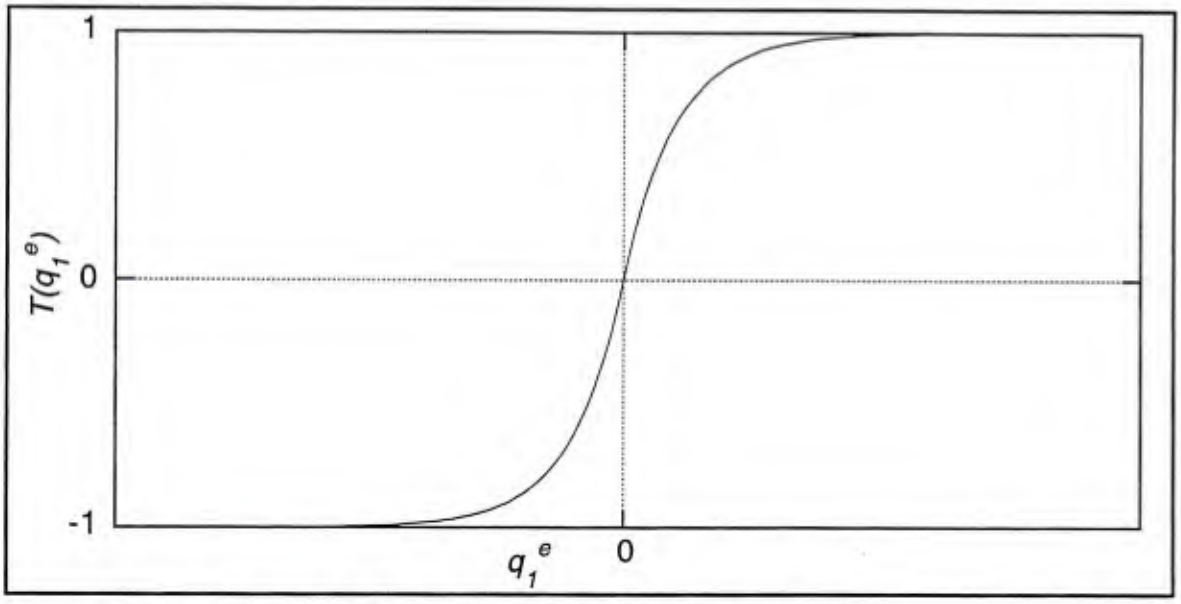

Figure 5.1-1 Schematic of a "T function" for a Cauchy elasticity law.

affect τ. Reciprocity is sacrificed when the contact behavior is incorporated in the elastic component of the model. It would be important to select the parameters so that $\mathbf{D}^e$ is always positive definite.

Assuming *T functions* that have the general form given in the above figure and positive definiteness of $\mathbf{D}^e$, the above elastic moduli vary with elastic deformation in a desirable manner. The modulus D_{11}^e has a reduced value at small slips that increases to a constant value; the q_2^e factor causes this trend to be secondary. The moduli D_{12}^e and D_{21}^e start at zero and increase to constant values. All of these trends are consistent with what would be expected to occur with contact. It is not likely that D_{22}^e would increase with slip because the wedging action causes less of the concrete to be in contact with the bar; this modulus might initially decrease with slip. The increase in D_{11}^e is probably inappropriate when adhesion is significant.

Even attempting to account for the underlying contact problem leads to significant complication of the elastic law that at this point is based upon hypotheses – not

experimental evidence. Nonetheless some of the behavior discussed above is retained, in a very elementary manner, in the elastic moduli adopted for this study.

The incremental elastic moduli are assumed to be of the following form

$$\mathbf{D}^{e} = \begin{bmatrix} D^{e}_{11} & -\overline{D}^{e}_{12}\,\mathrm{sgn}(q^{e}_{1})\,\mathrm{H}(|q^{e}_{1}|-\varepsilon) \\ -\overline{D}^{e}_{21}\,\mathrm{sgn}(q^{e}_{1})\,\mathrm{H}(|q^{e}_{1}|-\varepsilon) & D^{e}_{22} \end{bmatrix} \tag{5.1-3}$$

where ε is a small tolerance and H is the Heaviside function. These elastic moduli must be used incrementally and only apply to monotonic loading. In earlier papers (Cox and Herrmann [1992a & b]), for brevity we referred to ε as being "numerical zero;" in implementing the model we have used a small tolerance $O(10^{-5})$. The motivation for including the Heaviside function is due to the early use of a very simple *point model* for the Malvar specimens. For these specimens large confinement stresses were applied prior to pulling the bar. By symmetry, a radial contraction for this history should not produce a resultant tangent force so the D^{e}_{12} term must be zero until some slip occurs; the form of the D^{e}_{21} term is assumed to be the same. While the above moduli are defined for stress and strain increments, ε is taken so small that the behavior can't be distinguished from a true elastic response for any of the other validation tests.

Initially one might think of the bond zone as behaving like a thick-walled cylinder with respect to elastic slip. With this hypothesis, it would be reasonable to make D^{e}_{11} a function of the initial shear modulus of concrete. Since Poisson's ratio does not vary much (*e.g.*, 0.15 to 0.22 is typical), it's probably adequate to use the initial Young's modulus (E_c) instead. Considering the underlying contact problem, it seems this might be an appropriate quantity to characterize the effect of the concrete stiffness for all the moduli.

The thick-walled cylinder model of the bond zone also implies that the elastic constants can be a function of the assumed bond zone thickness. If the response is strongly localized near the rib face, this thickness dependence is not significant. As discussed for the yield surface, the bond zone thickness affects our interpretation of σ since hoop stress is not

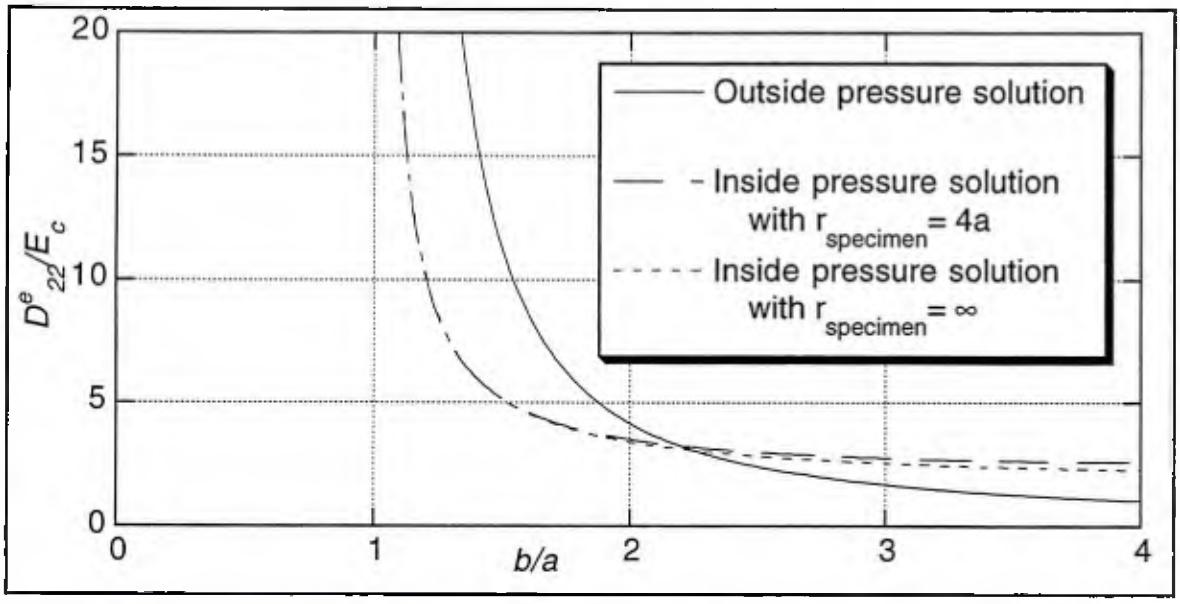

Figure 5.1-2 Thick-walled cylinder solutions for D^e_{22}/E_c as a function of ratio of the outer and inner radii of the bond zone.

directly included in the model. Figure 5.1-2 shows two elasticity solutions for D^e_{22}/E_c that reflect the thickness dependence associated with the thick-walled cylinder model and the ambiguity in the confinement stress. Both elasticity solutions are based upon the response of a thick-walled cylinder – one subjected to an external pressure and the other subjected to an internal pressure (see *e.g.*, Wang [1953]).*

For both solutions, the bar is assumed to be in a state of uniform biaxial compression. For the external pressure problem the effect of the bar is treated as a mixed boundary condition, while for the internal pressure problem (*i.e.*, due to wedging action) the contraction of the bar is merely accounted for in the calculation of δ_n. For the internal pressure problem two specimen sizes (not the bond zone size) are considered: 1) the size of the Malvar specimens, 4a, and 2) infinite. The graphical results reflect a 1/r singularity of the

* A solution that would probably be more valuable, but was not pursued in this study, is a long cylinder subjected to evenly spaced regions of uniform traction representing the wedging action of the ribs on the adjacent concrete.

solutions with respect to the ratio of the outer and inner diameters (b/a). Since our strain measure is a relative displacement, intuition tells us that as the thickness goes to zero the apparent stiffness must become infinite.

These results may have some meaning prior to slippage when the concrete is in full contact with the bar, but once the bar begins to slip the wedging action of the rib reduces the contact region, localizing the response. The very limited data available for determining D^e_{22} suggest a value orders of magnitude smaller than predicted by these simple analyses.

The presence of transverse cracks would also affect the elastic response. For example, D^e_{11} would be expected to decrease with an increase in the length of transverse cracks. Transverse cracking would tend to "diffuse" the elastic response over a larger region. In an approximate sense the elastic moduli include the effect of the transverse cracks since the values are based on experiments which inherently include some transverse cracking. Since I have simplified the model to have "constant moduli," they do not include the effects of the propagation of these cracks. The transverse cracks again appear to imply that the elastic moduli should be a function of the bond zone thickness. However, in homogenizing the effect of the ribs the very geometric discontinuities (and resulting gradients) that create the transverse cracks have been eliminated.*

The form of $\mathbf{D^e}$, Equation (5.1-3), and the definition of the generalized strains, Equation (3.1-2), suggests a linear dependence of the stiffness for δ upon D_b. Though obviously there is a linear relationship between the surface area of the bar and its diameter, this is accounted for in integrating the constitutive relationship over the surface of the bar. A possible explanation for why this particular definition of generalized strains appears to

---

* This does not imply that transverse cracks due to gradients along the bar will never exist. Rather it implies that the gradients have been smoothed in the homogenization process, so the regular spacing of transverse cracks emanating from the ribs will not be predicted when using the model.

work adequately is related to the localized response near the ribs and was previously discussed in Section 3.1.

5.2 Data Reduction

With the simplified elastic law given by Equation (5.1-3), only four constants remain to be determined. It has been assumed that the effect of the concrete properties is completely captured by making the constants proportional to E_c. Unfortunately the contact effects and elastoplastic coupling discussed above may be significant so the use of constants is admittedly simplistic. In examining experimental data to determine these constants, emphasis is usually placed upon the initial response for two reasons: 1) the initial response is dominated by elastic behavior, and thus to predict this regime accurately the data must be considered; and 2) unless the test contains an unloading segment, it is the only purely elastic data available.

One difficulty in determining the elastic moduli is that bond tests are not designed to identify the individual moduli. Fortunately, analysis of the data suggests that the off-diagonal terms are relatively small such that the coupling is not significant – at least not during the initial loading. This is consistent with the hypothesis that the wedging effect of the ribs is insignificant until local crushing has occurred at the face of the ribs.

Another difficulty in determining the elastic moduli, D^e_{11} in particular, is that significant response gradients along the length of the bar exist in the elastic range. Local measurements of bond stress and slip are inherently difficult, and while use of specimens with relatively short embedment lengths partially circumvent this problem, it is not a complete solution. The underlying assumption is that the rigidity of the bar is so great that global quantities such as bar force and end slip can be used to accurately calculate local bond stress and slip. This assumption is consistent with the model's results (see Chapter

7) near the maximum bond stress and during softening but not during the initial response. Using simple one-dimensional models, Appendix D examines the effect of gradients in determining D^e_{11}.

Finally the scatter of the experimental data complicates the determination of the elastic moduli. Most of the time the amount of scatter is unknown, but yet one wants the model to accurately predict the initial stiffness. It is difficult to even attribute a "standard range of scatter" to experimental results except in a very broad sense; some experiments have exhibited relatively narrow bands of scatter (see *e.g.*, Eligehausen *et al.* [1983]) and others have exhibited relatively large bands of scatter (see *e.g.*, Edwards and Yannopoulos [1979]). One cause of experimental scatter is the difficulty in measuring the small end slips which occur during the elastic response.

The determination of D^e_{11} has been based upon experimental data from many tests including: Malvar (1991); Gambarova *et al.* (1989); and Eligehausen *et al.* (1983). The value chosen for D^e_{11} was $0.1E_c$.

Figures 5.2-1 and -2 present the experimental data of Malvar (1991) for test series 2 and 3. Except as noted for test 8, the end slips are measured at the loaded end. The identification symbols shown in Figure 5.2-1 merely reflect the points digitized from graphical data; the symbols shown in Figure 5.2-2 reflect the digitizing rate of the data acquisition system adopted for the latter tests. Though these tests have different confinement stresses, there is no apparent trend between the confinement stress and the elastic response. These tests certainly suggest that the rib pattern strongly affects the elastic moduli. The pipe apparatus used to constrain the concrete in tests 1 and 2 differed from the other tests; this might be the main factor in producing the two groups of results for the series 2 tests. The series 3 tests (excluding test 8) show good agreement to an average bond stress of about 4 N/mm^2.

The model elastic stiffness is represented by two curves; the latter one (shown dashed) is adjusted for the relative stiffness of the rod as presented in Appendix D. Since this version of the model does not explicitly consider the rib pattern, an "average value" of the initial stiffness was selected that appears to be adequate for tests presented in many studies. Certainly making D_{11}^{e} dependent upon the rib pattern might produce more accurate predictions of the initial response. This could be pursued after initial validation efforts if a quantifiable trend is seen in multiple data sets. Experimental works that focus on the effect of the rib pattern (see Table 1.2) could provide important data for further development.

The determination of D_{22}^{e} has been based upon very little experimental data. A very simple mechanical model focusing on the contact between the rib face with the adjacent concrete is presented in the report by Herrmann and Cox (1994). That simple model suggests that the diagonal moduli are the same order of magnitude when the rib angle is near 45 degrees and the elastic response is localized near the rib faces. Originally the diagonal terms were taken to be equal, but later D_{22}^{e} was taken to have the value $0.04E_c$.

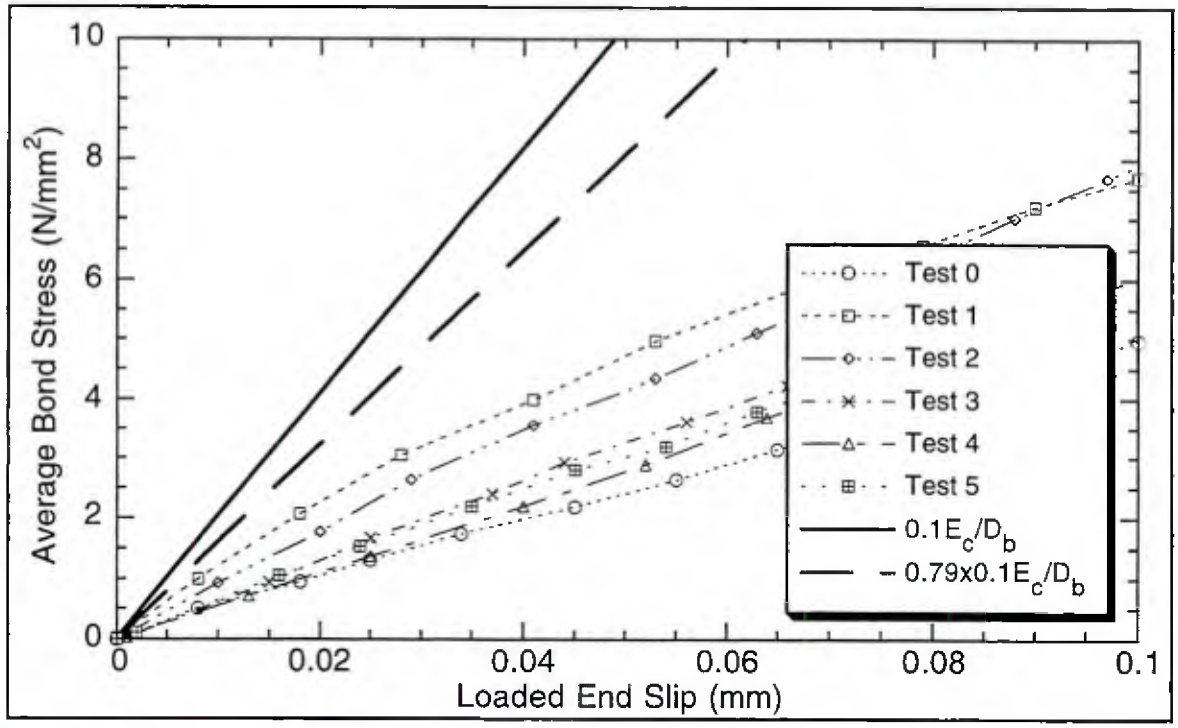

Figure 5.2-1 Comparison of model's D_{11}^e to initial slope of series 2 tests prior to cracking.

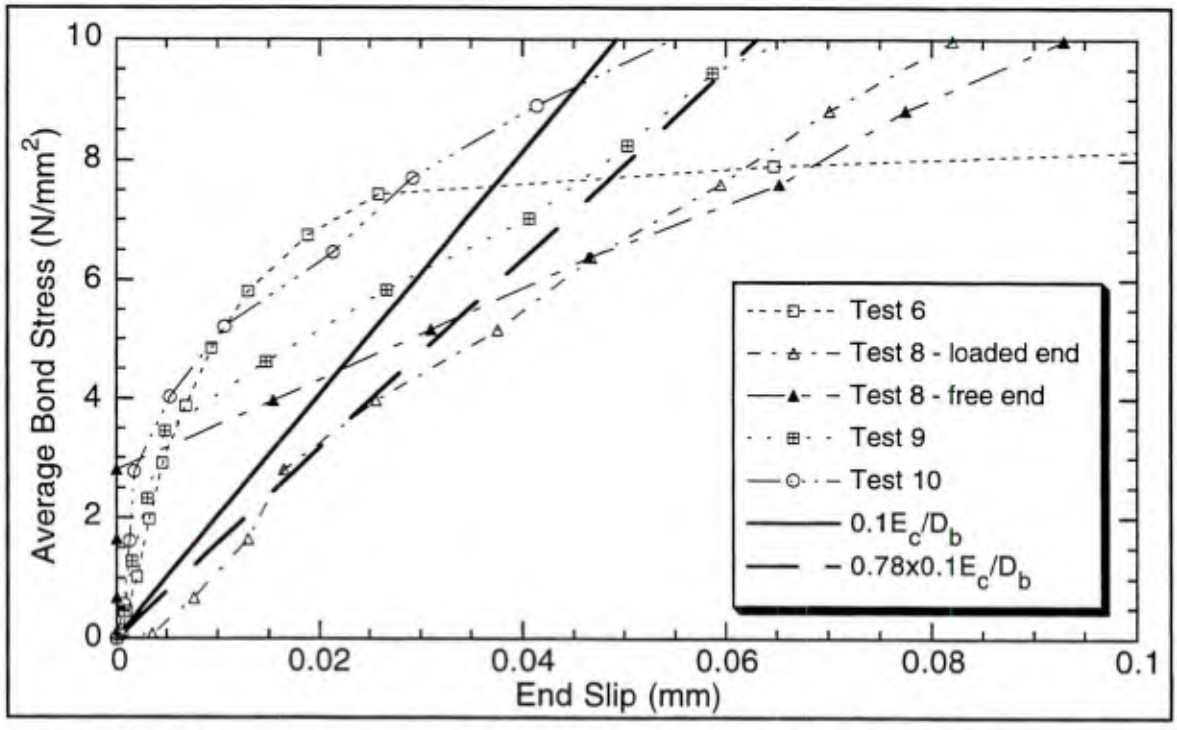

Figure 5.2-2 Comparison of model's D_{11}^e to initial slope of series 3 tests after cracking.

Two tests from Malvar's test series 4 (Malvar [1992]) give insight to the order of magnitude of D_{22}^{e}. These tests have fabricated longitudinal cracks in the specimens and thus their test numbers were prefixed by "PC" denoting "pre-cracked." Tests PC2 and PC4 had confinement stresses of 1500 and 2500 psi, respectively. Unlike earlier test series, the confinement stress was not held constant. Assuming the splitting cracks were open, the confinement stress was increased 1000 psi in both tests at a fixed end slip of about 4 mm. The specimens were then subjected to approximately two more millimeters of end slip followed by a return to the original confinement stress. Figures 5.2-3 and -4 present bond stress versus end slip and radial dilation versus end slip, respectively.

Figure 5.2-4 shows strikingly different dilation responses with respect to loading and unloading. The increase in confinement stress produces similar radial contractions in both specimens – O(0.08 mm). On the other hand, the elastic unloading recovers very little radial contraction – O(0.004 mm) for test PC2. The discrepancy between the loading and unloading responses is due to either elastoplastic coupling or plastic response during loading – neither of which the model would predict for the given loading path. Elastoplastic coupling (during the slippage from 4 to 6 mm) could increase the apparent stiffness since the additional radial contraction could close the splitting cracks; thus the confinement stress would be partially balanced by hoop stress, reducing the local response at the rib. Alternatively, much of the radial contraction during the increase in confinement stress could be plastic deformation due to the ribs crushing the material directly "above them." Assuming that E_c=39,000 N/mm^2 and that the contraction is elastic, D_{22}^{e} is estimated to be $0.002E_c$. The subsequent dilation in test PC2 corresponds to an approximate D_{22}^{e} of $0.04E_c$. This latter value is admittedly very subjective. The actual mechanics would be better understood if an unloading segment had been attempted prior to the 2 millimeters of induced slip, but the determination of D_{22}^{e} was not the goal of the tests.

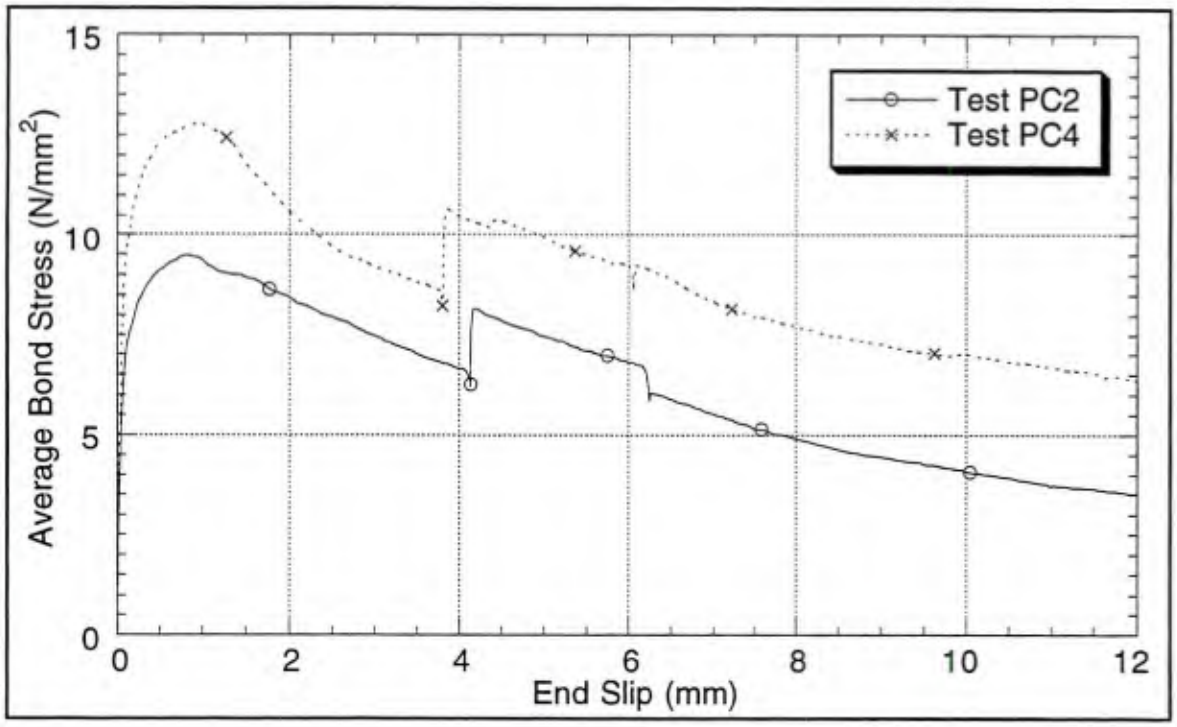

Figure 5.2-3 Average bond stress versus end slip for series 4 tests PC2 and PC4.

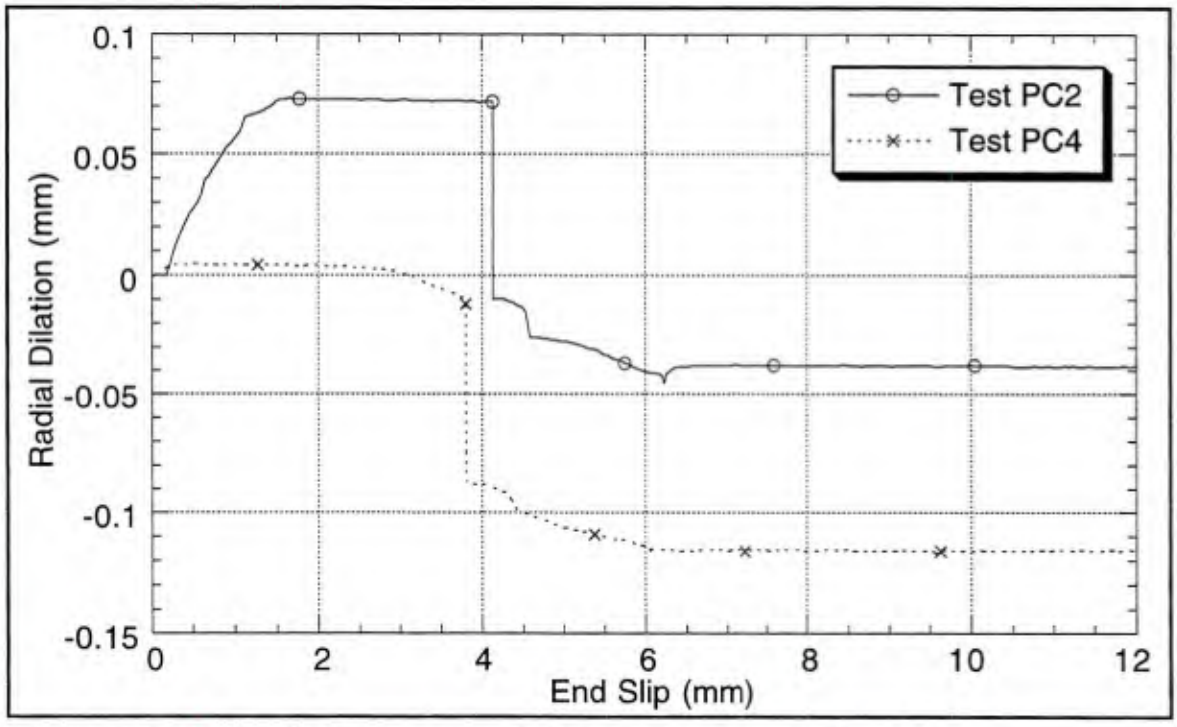

Figure 5.2-4 Radial dilation versus end slip for series 4 tests PC2 and PC4.

The previously referenced simple analysis (Herrmann and Cox [1994]) and validation studies suggests the latter hypothesis (that plasticity occurred when increasing the confinement stress) is more accurate since $0.04E_c$ is closer to the magnitude of D^e_{11}.

The only constant that must still be determined is D^e_{12}.* To determine the off-diagonal terms let's reexamine the data presented in Figures 4.1-1 and -2. If the elastic response is considered from a "stiffness" point of view and if we ignore that we are looking at two scalar components of vector quantities, these plots suggest very large off-diagonal terms. A correct interpretation of this data requires the history to be considered. For simplicity, assume the entire specimen represents the bond zone and that the normal stress once applied remains constant. The loading history can then be viewed as: 1) the normal stress is applied, and then 2) tangent stresses develop with the imposed slip. With this loading history we can interpret the initial rate of change of radial dilation with respect to bond stress as the compliance term $(\mathbf{D}^{e\,-1})_{21}$.

Figure 5.2-5 presents the experimental data of Malvar (1993) for test series 2 and 3 and two elastic models. Consider the following observations about the experimental data:

1. The bars of series 3, with normal ribs, exhibit no measurable elastic radial dilation.
2. In contrast, the bars of series 2 (with inclined ribs) are significantly more compliant.
3. There is significant scatter in the data of series 2 but the absolute differences in the radial dilations are very small.
4. The initial radial contraction given by test 10 is likely to be experimental error.

As with D^e_{11} the rib pattern appears to play a significant role; this is consistent with the hypothesis that the elastic response is localized near the rib face but could also be explained by the effect of the rib pattern on transverse cracking (recall this is "reloading data"). Since

---

* Recall we assumed that $D^e_{12} = D^e_{21}$.

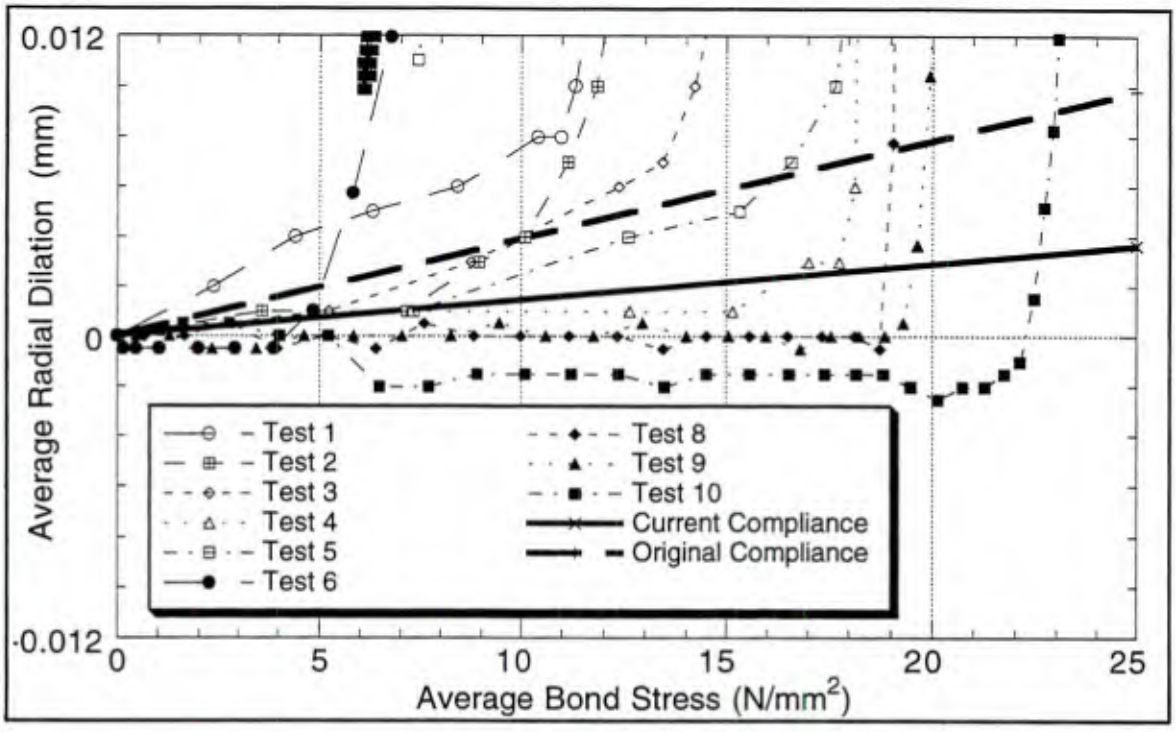

Figure 5.2-5 Experimental data and models for the compliance term $(\mathbf{D}^{e\,-1})_{21}$.

in this initial version of the model, the effect of the rib pattern is not included, an "average" value will be incorporated. The "original compliance," shown in Figure 5.2-5, was selected as having an "average compliance" for the series 2 tests. When this value was selected, the corresponding value for both D^e_{11} and D^e_{22} was $0.04E_c$. Consistent with the interpretation of the data for the off-diagonal terms, if this value is assumed to be the reciprocal of the diagonal compliance terms then the compliance moduli were given as

$$\mathbf{D}^{e\,-1} = \frac{1}{E_c}\begin{bmatrix} 25 & \frac{4}{5} \\ \frac{4}{5} & 25 \end{bmatrix}. \tag{5.2-1}$$

Inverting this gives the elastic moduli approximately as

$$\mathbf{D}^{e} = E_c\begin{bmatrix} 0.0400 & -0.00128 \\ -0.00128 & 0.0400 \end{bmatrix}. \tag{5.2-2}$$

For simplicity the off-diagonal terms were taken to be 3 percent of the diagonal terms, $0.0012E_c$. In subsequent calibration efforts, D^e_{11} was increased to $0.1E_c$ while the other

elastic moduli were left unchanged. Inverting the resulting matrix of elastic stiffness moduli gives the compliance matrix approximately as

$$\mathbf{D}^{e\,-1} = \frac{1}{E_c}\begin{bmatrix} 10 & \frac{3}{10} \\ \frac{3}{10} & 25 \end{bmatrix}. \tag{5.2-3}$$

Since the matrix is strongly diagonally dominant, the diagonal compliance moduli are essentially the reciprocal of the corresponding stiffness terms. Conversely, the change in D^e_{11} and the resulting increase in the determinant significantly reduces the off-diagonal terms. The reduced off-diagonal compliance term is denoted as "current compliance" in Figure 5.2-5 since it represents the calibration value used in this study. This value still gives a reasonable "average response" for the tests.

In retrospect, these off-diagonal (or coupling) terms are so small that it seems their effect might be considered secondary implying the use of a diagonal elastic matrix and relying on the flow rule to produce the significant wedging behavior.

For the calibration used in this study, the "incremental elastic moduli" are given as

$$\mathbf{D}^{e} = E_c\begin{bmatrix} 0.1 & -0.0012\,\mathrm{sgn}(\delta_t)\,\mathrm{H}(|\delta_t|-\varepsilon) \\ -0.0012\,\mathrm{sgn}(\delta_t)\,\mathrm{H}(|\delta_t|-\varepsilon) & 0.04 \end{bmatrix}. \tag{5.2-4}$$

Chapter 6

Numerical Implementation

This chapter presents a brief overview of the numerical implementation of the plasticity bond model. The model has been implemented and tested within the Geneseos finite element system (Cox [1995]). The first section briefly discusses this system, in particular the global algorithms used in the analyses. The second section outlines the cutting-plane algorithm -- the stress-point algorithm adopted for this study. In addition to the bond model, models of the actual tests require laws for the constitutive materials. Appendix E presents a discrete structural model of a reinforcing bar, and Appendix F presents a trivial, elastic-brittle, concrete model that allows longitudinal cracking to develop.

Originally I anticipated the numerical implementation would be a very significant component of the research, but originally I had no significant experience in material modeling. As reflected in this document, it soon became clear that the model development and validation would be the focus of this study. The development of the Geneseos system was a separately funded project that was conducted concurrently with this work. This study certainly influenced the Geneseos system; it contains several single-stress bond laws and special elements (nodal-link and interface) that allow wedge springs to be included in the model. None of these features will be discussed here since the current model supersedes these simpler approaches.

6.1 Geneseos FEM System

The Geneseos finite element system was developed to meet two needs: 1) algorithm prototyping and 2) development of custom analysis systems. For this study the former applies. One of the useful features of this system, with respect to algorithm prototyping, is the incorporation of a calculation language; this feature was inspired by the FEAP (Finite Element Analysis Program) code developed by Professor Bob Taylor (Zienkiewicz [1977]).

The incorporation of a calculation language allows algorithms to be modified without making changes in the actual code. In Geneseos, as with FEAP, the language is limited to a global description of the algorithm. For example, the statement *Update Stiffness_&_Residual* tells the system to update the global stiffness and residual vector, but does not address individual element or material law calculations.

Both of the global algorithms presented in this section use an approximation to the Newton-Raphson method. Technically it does not exactly correspond to Newton-Raphson's method because the elastoplastic moduli are not derived in an algorithmically consistent manner (see the next section), thus at the global level the "tangent stiffness" does not correspond to the true Jacobian.*

Algorithm 6.1-1 presents the calculation statement sequence used for most of the validation problems. The time step loop and global iteration loop are explicitly shown. The current version of the program does not adaptively refine the time step, so temporal convergence

* Since the tangent stiffness represents an approximation to the actual Jacobian, some might prefer to refer to the algorithms used here as being "quasi-Newton." Engineers and mathematicians sometimes have different definitions for "quasi-Newton," so for brevity I'll just refer to the nonlinear equation solver as the "Newton-Raphson method."

Algorithm 6.1-1 Quasistatic calculation statement sequence using the Newton-Raphson method and no step predictor.

```
Define_convergence_criterion 1
  Time_check  (* i.e. for the time step loop *)
End Define_convergence_criterion
Define_convergence_criterion 2
  Count_maximum= 50 Fatal (* OR *)
  residual <= 1.0E-6
End Define_convergence_criterion

Assign_equation_numbers
Determine_storage
Repeat (* time increment loop *)
  Print count Using "Load step number: "
  Increment Time
  Print Time
  Set First_iter
  Update Stiffness_&_residual
  Repeat (* nonlinear iteration loop *)
    Factor_K
    Forward_elim_backward_sub dUiter
    Increment dUstep  (* dUstep:= dUstep+dUiter *)
    Reset_internal_variables
    Update Stiffness_&_residual
    Print ||R||
  Until_criterion 2
  Update U  (* U:= U+dUstep *)
  Print U 1
  Update internal_variables
  Zero dUstep
  Update Uold  (* Uold:= U *)
  Print Stresses_&_strains 1
  Reset_internal_variables
Until_criterion 1
End Read_sequence
```

studies are necessary to ensure that accurate results are obtained. Examination of the statement sequence also reveals that a line search was not used.

Text shown within (* *)s represents comments in the statement sequence – not executable statements. Prior to describing the statement sequence, the following nomenclature should be established:

K ~ tangent stiffness matrix – the current estimate of the Jacobian for the Newton-Raphson method
R ~ residual vector – the vector of unbalanced equivalent nodal forces

U ~ the updated vector of nodal displacements at the end of the current step
Uold ~ the vector of nodal displacements at the beginning of the current step
dUstep ~ latest estimate of U–Uold
dUiter ~ correction to dUstep obtained in the last Newton-Raphson iteration.

The statement sequence begins by defining two convergence criteria. Criterion 1 indicates the time step loop will terminate when all of the time steps have been completed. Criterion 2 indicates that the global iteration loop (the inner loop) will be terminated when the norm of the residual is less than or equal to the tolerance of 10^{-6} or when 50 global iterations have occurred. The latter termination condition is defined to be a fatal condition.

Prior to entering the time step loop, equation numbers are assigned to nodes and the book-keeping of the matrix storage scheme is set. In the current version of the system, profile solvers are used, but the structure of the code allows other storage schemes to be used with no changes at the element level. Geneseos has not been extended to allow element birth and death; for problems which include element birth and death these two preliminary steps would occur within the time step loop.

Within the time step loop, the global iterations are performed, displacement vectors are updated, internal variables are updated, and element responses are output. The inclusion of *Factor_K* and Update *Stiffness_&_Residual* within the global iteration loop indicates that a "full Newton-Raphson method" is being used in the analysis. While a "modified Newton-Raphson method" requires fewer formulations and factorizations of the stiffness matrix, this advantage is generally at the cost of a lower rate of convergence. For problems which include cracking, the lack of continuity in the response seems to be tracked better with the "full-Newton method."

The linearized system of equations is solved with a direct, profile solver. In particular the solver uses a Crout decomposition form of Gauss elimination with the profile storage scheme defined for the SKYLDU solver (Perano [1986]).

Algorithm 6.1-2 Quasistatic calculation statement sequence using the Newton-Raphson method and a simple step predictor.

```
  Define_convergence_criterion 1
    Time_check  (* i.e. for the time step loop *)
  End Define_convergence_criterion
  Define_convergence_criterion 2
    Count_maximum= 50 Fatal (* OR *)
    residual <= 1.0E-6
  End Define_convergence_criterion

  Assign_equation_numbers
  Determine_profile
  Repeat (* time increment loop *)
    Print count Using "Load step number: "
    Increment Time
    Print Time
    Set First_iter
    Update Stiffness_&_residual
    Repeat (* nonlinear iteration loop *)
      Factor_k
      Forward_elim_backward_sub dUiter
      Increment dUstep  (* dUstep:= dUstep+dUiter *)
      Reset_internal_variables
      Update Stiffness_&_residual
      Print ||R||
    Until_criterion 2
    Update U  (* U:= U+dUstep *)
    Print U 1
    Update internal_variables
    Save dUstep  (* dUstep:= dUiter, copied for saving *)
    Zero dUstep
    Update Uold  (* Uold:= U *)
    Print Stresses_&_strains 1
    Predict dUstep (* copies dUiter back into dUstep unless
                      it's a new segment *)
    Reset_internal_variables
  Until_criterion 1
End Read_sequence
```

The internal variables for all element types are retained in a queue data type (*i.e.*, first in – first out) where *Reset_internal_variables* causes the pointer to be reset to the first element of the data. The internal variables are updated when the global iterations have converged.

Algorithm 6.1-2 presents a calculation statement sequence with a simple predictor. This algorithm uses the displacement step increment from the previous step as a predictor for the

current step; in many problems it simply gives the Newton-Raphson method a better starting point thus reducing the number of iterations that are required. The two new statements are underlined. They simply save the step increment for the next step instead of setting it to zero.

For the cases where specimen cracking occurred, the predictor would sometimes produce premature cracking. Therefore, Algorithm 6.1-1 was preferred for these cases. The predictor would produce displacement increments which cracked certain elements; without the predictor an equilibrium position would be found that did not crack the same elements.

This section gave an overview of global algorithms used to obtain the numerical results of the next chapter. The following subsection presents the stress-point integration algorithm used for the implementation of the bond model.

6.2 Stress-Point Integration Algorithm

This section outlines the cutting-plane algorithm and discusses some of its attributes; the algorithm is applied in this study to perform the stress-point integrations for the bond model. For additional details on the algorithm (including accuracy and stability analyses, and application to specific models), see Ortiz and Simo (1986), Ortiz and Popov (1985) and Hughes (1987).

Internal stresses within the elements contribute to the generalized nodal forces and thus to the global residual vector. Therefore, both the *Update Stiffness_&_residual* and *Print Stresses_&_strains* statements of Algorithms 6.1-1 and -2 implicitly contain code structures of the form shown below:

FOR each element group (or type depending upon the structure of the code)

FOR each element of the group (or type)

FOR each element integration point

Integrate the constitutive relations with the stress-point algorithm

END (element integration point loop)

END (element loop)

END (element group loop).

Since these loops are nested within the time step and global iteration loops of Algorithms 6.1-1 and -2, the efficiency of the stress-point algorithm can have a strong effect upon the efficiency of the analysis system in general. For small to moderate size nonlinear problems the costs of forming the residual vector and Jacobian often exceeds the costs associated with solving the resulting system of equations. The cutting-plane algorithm converges quadratically to a consistent material state. Other important issues for stress-point algorithms that affect the efficiency of the analysis system are the temporal rate of convergence (*i.e.*, its order of accuracy), stability and the algorithm's effect on the global rate of convergence.

First order convergence is synonymous with *consistency** of the algorithm (*i.e.*, in the limit the approximate equations reduce to the governing equations). Furthermore, the Lax equivalence theorem states that for a consistent difference approximation to a properly posed initial value problem convergence and stability are equivalent (see *e.g.*, Richtmyer and Morton [1967] and Rosinger [1980]) Ortiz and Popov (1985) reference the work of Marsden (1973) on this issue, and then show that "small-scale stability" (as used in their proof) implies the definition of "large-scale stability" used by Marsden (1973).

---

* This is distinctly different from plastic *consistency* and algorithmic consistency of the elastoplastic moduli with the Newton-Raphson method.

The principal motivation for using the cutting-plane algorithm was its explicit form in the updates for the internal variables and plastic strains. This form alleviated the need to calculate second order derivatives during the model development effort. Since many versions of the bond model were considered, this was an efficient choice (from a labor point of view). From a numerical point of view it is not the optimum algorithm. It is first order convergent, but it is only conditionally stable. Furthermore, typical stability proofs (see *e.g.*, Ortiz and Simo [1986]) rely on the assumption that the plastic potential function is convex; as discussed in Chapter 4, during plastic contraction this assumption is not valid, and thus the stability of the algorithm has not been proven for this phase of the model's response. Numerical results in the next chapter do not reveal any obvious signs of instability. Lastly expressions for algorithmically consistent elastoplastic moduli cannot be obtained in closed form. In this study the continuum theory elastoplastic moduli (Equation [2.5-4]) are used. Simo and Hughes (1987) have observed improved convergence when using the algorithmically consistent elastoplastic moduli derived for the closest point projection algorithm.

Kelly (1960) and others (see Cheney and Goldstein [1959]) independently developed the cutting-plane algorithm for solving problems in convex mathematical programming. Ortiz and Popov (1985) expressed the constraint of the yield surface in Kun-Tucker form as:

$$\phi(\underline{Q},\underline{h})\leq 0,\quad \lambda\geq 0,\quad \phi\lambda=0$$

From this perspective, the cutting-plane algorithm is incorporated to satisfy the inequality constraint in stress space offered by the yield surface (*i.e.*, the consistency condition). The algorithm is in the class of cutting-plane methods of constrained optimization (see *e.g.*, Luenberger [1984]). This is conceptually consistent with the development of rate independent plasticity given in Lubliner's (1992) text where it is treated as a limiting case of viscoplasticity as the viscosity goes to zero; this is analogous to penalty methods in

constrained optimization producing the exact solution in the limit when a penalty parameter goes to zero (or infinity depending upon the formulation).

In the context of stress-point integration, the cutting-plane algorithm falls within the category of *return mapping algorithms*. Ortiz (1981) noted that these algorithms reflect the additive form of the elastoplastic constitutive relations; application of the operator-splitting methodology produces an elastic stress prediction that is then plastically relaxed (or corrected) to a suitably updated yield surface. Successive plastic corrections produce convergence to a consistent state within an arbitrary accuracy. For each correction the yield function ϕ is linearized about the current material state to obtain an estimate for $\Delta\lambda$, the discrete analog of the loading index.

Algorithm 6.2-1 presents the cutting-plane algorithm nearly identical to the form presented in a report by Hughes (1987). The differences are limited to notation and the use of a simplified elastic model. The elastic response is essentially linear; the variation in the off-diagonal terms is not significant for monotonic loading. In general, the cutting-plane algorithm is valid for models incorporating nonlinear elasticity.

Most of the statements or individual steps in the algorithm are sequentially numbered. The subscript n denotes the n'th global step and the superscript k denotes the k'th local (or material) iteration. The following remarks are intended to give some insight to the nature of the algorithm and to clarify its application to the bond model.

The algorithm begins with the stresses, plastic strains, and internal variables that were determined at the end of the previous step. For the version of the monotonic model presented here, no distinct internal variables are needed; that is, d can be determined directly from $q^p_{1\,n}$. For other versions of the model, $\underline{h}_n$ has contained the values of C_n, W_{en} and $\widehat{\sigma}_n$. Also note that the $\underline{q}_{n+1}$ is the current estimate (*i.e.*, at a given point in the sequence of global iterations) of the total strain at the end of the step.

Statements	Remarks
(1)–(3)	These steps simply initialize variables to their values at the beginning of the step.
(4)–(16)	These steps are the body of the local iteration loop where a consistent material state is sought. The internal variables, plastic strains and stresses are corrected until a consistent state is attained.
(4)	For k=0 this step gives an initial elastic prediction of $\underline{Q}$. For k>0 this step gives a corrected $\underline{Q}$ accounting for the new estimate of $\underline{q}^{p}_{n+1}$.
(5)	This step gives the current estimate of the yield function (the left-hand side of Equation 3.3-2 minus the right-hand side).
(6)	The loop is exited if the response is elastic or if consistency is satisfied within some zero tolerance (10^{-6} to 10^{-4} in this study).
(7)	After max_iterations the local iteration and program execution are terminated.
(8)–(12)	Calculation of the first order derivatives and evolution laws. For the form of the bond model presented here, one can consider either $\{C, W_e, \widehat{\sigma}\}$ as the internal variables or simply d. Since the first set can be expressed explicitly in terms of d, the two interpretations are equivalent for these steps. There is one detail in these calculations that must be treated carefully. The deductions (3.3-8) showed that careful selection of the calibration constants will produce $\underline{Q} \in C^1(\underline{q})$; however, by design these same calibrations produce a singularity in C for d=0. In the implementation a statement of the following form was used to avoid this singularity:

IF ($d \leq$zero_damage_tolerance) AND (a_4<1) THEN
    dC/dd:= nearly_infinity
ELSE
    dC/dd:= *the derivative of Equation (3.3-6)*
END

The value for *zero_damage_tolerance* must be near the order of the unit roundoff for the particular system, otherwise the algorithm can fail to converge in a reasonable number of steps. For example choosing this tolerance to be 10^{-10} has failed to produce convergence in 50 iterations. The value of *nearly_infinity* should be close in magnitude to the maximum floating point number for the system. Currently *nearly_infinity* is set to the maximum floating point number divided by 100 to prevent an overflow error in subsequent calculations. Though admittedly "bad form," *zero_damage_tolerance* was set to 0 for this study with no apparent adverse effects (*e.g.*, numerical overflow).

(13) This step gives the update for $\Delta\lambda$ – the finite analog of the loading index. This relationship can be obtained by linearizing the consistency condition for the k+1'th iteration about the k'th iteration. Given a total strain estimate, total stress and elastic strain can be regarded as dependent upon the plastic strain. A Taylor series of ϕ is taken with respect to the internal variables and plastic strain. The resulting equation gives the value for $\Delta\lambda$.

(14)–(15) The linearization then produces updates in both the internal variables and plastic strains. This is where the closed form expressions for $\{C, W_e, \widehat{\sigma}\}$ are advantageous, because step (15) can be omitted for the form of the bond law presented here. For comparison, I obtained the derivatives of these three functions with respect to d and could then express their evolution in an incremental form. The functions C and $\widehat{\sigma}$, in particular, "reflect the scale the rib" in the early response and thus change very rapidly over a relatively small slip. The loss of accuracy due to the numerical integration of these functions was noticeable; for long embedment lengths the bond response distributions exhibited small oscillations unlike the smooth distributions shown in the next chapter. For cyclic loading these functions must be

expressed in an incremental form and thus this issue needs additional attention; accuracy was not quantitatively addressed in this study but must be in subsequent efforts for bond modeling to be incorporated in larger scale problems.

When the form of the bond model becomes relatively stable (*i.e.*, when refinements in the model are complete), more numerically efficient algorithms should be used in its implementation. A candidate algorithm is the *closest-point-projection algorithm* – a generalization of the algorithm proposed by Simo and Taylor (1986) for J_2, rate independent plasticity. This algorithm is amenable to exact linearization, that is closed form expressions for the algorithmically consistent elastoplastic moduli exist. Since the linearization is exact, the Newton-Raphson method is truly being used at the global level, and thus the implementation of the material law does not inhibit the coveted quadratic convergence in the neighborhood of the solution. In addition this algorithm has better stability properties than the cutting-plane algorithm for many plasticity models; however, I am also unaware of the ramifications of having a non-convex plastic potential function for this algorithm. The integrations are performed with an implicit backward-Euler difference scheme so that it is only first order accurate in its standard form. Modifications to obtain second order convergence would be highly desirable since the model "reflects" the scale of the ribs and thus necessitates an accurate integration method for larger scale problems.

With the model and its method of numerical implementation defined, the next chapter presents several calibration and validation results.

Algorithm 6.2-1 Cutting-plane algorithm for rate-independent, small-deformation, elastoplasticity using deformation dependent elastic moduli.

(* Given:

$\underline{Q}_n, \underline{q}^p_n$ and $\underline{h}_n$ ~ stress, plastic strain and internal variables at the beginning of the step

$\underline{q}_{n+1}$ ~ global estimate of total strain at the end of the step *)

(* Initialize Variables *)

k:= 0 (* iteration counter *)

$$\underline{q}^{p\,(0)}_{n+1} := \underline{q}^p_n \tag{1}$$

$$\underline{h}^{(0)}_{n+1} := \underline{h}_n \tag{2}$$

$$\mathbf{D}^e := \mathbf{D}^e(q_1 D_b) \quad (* \textit{ i.e.}, \text{ using Equation (5.2-4) } *) \tag{3}$$

LOOP (* for each local iteration *)

(* Compute the stress and evaluate the yield function *)

$$\underline{Q}^{(k)}_{n+1} := \mathbf{D}^e\left(\underline{q}_{n+1} - \underline{q}^{p\,(k)}_{n+1}\right) + \underline{Q}_n \quad (* \text{ "essentially" linear elastic } *) \tag{4}$$

$$\phi^{(k)}_{n+1} := \phi\left(\underline{Q}^{(k)}_{n+1}, \underline{h}^{(k)}_{n+1}\right) \tag{5}$$

(* Check for elastic response and consistency during elastoplastic response *)

IF (k=0 and $\phi^{(k)}_{n+1} \le$ zero_tolerance) or ($\left|\phi^{(k)}_{n+1}\right| \le$ zero_tolerance) THEN

EXIT LOOP (* have convergence *) (6)

ELSIF k>max_iterations THEN

terminate execution for convergence failure (7)

END

(* Calculate the derivatives, evolution laws and $\Delta\lambda$ *)

$$\left(\frac{\partial \phi}{\partial \underline{Q}}\right)^{(k)}_{n+1} := \frac{\partial \phi}{\partial \underline{Q}}\left(\underline{Q}^{(k)}_{n+1}, \underline{h}^{(k)}_{n+1}\right) \tag{8}$$

$$\underline{R}^{p(k)}_{n+1} := \underline{R}^p\left(\underline{Q}^{(k)}_{n+1}, \underline{h}^{(k)}_{n+1}\right) \tag{9}$$

$$\left(\frac{\partial \phi}{\partial \underline{h}}\right)^{(k)}_{n+1} := \frac{\partial \phi}{\partial \underline{h}}\left(\underline{Q}^{(k)}_{n+1}, \underline{h}^{(k)}_{n+1}\right) \tag{10}$$

$$\overline{\underline{h}}^{(k)}_{n+1} := \overline{\underline{h}}\left(\underline{Q}^{(k)}_{n+1}, \underline{h}^{(k)}_{n+1}\right) \tag{11}$$

$$K^p := -\left[\left(\frac{\partial \phi}{\partial \underline{h}}\right)^{(k)}_{n+1}\right]^T \overline{\underline{h}}^{(k)}_{n+1} \tag{12}$$

$$\Delta\lambda^{(k)}_{n+1} := \phi^{(k)}_{n+1}\left\{\left[\left(\frac{\partial \phi}{\partial \underline{Q}}\right)^{(k)}_{n+1}\right]^T \mathbf{D}^e \underline{R}^{p(k)}_{n+1} + K^p\right\}^{-1} \tag{13}$$

(* Update plastic strains and internal variables *)

$$\underline{q}^{p\,(k+1)}_{n+1} := \underline{q}^{p\,(k)}_{n+1} + \Delta\lambda^{(k)}_{n+1} \underline{R}^{p\,(k)}_{n+1} \tag{14}$$

$$\underline{h}^{(k+1)}_{n+1} := \underline{h}^{(k)}_{n+1} + \Delta\lambda^{(k)}_{n+1} \overline{\underline{h}}^{(k)}_{n+1} \tag{15}$$

INCREMENT(k) (16)

END LOOP

Chapter 7

Calibration and Validation Results

This chapter presents comparisons between experimental data and numerical models that incorporate the plasticity bond model developed in this study. Experimental data from six different research groups are considered in the validation effort. As shown in Figure 7-1 and Tables 7-1 and 7-2, the bond specimens used by the different research groups vary significantly in geometry and material properties. Each section in this chapter addresses a unique set of experiments. The subsections describe the experiments, the corresponding numerical models of the experiments, and the experimental and numerical results.

Validation is inherently a process that is never completed, but the results given in the following sections show that the bond model can reproduce the response of several experiments with "sufficient accuracy." The phrase "sufficient accuracy" is subjective and deserves some clarification. For a bond model that is developed for applications with large slips (*i.e.*, the mechanical interaction can completely fail), several aspects of the response can be used in its evaluation, including: 1) elastic or initial stiffness, 2) maximum bond stress, 3) slip at maximum bond stress, 4) frictional stress value following bond failure, 5) energy dissipation, 6) a norm of the error in bond stress for the full range of slip, and 7) transverse or radial response. All of these aspects of the response are mentioned in the following sections.

The overall accuracy goal was to achieve a bond stress-slip response that was accurate to about 20 percent over the full range of slip for several experiments. This goal is more ambitious than it might first appear because of the large amount of experimental scatter that

Table 7-1. Specimen bar data in metric units.

Specimens	Bar Diameter D_b (mm)	Rib Spacing s_r (mm) & s_r/D_b	Rib Height h_r (mm) & h_r/D_b	Rib Angle (degrees)	Related Rib Area
Malvar (1991) Specimens 1-5	19.05 (# 6)	12.2 0.64	1.5[1] 0.079	68	0.064
Specimens 6-10	19.05 (# 6)	12.8 0.67	1.3[1] 0.068	90	0.066
Gambarova *et al.* (1989) Phase C	17.3[2]	10.8 0.62	1.3 0.075	52	0.0602[3]
Eligehausen *et al.* (1983) Series 2	24.7[4]	14.0 0.57	1.26 0.051	71	0.066
Rehm & Eligehausen (1979)	14	8.4[5] 0.60	–	–	0.075
Shima *et al.* (1987) Specimens 1-4	25.4	13.9 0.547	1.8 0.071	[6]	0.088[7]
Specimen 7	30.7	16.6 0.522	2.1 0.066		
Tepfers & Olsson (1992) Test 1	16[2]	12 0.75	1.25 0.078	90	0.064
Test 3		8 0.5			0.127
Series 4		12 0.75		45	0.064

[1]Estimated from other dimensions.

[2]Actual diameter of the core portion of the bar.

[3]Authors refer to as "surface ratio" and "bond index."

[4]Obtained from the weight of the bar.

[5]Estimated from a sketch or photograph.

[6]Spiral pattern – angle not given.

[7]Author refers to as "bearing area coefficient."

Table 7-2. General specimen data in metric units.

Specimens	Size $L \times W \times H$ (cm)	Bond Length L_b (cm)	L_b/D_b L_b/s_r	f_c and f_t (MPa)
Malvar (1991) Specimens 1-5	10.16×7.62	6.1	3.20 5	40.2[1] 4.93[2]
Specimens 6-10		6.4	3.36 5	38.4[1] 4.69[2]
Gambarova *et al.* (1989) Phase C	22.5×9×11[3]	5.4	3.12 5	40.2[4] 4.08[5]
Eligehausen, Popov & Bertero (1983) Series 2	38.1×17.8×30.4	12.7	5 9.07	30[6] 2.66-2.89
Rehm & Eligehausen (1979)	18.2×14	4.2	3 5	23.5[7] –
Shima *et al.* (1987) Specimen 1	38.1×50	12.7	5 9.14	21.8
Specimen 2	50.8×50	25.4	10 18.3	
Specimen 3	63.5×50	38.1	15 27.4	
Specimen 4	76.2×50	50.8	20 36.5	
Specimen 7	49.1×50	18.4	6 11.1	18.5
Tepfers & Olsson (1992) Test 1	4.8×11.4	4.8	3 4	25.5[8] 2.4[8]
Test 3			3 6	27.6[8] 3.0[8]
Series 4			3 4	22.0[8] 1.9[8]

[1] Average 28-day compressive strength of three 3"×6" cylinders.

[2] Average 28-day split cylinder strength of three 3"×6" cylinders.

[3] The actual shape is trapezoidal so the 22.5 cm represents the average length – (30+15)/2 cm.

[4] Average from two series of tests. The two series had average f_c values of 35.8 and 44.5 MPa. These values were obtained from the average of three 10-cm diameter cylinders with respective ages of 120 and 210 days.

[5] Average split cylinder strengths from two series of tests. The two series had average f_{ct} of 3.65 and 4.50 MPa, respectively.

[6] Nominal value, actual values varied from 28.5 to 30.7 MPa.

[7] Measured on cubes with side length of 20 cm.

[8] Measured on cubes with side length of 15 cm.

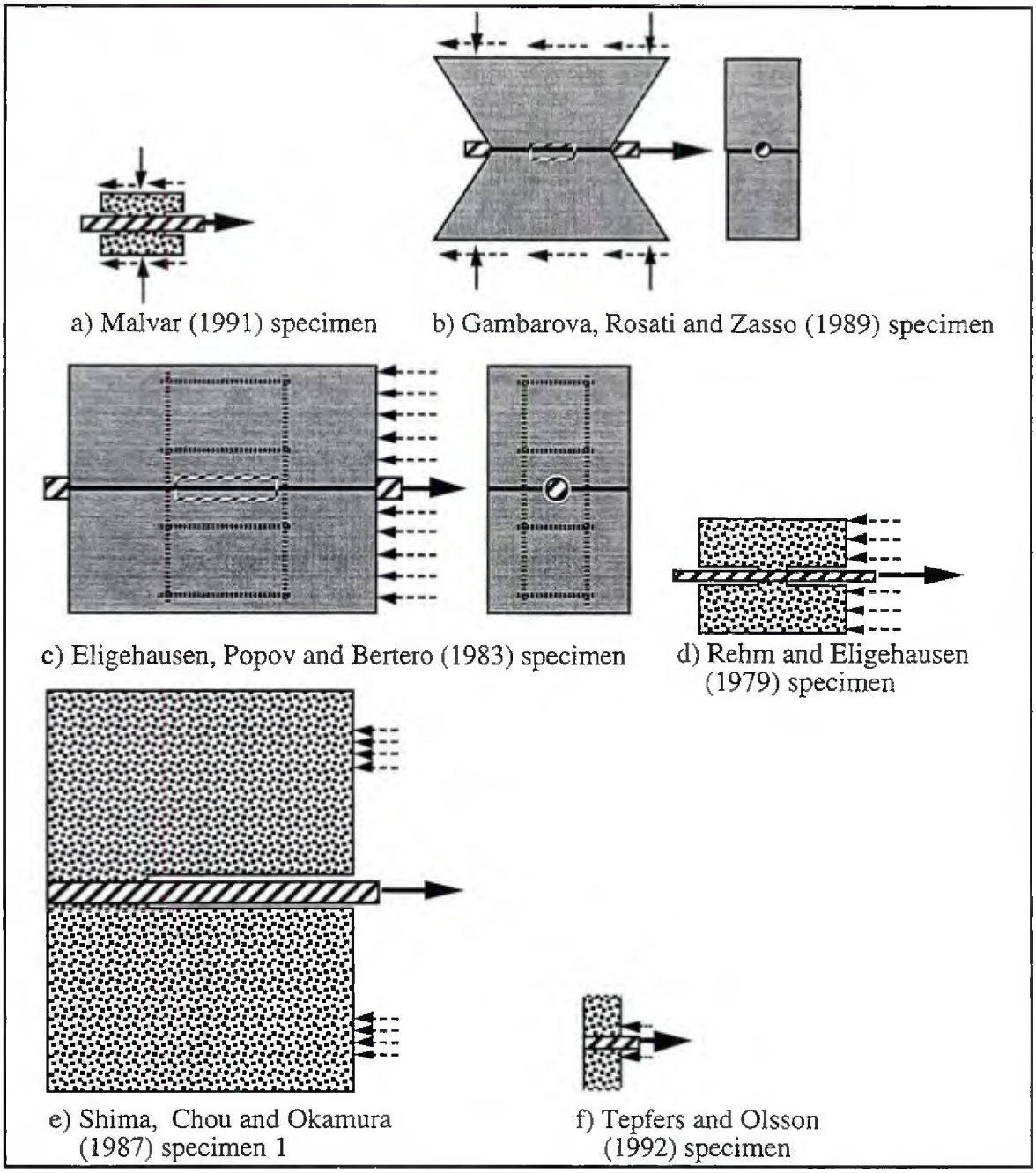

Figure 7-1 Schematics of bond specimens (to scale) used to calibrate and validate the bond model.*

* Solid arrows represent applied or controlled loads – some displacement controlled, some stress controlled. Dashed arrows represent reactions. All of the specimens except *b* and *c* were axisymmetric. For the axisymmetric specimens the unbonded length is explicitly shown. For the nonaxisymmetric specimens side and end views are given, and the bonded region is denoted in the side view with a dashed rectangle. For the Eligehausen et al. (1983) specimen dashed lines are also used to show the position of secondary reinforcement (stirrups and vertical bars). Unless noted otherwise all subsequent models use E_s= 190,000 MPa, ν_s= 0.3, and ν_c= 0.17.

has been observed in bond tests (Herrmann and Cox [1994]). Thus experiments with a measure of the experimental scatter are inherently more valuable in validating the model.

In addition to the bond stress-slip response, the radial behavior is important to the evaluation of the model too; the radial behavior directly affects the overall response (*i.e.*, there are two generalized stresses and strains) and can lead to failure modes involving splitting that cannot be predicted by single-stress models. Measures of the radial response include 1) radial dilation, 2) crack opening, 3) transverse force, and 4) hoop stress. Typically these quantities are either difficult to measure or are more sensitive to assumptions made in modeling the specimen, thus they have received less emphasis in evaluating the model. The existence and propagation of transverse splitting cracks also gives a qualitative measure of the goodness of the radial response.

In addition to accuracy, the general behavior of the model will also be discussed – relative to the experiments examined here and others.

All of the experiments examined in this chapter use pull-out type specimens, most of which have relatively short embedment lengths. The model's behavior has not been compared to tests with tensile specimens; these comparisons could provide an additional "level of validation." However, the behavior of tensile specimens is likely to be more dependent upon the cracking behavior of the concrete.

Except for the results of Shima *et al.* (1987), the measured responses are "global quantities" such as end slips and bar forces. In all cases except the data of Malvar (1991), *end slip* denotes the relative displacement between the free end of the bar and a point on the specimen where the transducer is connected – not δ_t.

The following sections are presented nearly in the chronological order of the model validation. The main exceptions are the axisymmetric FEM analyses of the Malvar tests and the stability analyses, which were both considered late in the validation effort.

7.1 Malvar Experiments

These experiments have been previously discussed in the chapters on the model development. In particular Section 3.2 gives a brief overview of the different series of experiments performed. There are no direct data available on the experimental scatter, but the trends in the bond stress-slip response with changing confinement stress suggest the experimental scatter is not excessive. The following subsections present 1) the specimen models used, 2) model calibration results using a point model, 3) axisymmetric FEM model results, and 4) a numerical study of the material law instability.

Specimen_Models

Two different models of the Malvar specimens were considered – a point model and an axisymmetric FEM model. The first model, schematically shown in Figure 7.1-1, is a point model that incorporates the simplifying assumptions used in the model development. The second model treats the concrete as a continuum which develops longitudinal cracks when the tensile strength is exceeded (reference Chapter 6). The FEM mesh for the model is shown in Figure 7.1-2.

The point model used in this case is very simple since it reflects the assumptions made during the model development; essentially the entire specimen was treated as being part of the bond zone, the "thick bond zone interpretation," and the behavior is assumed to be constant over the length of the specimen With this interpretation, the normal stress at the bond zone (shown

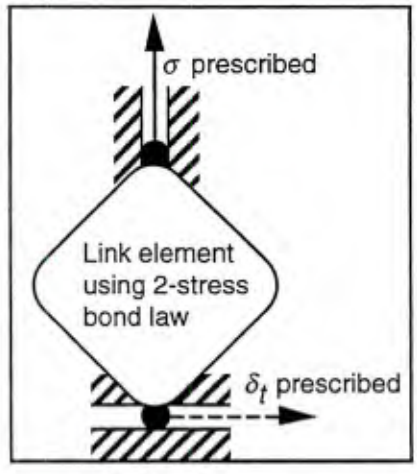

Figure 7.1-1 Simple point model of Malvar specimen.*

* In this and subsequent schematic drawings of models, solid arrows represent prescribed nonzero traction boundary conditions and dashed arrows represent prescribed nonzero displacement boundary conditions.

positive in Figure 7.1-1 – as a tensile stress) is treated as a known quantity. Thus this point model consists of one link element that represents the bond zone behavior. The confinement stress is applied directly to one node of the element and the prescribed displacement (end-slip) is applied to the other node. The resulting initial radial deformation is given by Q_2/D^e_{22}. Since D^e_{22} is interpreted as modeling the local interaction between the ribs and the adjacent concrete it has a relatively small value; thus the initial radial deformations are considered erroneous since they do not include the effects of 1) hoop stresses in the concrete, or 2) full contact between the bar and adjacent concrete. The radial displacements, presented in the next subsection, are relative displacements from this initial displaced position which is consistent with the measurements made in the experiments.

The Malvar specimen was designed to more accurately evaluate the state of the bond zone – thus its relatively small size (Figure 7-1). Because of its small size it is the only experiment where the entire specimen is treated as being part of the bond zone. This leads to noticeably different behaviors between models that treat the bond zone as "thick" and "thin" since the model with the thick bond zone (in this case) completely eliminates the thick-walled cylinder behavior of the specimen. Omitting this behavior is not physically accurate, but it does offer a consistency check between the model development, calibration and implementation because they all contain the same simplifying assumptions.* Both the point model presented in Herrmann and Cox (1994) (which treats the concrete as a cracking thick-walled cylinder) and the following axisymmetric FEM model treat the behavior of the entire specimen in a more accurate manner. The significance of these differences will be seen in the models' behaviors.

* It also indicates the effect of using simple models which are attractive for extending the model's application to large scale problems.

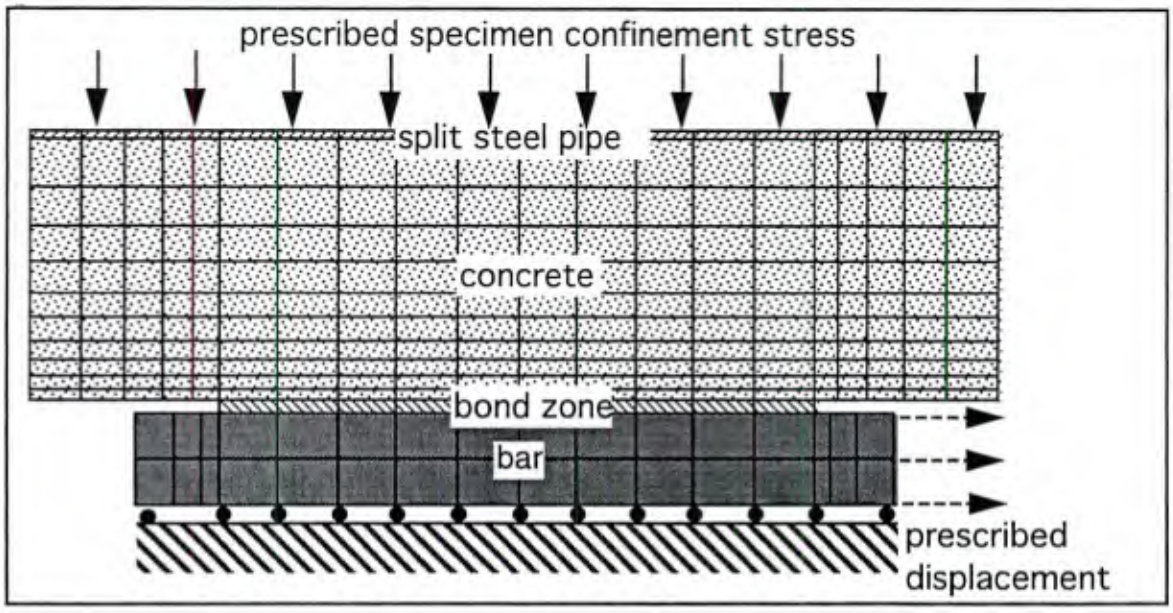

Figure 7.1-2 Axisymmetric FEM model of Malvar's specimen.

A mesh for the axisymmetric FEM model is shown in Figure 7.1-2. Only nonzero traction and displacement boundary conditions are explicitly shown. The "pipe elements" were not continuum elements. Axisymmetric elements would normally carry hoop stress that is not present in the split pipe, so interface elements (with nonzero initial thicknesses and oriented with vertical interface surfaces) were used as a means to impose a radial displacement constraint. A single-stress elastic law was used for the interface with a modulus of elasticity of 1,000,000. The nodes on the inner surface of the "pipe elements" were restrained from longitudinal translation and those on the outer surface were fixed. Thus the split pipe/steel band assembly was idealized as preventing longitudinal translation and constraining radial displacement to be approximately uniform at the outer surface of the concrete. The end displacement was taken to be the longitudinal translation at the center (*i.e.*, on the axis) of the bar's loaded end, thus the model's truncated bar eliminates some of the apparent slip due to bar strain. Malvar eliminated (in his data reduction) this apparent slip from the series 3 data.

Table 7.1-1 Material properties for models of Malvar experiments, series 2 and 3.

Model	s_r (mm)	f_c (MPa)	Bond Model f_t (MPa)	Concrete Model f_t (MPa)
Point	12.6	38.4	3.415	not applicable
Axisymmetric				values of Table 7.1-2 and 0

The material properties used for the model are given in Table 7.1-1. Note the tensile strength used for the bond model was obtained from Equation (B-1) using the concrete compressive strength for test series 3. The tensile strengths used for the specimens were the measured split-cylinder strengths for uncracked specimens and 0 MPa for the precracked specimens. In this study the "precracking history" is not completely accounted for because the monotonic model does not accurately capture the "recompaction of damaged material" that occurs during reloading. In Herrmann and Cox (1994) the load history is more accurately represented since the cyclic model accounts for this behavior. The simple elastic-brittle material model used for the concrete is discussed in Appendix F.

Point Model Results

The results for the point model are compared with the experimental results in Figures 7.1-3 through Figures 7.1-7. As noted previously, for the Malvar data *end slip* denotes the slip at the loaded end of the specimen (except for test 8 where the slip at the free end is also shown). The model predictions for each of the five confinement stresses is represented by a set of four plots. Bond stress versus slip and bond stress versus average radial dilation are each shown at two different scales – one showing the full response and one showing the initial response.

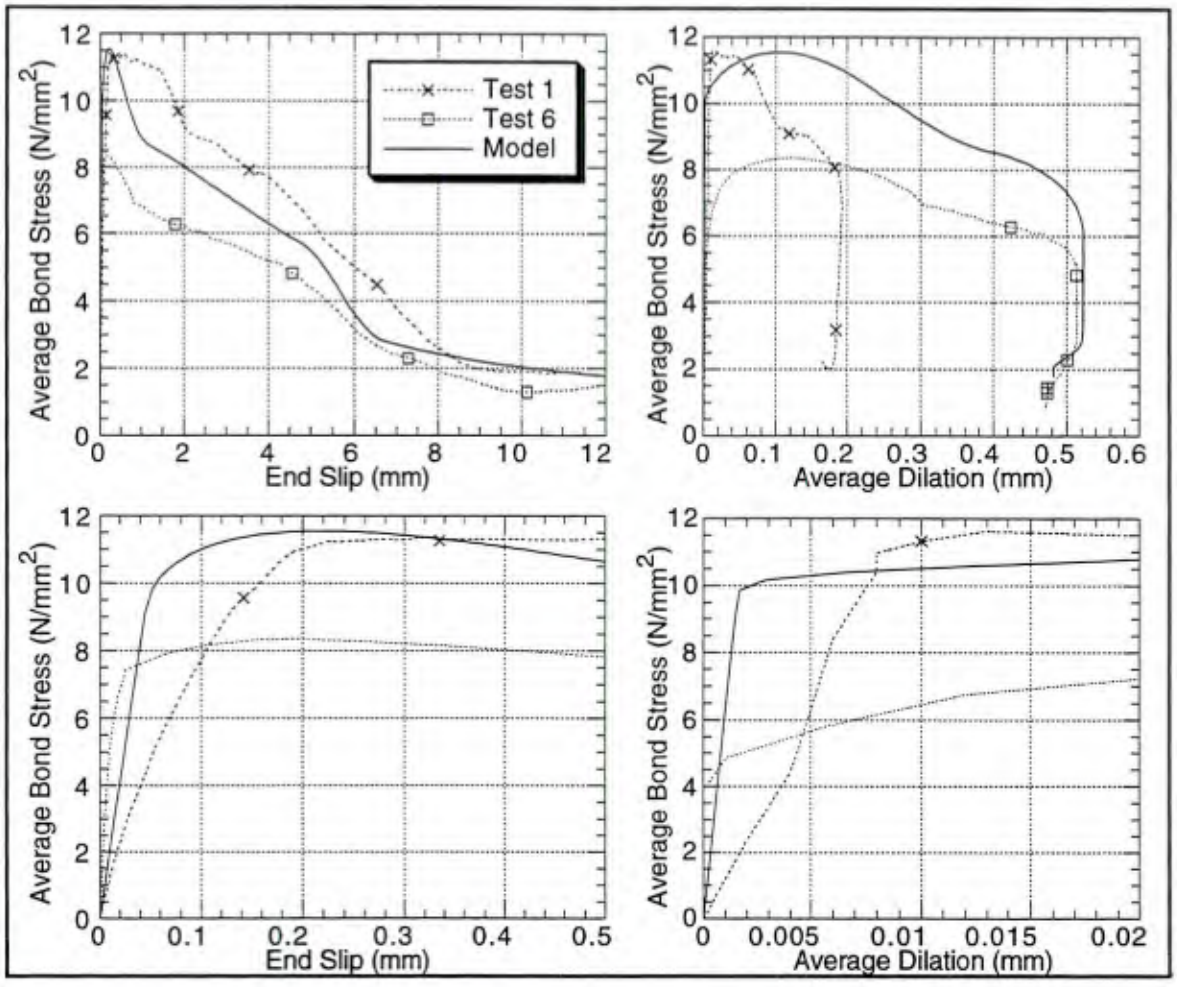

Figure 7.1-3 Calibration results (Malvar) for $\sigma = -3.45$ N/mm^2 (500 psi).

First let's consider the initial response. For the case where the end slip is measured at the loaded end, the point model (which treats the bar as rigid) will predict a stiffer initial elastic response (bond stress versus slip) than a model that accounts for the gradient along the bar. This is discussed in Appendix D and shown graphically in Chapter 5. Typically the initial response (bond stress versus both slip and average radial dilation) of the model falls between the series 2 and series 3 responses – the latter of which is the stiffer of the two. The model's bond stress versus slip response remains elastic, and therefore linear, to a large enough value of slip that the model's bond stress exceeds the series 3 test results below a bond stress of 10 N/mm^2; this would occur at a higher value if the gradient along

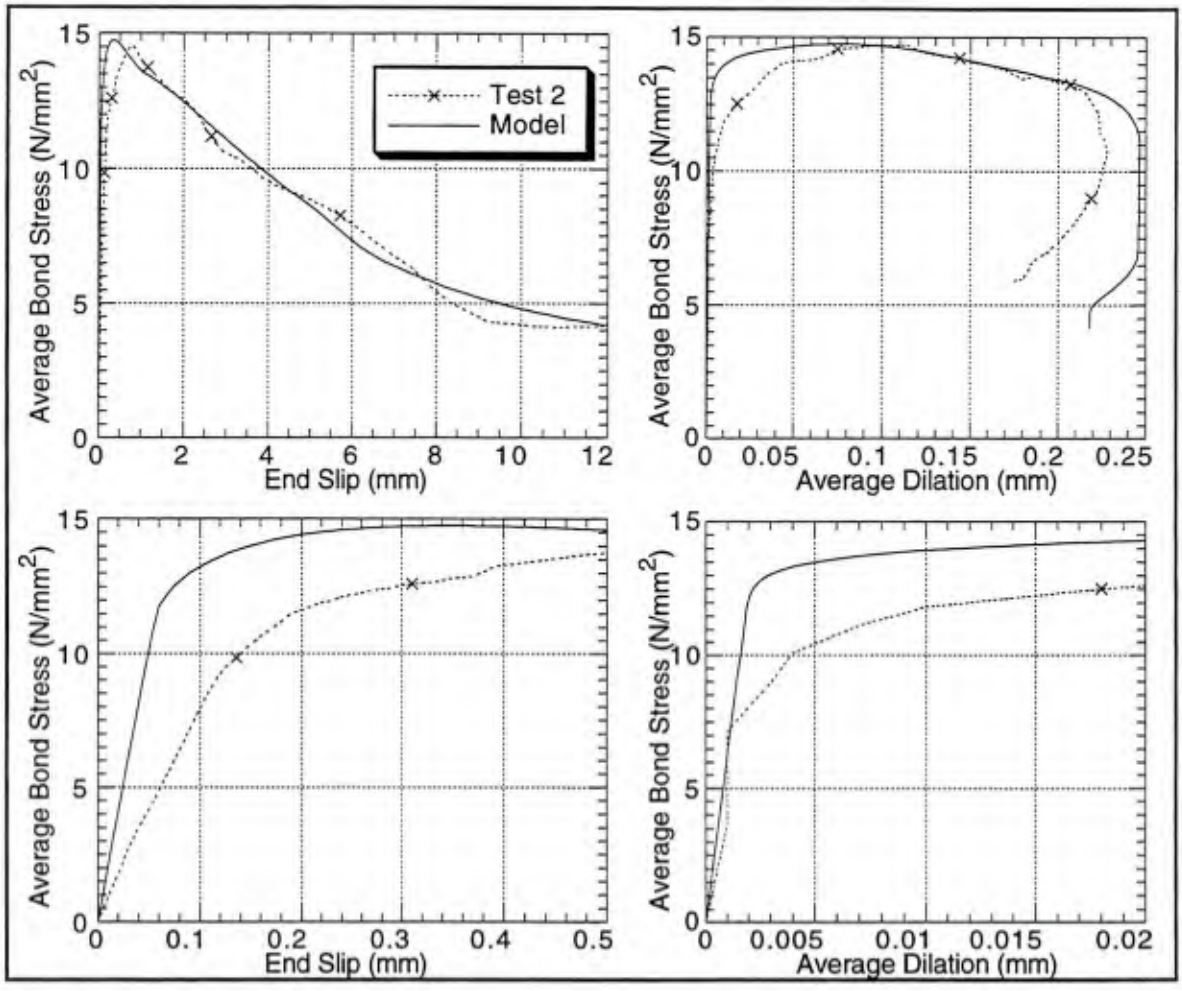

Figure 7.1-4 Calibration results (Malvar) for $\sigma = -10.3$ N/mm^2 (1500 psi).

the bar were considered. The initial radial response agrees more closely with the series 2 tests except at σ=–3.45 N/mm^2 (500 psi).

The bond stress versus slip response over the full scale is very representative of the experimental results. At the low confinement stress of 3.45 N/mm^2, both the kinematic softening and the effect of the yield surface weighting or transition function (W_e) are readily apparent. Similarly at this level of confinement stress, the experimental results show the greatest deviation from a "simple response" in the descending portion of the curve. As previously discussed, "tensile mechanisms" are expected to contribute more to

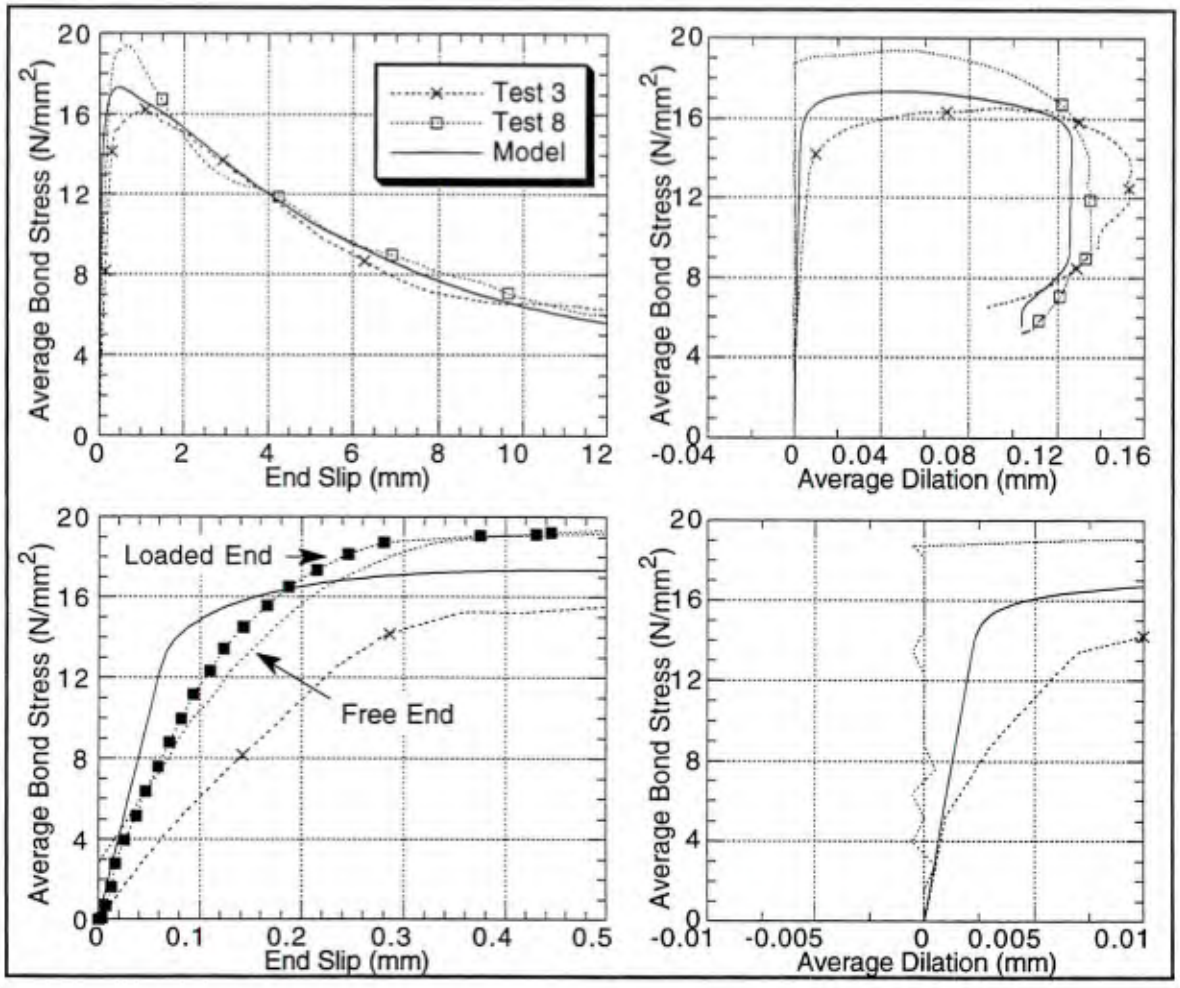

Figure 7.1-5 Calibration results (Malvar) for $\sigma = -17.2$ N/mm^2 (2500 psi).

the bond behavior under low confinement stress and thus a greater variation is expected in the experimental data.

The effect of the kinematic softening is most pronounced under low confinement stress by design, for it is under these conditions that fracture and *geometric dilation* play a greater role in the response. At σ=–10.3 N/mm^2 (1500 psi), the effects of both the kinematic softening and transition function are not very pronounced.

The combination of the isotropic hardening and kinematic softening successfully produces an increase of slip at the maximum bond stress with an increase in confinement stress.

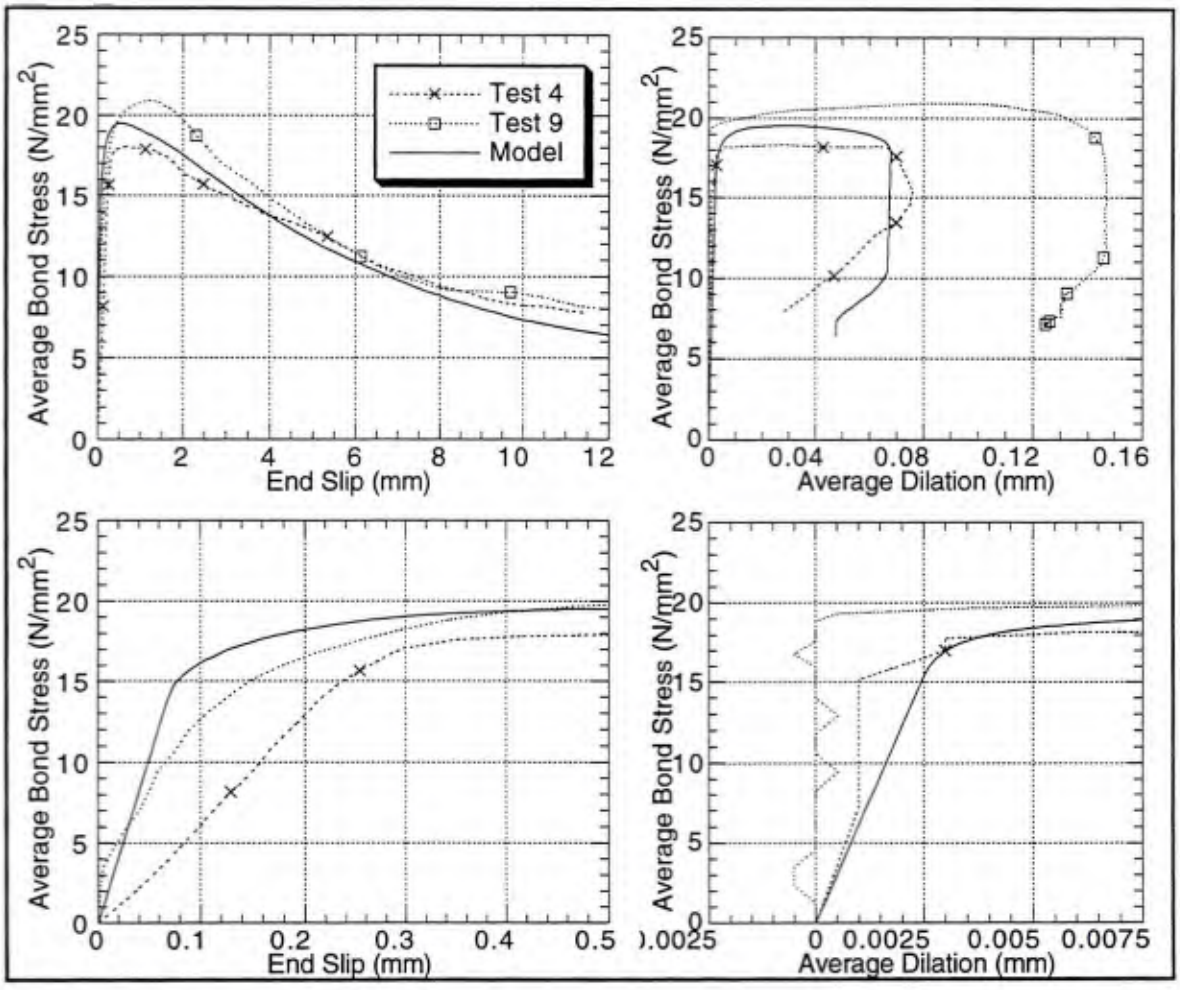

Figure 7.1-6 Calibration results (Malvar) for $\sigma = -24.1$ N/mm^2 (3500 psi).

This effect is more pronounced in the experimental data suggesting the calibration could be improved upon; subsequent results may suggest otherwise.

The two test series differ in maximum bond stress – the series 3 tests typically giving higher values. The magnitude of these differences, though probably attributable to the difference in rib geometry, has essentially treated as a measure of the experimental scatter. The model falls between the experimental results except when σ=–3.45 N/mm^2.

The softening and friction response does not appear to vary significantly with the rib geometry except when σ=–3.45 N/mm^2. Both of these stages of response are accurately represented by the model.

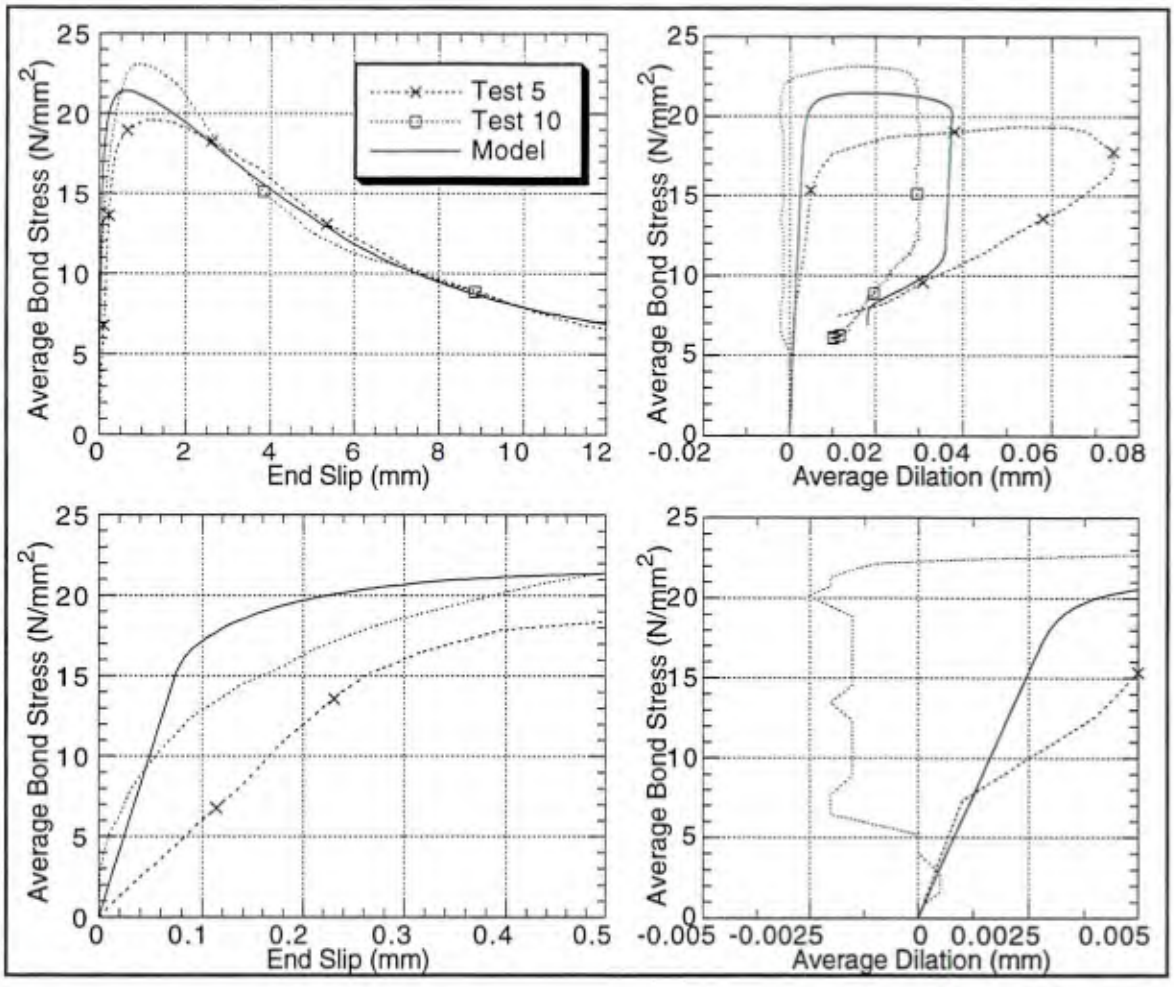

Figure 7.1-7 Calibration results (Malvar) for $\sigma = -31.0$ N/mm^2 (4500 psi).

The bond stress versus average dilation response over the full scale is also very representative of the experimental results. Since the development of the flow rule was based more upon the data of the series 3 tests, the model more closely predicts those test results except for data that were considered invalid (*i.e.*, the radial response of test 9). The shape of the response graphs also closely reflect the response of the series 3 tests; the series 2 tests generally lack the stage of zero dilation that occurs between the radial dilation and contraction. This type of data has significantly more variation between the series of tests than the bond stress versus slip response; the exception is shown in Figure 7.1-5.

The overall calibration is considered adequate considering: 1) the assumptions made in modeling the specimen, 2) the apparent variation in the results with rib geometry and 3) the uncertainty in the experimental scatter.

Axisymmetric Model Results

In this section we examine the response of axisymmetric FEM models of the Malvar bond specimens. In some ways this might be considered as the first set of validation results, but more importantly it shows the significance of the simplifying assumptions made in the model development. In particular, though the stress history does not appear to vary greatly between this model and the point model for low confinement stress, as the confinement stress increases the effect on the results becomes significant .

Figures 7.1-8, 7.1-13 and 7.1-16 present the same four plots as used before (*i.e.*, for the point model) but only for three confinement stresses. In Figure 7.1-8 the additional model response, assuming the specimen is not precracked, is also presented. For the axisymmetric model, the radial displacement of the edge of the specimen (as measured) is presented as well as the average radial displacement of the bond zone.

For the initially uncracked specimen, higher bond stresses are achieved because the tensile hoop stress in the concrete allows higher confinement stresses to develop in the bond layer. This is a direct result of the bond stress on the yield surface increasing monotonically with confinement stress. The longitudinal cracks eventually become unstable and split the specimen causing a drop in the confinement stress and thus in the bond stress too. The elevated confinement stress during the radial dilation stage produces a small reduction in the radial dilation, thus its reduced maximum value.

Measuring the radial dilation at the edge of the specimen has little effect on the overall response, but the initial response is significantly stiffer since the initial radial displacement

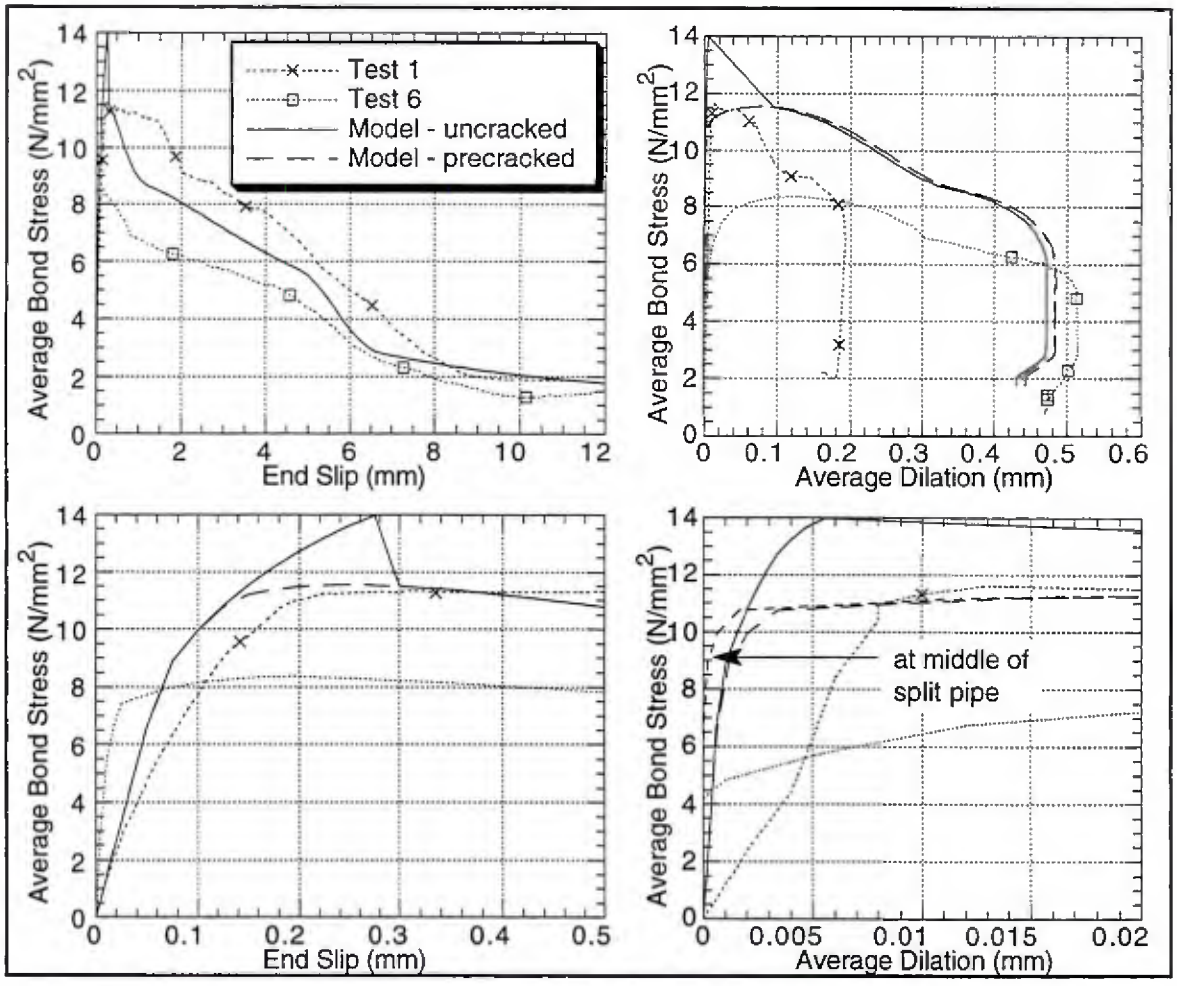

Figure 7.1-8 Axisymmetric model results for Malvar tests with σ=–3.45 N/mm^2 (500 psi).

at the bond zone produces elastic deformation of the concrete cylinder and opens existing cracks.

The effect of the gradient along the bar is apparent in the reduction of the bond stress versus slip stiffness (*cf* the initial response shown in Figure 7.1-3). Figures 7.1-9 through -11 show the model's prediction of the distribution of bond stress, slip and normal stress, respectively, along the length of the bar . The curves represent the model's responses for the first 13 steps after the confinement stress has been applied. The response curves for the first step include xs at each of the interface element Gauss points. Odd and evenly numbered steps are shown as solid and dashed, respectively. The vertical grid lines

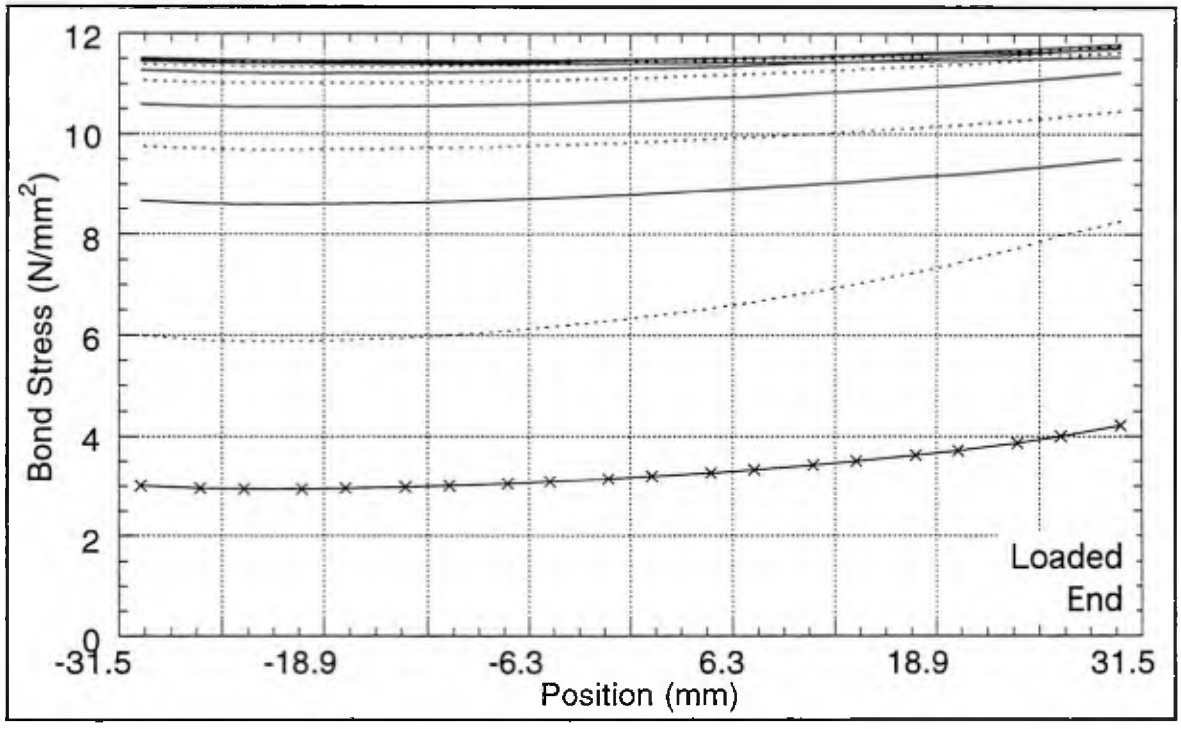

Figure 7.1-9 Model prediction of bond stress distribution along the precracked Malvar specimen – 13 steps with σ=–3.45 N/mm^2 (500 psi).

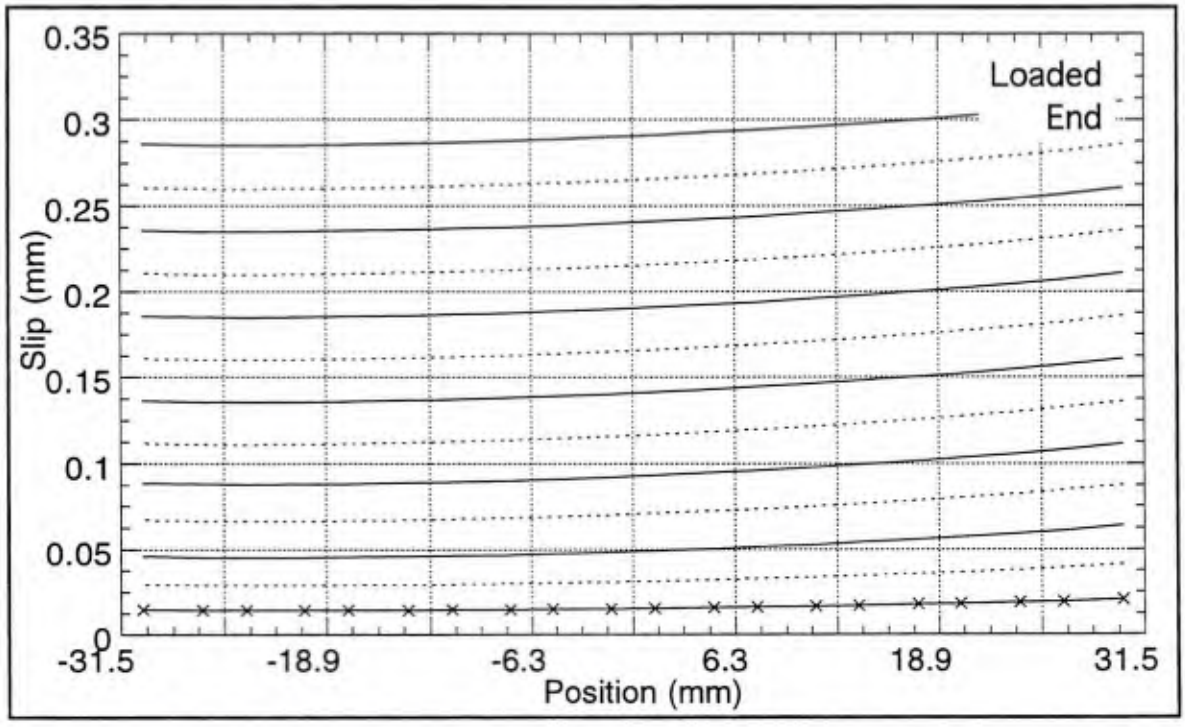

Figure 7.1-10 Model prediction of slip distribution along the precracked Malvar specimen – 13 steps with σ=–3.45 N/mm^2 (500 psi).

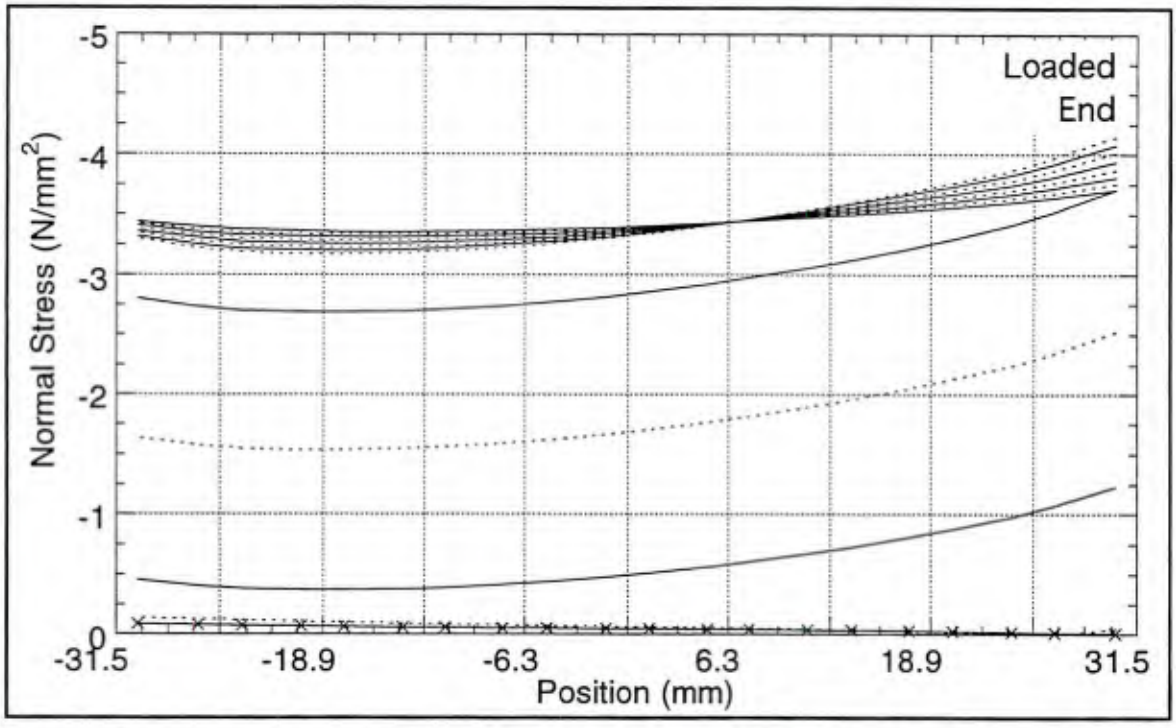

Figure 7.1-11 Model prediction of the normal stress distribution along the precracked Malvar specimen – 13 steps with σ=–3.45 N/mm^2 (500 psi).

occur at nodes on the interface. Response distributions shown here are typical of bond specimens with short embedment lengths.

The response during the first step (end slip = 0.025 mm) is completely elastic. At the end of the second time step (end slip = 0.05 mm) only the Gauss point closest to the loaded end has become plastic. By the end of the third time step (end slip = 0.075 mm) the remainder of the bond zone is exhibiting plastic response.

While the initial gradients in the slip and bond stress along this short bar are not great, the end values differ by about 40 percent. With additional loading the bond zone becomes plastic, and thus the gradients in the bond stress decrease. Continued reduction of the gradient produces a nearly uniform bond stress near the point of maximum bar force. The increase in bond stress (which has a nearly uniform distribution) implies an increase in the gradient in bar strain which suggests an increase in the gradient of the local slip.

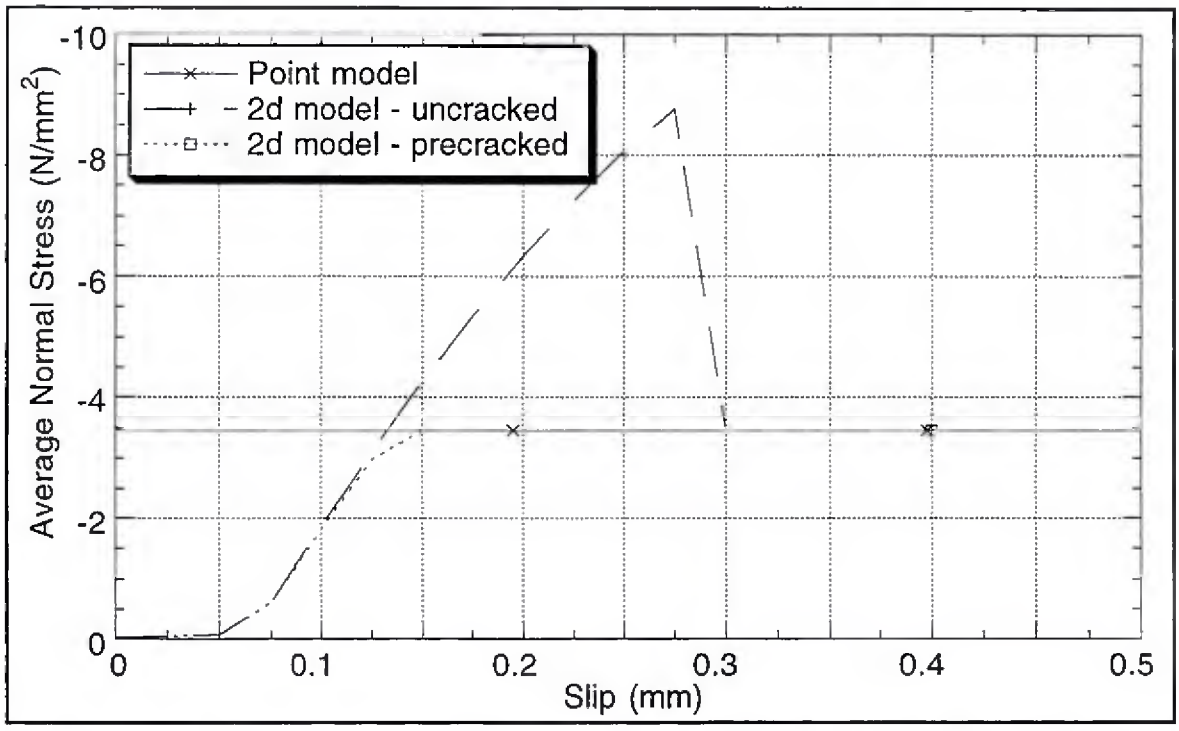

Figure 7.1-12 Comparison of average normal stress values in the bond zone for the different models --σ=-3.45 N/mm^2 (500 psi).

The variation in the normal stress distribution (Figure 7.1-11) has an interesting history. The initial elastic load step causes a rotation about the θ-axis which increases the normal stress near the free end of the specimen. This effect is quickly overshadowed by the plastic dilation which occurs near the loaded end of the bar first and produces relatively high gradients in the normal stress. After a few steps with relatively high gradients, the normal stress redistributes (decreasing near the loaded end and increasing near the free end) and becomes more uniform. This redistribution of the normal stresses is in part due to the lag in plastic slip, and therefore damage, along the length of the bar.

The effect of the axisymmetric model is graphically seen in Figure 7.1-12. The normal stress history at the bond zone is strongly dependent upon the hoop stress the specimen carries. The lack of hoop stress in the point model significantly changes the history because the elastic deformation of the bond zone occurs prior to the bar loading; thus this

negative (*i.e.*, radially inward) deformation is not included in the point model response. For the axisymmetric model, almost all of this elastic radial contraction occurs during the bar loading, and thus the radial dilation of the axisymmetric model (Figure 7.1-8) is less than that of the point model (Figure 7.1-3). Though this effect is not significant at this level of confinement stress, it will be at increased levels of confinement stress.

As an additional check on the radial dilation, the model was unloaded after the specimen split. A permanent end slip of 0.22 mm was obtained which is very close to the values measured for the series 2 tests (Table 3.2-1).

Figure 7.1-13 shows the results of the axisymmetric model for the middle confinement stress of the Malvar test series. The initial bond stress versus slip response now falls between the experimental results. Compared with the point model (Figure 7.1-5), the maximum bond stress has been slightly reduced and occurs at a greater value of slip; the response now more closely follows the results from test 3 over the full range of slip. The most significant difference in the axisymmetric model results is the reduction in the radial dilation. The axisymmetric model gives a maximum radial dilation that is approximately one fourth of the experimental values. The difference between the axisymmetric and point model results can be attributed almost completely to the lack of elastic, radial contraction in the point model. The elastic, radial contraction for this confinement stress is about 0.21 mm.

Figure 7.1-14 shows the average normal stress versus end slip. Under higher confinement stress (*cf* Figure 7.1-12), a greater amount of slip is required to produce the dilation necessary to open the existing splitting cracks. In this case the maximum normal stress and bond stress are attained at nearly the same time.

Figure 7.1-15 addresses the convergence of the numerical results. Two numerical discretizations are used. The "coarse discretization" corresponds to the discretization used

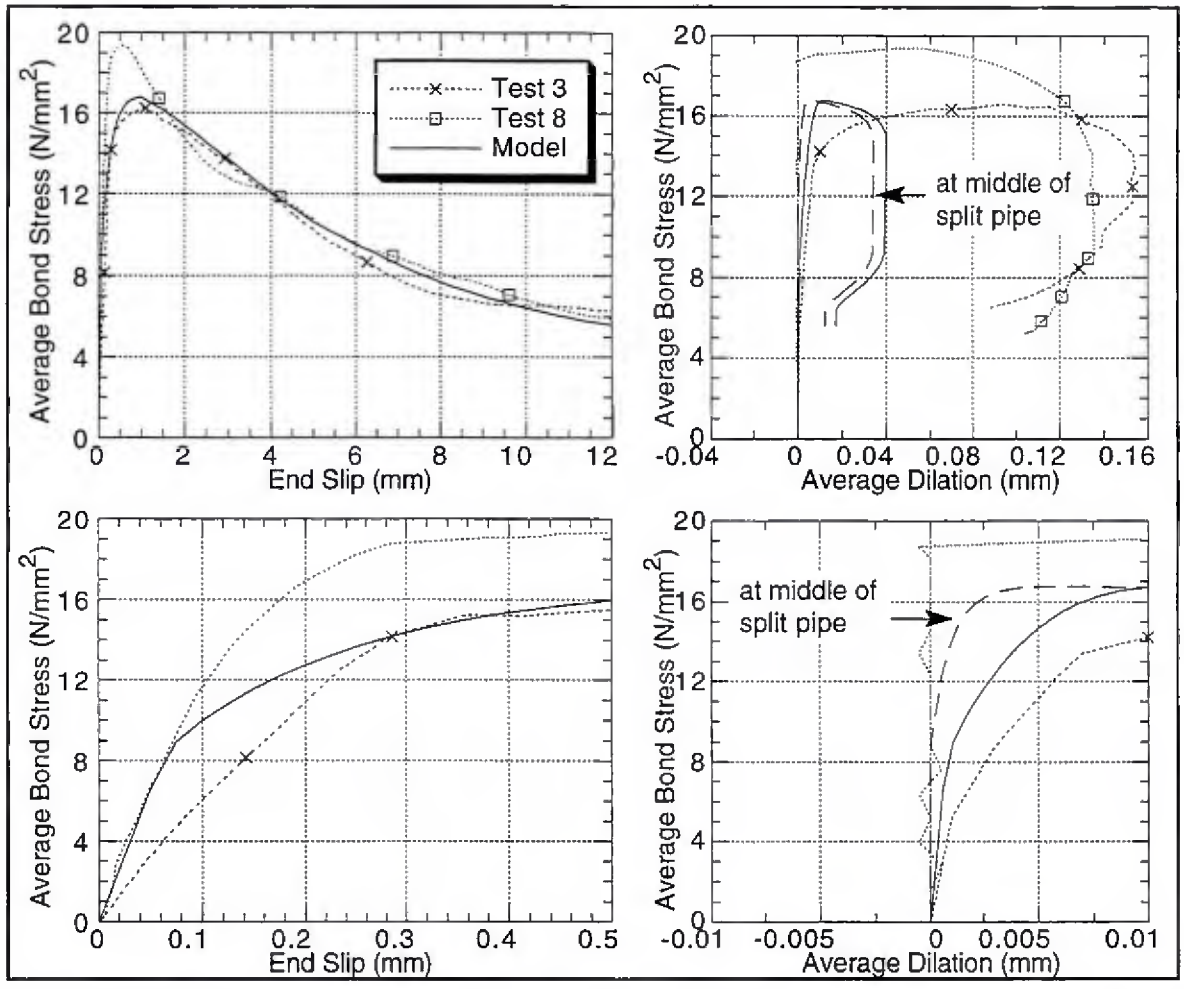

Figure 7.1-13 Axisymmetric model results for Malvar tests with σ=–17.2 N/mm^2 (2500 psi).

for all of the other results presented in this section (Figure 7.1-2 shows the mesh). The "fine discretization" has a mesh with twice as many elements in each coordinate direction and twice as many time steps. Convergence studies were completed for each specimen but are omitted for brevity. Note that the average bond stress versus end slip is indistinguishable for the two discretizations. The maximum radial dilation decreased by about 8 percent with the finer discretization. Though this might appear to reflect a significant lack of convergence in the radial displacement results, one must consider the small magnitude of the model's predictions; the difference between the two numerical predictions is only about 2 percent of the experimental maximum radial dilation.

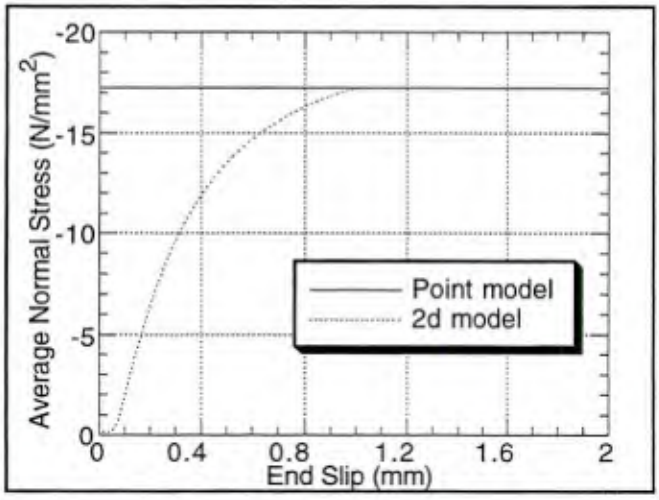

Figure 7.1-14 Comparison of average normal stress in the bond zone for the different models – σ=–17.2 N/mm^2 (2500 psi).

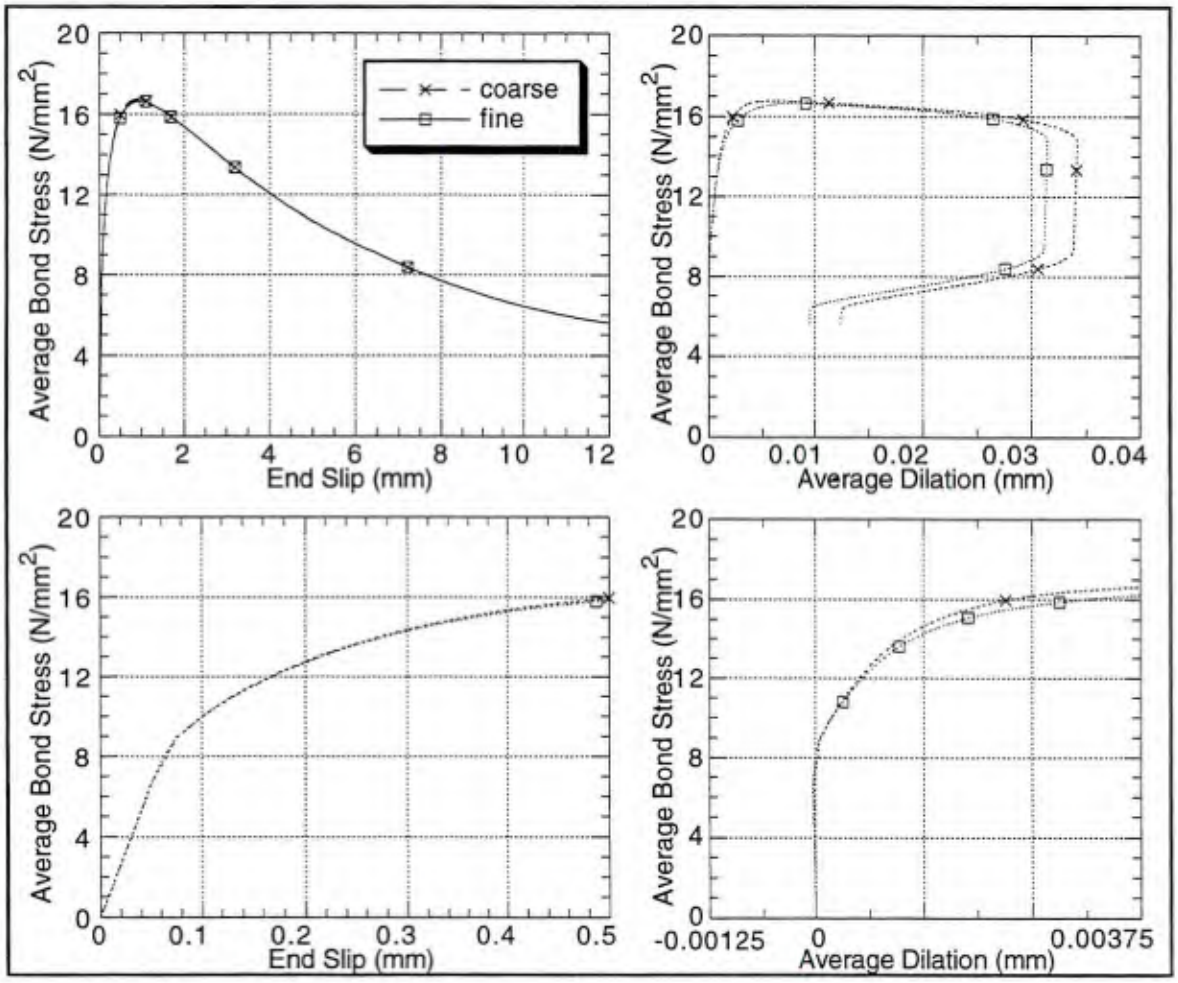

Figure 7.1-15 Convergence test for σ=–17.2 N/mm^2 (2500 psi). The fine mesh has approximately four times as many elements and two times as many time steps.

The change in radial dilation observed in these results is principally due to the integration of the incremental relationship for the plastic dilation. The finer time step size made the integration of g (*cf* Figures 4.3-7 and -8) more accurate. The high gradients near the slope discontinuity in $g(\sigma,d)$ make this function somewhat difficult to integrate. A higher order integration method would help alleviate this difficulty. For this test the bond stress was relatively insensitive to the finer discretization for two obvious reasons: 1) once the cracks opened the confinement stress was not dependent upon the radial dilation; and 2) the quantities C, $\widehat{\sigma}$, and W_e are expressed as explicit functions of d and thus are not as dependent upon the accuracy of the integration.

Figure 7.1-16 shows the axisymmetric model results for the highest applied confinement stress of the Malvar tests. Comparison of these results with those of the point model (Figure 7.1-7) shows the same changes as observed for σ=–17.2 N/mm^2 (2500 psi): 1) the initial stiffness of bond stress versus slip is reduced (an improvement); 2) the maximum bond stress is reduced and the slip at which it occurs increased; and 3) the maximum radial dilation is greatly reduced.

The initial concern is the reduction in the maximum bond stress. The slip value at which this maximum occurs is in better agreement with the experiments using the axisymmetric model, but the maximum bond stress is about 13 percent less than the smallest experimental value (test 5). Though this result is within the objective error range of 20 percent, I expected better agreement on the Malvar tests. Figure 7.1-17 reveals why the bond stress was under predicted; the radial dilation was not only small, it was insufficient to open the existing longitudinal cracks. Therefore the expected normal stress at the bar was never attained. Since the shape of the yield surface is such that the bond stress monotonically decreases with a decrease in the confinement stress, the bond stress is reduced.

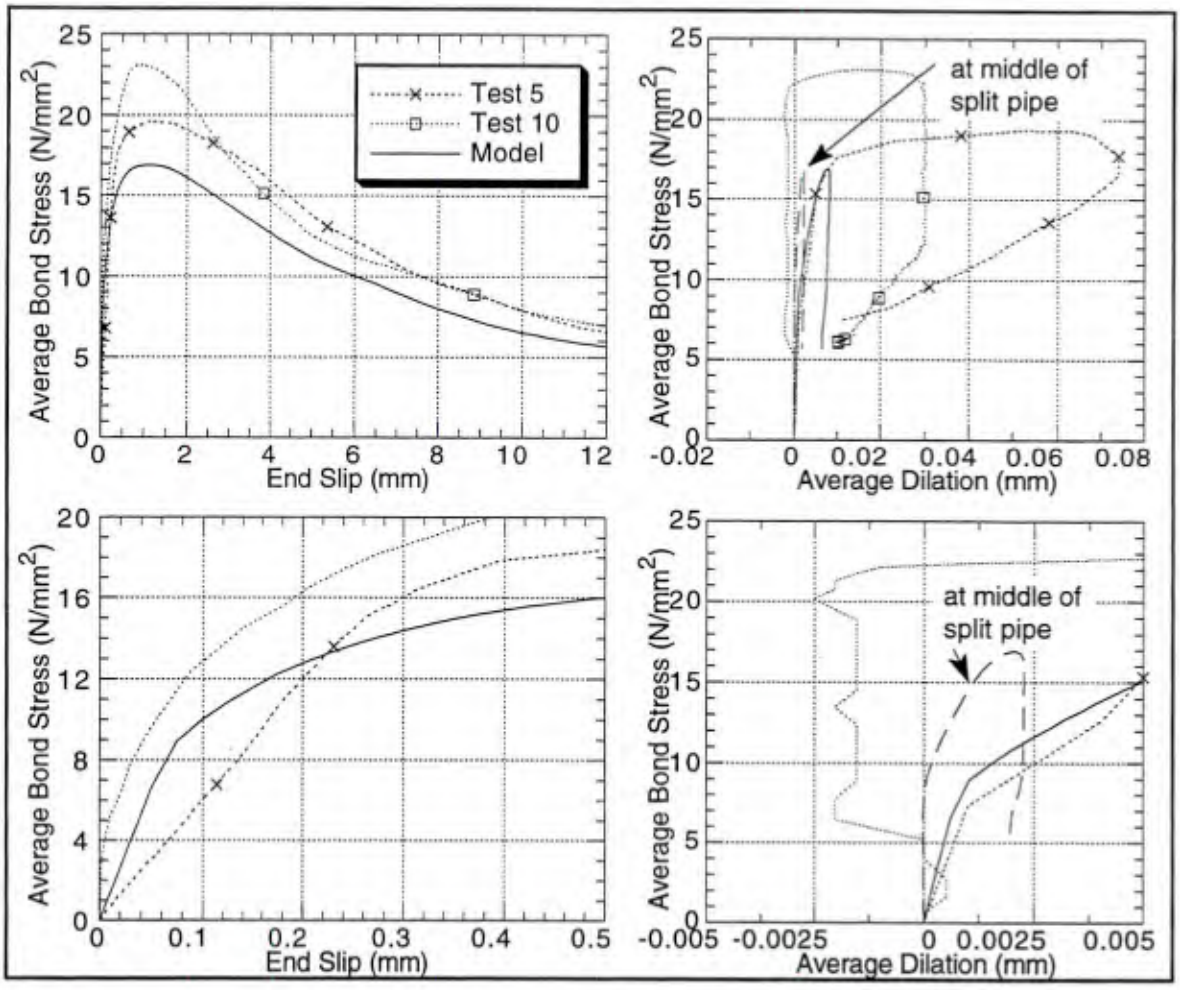

Figure 7.1-16 Axisymmetric model results for Malvar tests with σ=–31.0 N/mm^2 (4500 psi).

For all of the axisymmetric model results, the radial dilation is under predicted due to the difference in the stress and deformation histories of the models. As previously noted, these analyses were completed after all of the validation problems except those of Tepfers and Olsson (1992). These analyses provide additional insight to 1) the interpretation of the experimental data (*i.e.*, assumptions made during the model development), 2) the difficulties in capturing the effect of the *rib-scale mechanics*, and 3) weaknesses in the current calibration.

As discussed above, the error in bond stress versus slip is directly coupled to the radial dilation response. As discussed in the chapters on the model development, both the flow rule and elastic moduli are based upon sparse data. The unloading response in Figure 5.2-4 suggests that the elastic modulus D_{22}^{e} should be dependent upon the stress state (*i.e.*, nonlinear elasticity would be more appropriate) and/or should be dependent upon the history (*i.e.*, elastoplastic coupling should be included). For the sake of simplicity and the lack of pertinent data, the elastic moduli were essentially assumed to remain constant. As discussed in Chapter 5, this simplification might not be sufficient to model the behavior of the underlying contact between the rib and adjacent concrete.

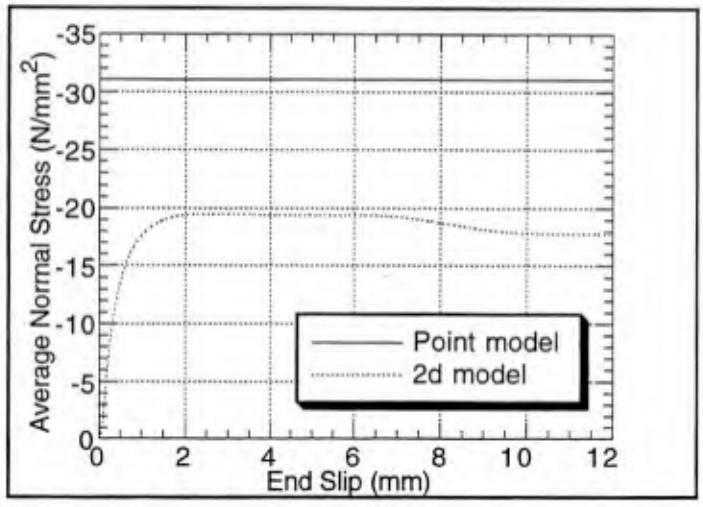

Figure 7.1-17 Comparison of average normal stress in the bond zone for the different models – σ=–30.0 N/mm^2 (4500 psi).

On the other hand, the difference between the axisymmetric model results and the experimental data might simply suggest the calibration could be improved upon. In fact the calibration presented in Herrmann and Cox (1994) gives better results for the maximum radial displacement partly by using a larger elastic modulus. For a compressive normal stress, the radial deformation consists of two components: an elastic radial contraction and a plastic radial dilation. To improve the current radial dilation results, one could decrease the elastic contraction and/or increase the plastic dilation.

A quick attempt to simply increase the plastic dilation to match the experimental results violated the second law of thermodynamics (see Section 4.4); this is because the plastic

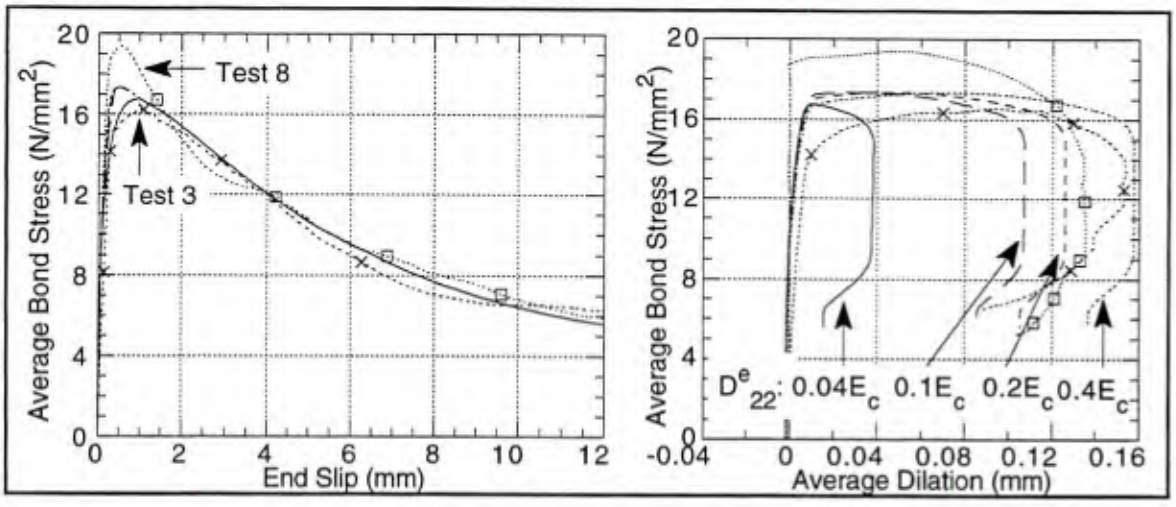

Figure 7.1-18 Parameter study on D^e_{22} with σ=–17.2 N/mm^2 (2500psi). (Experimental results have symbols and are noted in the left graph, and model results do not have symbols and are marked on the right graph.)

dilation had to overcome elastic contractions that increased with the confinement stress, thus requiring plastic dilation to increase with confinement stress. This result suggests that if a constant elastic modulus is to be used it must be larger.

Figure 7.1-18 shows the average bond stress versus slip and radial dilation of the bond zone for four different values of D^e_{22} with σ=–17.2 N/mm^2. For these tests the bond stress is not sensitive to the value of D^e_{22} because the existing longitudinal cracks open in each case and the maximum normal stress is attained. In contrast, the maximum radial dilation is strongly affected by the value of the elastic modulus. These analyses suggest that increasing the elastic modulus could produce excellent agreement between the axisymmetric model and the experimental results. Actually the "ideal calibration" would probably adjust both the elastic modulus and the plastic dilation (*i.e.*, the flow rule).

Clearly the assumptions made during the development of the flow rule: 1) that the radial elastic contraction due to the applied confinement stress is not significant, and 2) the values of $-\sigma$ reported by Malvar represent the normal stress at the bar, may not be accurate. However, these assumptions did allow the data to be analyzed to the extent that allowed a

model and preliminary calibration to be obtained. The resulting bond stresses are reasonably accurate for the axisymmetric model, but the radial dilations appear to be too small at higher confinement stresses.

The under prediction of the radial dilations at high pressure must be kept in perspective. The errors are on the order of 0.1 mm, and the radial dilation is the most difficult quantity to measure. The following validation problems give additional qualitative information on the radial response that will influence future recalibrations; there are probably several calibrations that would reproduce the Malvar results well, but these results combined with the other validation results might provide more insight to the mechanics. Considering the actual chronology of this study, the pragmatic issue was "how can the radial dilation behavior of the axisymmetric model be improved without adversely affecting the accuracy of the other validation problems?" Even with a qualitative understanding of the rib-concrete interaction, additional experiments would be invaluable toward understanding the properties of the damaged concrete near the ribs, especially with respect to response in the normal direction (which has received little attention).

While we are still considering the Malvar specimen, the next subsection digresses to the issue of material instability. Depending on your interest, this subsection can be skipped without any loss in evaluating the effectiveness of the model.

A Numerical Study of the Bond Law Instability

In this section we will examine the two cases where the bond model has the potential for material instability. The first is the case of material softening at which point the bond zone is attributed with being the location of a localization. This case is unstable under stress control. The second case is unique to materials with nonassociative flow rules and has the potential to occur when the stress path traverses the wedge region defined in Figure 2.6-2.

Both of these cases are examined with respect to *instability in the small in the forward sense* (Inequality [2.6-7]).

The simple point model used for the Malvar specimen lends itself to this brief study because I can directly prescribe two of the complimentary generalized stresses or strains. A confinement stress of 17.2 N/mm^2 (2500 psi) is initially applied in examining both potential cases of instability. The elastoplastic moduli considered in this section are calculated by Equation (2.5-4); they are not the algorithmically consistent values that yield quadratic convergence with the Newton-Raphson method. These moduli, and the corresponding eigenvalues, are divided by the bar diameter in the following results. As previously mentioned the actual output of the bond model relates interface stresses to relative displacements ($\underline{\delta}$ not $\underline{q}$), thus the moduli and eigenvalues shown are the values that correspond to the actual implementation.

For the first case, softening in the bond slip response, additional data were examined corresponding to the calibration results shown in Figure 7.1-5. Figure 7.1-19 shows the elastoplastic moduli as a function of average slip. Additional detail in the early response can be found in Figure 7.1-20.

Consider the following observations on the model response:

1. D_{22}, which relates normal stress to radial dilation, remains nearly constant over the full history, so this term is dominated by the elastic contribution of D^e_{22}.
2. D_{11}, which relates shear stress to slip, has a relatively large initial elastic value that rapidly decreases in a monotonic manner during the early plastic response. Relatively early in the softening response it becomes negative and then approaches zero from below as the behavior becomes frictional in nature. The change in the maximum modulus produces an interesting behavior in the spectrum of $\mathbf{D}$ that will be discussed below.

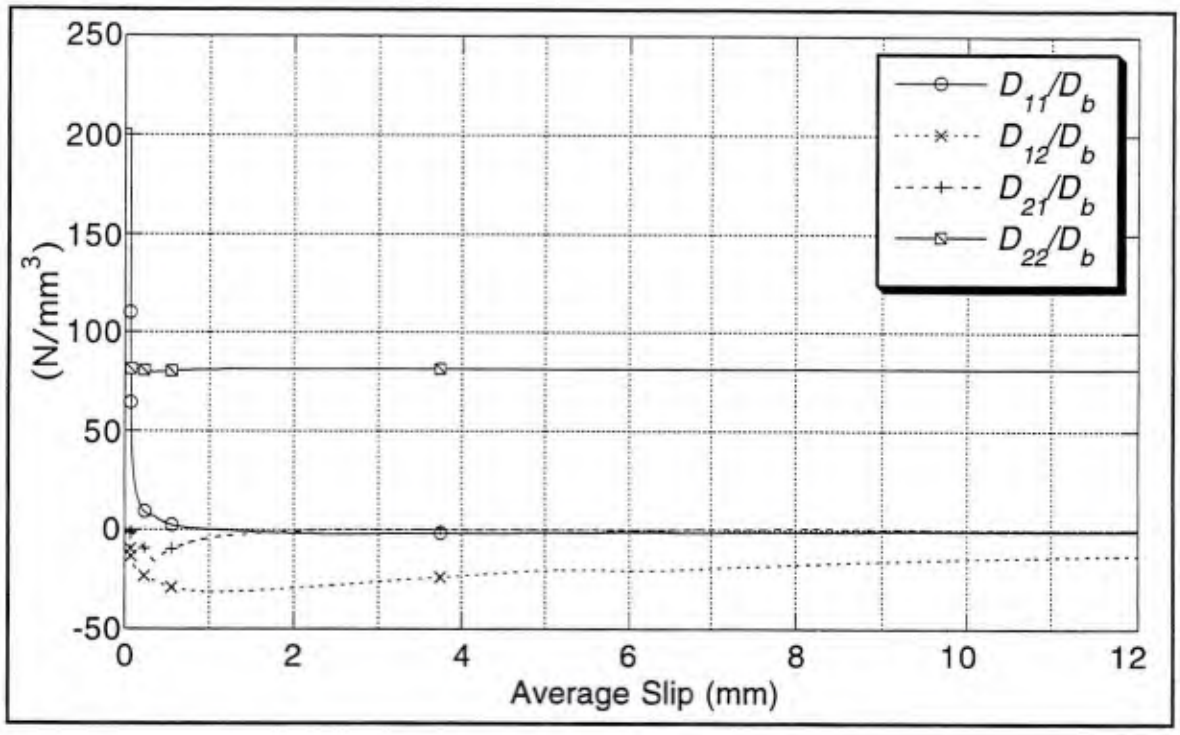

Figure 7.1-19 Elastoplastic moduli as a function of slip for monotonic loading with σ=-17.2 N/mm^2 (2500 psi).

3. The off-diagonal terms (D_{12} and D_{21}) are zero during the application of the confinement stress and then jump to their elastic values. When the plastic response begins the constitutive matrix becomes nonsymmetric (*i.e.*, the off-diagonal terms are no longer equal) due to the nonassociative flow rule.

4. The D_{21} modulus appears to be strongly affected by the form of the flow rule; that is, the variations in g (see for example Figure 4.3-1) are reflected in the graph of this modulus. This modulus decreases to a minimum near a slip of 0.35 mm which corresponds to g attaining its maximum. Physically, at this point the model produces the greatest incremental increase in confinement stress with an increment of slip. With increased slip (though barely perceivable at the scale of Figure 7.1-19) this modulus also reflects the contraction portion of the response shown in Figure 4.3-1; it has a local positive maximum – the point of greatest incremental increase in normal stress with an increment

in slip. As with D_{11} this modulus goes to zero for friction behavior since an incremental slip should not affect the normal stress at this stage.

5. The D_{12} modulus does not appear to be strongly affected by the form of g. It appears to approach a constant nonzero value during the frictional response.

The behavior of both the off-diagonal terms is easily explainable by the form of Equations (2.5-4) and (4.1-1b). The second term in Equation (2.5-4) is a rank one matrix formed by an outer product. If we denote the result of this outer product as **O**, the off-diagonal terms are given by

$$O_{12}=\left(D^e_{11}\mathrm{sgn}(\tau)+D^e_{12}g\right)\left(\phi_{,1}D^e_{12}+\phi_{,2}D^e_{22}\right) \tag{7.1-1a}$$

$$O_{21}=\left(D^e_{21}\mathrm{sgn}(\tau)+D^e_{22}g\right)\left(\phi_{,1}D^e_{11}+\phi_{,2}D^e_{21}\right) \tag{7.1-1b}$$

where the derivatives of the yield criterion (ϕ) are with respect to the generalized stress components. Since the elastic moduli are calibrated to be strongly diagonally dominant the form of the first factors in these equations suggests that g is much more likely to affect D_{21} than D_{12}. Conversely the form of the second factors suggests that the gradient of the yield surface with respect to stress is much more likely to affect D_{12}. than D_{21} . This observation is very apparent when we consider the limiting case of a diagonal elastic stiffness matrix (*i.e.*, the axes of orthotropy align with the normal and tangent directions). For this limiting case the off-diagonal terms are given by

$$O_{12}=\left(D^e_{11}\mathrm{sgn}(\tau)\right)\left(\phi_{,2}D^e_{22}\right) \tag{7.1-2a}$$

$$O_{21}=\left(D^e_{22}g\right)\left(\phi_{,1}D^e_{11}\right). \tag{7.1-2b}$$

This is very close to the case we have with the current calibration because, as shown in Equation (5.2-4), the off-diagonal terms are only 3 percent of the smallest diagonal term. For monotonic loading only one factor varies in each of Equations (7.1-2). In Equation

(7.1-2a) $\phi_{,2}$ varies and is essentially the *instantaneous coefficient of friction*. In Equation (7.1-2b) g varies while $\phi_{,1}$, by Equation (3.3-2), is simply given by $\text{sgn}(\dot{\tau})/f_t$.

As discussed in Chapter 2, *stability in the small in the forward sense* can be examined via the spectrum of $\mathbf{D}^s$ (the symmetric component of $\mathbf{D}$). With the special problem considered here, after the confinement stress has been applied $\dot{\sigma}=0$ and $\dot{\delta}_t\neq 0$. Thus for this problem *instability in the small in the forward sense* occurs just after $\dot{\tau}=0$, or equivalently the incremental generalized strain is an eigenvector of the elastoplastic moduli corresponding to a zero eigenvalue. So the spectrum of $\mathbf{D}$, instead of its symmetric component, can be examined in this case.

Figure 7.1-21 presents the spectrum of $\mathbf{D}/D_b$, the plastic modulus (K^p), and a numerical approximation to the second order work term $\dot{\sigma}_{ij}\dot{\varepsilon}_{ij}$ (*i.e.*, $\dot{\underline{Q}}^T\dot{\underline{q}}$ for the bond model). For this particular problem the eigenvalues of $\mathbf{D}$ are real, and λ_1, K^p and $\dot{\underline{Q}}^T\dot{\underline{q}}$ all become zero simultaneously. The constraint of a constant confinement stress in this case causes the plastic modulus and bond stress to have the same sign (*i.e.*, when K^p becomes negative τ decreases). In addition, this constraint and prescribed positive increments in slip result in the sign of the second order work to be completely determined by the sign of the bond stress.

In general the second order plastic work can remain positive after the plastic modulus becomes negative; a simple case for which this occurs can be easily visualized. Consider a point on the yield surface where the yield surface is closing (*i.e.*, moving toward the σ-axis) and thus K^p is negative. By increasing both the bond stress and confinement stress (decreasing σ), one can define a path in stress space that produces plastic loading and a positive second order work.

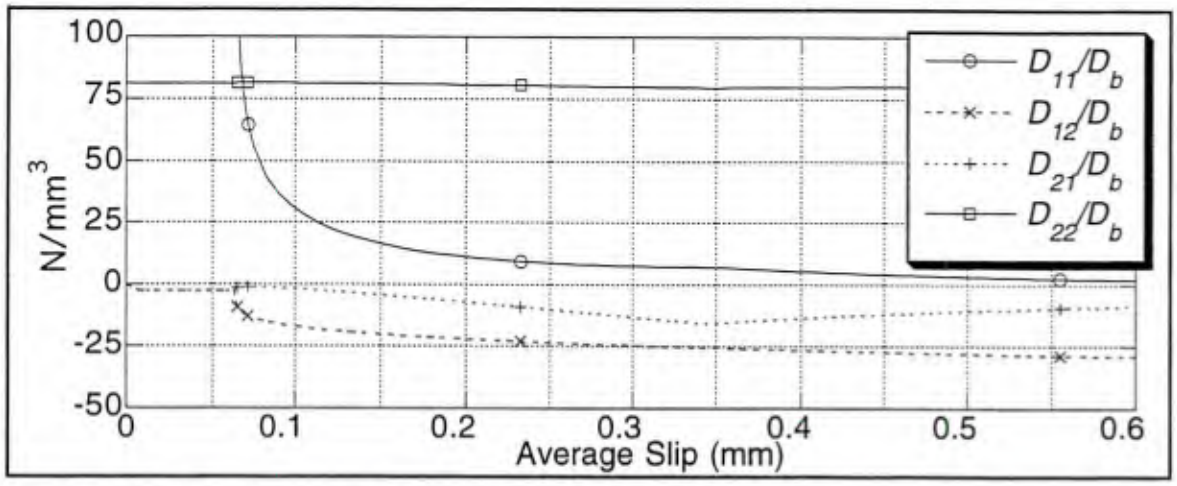

Figure 7.1-20 Softening analysis – elastoplastic moduli *vs* slip.

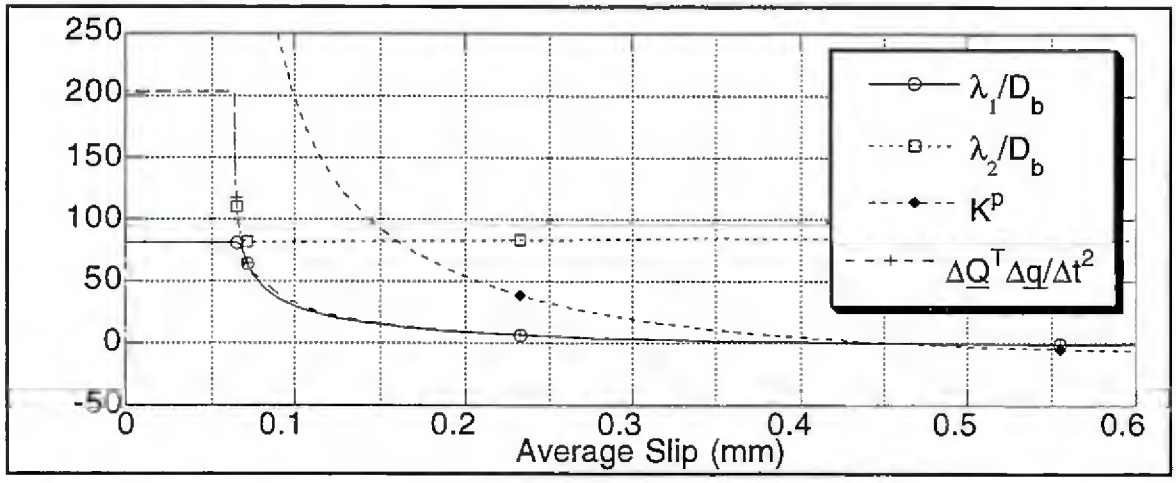

Figure 7.1-21 Softening analysis – $\lambda(\mathbf{D}/D_b)$, K^p, and second order plastic work *vs* slip.

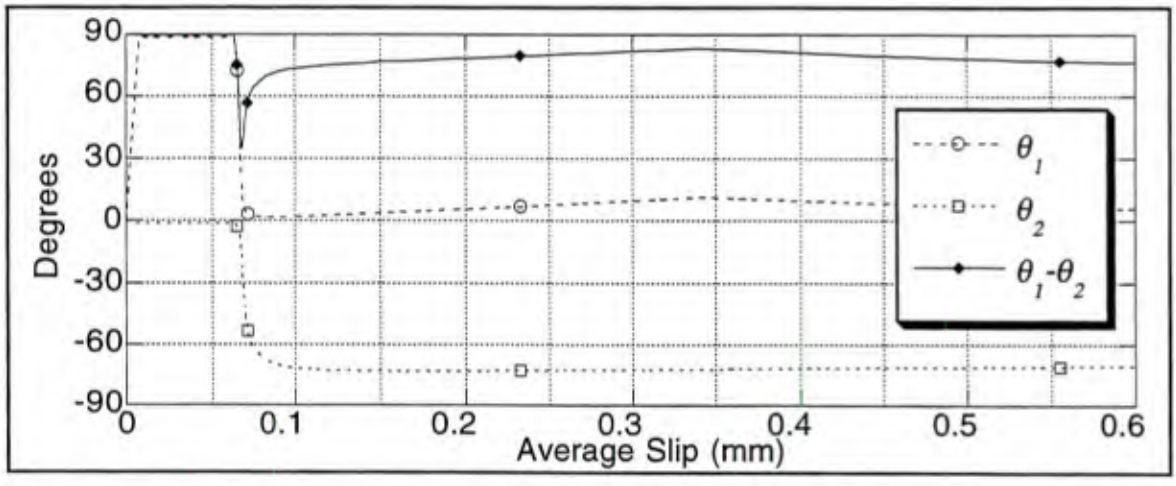

Figure 7.1-22 Softening analysis – eigenvector directions and relative angle *vs* slip.

During elastic loading, the elastoplastic moduli are symmetric and thus the eigenvalues are real and the eigenvectors are orthogonal (see Figure 7.1-22). The diagonal dominance of the constitutive matrix is reflected in the directions of the eigenvectors which are nearly in the normal (90 degrees) and tangent (0 degrees) directions; in addition the eigenvalues nearly correspond to the diagonal terms in the constitutive matrix. The positive definiteness of the elastic moduli requires both eigenvalues to also be positive.

In developing the model, the form of the yield surface was defined to give continuous elastoplastic moduli and thus C^1 continuity in the generalized stress versus strain responses. This was accomplished by defining C and σ_o such that K^p would be infinite when plasticity initiates for the first time. The form of Equation (2.5-4) (with K^p in the denominator of the second term) is such that the rapid decrease in K^p produces a rapid decrease in D_{11} and thus in the corresponding eigenvalue $-\lambda_2$ initially.

When D_{11} approaches D_{22} the right eigenvectors achieve a relative angle as small as 35 degrees while "spinning to trade roles;" for example, the eigenvector with the largest component in the tangent direction rotates to a direction with its largest component in the normal direction and visa versa. While in Figure 7.1-21 it appears there might have been an eigenvalue of multiplicity two, Figure 7.1-23 shows that upon closer examination the eigenvalues remain distinct. The eigenvalues of **D** are given by

$$\lambda_{1,2}=\frac{D_{11}+D_{22}\pm\sqrt{(D_{11}-D_{22})^2+4D_{12}D_{21}}}{2}. \qquad (7.1\text{-}3)$$

While I initially suspected the behavior was a manifestation of the numerical approximations, convergence studies have not confirmed this suspicion. The argument of the radical in Equation (7.1-3) must go to zero for an eigenvalue of multiplicity two to exist. The results shown in Figure 7.1-23 used 100 time steps between slips 0.06 mm and 0.075 mm; in this particular analysis the argument to the radical varied from about 14,800 to a low of about 50. With a time step two and a half times larger, the lower bound on the

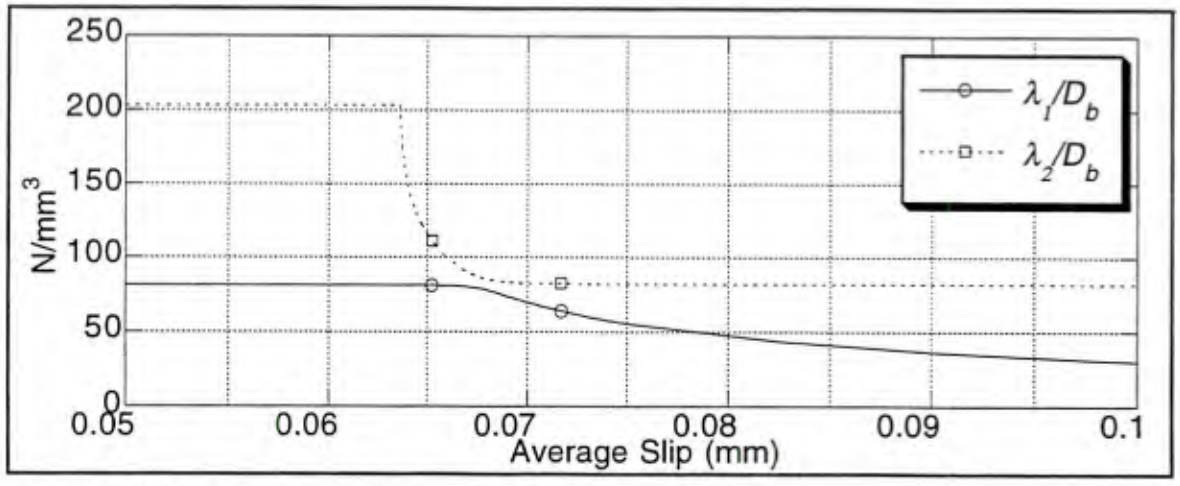

Figure 7.1-23 Softening analysis – a closer look at $\lambda(\mathbf{D}/D_b)$.

argument was less than 1 percent larger. Thus considering that double precision was used in all the calculations, the eigenvalues do not appear to be converging to "numerically equal values."

Since the confinement stress is held constant the second order plastic work is determined by the bond stress-slip product alone. Thus the graph of the second order work versus slip is nearly equal to the eigenvalue associated with the tangent direction – initially λ_2 and later λ_1.

The history of the smallest eigenvalue indicates that with continued slip (and therefore damage), eventually a state is reached where an increment in generalized strains could produce a decrement in generalized stresses (*i.e.*, a negative eigenvalue exists). A negative second order plastic work indicates the actual path has a direction "close to" the corresponding eigenvector which is also reflected in the negative value of D_{11}.

In the case of softening, *instability in the small in the forward sense* accurately represents a physical instability that can occur in the system; a localization occurs in the bond region for which the model is designed to represent. Under displacement control both the physical system and the model remain stable, but the material instability (a potential source for

system instability under different boundary conditions) is apparent in both the second order work and the spectrum of **D**. Under general boundary conditions the spectrum of $\mathbf{D}^s$ must be examined instead.

The second case for which material stability will be examined is unique to material models with a nonassociative flow rule – typical of frictional materials. For materials of this type, there is the potential for material stability even during hardening when the stress path traverses the wedge region (see Figure 2.6-2).

The wedge path requires a stress history where, from a plastic state, both the confinement and bond stresses are reduced. Figure 7.1-24 shows several paths in stress space which remain in the wedge path for a finite portion of the history. All of the stress histories begin at a zero stress. The confinement stress is then applied to a level of 17.2 N/mm^2. This is followed by an increase in the bond stress from 0 to 15 N/mm^2 where plasticity initiates just below τ=13 N/mm^2. During this hardening phase both the second order plastic and total work remain positive. From this state several straight paths in stress space are followed to examine the behavior in the wedge region. In the wedge region, by definition, the second order plastic work is negative.

Paths a, b and c pass below the tangent to the yield surface and thus elastic unloading occurs until they intersect the yield surface later in their histories; the sequence of paths come progressively closer to the yield surface tangent and thus the length of the elastic response decreases. Paths e and d pass above the initial yield surface tangent and thus exhibit plastic behavior over their full range. Each of the paths traverse the wedge region (bounded by triangles and denoted by a solid line) for part of their history. Paths a, b and c are longer, and thus their departure (*i.e.*, the point where the second order plastic work becomes positive) from the wedge region is apparent. In addition the angle of incidence (relative to the tangent to the yield surface) increases from path c down to path a which reduces the "time" spent in the wedge region.

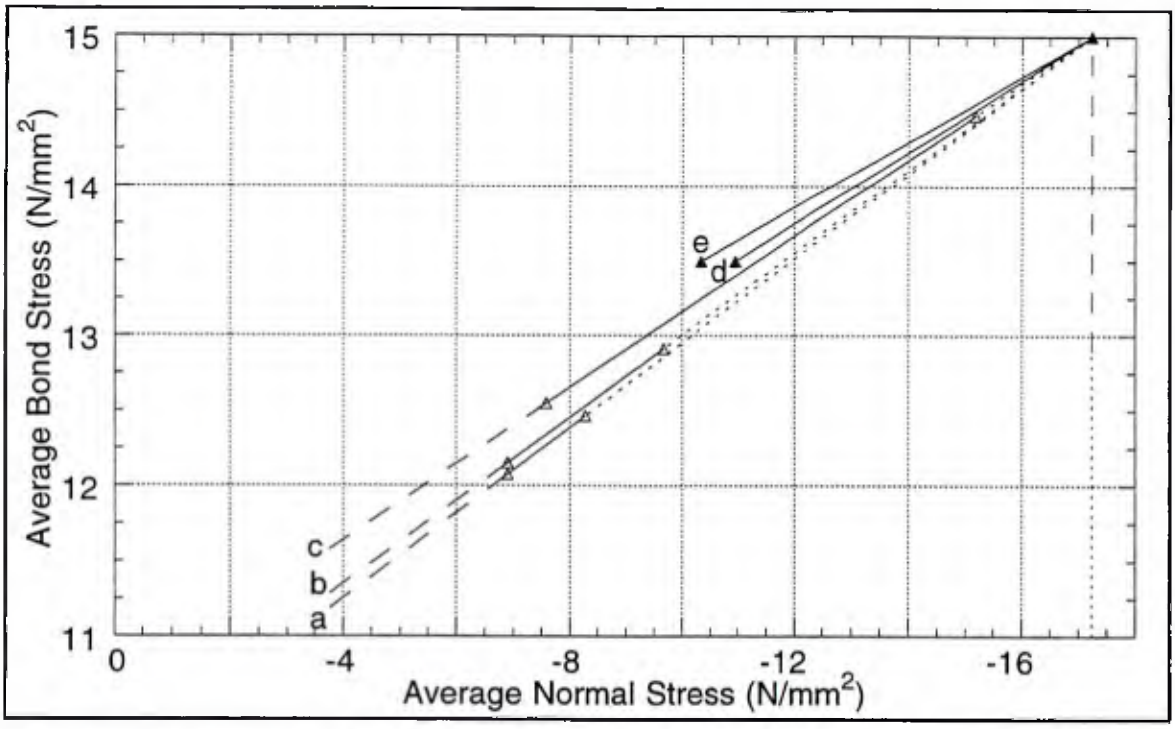

Figure 7.1-24 Examples of stress paths which traverse the "wedge region" for part of their history. Small dashes denote elastic loading or unloading; large dashes denote plastic response where $\dot{\underline{Q}} \cdot \dot{\underline{q}}^p > 0$; and the solid lines denote plastic responses where $\dot{\underline{Q}} \cdot \dot{\underline{q}}^p < 0$ – a wedge path.

For all of the stress path segments through the wedge region, the second order work remained positive despite the second order plastic work component; that is, the elastic component was sufficient to maintain material stability. Figure 7.1-25 shows the smallest eigenvalue of $\mathbf{D}^s/D_b$ for the different stress paths. While all of the eigenvalues decrease, for the wedge path segment of the history, none of them become negative, thus *stability in the small in the forward sense* is maintained.

At first glance one might conclude that path c comes close to exhibiting instability during hardening since it appears its eigenvalue is approaching zero. However, the bound of the wedge path segment is not shown in this figure for the paths. As the softening example, the eigenvalues start at their elastic values and then decrease during hardening. The eigenvalues for the three paths that exhibit elastic unloading jump to their elastic values and

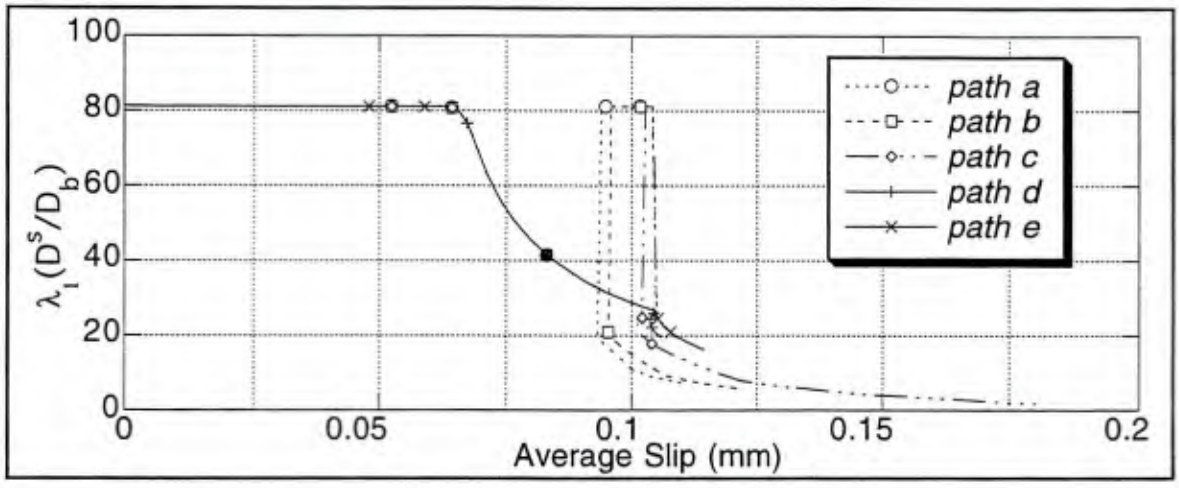

Figure 7.1-25 Smallest eigenvalue histories of all paths that traverse the wedge region.

then jump back to a smaller value upon subsequent plastic response (in the wedge region). For paths a and b the second order plastic work is positive just prior to slipping to 0.1 mm; for path c this occurs at a slip of about 0.11 mm. Thus it is clear the eigenvalue for path c is approaching zero as it nears the softening response.

Path d is closest to the tangent to the yield surface and thus has the largest magnitude of negative second order plastic work. It follows that this path gives the greatest decrease in the eigenvalue with respect to slip. In fact initially the total slip decreases (due to a reduction in the elastic slip) while the plastic slip increases. If a curved path in stress space were taken that was continuously just inside the tangent to the yield surface, then it might be possible to achieve the case of instability during hardening. It's not clear that this would occur prior to eliminating the normal stress. Certainly the example paths shown here do not constitute a proof of stability during hardening, but they do reflect that under many cases the wedge path can be traversed without encountering material instability. Certainly if the wedge path were attempted after additional hardening occurred it might be more likely that the instability during hardening could be encountered. However, if the instability is only going to be encountered at an "epsilon away from" the softening response, it seems to be a mute issue for this model.

In an earlier subsection, I noted that further calibration work might be needed to better match experimental results. If the elastic moduli are increased (particularly the diagonal terms), the potential for instability in the wedge region increases as there will be a smaller elastic component to stabilize the response.

Whether this potential instability will pose any problem when the model is used in general applications remains to be determined. A stress path that could produce this instability is conceivable. As an example, consider a reinforcing bar of building's floor beam, in particular the section of the bar embedded in a beam-column connection. As the building responds to a dynamic event the stress path, in the bond zone of the bar, could easily traverse the wedge region as the axial and flexural loads in the "column" change.

7.2 Gambarova, Rosati and Zasso Experiments

These experiments apparently grew out of earlier efforts to measure aggregate interlock behavior as a function of crack opening (Bazant and Gambarova [1980]). The general methodology of these experiments has been discussed in Section 3.2. As with much experimental bond data, there is no measure of experimental scatter presented with the results of these tests.

In this study only the phase C test with a prescribed crack opening of zero is considered. In Herrmann and Cox (1994), where a different isotropic hardening law is presented, the model is compared to all the phase C tests with a range of crack openings.

For the case of a closed crack, the initial conditions (for a model) are relatively clear; for the case of an open crack the initial conditions are very subjective since the bond model treats the mechanical interaction in a phenomenological manner. The tests with nonzero crack openings are unlikely to have a physical analog in a real structure because the splitting cracks in a real structure are due in part to the wedging action of the ribs. Thus the existence of the crack implies the bond zone is in a damaged state – not the virgin state of the tests.*

The following subsections present 1) the specimen models used, 2) model validation results for the point models, and 3) model validation results for the two-dimensional FEM model. The material properties for all the models of this specimen are given in Table 7-2.

* Though the tests with a nonzero crack opening introduce special modeling difficulties, they also provide very useful data on the upper bound of bond strength as a function of crack opening.

Specimen Models

A few different models of the specimen were considered. Three point models were employed with various idealizations of the bar. A two-dimensional FEM model was also developed; it directly addresses the control of the crack opening but still contains many simplifying assumptions in modeling the behavior of the specimen.

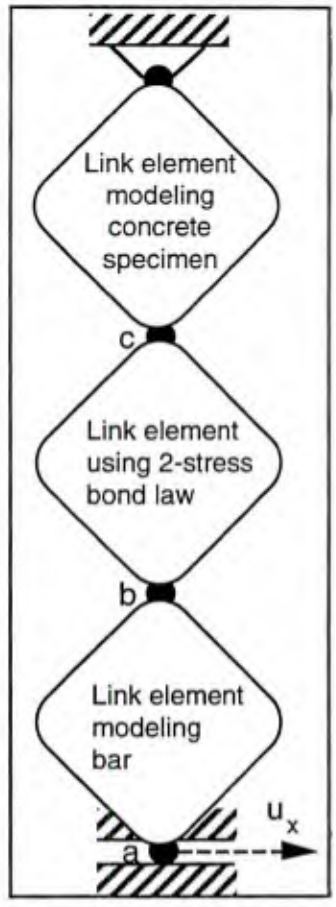

Figure 7.2-1 Point model of the Gambarova specimen.

A schematic of the more complicated point models is presented in Figure 7.2-1. Three link elements are used to model the specimen. The first link element represents the response of the bar. It uses the simple two-stress rebar element presented in Appendix E. The second link element uses the bond model to represent the response of the entire bond zone (assuming uniform stresses in the bond zone), and the last link element represents the response of the remaining concrete. The remaining concrete is treated as a block of concrete (dimensions given in Table 7-2) under uniform shear and compression stress. Thus the response of this link element can be expressed as two "one-dimensional laws" as

$$\tau = \left(\frac{2LWG_c}{D_b L_b H \pi}\right)\delta_t \quad \text{and} \quad \sigma = \left(\frac{LWE_c}{D_b L_b H}\right)\delta_n \tag{7.2-1}$$

where L, W, and H ~ dimensions of the specimen,

E_c and G_c ~ denote the Young's and shear modulus of the concrete respectively,

and L_b~ embedded or bonded length of the bar.

The slip for the three-link model was the prescribed horizontal displacement at point *a* less the horizontal displacement at point *c*. The contribution of axial bar strain to the end slip is over predicted by the rebar link element because the end slip is measured at the free end. The differences in the three point models are summarized in Table 7.2-1. Model 2 uses the actual core diameter of the bar whereas the other two models use the nominal bar diameter. Model 3 omits the bar link and thus completely incorporates the rigid bar assumption. Figure 7.2-1 explicitly shows that the crack opening displacement is not controlled in these point models.

Table 7.2-1 Differences between the three point models for Gambarova *et al.* (1989)

Model	D_b (mm)	Number of Links
1	18	3
2	17.3	3
3	18	2

Figure 7.2-2 shows the two-dimensional finite element model of the specimen. The series A tests of Gambarova *et al.* (1989) used a thinner specimen which developed in-plane splitting cracks from the wedging action of the ribs. Even with the thicker specimen of the series C tests, it is unlikely that the out of plane stresses are trivial. Considering the width of the specimen is more than six times the diameter of the bar and that the stress gradient is high near the bar, the assumption of a plane stress state is a crude approximation. This specimen in many ways deserves a three-dimensional model. If we assume that most of the response is due to the behavior of the bond zone then our expectations for the specimen model are less. In this case, the two-dimensional model does allow us to treat the crack opening boundary condition by monitoring opening at the same points considered in the experiment. In addition gradients along the length of the bar are included (though their contribution is of second order for this specimen).

The specimen model is comprised of two layers. The first layer (at the bottom of Figure 7.2-2) includes the bar and the bond zone elements. The second layer consists of elements

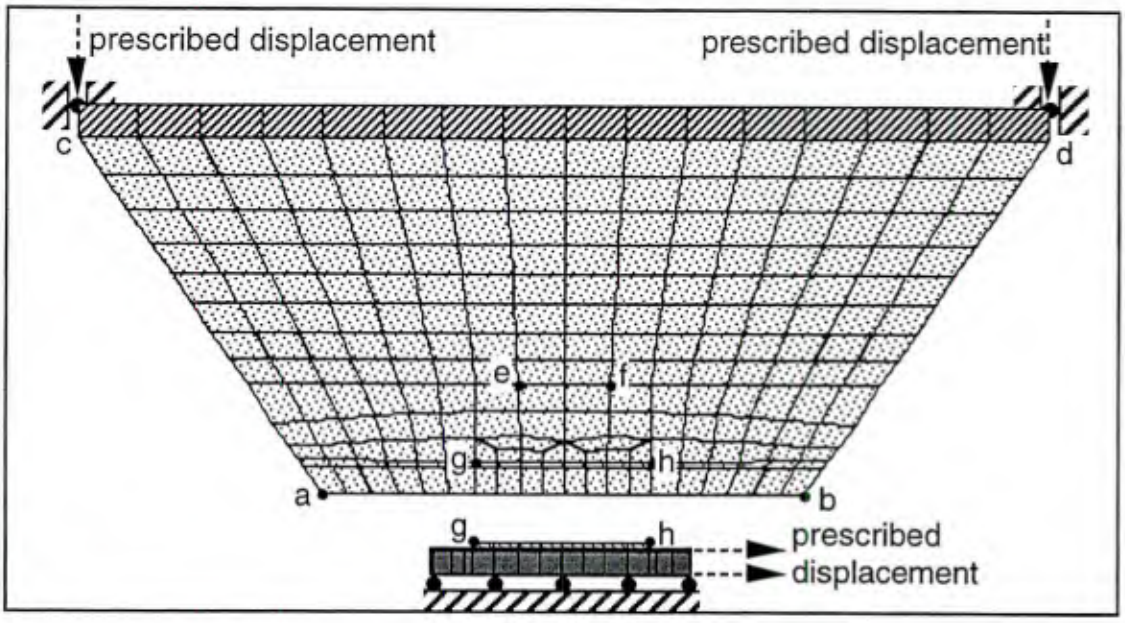

Figure 7.2-2 Two-dimensional model of the Gambarova *et al.* (1989) specimen.

to model the remainder of the specimen, including a top region that is assumed to be essentially rigid (20 mm thick of steel). The layers are attached along the line *g-h*.

In the experiments the crack opening was monitored with mechanical gages at points *a* and *b*. The crack opening was maintained at its prescribed value (with a tolerance of 0.01 mm) by mechanically adjusting the prescribed displacements at points *c* and *d*. The rate of loading was approximately 0.05 mm/hr, and each test required approximately 5 days to complete. The end slip was measured by a mechanical gage attached to the end of the bar and a bracket attached to points *e* and *f*.

In the two-dimensional analysis, the end slip was taken to be the displacement of the free end of the bar relative to point *e* (a point where the displacement transducer is connected). The zero crack opening condition was satisfied by successive improvement of the displacement boundary conditions at points *c* and *d*. This was accomplished by running the analysis code within a shell that adjusted the boundary conditions for each successive analysis by the formulas

$$u_c^r(t)=u_c^{r-1}(t)-u_a^{r-1}(t) \quad \text{and} \quad u_d^r(t)=u_d^{r-1}(t)-u_b^{r-1}(t) \tag{7.2-2}$$

where the r denotes the analysis or run number and the subscripts denote the points. The prescribed displacements were taken to be zero for the first analysis. After two iterations (*i.e.*, analyses) the experimental tolerance was achieved, and after five iterations points a and b never translated vertically more than 0.00033 mm over the whole history.

For the kinematics of this specimen to be reproduced "correctly" the round bar is replaced with an orthotropic square bar. The cross-sectional area of the bar and axial stress differ with the round bar, but the transverse strain, longitudinal strain, axial force and normal stress are preserved. An assumption on the out of plane normal force is required to maintain symmetry in the elastic moduli (a requirement in the current implementation of orthotropic elasticity in Geneseos).

The development of the equivalent orthotropic properties is outlined here for brevity. A round subscript explicitly denotes quantities related to the round bar. Isotropic material constants and orthotropic material constants correspond to the round and square bars, respectively. Let $\sigma_{zo}=n\sigma_{yo}$ where $n\in[0,1]$ (*i.e.*, the out of plane normal stress is an unspecified fraction of the vertical normal stress). Equating axial strains in the bars and noting that the vertical and horizontal forces are independent, we obtain

$$E_x=\frac{\pi}{4}E \quad \text{and} \quad \nu_{yx}=\frac{(1+n)E_y}{E}\nu. \tag{7.2-3a,b}$$

In a similar manner, equating the vertical extensional strain in the bars gives

$$E_y=\frac{E}{(1-n\nu)} \quad \text{and} \quad \nu_{xy}=\nu. \tag{7.2-4a,b}$$

Assuming that an elastic potential function exists (for the sake of not changing another material law) implies symmetry in the elastic moduli (*i.e.*, $\nu_{yx}/E_y=\nu_{xy}/E_x$) which gives

$$n=\frac{4}{\pi}-1. \tag{7.2-5}$$

(*i.e.*, $\sigma_{zo}\approx 0.27\sigma_{yo}$). The first two point models assume $n=1$, but the Poisson effect is secondary in short embedment length bars since the bar strains are typically small.

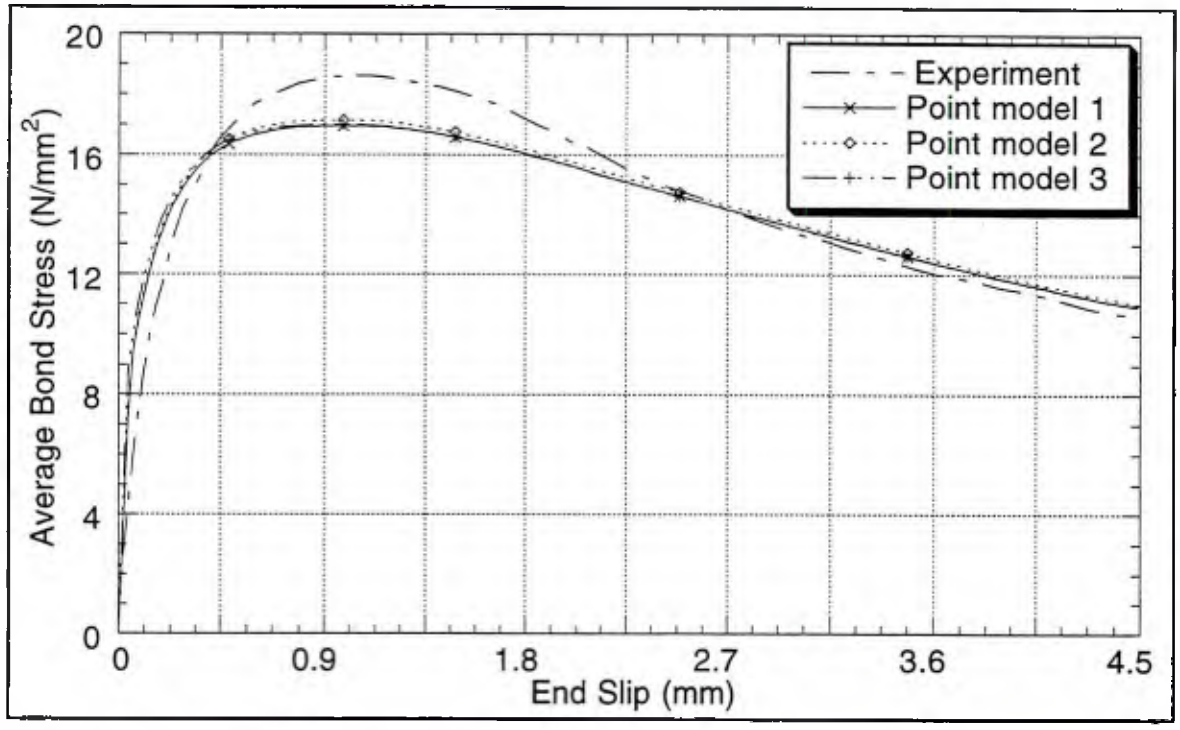

Figure 7.2-3 Average bond stress versus "end slip"* for various point models of the Gambarova *et al.* (1989) test with a zero crack opening.

Point Model Results

Figure 7.2-3 compares the point model and experimental responses for bond stress versus end slip. Compared to their variation from the experimental results, the point models give nearly identical response. Point model 3, having only two links, is slightly more stiff initially than the other two models since the strain in the bar does not contribute to its end slip. The use of the actual versus nominal bar diameter also has an insignificant effect on the response.

Over the full range of slip the model compares well with the experimental results. The initial elastic stiffness is over predicted by the model and the maximum bond stress is

* For models 1 and 2 the slip is an approximation to the slip at the loaded end of the bar since it includes the effect of bar extension from the mid-point to the load. For model 3 the bar is essentially rigid.

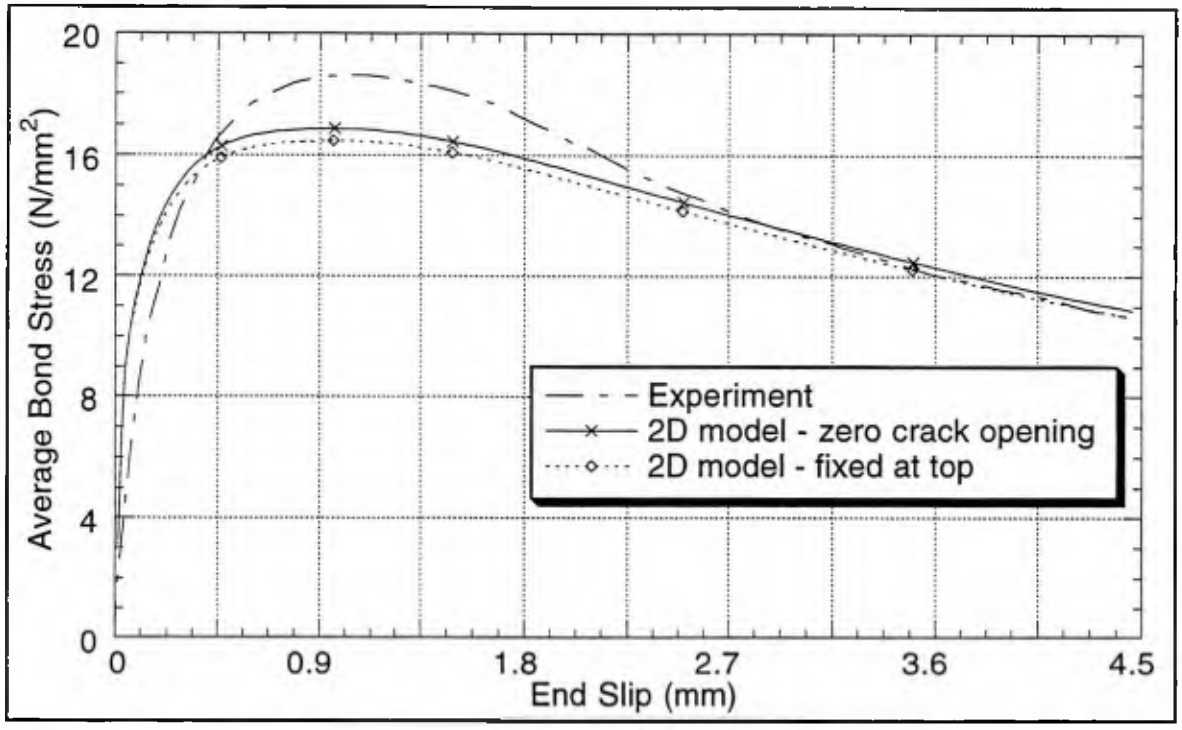

Figure 7.2-4 Average bond stress versus end slip for the two-dimensional models of the Gambarova *et al.* (1989) test with a zero crack opening.

underestimated by about 9 percent. The slip at which the maximum bond stress occurs appears to be very accurate. Softening is also predicted very accurately by the model.

Two-Dimensional Model Results

Figure 7.2-4 compares the two-dimensional model and experimental responses for bond stress versus end slip. The case of the specimen fixed at the top represents the results of the first iteration in the analysis where the boundary conditions are successively corrected to eliminate the crack opening. Maintaining the zero crack opening increases the normal stress at the bar and thus slightly increases the bond stress response. This small difference does not occur until plastic dilation begins.

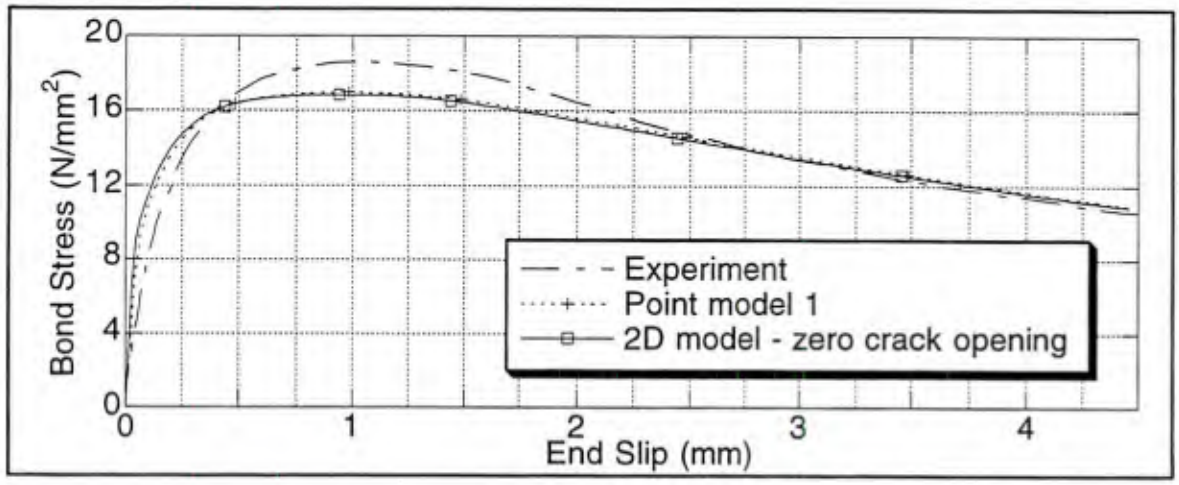

Figure 7.2-5 Average bond stress versus end slip for the Gambarova *et al.* (1989) test with a zero crack opening – comparison of the point and two-dimensional models.

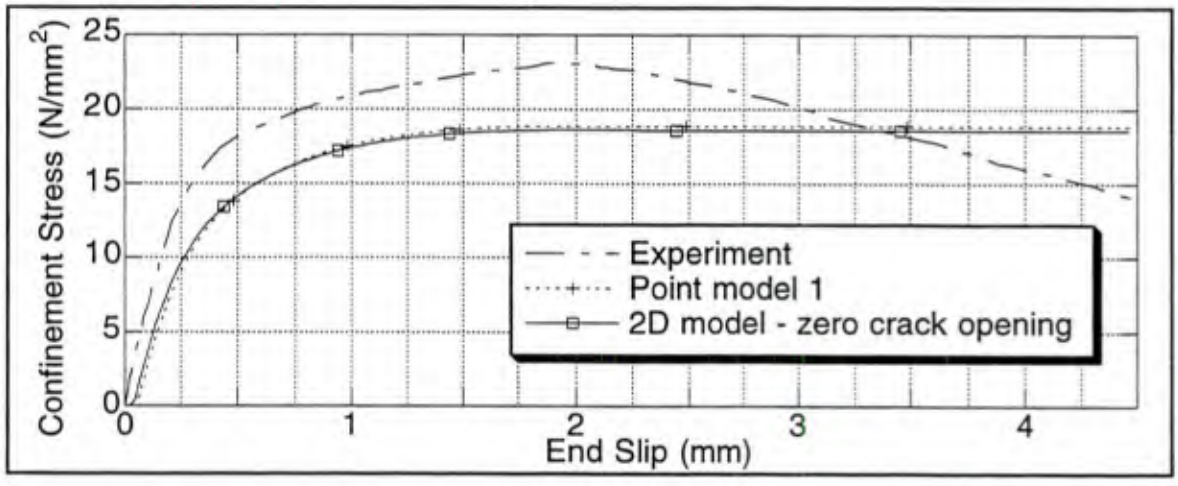

Figure 7.2-6 Average confinement stress versus end slip for the Gambarova *et al.* (1989) test with a zero crack opening – comparison of the point and two-dimensional models.

The relative lack of sensitivity of the two-dimensional model to the boundary condition at points *c* and *d* and the small embedment length suggest the point model is probably sufficient for this analysis. Figures 7.2-5 and -6 confirm this conclusion. The difference in the results is extremely minor. The two-dimensional model is slightly stiffer during the elastic response since the slip is measured at the free end of the bar.

Both models underestimate the maximum confinement stress by about 18 percent. This result is consistent with axisymmetric analyses of the Malvar (1991) specimen that indicate additional radial dilation is needed in the model. If D_{22}^{ε} were increased, the two-dimensional model would become more sensitive to the boundary conditions and thus its results would differ more with the point model. The enforcement of the zero crack opening would produce greater confinement stress and thus greater bond stress both of which are under predicted. It is also significant that the relative magnitude of the errors is consistent with the shape of the yield surface; that is, for a given increase in the confinement stress the increase in bond stress is likely to be smaller since the secant will have a slope of less than unity for confinement stresses of this magnitude (see Figure 3.3-4).

Both models also lack the subsequent decrease in confinement stress which occurs in the experimental results. This is due to the form of the flow rule. As previously noted (see *e.g.*, Figure 7.1-5), the bond model is calibrated to results for bars that have ribs aligned normal to the axis of the bar (the series 3 Malvar tests). These bars always exhibit a stage of sustained slip without radial contraction (the constant radius stage of Figure 4.2-1). The series 2 bars of Malvar (1991), which have inclined ribs, lack this stage and transition immediately from radial expansion to radial contraction. Thus it appears that if the flow rule were further developed to account for the rib angle, this behavior could be modeled more accurately. This might be a very desirable change if the model is recalibrated to increase radial dilation because the resulting increase in confinement stress might cause excess bond stress during softening. However, if the flow rule were such that radial contraction occurred earlier this effect could be negated. This increase in bond stress during softening might not be significant since the yield surface is relatively flat for states of high confinement stress and damage near unity.

An important behavior that the model does reproduce is the lag in the development of confinement stress. Gambarova *et al.* (1989) refer to this phenomenon as *confinement lag*,

and note that it is almost negligible in the phase *C* tests. It appears to have been subtracted from their reported data but is explicitly shown in an annotated graph. Its existence suggests that the current calibration correctly captures the mechanics; during the elastic response the wedging effect of the ribs is insignificant (as reflected in small coupling terms in the elastic moduli). As plasticity initiates, damaged material near the face of the ribs rapidly increases the wedging effect and the corresponding confinement stress (as reflected in the steep initial slope in the flow rule).

While improvements in the results are anticipated with advanced calibration efforts the bond stress response is very acceptable with an error of about 9 percent. While the confinement stress has a greater error, assumptions of its uniform distribution (for the point model) are proportionately more difficult to accept. Recall that the average confinement stress in the experiment is obtained from the vertical forces measured at points *c* and *d*.

7.3 Eligehausen, Popov and Bertero Experiments

This very extensive set of experiments was designed to represent the stress history found in the highly confined region of a beam-column connection. The study included extensive data on cyclic bond response, and usually included multiple tests so that experimental scatter could be evaluated. The secondary reinforcement cage, explicitly shown in Figure 7-1, consisted of four vertical steel bars (#4s) welded to four stirrups. This study was exclusively used in extending the bond model to cyclic loading (Herrmann and Cox [1994]) and is too important to ignore. On the other hand, its focus was on the response of a bar in a particular structural component – one that is inherently difficult to model. Like the majority of bond tests there is no measurement that provides even an estimate of the normal stress near the bar; that simply was not the goal.*

As shown in Figure 7-1 (also see Table 7-2) the specimen has an embedded length of nearly twice those of Malvar (1991) and Gambarova *et al.* (1989). Like more typical pull-out tests, the reaction support is provided by bearing against the face of the specimen instead of being supported along its outer surfaces. As with the Gambarova specimen, this specimen has a fabricated splitting crack. In this case the crack is exterior to the secondary reinforcement. This specimen is somewhat paradoxical from a modeling point of view because the secondary reinforcement can exhibit bond slip behavior as well. As with the previous tests the bar is pulled under displacement control. The following sections present the specimen models used and the corresponding results.

* The authors did consider various vertical forces applied to the column stub, but resulting confinement stress in the bond zone is unknown.

Specimen Models

Only point models were used to represent this specimen. The specimen appears to merit a three-dimensional model, but yet the bond zone is so highly constrained that variations in the simplified models have little effect on the response. As with the Gambarova specimen, two-dimensional models are likely to offer only minor advantages over point models since both include numerous approximations; however, they would better introduce the effects of response gradients. The increased embedment length suggests that these are likely to be more significant for this specimen (see Appendix D). Thus the point models considered here are expected to underestimate the initial stiffness as compared to what a two-dimensional model would predict.

The use of a point model implies the assumption that most of the nonlinear behavior is either attributable to the bond zone or can be adequately treated with simplifying assumptions. Figure 7.3-1 shows a schematic of some of the point models considered in this study. In contrast to the previous point model, the top link in this case represents the constraint imposed by the secondary reinforcement – in particular the vertical bars. Figure 7.3-2 shows the forces on the bottom block of the specimen which contribute to equilibrium perpendicular to the plane of the crack.

Two models were considered for this top link. The first, developed in detail in Herrmann and Cox (1994), attempts to account for the bond of the vertical reinforcement by deriving a nonlinear bond slip relationship for a semi-infinite bar embedded in a half-space of concrete. Using an empirical, local bond-slip relationship (derived from experimental data for large specimens by Shima *et al.* [1987]) and the equation of equilibrium (Appendix D) for a "one-dimensional member subjected to bond stresses," a differential equation in slip is obtained. A finite difference solution then gives the relationship between end slip (δ_v) and bar force (F_v) as:

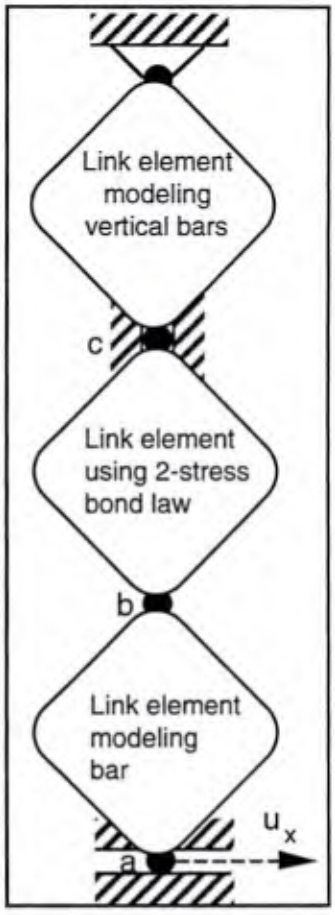

Figure 7.3-1 Point model of the Eligehausen specimen

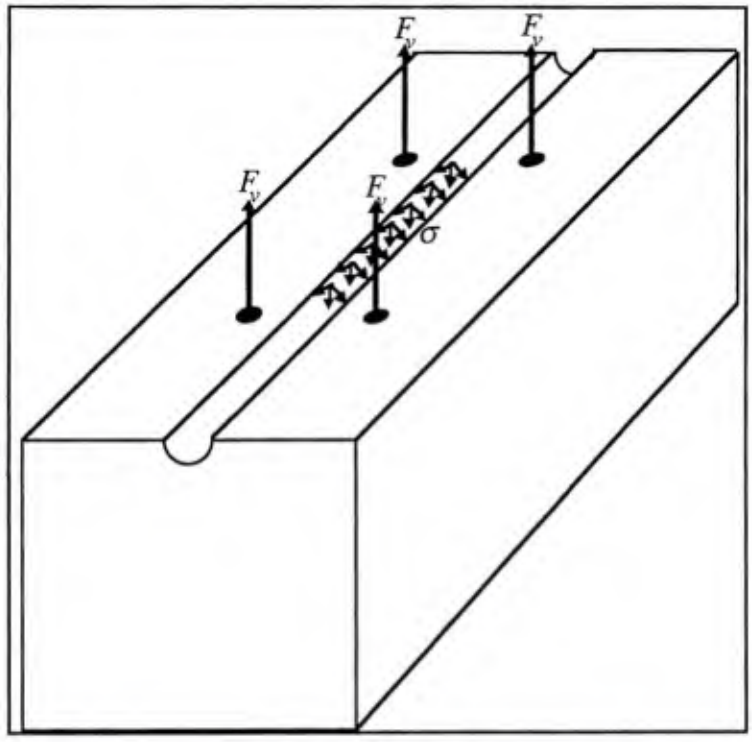

Figure 7.3-2 Free-body diagram for vertical direction of lower specimen block.

$$F_v(\delta_v) = \frac{\pi D_v^2 E_v}{4}\left(\frac{\delta_{v\,max}}{D_v \eta}\right)^{\frac{1}{1.62}} + \left(\frac{\delta_v - \delta_{v\,max}}{D_v}\right) E_{un} \qquad (7.3\text{-}1)$$

where D_v ~ bar diameter (12.7 mm), E_v ~ Young's modulus, η = 365, $\delta_{v\,max}$ ~ maximum end slip, and $E_{un} \approx$ 6,860,000. The quantity η is a function of the concrete strength, and the unloading modulus (E_{un}) is a function of properties of the bar, concrete and bond zone. The maximum end slip of the vertical bars ($\delta_{v\,max}$) is retained as a material variable, so that during loading only the first term contributes and during unloading the response is incrementally linear with a slope equal to the unloading modulus.

Alternatively the second model simply assumes the vertical bars are unbonded to the first stirrups where they are rigidly connected; thus they just act as linear springs.

For all the point models the normal stress on the bond zone is assumed to be uniform, and the forces in the vertical bars are assumed to be equal. The relationship between these quantities follows trivially from equilibrium in the vertical direction (see Figure 7.3-2).

Variations in response with respect to the "axis-direction" have been previously discussed, but variations in response with respect to the θ-direction have not been considered. The actual stress distributions with respect to θ, are not likely to be constant (even if the concrete did behave as if it were isotropic and homogeneous). Two obvious reasons are radial cracking and non-axisymmetric rib geometries. However, for the point models a uniform stress distribution is a sufficiently accurate assumption.

The deformation with respect to the θ-direction is also not trivial. Since a splitting crack is fabricated outside of the secondary reinforcement, it is likely to extend through the bond zone early in the loading. Two alternative displacement modes are considered in the point models.

The first mode of radial deformation was developed in detail in Herrmann and Cox (1994) and applied to the experiments of Gambarova *et al.* (1989) and Eligehausen *et al.* (1983). It is based upon the assumption that, as the splitting crack opens, the in-plane displacement is in the vertical direction, and thus the normal displacement of the bond zone varies as $\sin(\theta)$ for small crack openings. This implies the average normal displacement in the bond zone can be given by $\delta_n \approx 0.64\delta_v$.

The second mode of radial deformation treats the bond zone in an axisymmetric manner. It is based upon the assumption that, though the crack opens, the constraint of the vertical reinforcement is sufficient to force uniform radial displacement (with respect to θ) in the bond zone. For this case the normal displacement of the bond zone and the end slip of the vertical reinforcement are taken to be equal.

The differences in the point models are summarized in Table 7.3-1. The models are ordered by complexity – from the most complicated to the simplest. Model 4 omits the bar response by eliminating the first link and applying the end displacement directly to the bond link.

Table 7.3-1 Differences between the point models for Eligehausen *et al.* (1983).

Model	Number of Links	Vertical Steel Model	δ_n Measure
1	3	bonded (nonlinear)	0.64 δ_v
2	3	unbonded (linear)	0.64 δ_v
3	3	unbonded (linear)	δ_v
4	2	unbonded (linear)	δ_v

Results

The response of all of the point models is compared with the series 2 tests of Eligehausen *et al.* (1983). For this test series the experimental scatter is well quantified.

Figure 7.3-3 presents the bond versus slip response of all the 3-link models to the range of experimental results. The models give nearly identical results and fall within the experimental scatter over the full range of slip. The prediction of maximum bond stress and softening is excellent. While the maximum bond stress occurs at a smaller value of slip than the average experimental response, it is likely to fall within the experimental scatter. The largest deviation from the average experimental curve occurs during the initial elastic and subsequent hardening responses. Considering the simplicity of the specimen models the overall agreement is excellent.

Figure 7.3-4 presents the normal stress versus slip response for the 3-link models. While the variation between the models is larger for this response, it is still insignificant relative to the scatter in the experimental data. Reducing δ_v from δ_n/0.64 to δ_n has the effect of reducing the stiffness of the vertical reinforcing bars by a factor of 0.64. Thus the normal stress, though very slight, is less for model 3 than the first two models. The variation is

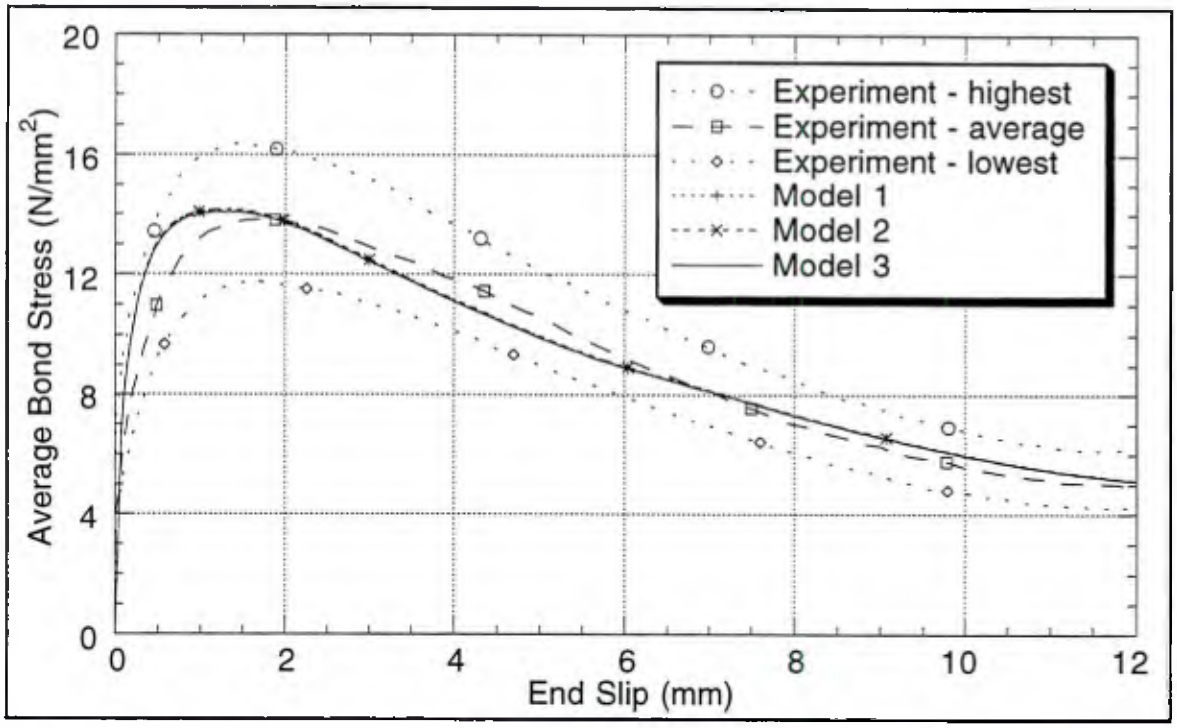

Figure 7.3-3 Average bond stress versus "end slip" for the first three point models of the Eligehausen specimen, series 2 tests.

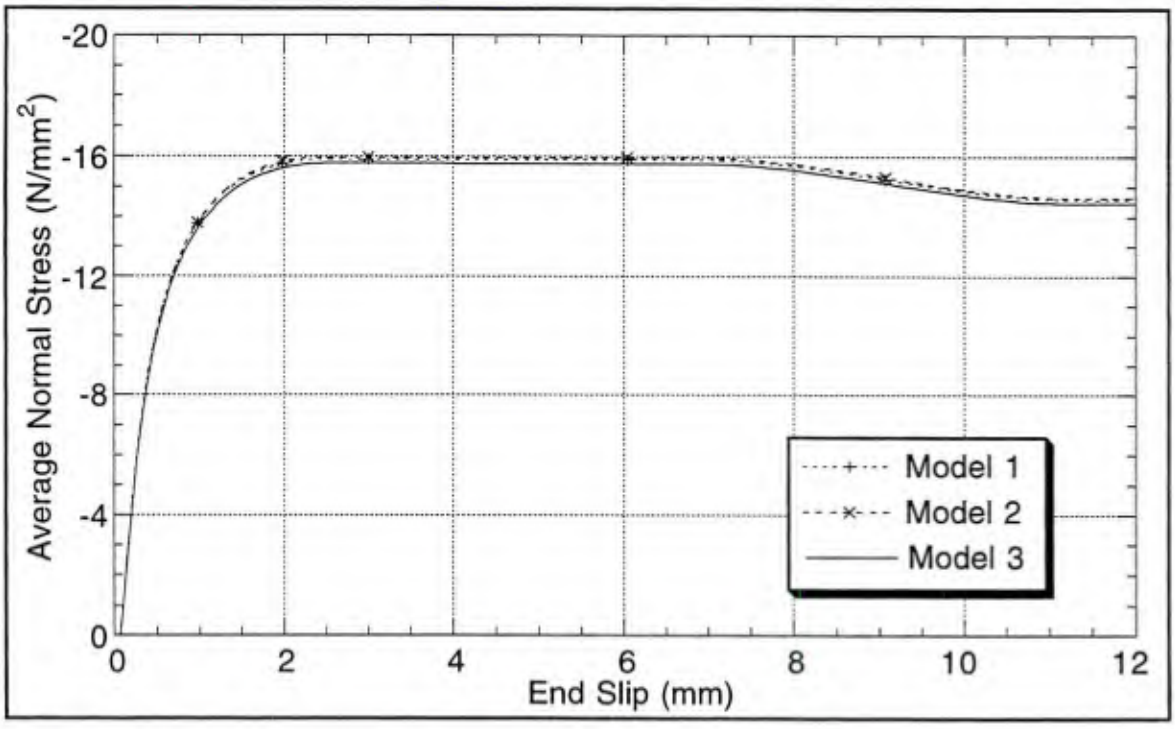

Figure 7.3-4 Average normal stress versus "end slip" for the first three point models of the Eligehausen specimen, series 2 tests.

less in the bond stress versus slip response principally because of the shape of the yield surface (as discussed in the previous section).

As with previous results the *confinement lag* is apparent in the models' predictions.

The lack of variation in the model predictions might initially be somewhat surprising, however it is qualitatively consistent with the experimental studies. The authors studied the effect of the vertical steel using #2, #4 and #8 bars in different experiments. They observed negligible differences between tests that used #4 and #8 bars. I prescribe more to the assumptions corresponding to the second displacement mode (models 3 and 4); therefore models 1 and 2 can be interpreted as having bars that are stiffer than #4s. Both the models and experiments indicate that additional stiffness in the vertical steel (beyond a #4) will have essentially no effect because the bond zone is already "fully constrained."

Eligehausen *et al.* (1985) did see about a 10 to 15 percent reduction in the maximum bond stress when #2 bars were used for the vertical steel. This behavior was not examined in this study, but it does offer an indirect test on the dilation response of the model if additional calibration work is pursued. The point model might not be sensitive enough to detect the difference.

Figure 7.3-5 presents the "normal stress" versus "dilation response" of all the point models. Unlike the other responses, there is a significant variation among the different models. Comparing models 1 and 2, it is clear the linear model for the vertical bars (of model 2) nearly gives a "secant approximation" to the response given by the more complex model 1. Comparing models 2 and 3, we see that the effect of the different assumed displacement modes is to scale the stiffness of the vertical bars which serve as a constraint to the bond model in the normal direction.

For the first three models the link representing the reinforcing bar also affects the normal response. It is the sole reason that the responses of models 2 and 3 are not straight lines.

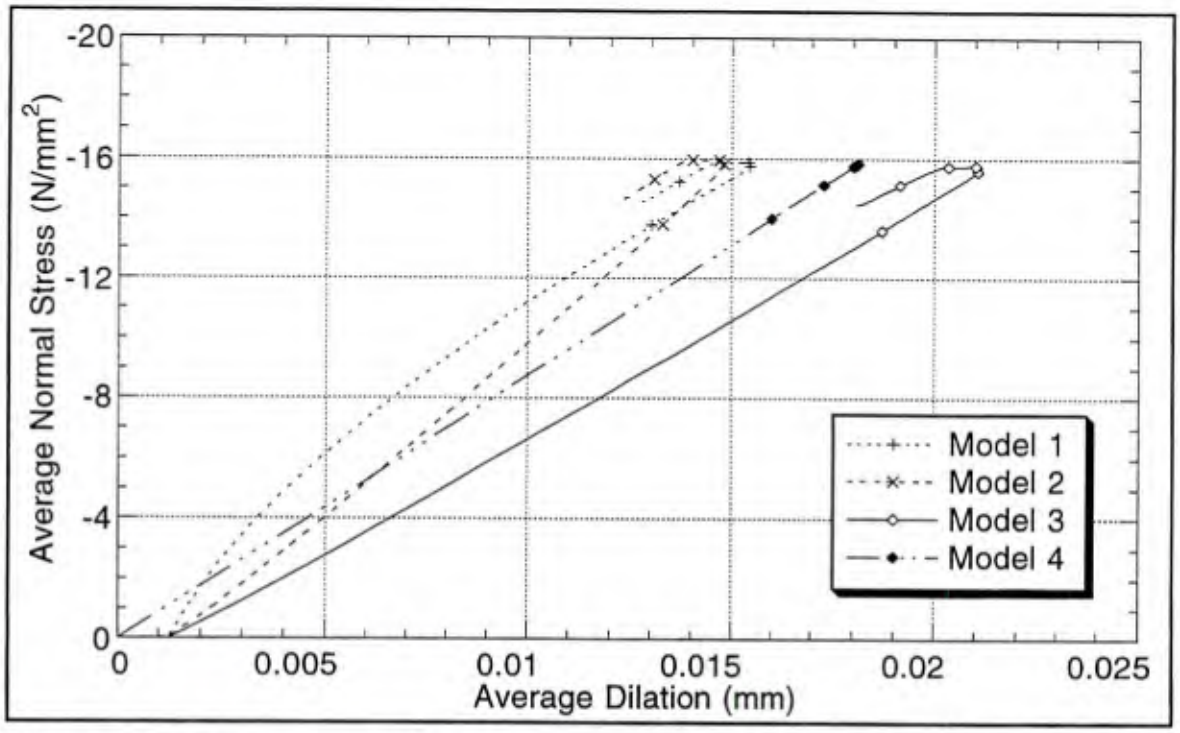

Figure 7.3-5 Average normal stress versus average dilation for all the point models of the Eligehausen specimen, series 2 tests.

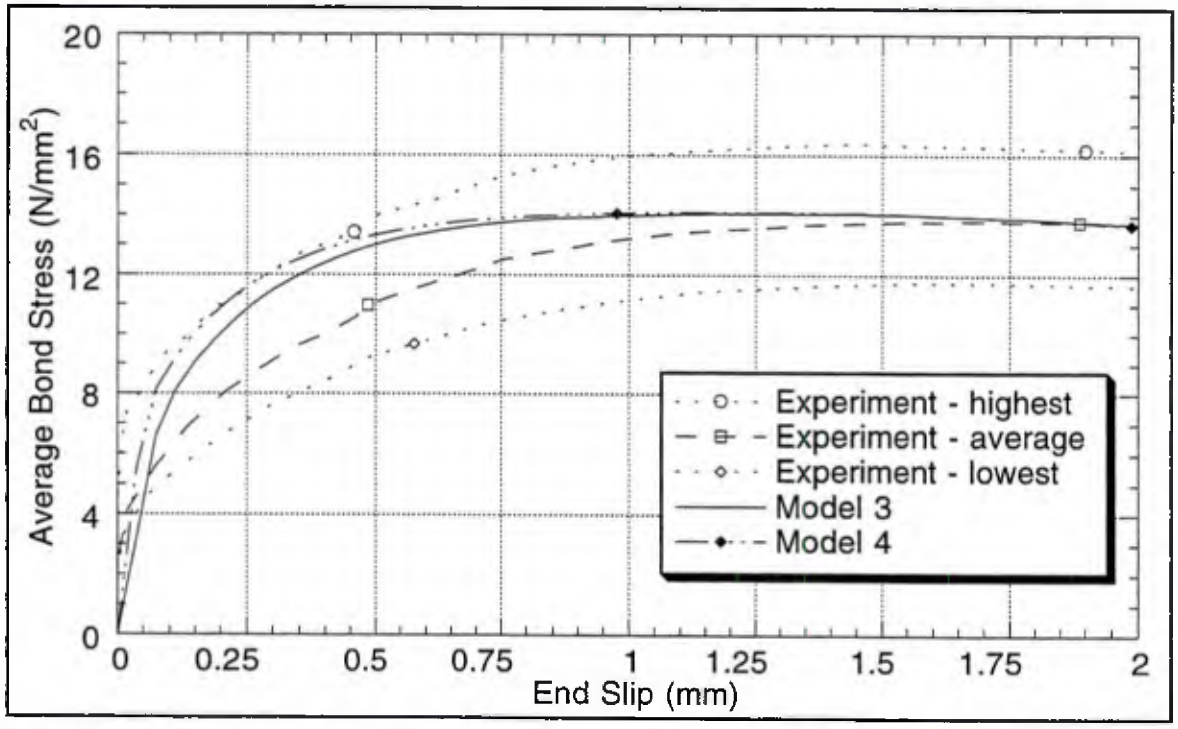

Figure 7.3-6 Average normal stress versus average dilation for all the point models of the Eligehausen specimen, series 2 tests.

In contrast, model 4 loads and unloads along a straight line. During the initial elastic response, models 1 through 3 feel the Poisson effect of the bar and thus the dilation increases a small amount. As the bar contracts due to the axial stress, the bond zone dilates due to its small stiffness (relative to that of the vertical bars and the main bar - the latter radially). Because this stiffness is small, negligible normal stress is developed which is negated by the contribution of the elastic coupling term D_{22}^{e} of the bond model (see Equation 5.2-4). These same factors cause models 2 and 3 to vary slightly from a straight line response as the normal stress increases. During the *constant radius stage* of the flow rule, the yield surface is locally contracting. This reduces the axial force in the bar causing the bar to expand from Poisson's effect; thus the bond zone contracts giving the nearly horizontal segment in the response of models 1 through 3. When the flow rule begins radial contraction, all the models unload along a line nearly parallel to the most recent segment of the loading curve. During the sliding stage (frictional response), the response is stationary in σ-δ_n space.

Figure 7.3-6 compares the bond stress versus slip response of models 3 and 4 over a short range of slip. After attaining their maximum bond stresses, the curves appear coincident. The predictable effect of the reinforcing bar link element (see Appendix D) is to reduce the initial stiffness of the model. This simple model for the rebar measures the slip at the loaded end of the bar and thus erroneously includes the bar strain in the end slip approximation. While it gives an indication of the magnitude of the effect of axial bar strain, it's in the wrong direction. As shown in Appendix D, measuring the slip at the free end of the bar produces a stiffer initial response than the rigid bar assumption. The experimental results with initial bond stress and no apparent corresponding end slip are typical of the results given by two-dimensional models which account for the gradients along the length of the bar.

7.4 Rehm and Eligehausen Experiments

Rehm and Eligehausen (1979) sought to experimentally determine the behavior of ribbed bars under repeated loading. Both pull-out failures, which failed the concrete between the ribs, and splitting failures were considered in their studies. The former was examined using pull-out specimens that had a large concrete cover, and the latter was studied using beam specimens with spliced reinforcement. To develop fatigue strength data they conducted their tests under stress control. Monotonic tests were conducted to determine the ultimate bond strength; though these tests were not the focus of the study, they provide another validation opportunity. As shown in Figure 7-1, the specimen is axisymmetric and has a short bonded length.

The available English paper on this study (Rehm and Eligehausen [1979]) was intended to provide an overview of the complete study. The paper did not address the scatter in the monotonic response. In addition bar characteristics other than the diameter were not given. As indicated in Table 7-1 the rib spacing (the other bar geometry parameter for the bond model) was measured from photographs given in the paper.

Specimen Model

A single axisymmetric specimen model is presented in this section. The mesh and boundary conditions are depicted in Figure 7.4-1. In the Geneseos analysis system (Cox [1994]), the "y-axis" is taken as the axis of symmetry, and thus processed results (*i.e.*, shaded "contour plots") have this same orientation. For clarity the model is presented with a consistent orientation.

Though the bonded length for this specimen is as small as any of the other specimens considered, the small value of L_b/L makes an axisymmetric model preferable since it is

difficult to apply the solution for a thick-walled cylinder. In this problem, the extent of longitudinal cracking is also of interest and is more accurately modeled by an axisymmetric model.

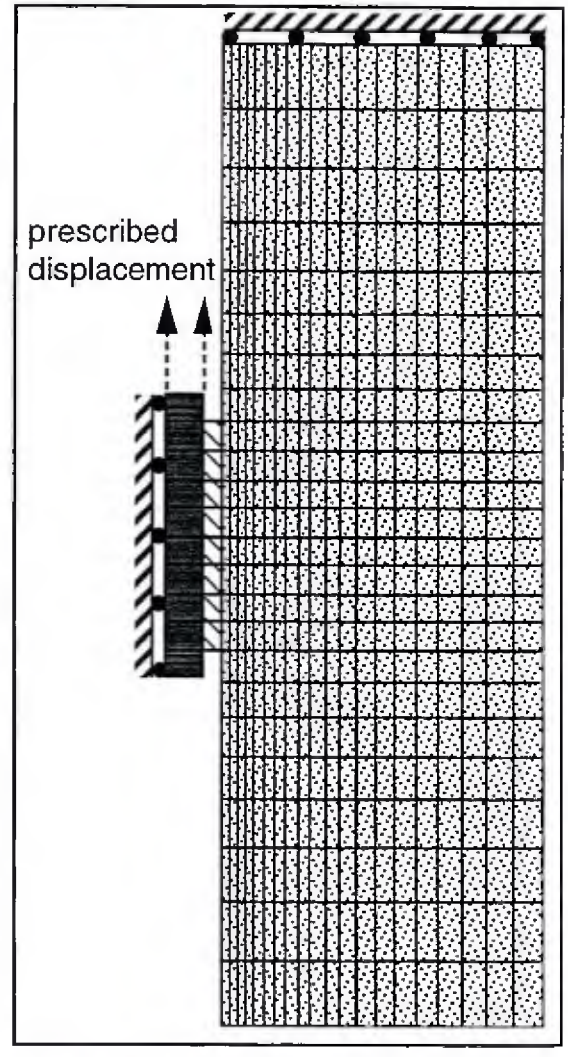

Figure 7.4-1 Axisymmetric model of the Rehm and Eligehausen specimen.

The roller boundary condition on the bearing face is likely to be a poor approximation to a frictional contact surface, but further details on the test arrangement are not provided by the authors. The displacement boundary condition on the bar end also differs from the experiment so that a stable solution to the quasistatic analysis could be obtained. The effect of these approximations will be discussed in the next subsection.

For modeling convenience the bond zone thickness was taken to be the thickness of the gap in the unbonded regions. Parameter studies, not included here, showed almost no variation in the results with the thickness of the bond zone. The effect of the bond zone thickness will be considered in the next subsection.

The concrete material model (Appendix F) allows longitudinal cracks to open once the tensile strength of the concrete is exceeded. The inclusion of softening behavior in this model would reduce the extent of longitudinal cracking as would an accurate representation of the nonlinear behavior in compression.

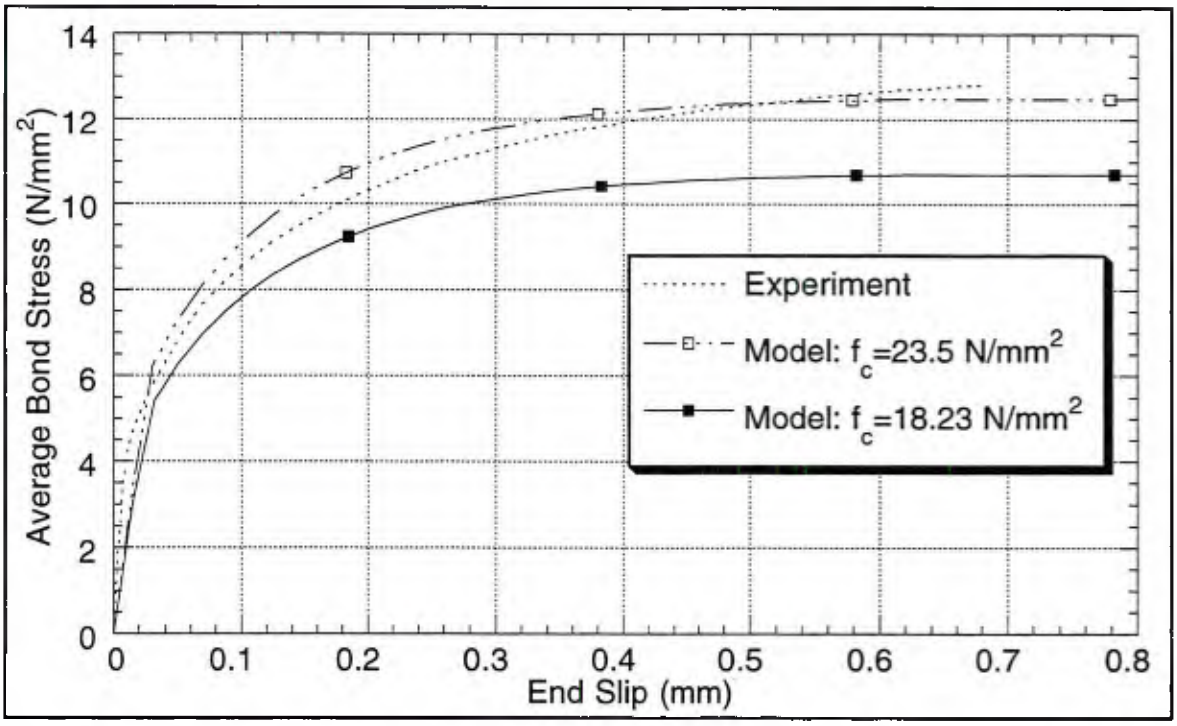

Figure 7.4-2 Average bond stress versus end slip for the model of the Rehm and Eligehausen specimen.

Two sets of concrete material properties were considered. The first case uses a compressive strength of 23.5 N/mm^2. As noted in Table 7-2, this value was obtained from cube tests. The second case uses an "equivalent cylinder strength" of approximately 18.23 N/mm^2; this value was obtained from the relationship given by L'Hermite (1955). In both cases the tensile strength was estimated from Equation (B-1).

Results

Figure 7.4-2 compares the average bond stress versus end slip response of the model to the experimental results. While the initial stiffness of the model is less than the experimental results, the elastic response is a reasonably accurate secant to the experimental results to the point where the model's plasticity initiates. The results based upon the concrete cube strength (f_c=23.5 N/mm^2) accurately predict the experimental results over the full range. The results based upon the estimated cylinder strength (f_c=18.23 N/mm^2) qualitatively have

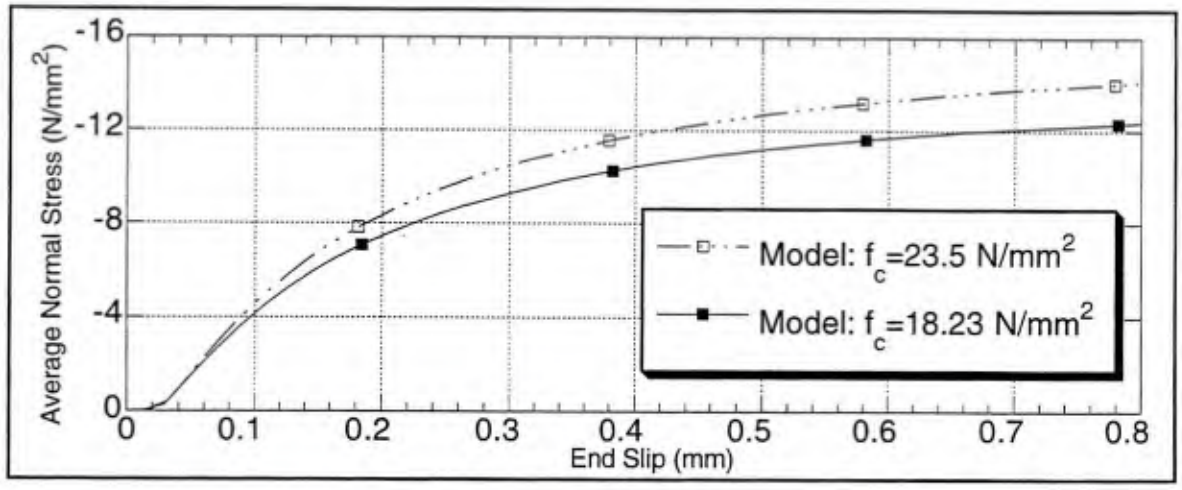

Figure 7.4-3 Average normal stress versus end slip for the model of the Rehm and Eligehausen specimen.

the correct form but are less accurate; the maximum bond strength is under predicted by about 16.5 percent.

Figure 7.4-3 compares the average normal stress versus end slip for the model with the two different concrete strengths. Again the model response includes the confinement lag observed in some of the Gambarova *et al.* (1989) experiments.

If we assume 1) the empirical relations used to determine the concrete material properties are accurate (including the scaling to the "equivalent cylinder strength"), 2) the concrete material model is accurate for this specimen model, 3) rate dependency is not significant,* and 4) that the experimental data have relatively little scatter, the bond stress results suggest that the proposed recalibration could further improve these results. That is, increasing the radial dilation would increase the normal stress. Assuming the specimen does not split, the monotonically increasing shape of the yield surface would increase the bond stress.

* The issue of rate dependency is mentioned because the monotonic tests appear to have been conducted under stress control just at the cyclic tests. With the instability that occurs in this test under stress control, the slip rates are likely to be very high near the ultimate bond stress.

The assumption that the specimen does not split is critical. This specimen was specifically designed to fail in a pull-out mode (*i.e.*, not by splitting), and the current calibration predicts this mode of failure. Figure 7.4-4a shows the prediction of longitudinal cracking near the ultimate bond stress. Increasing the dilation would increase the chance of splitting failure. There are a few approximations in the current specimen model that increase the likeliness of a splitting failure - both of which could be refined. The first is the roller boundary condition. The neglected frictional forces on the bearing surface would tend to inhibit radial displacement of the specimen and thus inhibit the increase of hoop stress. The second approximation that could be refined is the material law behavior. Both linear compression response and cracking without softening tend to increase the likelihood of a splitting failure.

Figures 7.4-4 show several field responses for the specimen at an end slip of 0.8 mm (*i.e.*, near the ultimate bond stress). As previously noted the longitudinal cracking remains stable within the specimen. The increased extent of the cracking toward the top of the specimen is consistent with the displaced shape shown in Figure 7.4-4b. The dilation of the bond zone tends to be greater near the top of the bar. A contributing factor to this is the "rotation" of the specimen which decreases the confinement stress near the top of the specimen and increases it near the bottom of the specimen. This variation in the normal stress then, via the flow rule, creates additional dilation toward the front of the bond zone. Another contributing factor is that locally the slip is greater near the front of the bar which means the flow rule has been integrated to a larger value of damage in this region.

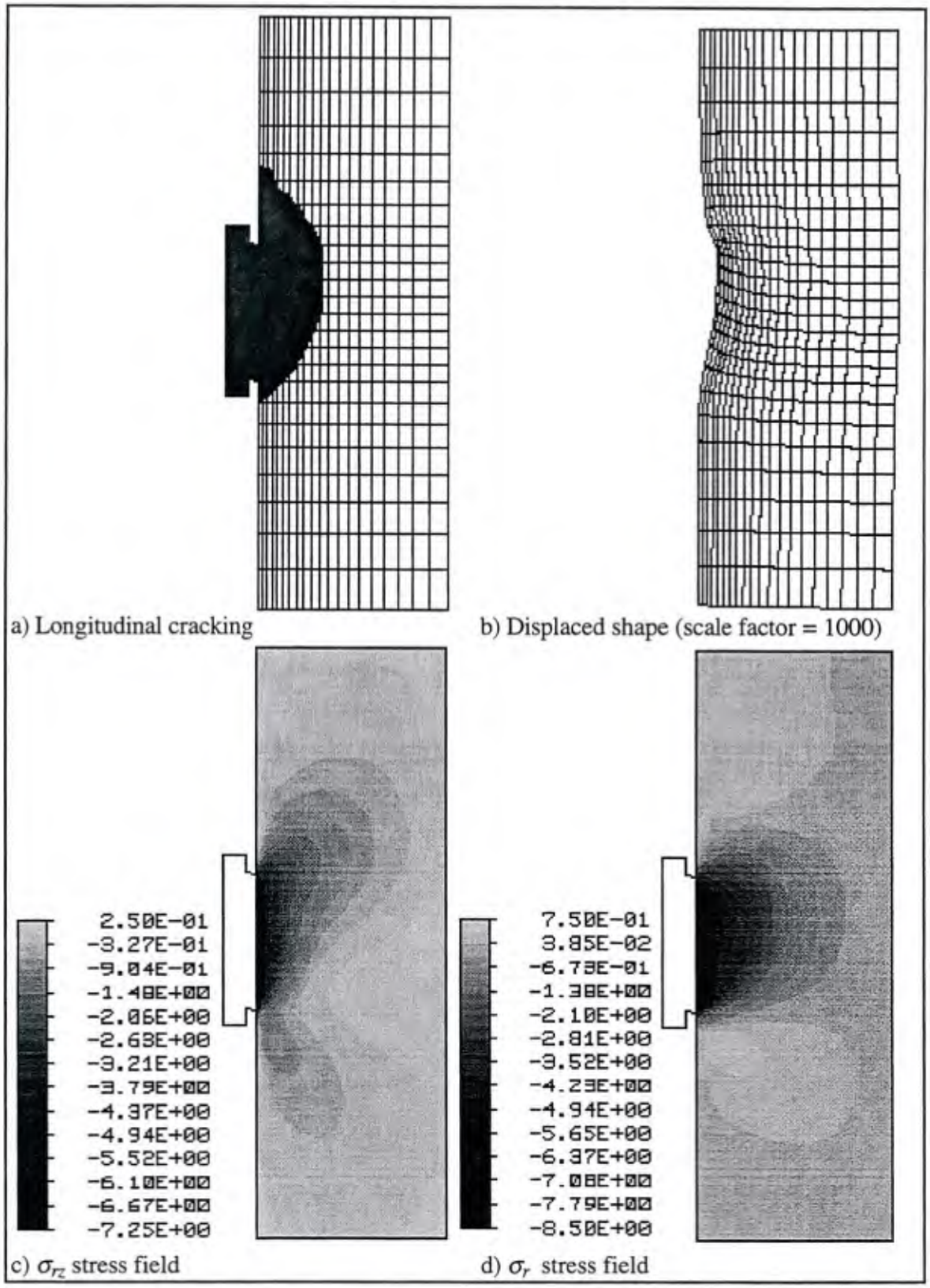

Figure 7.4-4 Field responses of the Rehm and Eligehausen specimen for an end slip of approximately 0.8 mm (f_c = 18.23 MPa).

Figures 7.4-4c and -4d show two components of the stress tensor in the specimen.* These results indicate how localized the response is near the bond zone, and thus give some support for the use of a simple concrete model. While the stress gradients are high near the bar, it is unlikely that they are very representative of the actual stresses in the concrete specimen. The bond model was designed to introduce the effect of the ribs in a generalized sense. The resulting generalized stresses and strains eliminate the actual stress concentrations near the ribs and the resulting transverse cracking and local material nonlinearities. Though with a more accurate concrete model some transverse cracking (for example) might be predicted, it is not clear that it would produce a more representative approximation to the actual state of the material.

I do not expect a concrete material law to represent local responses near the bar accurately. However, its interaction with the bond law (*e.g.*, its radial stiffness) and ability to predict failure modes such as splitting and cone pull-out failures is important. The stress fields predicted for the bond specimen in general only give a qualitative indication of the specimen response, and the longitudinal cracking prediction gives "Boolean validation data" – the specimen split, true or false.

The bond model results for this specimen were good, and a moderate increase of radial dilation in subsequent calibrations is likely to improve the results assuming the specimen does not fail in splitting.

* The equivalence of the bond and normal stress with these tensor components is not recognized in the plotting program, thus the bond zone shows values of zero.

7.5 Shima, Chou and Okamura Experiments

Shima, Chou and Okamura (1987) performed many monotonic pull-out tests, some of which were loaded beyond the yield point of the bar. To prevent splitting failures the axisymmetric specimens were designed with a diameter of 50 cm. Figure 7-1 shows the smallest Shima specimen considered in the validation analyses and indicates that these specimens are massive compared to the others.

In their tests series Shima *et al.* (1987) investigated the effects of unbonded concrete (*i.e.*, the specimen extension beyond the free end), bar strain, concrete strength, and bar diameter. They claim that the measurement of steel strain along the bar is the most important component of their study. Their one-dimensional bond model includes the bar strain as a parameter. Their main premises are that the principal mechanism of slip is transverse cracking and bar strain gives a measure of this effect since the variation in crack openings is related to the strain in the bar.

Except for a parameter study on the effect of the specimen length beyond the free end of the bar, their paper contains no measure of experimental scatter. All the other validation problems have only addressed global quantities (*e.g.*, end slip and bar force) from which estimates of local quantities (*e.g.*, bond stress) are obtained. While local measurements give an indication of the distribution of the "bond response," they are also notoriously difficult to measure accurately and thus a measure of experimental scatter is all the more important (see *e.g.* Cowell *et al.* [1982]). In the following validation analyses emphasis is placed on the global measurements, and local responses are treated more skeptically.

The validation results presented here only address the tests where the experimentalists claim the bars remain elastic. In addition, only specimens which lack concrete beyond the free

end of the bar are considered. As part of their investigation, they experimentally demonstrate that the unbonded region beyond the free end of the bar does not affect the response.

Specimen Models

Several Shima specimens are considered in the validation analyses. The mesh and boundary conditions of a typical specimen model (in this case for specimen 1) are shown in Figure 7.5-1. The mesh density of this model is typical of the models used for these experiments. Finer mesh densities were considered in convergence studies.

The hydraulic jack used to apply the bar load bore against the specimen over a ring region; as with previous specimen models this was modeled as a roller boundary condition. This boundary condition could be refined to include friction, but with an unbonded region of length $10D_b$, the effects of such a refinement are expected to be secondary. As previously discussed, the boundary condition could influence the extent of longitudinal cracking; if the model failed in splitting the refinement would be considered.

The end slip of the model was taken to be the vertical displacement of point *a* relative to point *b*. This is consistent with the connection of the displacement transducer in the actual experiments.

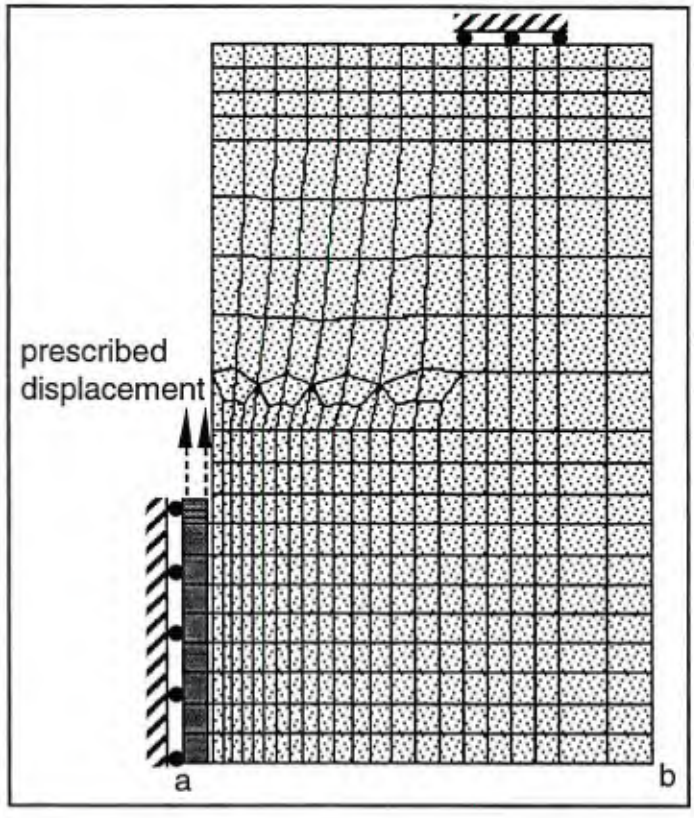

Figure 7.5-1 Model of Shima specimen 1.

The bond zone was taken to be the rib height plus 1.5 mm for all the models except for those analyzed to show the insensitivity of the models to this assumption. The behavior of the concrete was represented by the simple elastic-brittle model discussed in Appendix F. The tensile strength for both the bond and concrete models was determined by Equation (B-1).

Results

This subsection presents the results for five different specimens. Both global and local responses are considered. The response distribution of the model is examined and qualitatively compared with the experimental response distribution of bar strain. Lastly the effect of the bond zone size is considered with three analyses that vary this size by a factor of approximately 31. In the analysis of earlier validation problems, parameter studies of this type were also performed but were omitted for brevity.

Figure 7.5-2 shows the bar force versus end slip response for specimens (1 through 4) ranging in embedment length from $5D_b$ to $20D_b$. The experimental data were originally presented with ordinate axes of average bond stress (Shima *et al.*, 1987, Figure 2.4) and bar strain at the loaded end (Shima *et al.*, 1987, Figure 2.18). These global results were probably obtained directly from load cell and displacement transducer data and thus are typically more accurate than the local measurements.

Qualitatively the predictions are very good. As the length of the specimen increases so do both the initial stiffness and the ultimate pull-out force. The initial response represents the transition along the length of the bar from elastic to elastoplastic behavior. So as the embedded length increases, it requires a greater bar force to produce this transition and thus the greater force for a given end slip. As shown in Appendix D, even an elastic analysis predicts the increase in initial stiffness with embedded length, but that is the only behavior it predicts. The model also qualitatively predicts the yielding behavior very well.

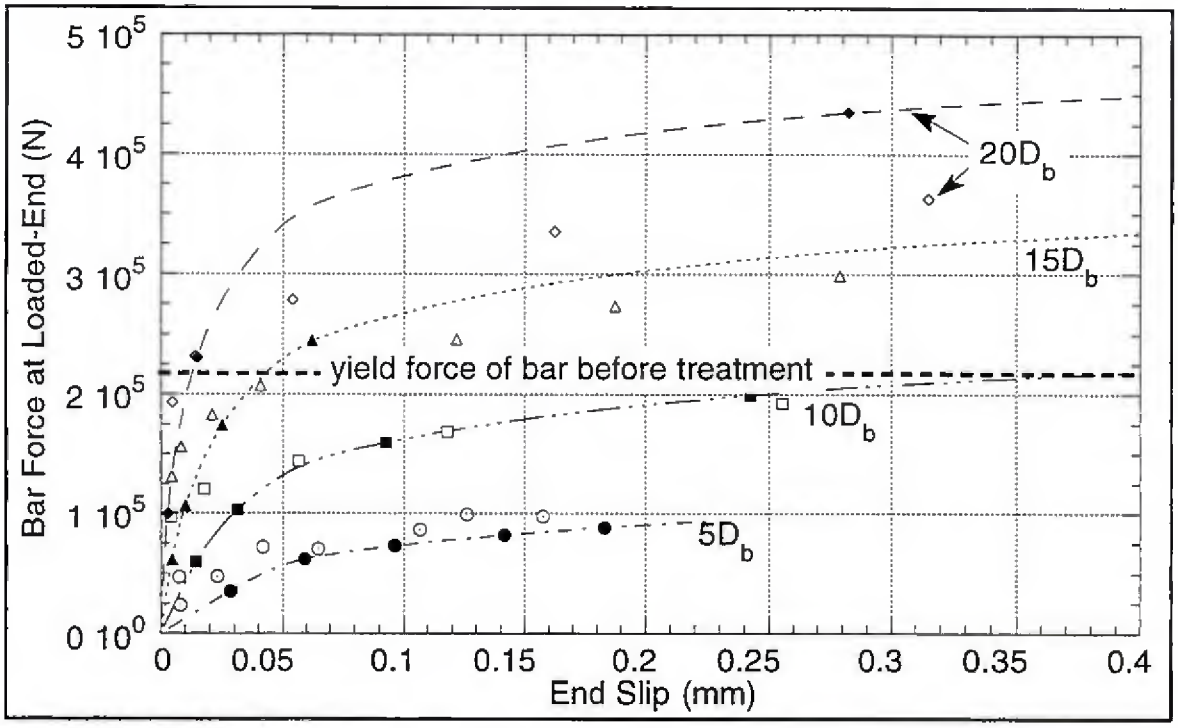

Figure 7.5-2 Bar force versus end slip for the Shima specimens with four different embedment lengths.

The largest discrepancy between the experimental and predicted results occurs for specimen 4 with an embedded length of $20D_b$; at an end slip of 0.4 mm, the model appears (assuming the experimental data varies almost linearly to this value of slip) to overestimate the bar force by about 20 percent. The trend in all of the model's predictions is a greater change in the bar force with increased embedment length than is seen in the experimental results.

The bars used in these experiments were heat treated by the researchers. It is interesting that the model predictions begin to loose accuracy above the original yield force of the bar. It is also curious that in the second part of the paper by Shima and his colleagues, which addresses bond behavior of high strength bars during yielding, they use a commercial bar instead of their own heat-treated bars. They provide no information on the response of their special bars. It is likely that the hardenability of the reinforcing bar was inadequate for

complete hardening which would result in a softer inner core; if this occurred it would produce a nonlinear bar response with earlier yielding in the core of the bar. In addition to the axial response, the radial response of the bar could also be a significant factor. If bar core material is accurately represented by a Mises yield surface and an associative flow rule plastic volumetric strain increments are zero. Thus with plastic deformation of the core, the confinement stresses and the related bond stresses would decrease, implying that the bond model might be over predicting the response due to our inaccurate model of the bar.

In Figure 7.5-2 the model appears to predict a linear increase in bar force with embedment length. This is consistent with the predictions of Shen and Xu (1992) for bars stressed below the yield strength. It is also consistent with the experimental results of Teng and Ye (1992), but these results are for high strength concrete and the bars yield for many specimens. Figure 7.5-3 shows that the maximum average bond stress (*i.e.*, the bar force normalized by the area of contact) predicted by the model is nearly equal for all of the specimens – thus the linear relationship between bar force and embedment length. While the initial stiffness values are closer for average bond stress than for bar force, the effect of the response gradients via the end slip measurement is still obvious.

Figure 7.5-4 presents the average normal stress versus end slip. The maximum value of the average of this stress component is also nearly equal for the four specimens. Here the effect of the response gradients is even more prevalent in the initial response. The confinement lag, which was noticed in the experiments by Gambarova *et al.* (1989), is seen to diminish with embedment length. This effect will be further explained in terms of the response gradients.

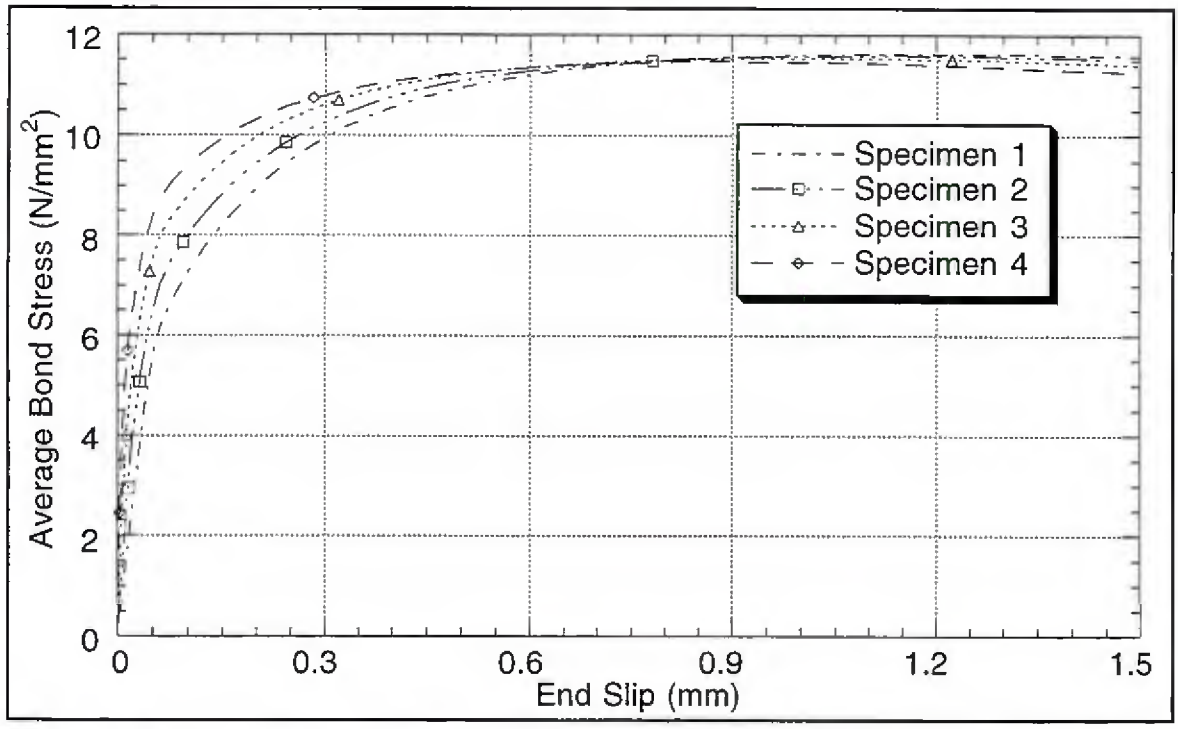

Figure 7.5-3 Average bond stress versus end slip for Shima specimens with four different embedment lengths.

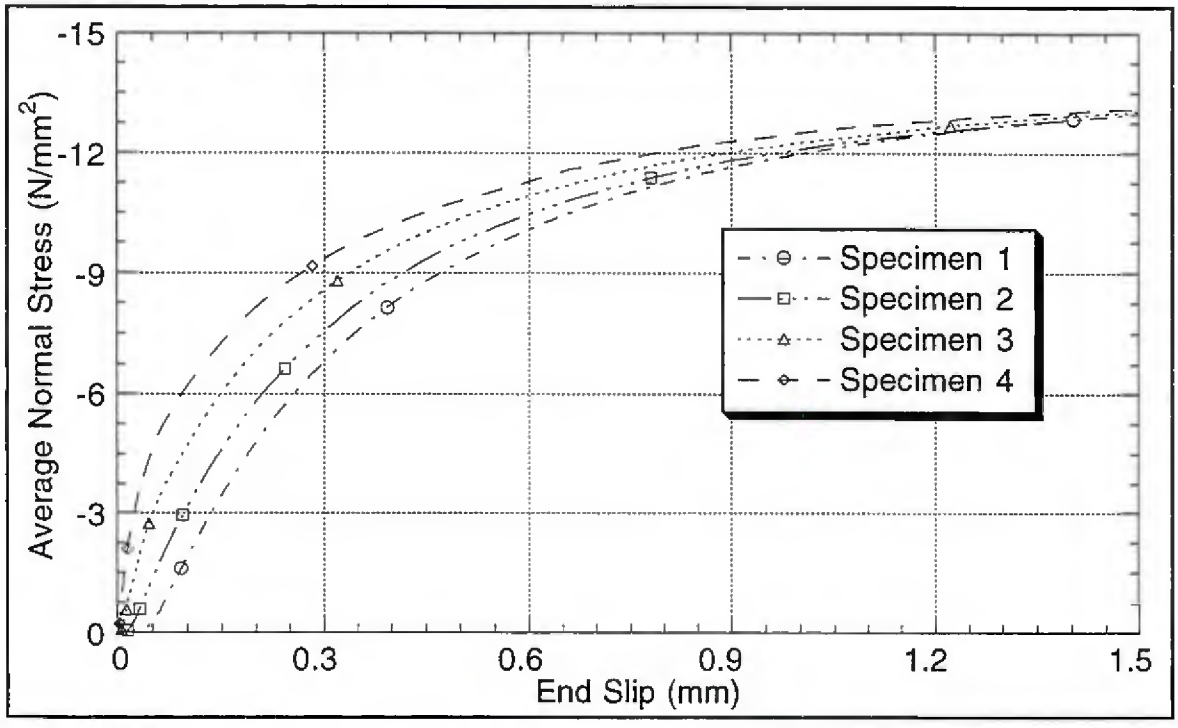

Figure 7.5-4 Average normal stress versus end slip for Shima specimens with four different embedment lengths.

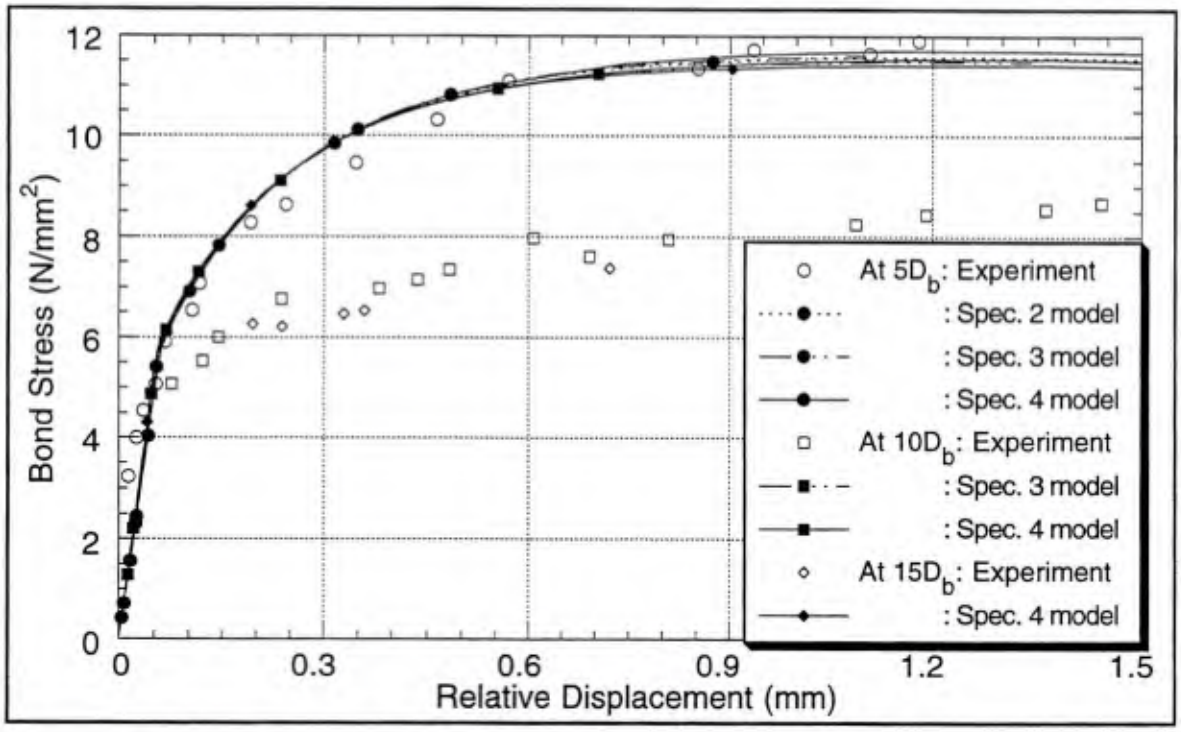

Figure 7.5-5 Local bond stress versus relative displacement at three points in Shima specimens with varying embedment lengths.

Figure 7.5-5 compares local bond stress versus relative displacement results for the experiment and model at various distances from the free end of the bar. The slip measure used by the authors is given by

$$s(\Delta L) = \int_0^{\Delta L} \varepsilon(x)dx + s_0 \tag{7.5-1}$$

where s_0 denotes the end slip (*i.e.*, relative displacement of points *a* and *b* of Figure 7.5-1) and integration of the axial bar strain gives the relative displacement of the free end to some point on the bar a distance ΔL away. So this slip measure is just the relative displacement between the specified point on the bar and point *b* (where the displacement transducer is connected). The more traditional definition of slip accounts for the deformation of the concrete, but at the cost of difficult longitudinal strain measurements in the concrete near the bar (see *e.g.*, Nilson [1972]).

The model's predictions agree very well with the results the authors give for a point $5D_b$ from the free end, however they differ significantly with the response at more interior points. As suggested by the earlier model results, this figure indicates the model's local response has little variation along the length of the bar. In contrast, the authors indicate the experimental results show a significant increase in bond stress near the free end of the specimen.

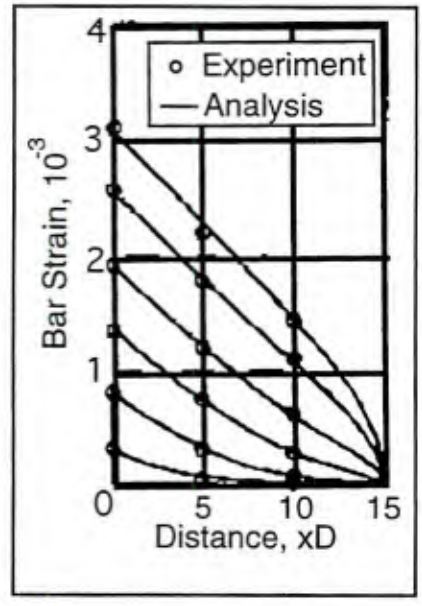

Figure 7.5-6 Bar strain distribution of specimen 3 (Shima *et al.* [1987], Figure 2.17).

This variation in the local bond stress presented by the authors is obtained from derivatives of bar strain (or bar force) distributions as presented in Figure 7.5-6 for specimen three. With only one load cell and two strain gage measurements* an error in any of the measurements significantly affects the estimate of the local bond stress. Their interpretation of a higher bond stress at $5D_b$ from the free end appears to be very subjective. If we assume their data are accurate, they do indicate that higher bond stresses are present near the free end since the bar strain must go to zero.

Let's qualitatively compare the response distribution of the model to the experimental results. Figures 7.5-7 through -10 present the distributions of bond stress, normal stress, slip and radial dilation, respectively. The first response curves have xs at the element integration points, and the vertical grid lines correspond to the node positions. The bold, dashed curve of smallest response magnitude (marked with circles) represents the last fully elastic response of the analysis. Subsequent response curves represent the transition to

* The authors actually had two strain gages at each position on opposing sides of the bar, but no indication of the scatter in these values is given.

elastoplastic response along the length of the bar. This will be referred to as the *transition phase*. The other boldly, dashed curve (marked with squares) represents the last transition response; for the subsequent response curves the bond zone is fully plastic. The elastic response lines are shown for prescribed displacement increments of approximately 0.0133 mm. The transition and fully plastic response curves are shown for prescribed displacement increments of 0.12 mm (9 times larger).

For the elastic response phase the gradients in the bond stress are high near the loaded end. The normal stress is nearly zero. The slip and dilation are obviously nonzero near the loaded end but are relatively small. During this response phase the crushing and cracking in the bond zone are not considered to be significant; the material is assumed to be undamaged. As designed, the model produces almost no radial response during this phase.

For the transition phase the bond stresses continue to increase, but the bond stress gradients near the loaded end decrease as the model hardens. The propagation of the plastic response down the length of the bar is clearly shown; this is interpreted as representing a progression of ribs that are damaging the adjacent concrete. With this damage the wedging action of the ribs becomes more pronounced resulting in significantly increased radial dilation and confinement stress. The effect of attributing most radial dilation to the plastic response is clearly seen; the normal stress quickly builds just after the bond zone becomes plastic – when the local ribs begin to fail the concrete on the rib face. The slip gradient at the end of this phase clearly shows why stiffness measurements based upon end slip progressively increase with embedment length. Compare these gradients with those of Figures 7.1-9 through -11.

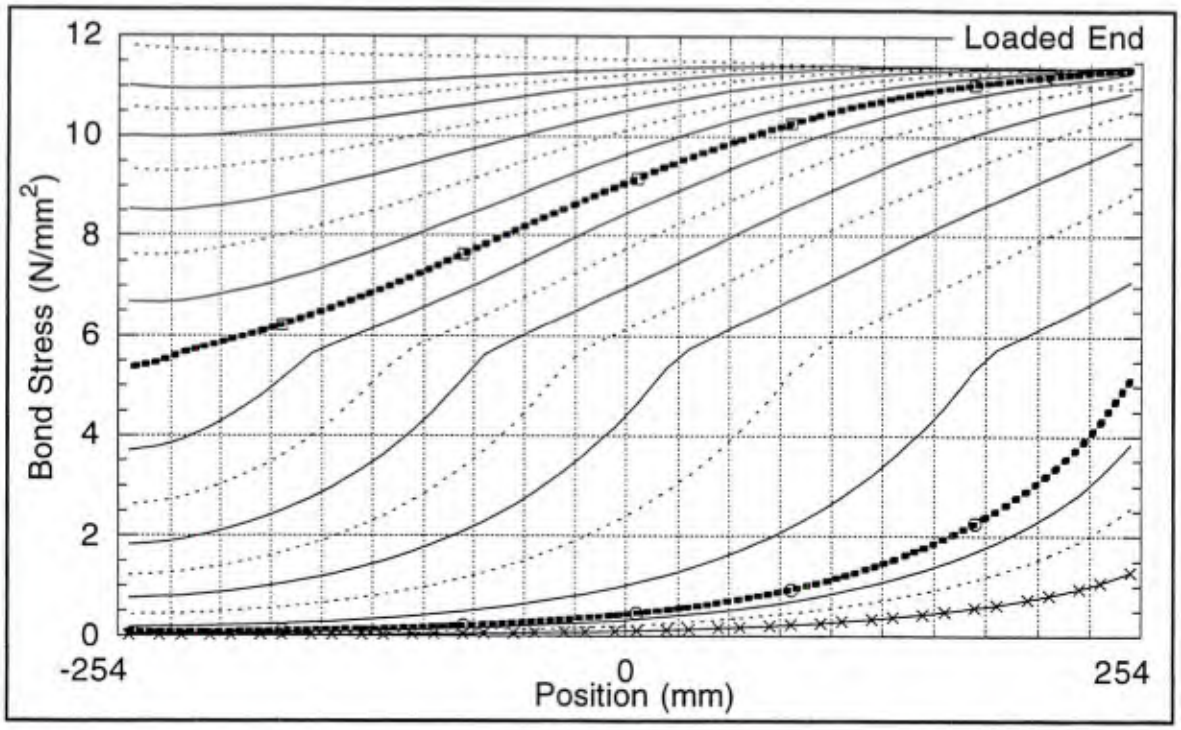

Figure 7.5-7 Bond stress distributions predicted by a model of Shima specimen 4 up to the maximum bar force.

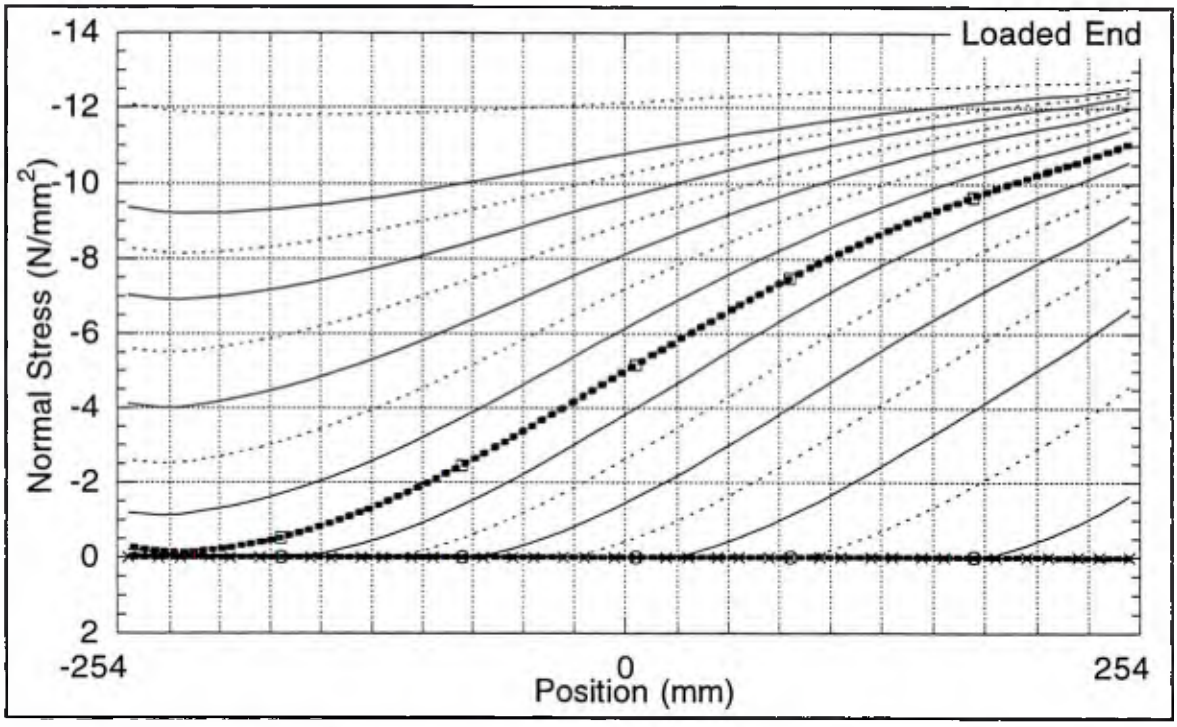

Figure 7.5-8 Normal stress distributions predicted by a model of Shima specimen 4 up to the maximum bar force.

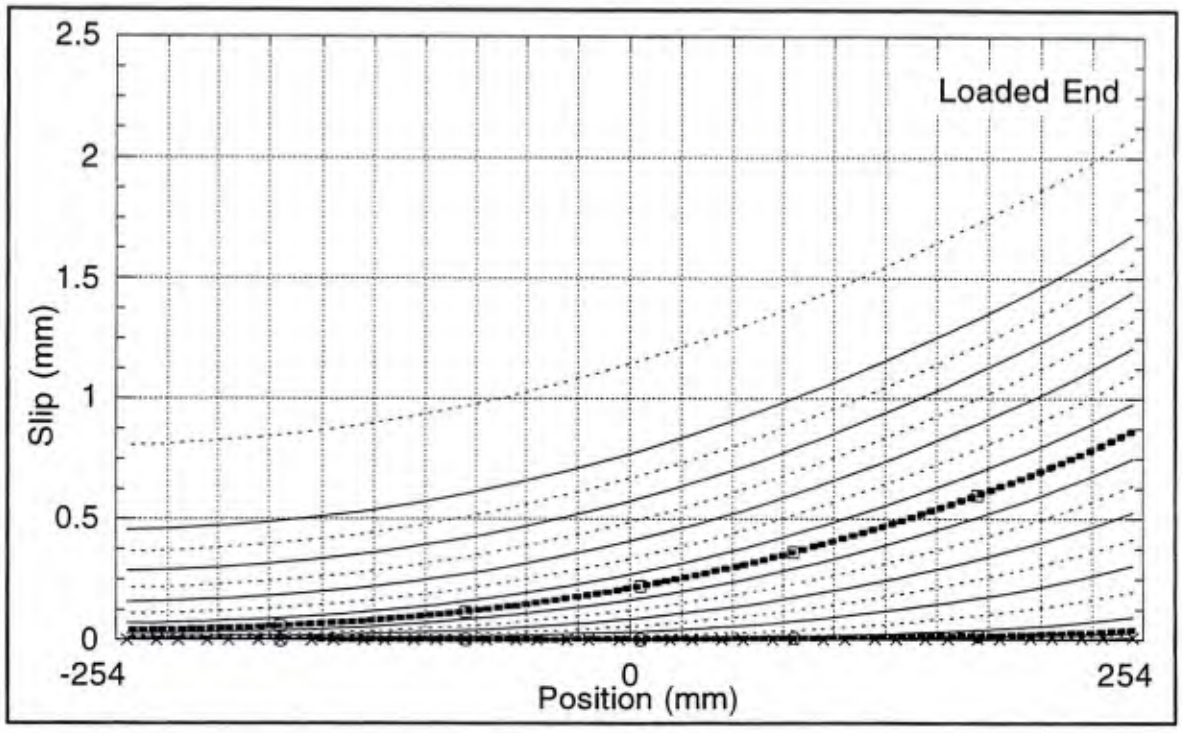

Figure 7.5-9 Slip distributions predicted by a model of Shima specimen 4 up to the maximum bar force.

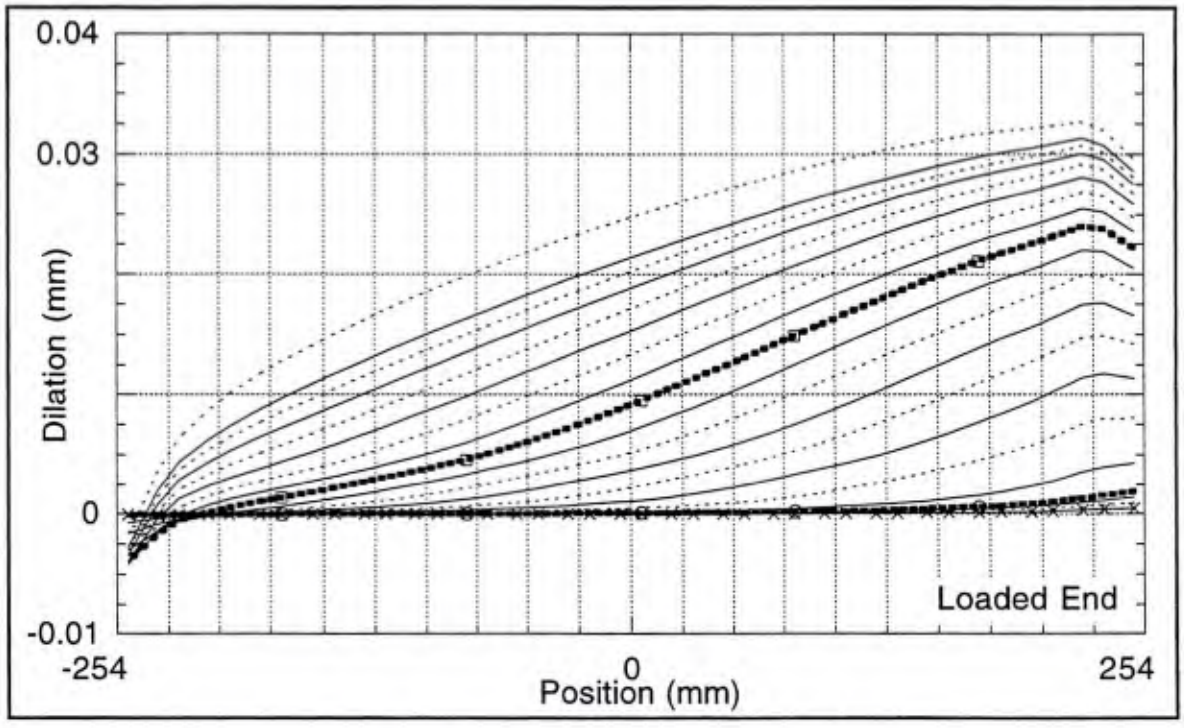

Figure 7.5-10 Radial dilation distributions predicted by a model of Shima specimen 4 up to the maximum bar force.

For the fully plastic phase the bond and normal stresses continue to increase (except for the bond stress near the loaded end). They both evolve to have a nearly uniform distribution when the bar force becomes a maximum. The linear variation of bar force with embedment length is dependent upon both traction components becoming uniform since they are coupled in the bond law. Furthermore, the nearly identical local responses shown in Figure 7.5-5 indicate that variation in the response distributions is due to a variation in slip (and thus damage) along the length of the bar; that is, locally the responses are "out of phase."

The slip distribution continues to exhibit higher gradients with continued loading. The "slip" plotted in Figure 7.5-9 is local slip as defined in this study – not the relative displacement measure used by Shima *et al.* (1987).

The "radial responses" (normal stress and radial dilation) are more difficult to evaluate since no known experimental data on their distributions exist. The dilation distributions, shown in Figure 7.5-10, suggest that additional development in the radial response could further improve the results. During the transition phase, dilation occurs along the specimen length except for the last two D_b of embedment. In this region the plastic slip is insignificant still, and the elastic bond response is inadequate to constrain the θ-rotation produced in the specimen. Clearly the constant value of D_{22}^{e} is too small in this end region. This region has experienced very little plastic slip so there is likely to be full contact between the bar and the concrete. With "full contact," the localized response near the rib is less likely to influence the response, and the analytical solutions presented in Figure 5.1-2 are more relevant. Based on Figure 5.1-2, a bond zone of thickness D_b (b/a=3) gives D_{22}^{e} on the order of $2.5E_c$. A radial contraction of the bond zone of 0.005 mm then results in a normal stress of approximately 400 N/mm^2. Though unrealistically high, this does suggest that the model should predict higher values near the free end of the specimen.

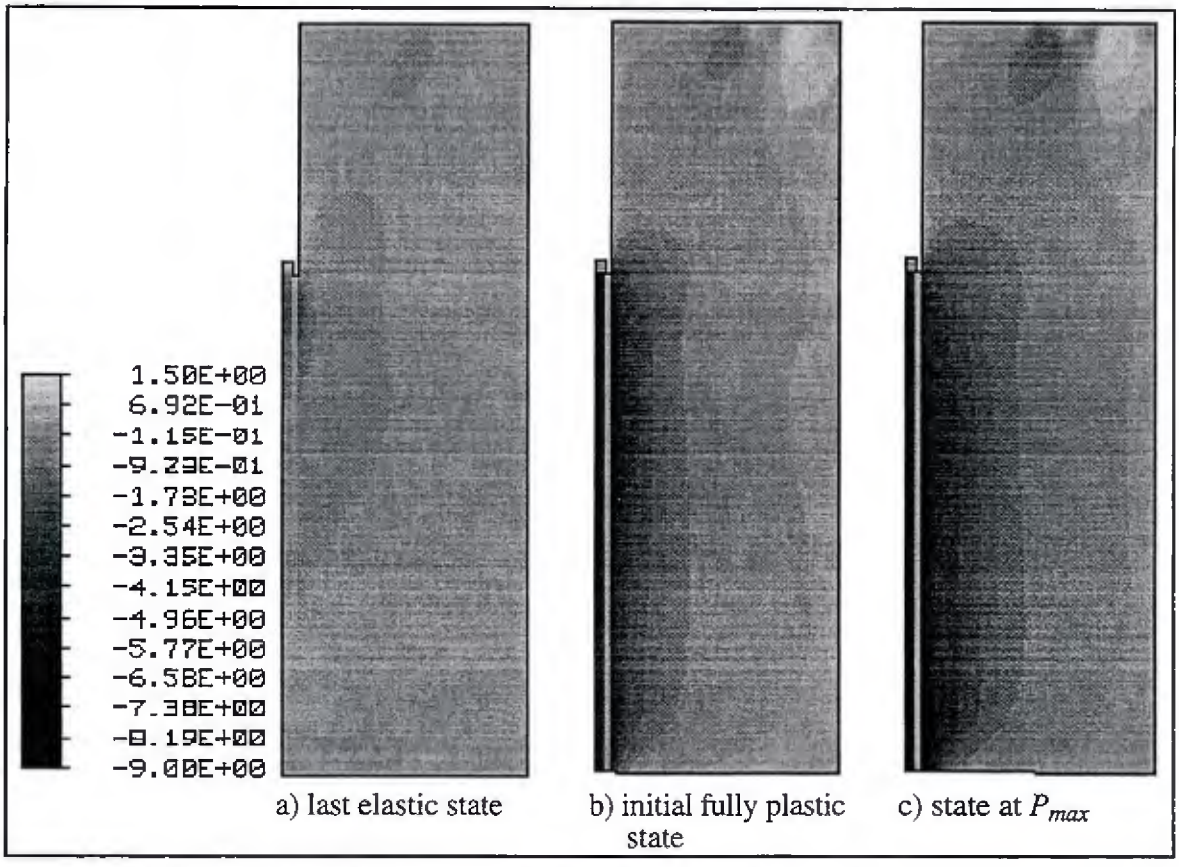

Figure 7.5-11 σ_{rz} stress field for Shima specimen 4 at three states.

As mentioned in Chapter 5, to reflect the underlying contact problem D_{22}^{e} should have a nonlinear description that, for example, decreases with plastic dilation. This change would be likely to predict locally higher normal and bond stresses near the free end consistent with the authors' experimental data.

Figure 7.5-11 shows the shear stress field in the specimen at three states of loading. As with the bond responses, the response is very localized during the elastic phase and becomes more uniform (relative to the position along the bar) near the maximum load. Radially the response is always localized near the bar. The unbonded length appears to adequately isolate the effect of the ring restraint boundary condition, which suggests that refinement of the boundary condition would have a second order effect.

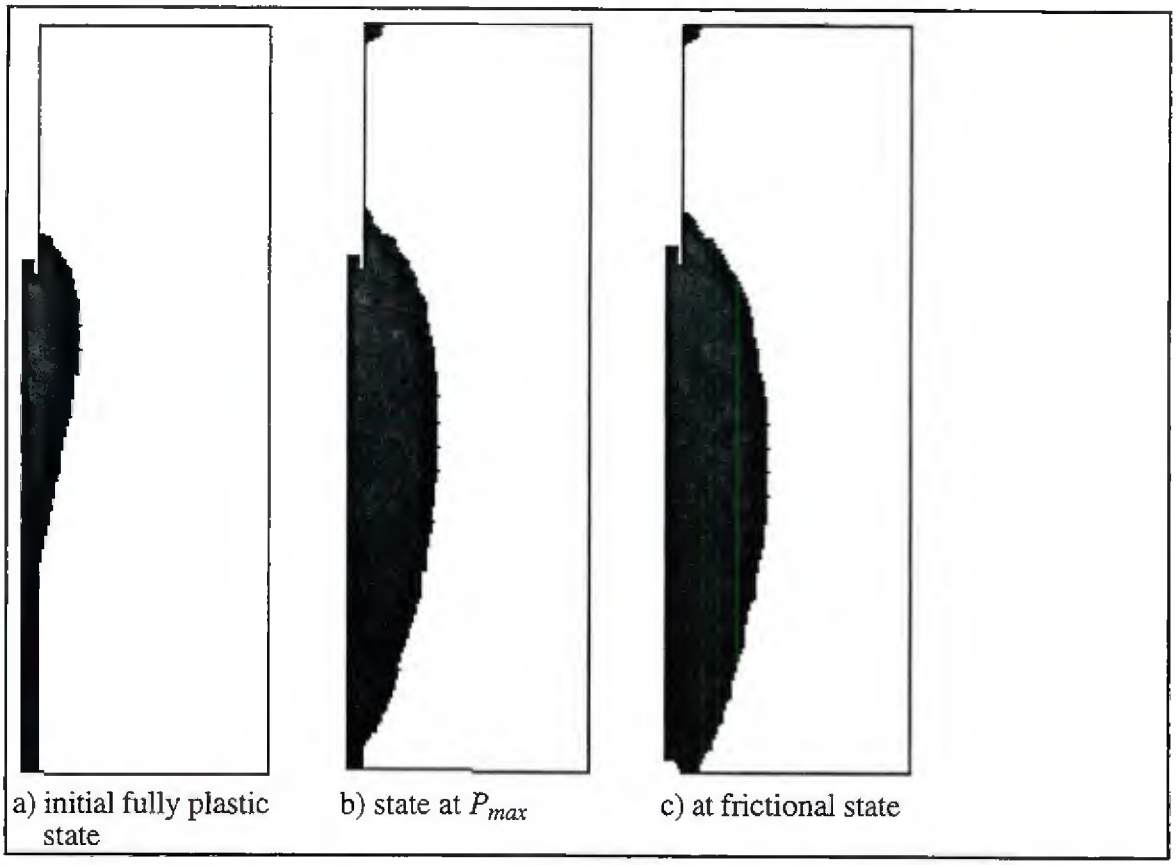

Figure 7.5-12 Longitudinal cracking for Shima specimen 4 at three states.

Figure 7.5-12 shows the predicted extent of longitudinal cracking at three key states. During the elastic response no wedging action is attributed to the ribs, and so by design the model has not experienced longitudinal cracking. When the bond zone has just become fully plastic, the longitudinal cracking is concentrated near the loaded end of the bar. Until more slip is produced near the free end of the bar, the wedging action does not become large enough to longitudinally crack the concrete. At the state of the maximum bar force, the longitudinal crack has grown to almost the full length of the specimen. Continued loading to the frictional response of the model results in little additional longitudinal cracking. The response is qualitatively consistent with the experiment. Though longitudinal cracking occurred, it was not likely to be seen on the exterior of the specimen and it remained stable throughout the tests.

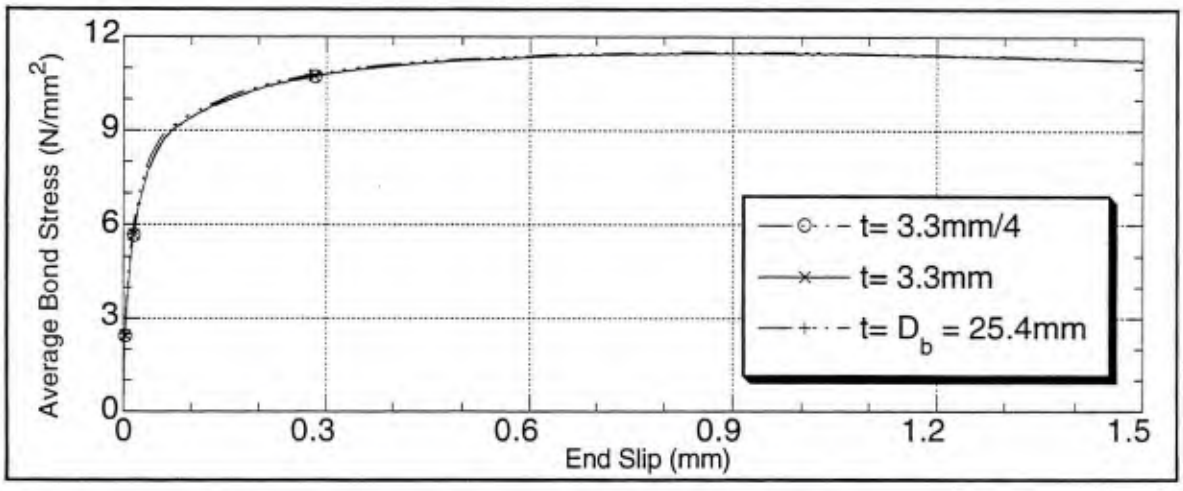

Figure 7.5-13 Average bond stress versus end slip for various bond zone thicknesses.

The last response of specimen 4 to be examined addresses the numerical issue of mesh sensitivity of the bond model – specifically with respect to the assumed thickness of the bond zone. Figure 7.5-13 shows nearly identical results for the model using bond zone thicknesses that vary from less than half a rib height to the bar diameter. This insensitivity is expected since: 1) there are no volume integrations associated with the finite thickness interface elements (Appendix G); 2) reasonable bond zone thicknesses are much less than the specimen diameter; and 3) the concrete model is "nearly linear." The Malvar results showed a large difference between the point model and axisymmetric model responses because the thick bond zone assumption of the point model eliminated the thick-walled cylinder response of the specimen. Similarly if a more sophisticated concrete model was used, thickening the bond zone could eliminate some of its nonlinear response. With a simple concrete model, as used in this example, replacement of a relatively small amount of concrete with the bond zone does not eliminate either a contributing mechanism or a region of significant nonlinear response. Though not shown the responses of the three models were nearly identical over the full range of slip.

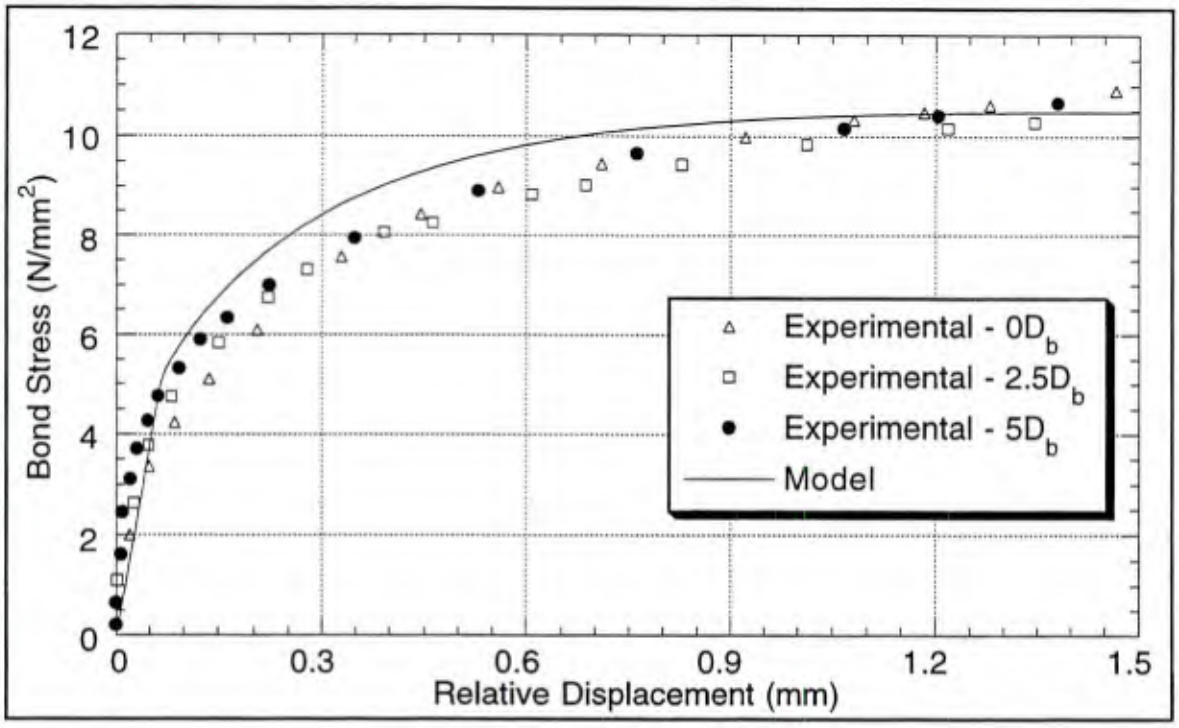

Figure 7.5-14 Bond stress versus relative displacement at $2D_b$ from the free end– a comparison of the model to Shima specimens with a bonded length of $6D_b$.

Figure 7.5-14 shows one last result in comparing the bond model to the results of Shima *et al.* (1987). As shown in Tables 7-1 and 7-2, specimen 7 differs in concrete strength and bar diameter from the other specimens. Its embedment length is $6D_b$. The three experiments differed in the unbonded length of the specimen that extended beyond the free end of the bar. Except for an apparent trend in the initial stiffness the results are almost identical.*

The local response of the model agrees very well with the experimental results. The elastic response of the model gives a good secant approximation to the initial experimental response. The subsequent elastoplastic response is also relatively accurate. Even when the

* If these results are an accurate measure on the authors' experimental scatter, the data is uncharacteristically repeatable.

results are good, we must recall that local experimental values are obtained from derivatives of bar strain data. For these specimens the strain gages were spaced at $2D_b$.

Overall the model reproduced the results of these experiments adequately. The global responses were predicted accurately for embedment lengths which would produce bar forces nearly 50 percent larger than the initial yield strength. The model's linear variation of maximum bond force with embedment length over predicts the test having a $20D_b$ embedment length by about 20 percent; the authors' heat treatment of standard bars might have produced this discrepancy. The model's local bond responses are not strongly dependent upon the position along the bar; in contrast, the experimental results showed significant variations near the free end of the bar. The interpretation of the experimental data yielding local bond stresses is very subjective. However, if the authors' experimental data are accurate they suggest a nonlinear representation of D_{22}^e (possibly including elastoplastic coupling) could improve the results.

It is not clear how previously suggested revisions in the calibration to produce greater radial dilation in the Malvar experiments would effect these results; a simple magnitude adjustment of D_{22}^e without adjusting the flow rule is likely to produce 1) excessively high responses, and/or 2) splitting failures.

As discussed for previous validation tests, a "more accurate nonlinear material law" for the concrete might affect the model's results, but it would probably be of secondary importance since the behavior it so localized near the bond zone.

7.6 Tepfers and Olsson Experiments

Tepfers and Olsson (1992) have a very unique test specimen that was designed to measure the splitting tendency of different rib shapes. Their cylindrical pull-out specimen is cast within a steel tube (of 0.65 mm thickness) which is strain gauged on opposite sides to determine the hoop strain in the ring. Assuming a uniform strain in the ring they can deduce the normal stress at the bar – assuming the latter is uniform too. The authors examine Swedish standard, high bond bars and specially turned bars. With the specially turned bars, they study the effects of rib height, spacing and related area on both bond stress and traction angle. Measurement of the traction angle* is motivated by Tepfers' (1973,1979) earlier efforts to provide an analytical expression for splitting resistance of concrete in anchorage zones. The traction angle gives an indirect measure of the normal stresses that occur in the bond zone.

As shown in Figure 7-1, the specimen of Tepfers and Olsson is overall the smallest specimen considered in the validation study. Table 7-2 indicates that the relative embedded length, L_b/D_b, is also the smallest considered (identical to Rehm and Eligehausen [1979]). Unlike any of the other specimens, this specimen does not have an unbonded region at the loaded end of the specimen; this could be significant since the teflon bearing is relatively flexible and might provide significantly less confinement to the concrete.

Once the longitudinal cracks have extended to the steel ring, it is not clear how quickly the steel ring debonds from the concrete. This is important because the hoop strain can only provide an accurate measure of the radial force if the ring is allowed to uniformly expand circumferentially.

* This is referred to as the angle between the bond forces by the authors.

Specimen Models

Figure 7.6-1 shows the mesh of the finite element model which is identical for all three specimens considered. Though not perceivable at the scale shown the thin steel pipe was modeled with four elements through the thickness; unfortunately an axisymmetric shell element is not yet available in Geneseos.

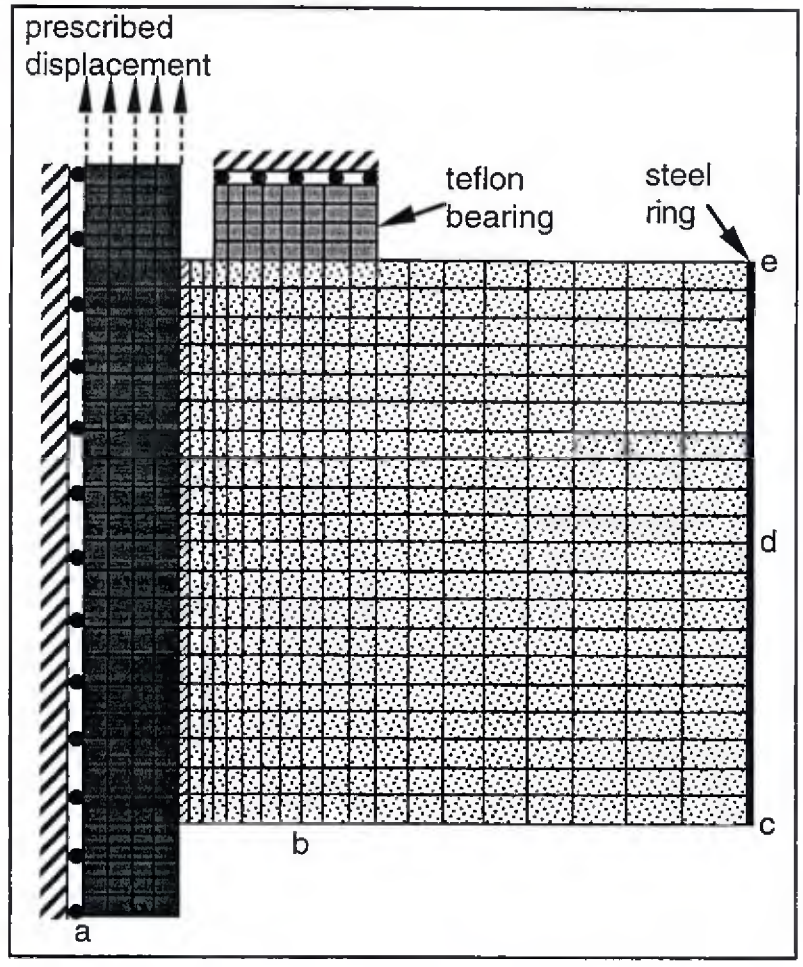

Figure 7.6-1 Axisymmetric model of the Tepfers and Olsson specimen.

The teflon ring was included in the model since it might provide significantly less confinement to the adjacent concrete than a roller boundary condition. However, this effect is probably negated by the elimination of transverse cracks (in the homogenization) and the use of a simple concrete model. The ring might slide against the concrete surface but is modeled as being connected; the relatively flexible teflon is assumed to provide negligible restraint to the cracking of the concrete.

The end slip was taken to be the vertical displacement of point *a* relative to point *b*. This is consistent with the schematic of the test arrangement given by the authors.

The bond zone was taken to be 1 mm thick. The concrete is modeled by the simple elastic-brittle model discussed in Appendix D using the tensile strengths given in Table 7-2. Two concrete tensile strengths for the bond zone were considered. The first was obtained by determining an "equivalent compressive cylinder strength" from the relationship given by L'Hermite (1955) and then using Equation (B-1) to determine the tensile strength. The second tensile strength considered was simply the cube splitting strength given in Table 7-2.

Results

This subsection presents results for three different specimens (the last of which consists of several distinct tests). The first two specimens considered use standard Swedish bars with rib angles of 90 degrees (see Table 7-1). The rib spacings (relative to the bar diameter) of these two bars serve as upper and lower bounds of the previously considered specimens. The last series of tests considered use specially turned bars with a rib angle of 45 degrees

Bond stress versus slip is examined for all the specimens. For the first specimen (test 1) the effects of the relative displacement measurement and steel tube strain measurement are briefly considered. For all the figures in this subsection when the model results are presented for two tensile strengths, the first represents the "formula value" (see previous section) and the second represents the cube splitting strength. If not specified, the "formula value" is used for the tensile strength in the bond law.

Figures 7.6-2 and -3 compare the average bond stress versus slip response of the authors' first test and variations on the model. In Figure 7.6-2 the end slip is measured relative to two points – one near point *b* and one near point *c* (see Figure 7.6-1). In Figure 7.6-3 the effect of using an estimated tensile strength in the bond law versus using the actual cube splitting strength is considered.

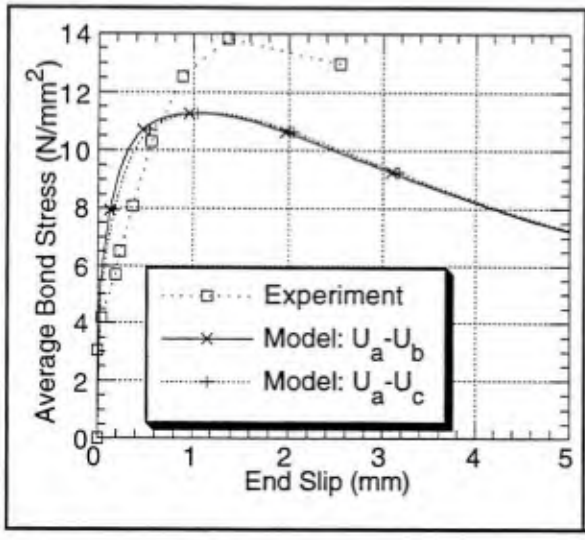

Figure 7.6-2 Average bond stress versus end slip for models with two different end slip measurements – Tepfers and Olsson's first specimen.

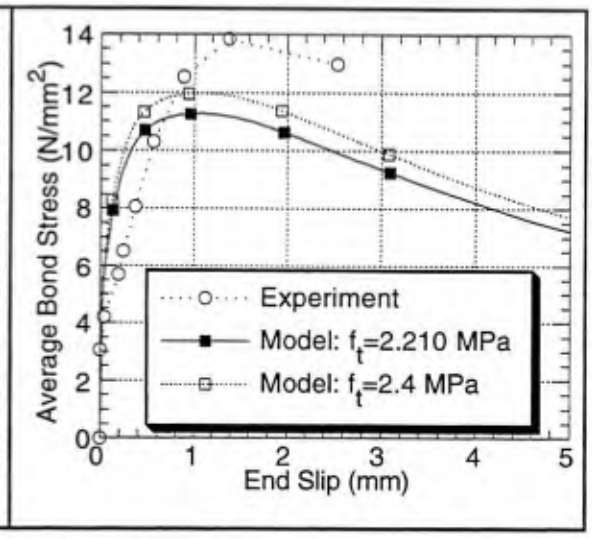

Figure 7.6-3 Average bond stress versus end slip for models with two different tensile strengths – Tepfers and Olsson's first specimen.

Figure 7.6-2 shows that the effect of the "transducer" position on the model response is not very significant. The only noticeable effect is a reduction in the initial stiffness as the transducer is mounted further from the end of the bar; this is caused by the reduction in vertical displacement near the edge of the specimen. Clearly the position of the transducer can be deduced accurately enough from the authors' schematic diagram. It is likely that the effect of vertical displacement gradients could be more significant in the actual specimen since the model tends to smear the effect of transverse cracking.

Figure 7.6-3 shows that the use of the actual cube splitting strength (about 13 percent error in τ_{max}) for f_t is more accurate than using the "formula value" (about 19 percent error in τ_{max}). At the scale shown, both the model and experimental responses have a high initial stiffness. At a bond stress of about 4 N/mm^2 the experimental response shows a decrease in stiffness that the model does not predict. This could be a result of the specimen lacking an unbonded region at the loaded end. The teflon bearing, being relatively flexible, could

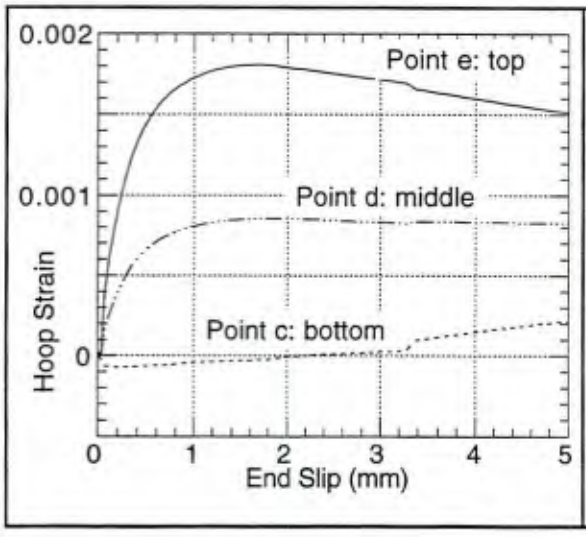

Figure 7.6-4 Hoop strain versus end slip predictions of the model at three points on the steel ring – Tepfers and Olsson's first specimen.

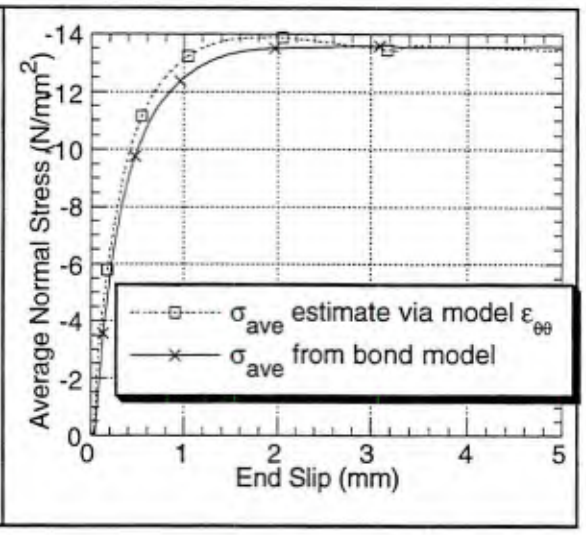

Figure 7.6-5 Two model estimates of average normal stress versus end slip – Tepfers and Olsson's first specimen.

accommodate a significant vertical displacement gradient on the loaded face of the specimen. Thus the effect of transverse cracks might be more pronounced for these tests.

Tepfers and Olsson assume that the measurement of hoop strain near the center of the steel tube (point *d* on Figure 7.6-1) provides a good measure of the normal stress in the bond zone. Figure 7.6-4 presents the model's prediction of hoop strain at the middle and edges of the steel tube. As with previously considered validation tests, the model predicts greater radial dilation near the loaded end of the specimen. Based upon these discrete results, it appears that the hoop strain at the middle of the tube might be representative of the average value and that the hoop strain tends to vary linearly over the height of the tube.*

Figure 7.6-5 shows the estimate of the normal stress based upon the single hoop strain measurement is very close to that obtained directly from the bond zone elements. Thus if

* In future ring tests additional strain measurements (along the height of the tube) might provide additional insight to the response of this specimen.

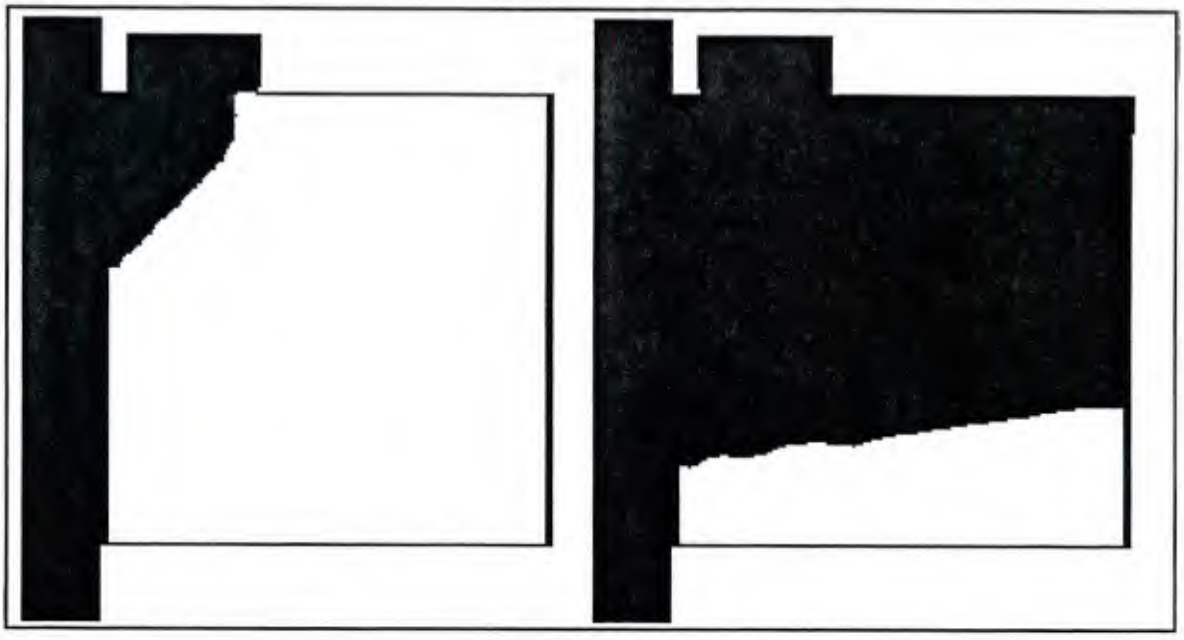

Figure 7.6-6 Example of the unstable propagation of the longitudinal cracks for Tepfers and Olsson's test 1. The prescribed bar displacements for the left and right plots were 0.14 mm and 0.16 mm, respectively.

the model accurately represents the actual specimen response, Tepfers and Olsson's assumption appears to be justified.

Except for the tests of Malvar, none of the other validation tests have exhibited externally detectable longitudinal cracking. Figure 7.6-6 shows the extent of longitudinal cracking for the analysis states bounding the unstable propagation of the longitudinal cracks in test 1. If softening were included in the concrete material model, the extent of longitudinal cracking would not experience as large of a jump in one step. The distribution of the cracking is consistent with the apparently greater radial dilation of the bond zone near the loaded end (as evidenced by Figure 7.6-4). To a lesser extent this "apparent rotation" of "half the cross-section" about the θ-axis has been observed in all the axisymmetric specimens.

The second test considered is test 3 of the authors' study. It has a different rib configuration (Table 7-2) and concrete strength (Table 7-1) than the first test. Figure 7.6-7

compares the average bond stress versus end slip response of the model (with two different tensile strengths) to the experimental results.

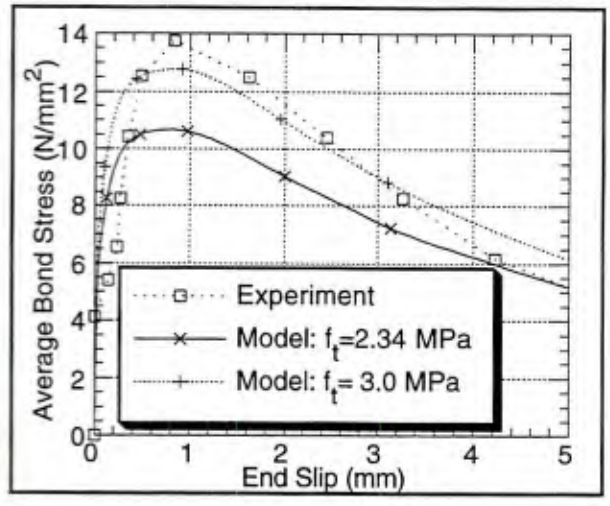

Figure 7.6-7 Average bond stress versus end slip for models with two different tensile strengths – Tepfers and Olsson's test 3.

For this test the tensile strength obtained from Equation (B-1) differs significantly from the measured cube splitting strength. As with the previous test, the model results based upon the cube splitting strength are more accurate than those obtained using the "formula value" – about 7 percent versus 22 percent "error."

One of the more attractive aspects of these tests is that the hoop strain provides an indirect measure of the normal stress produced in the bond zone. The authors reference the experimental work of Baranek (a personal communication) to argue that many radial cracks occur and therefore hoop stress in the cracked concrete can be considered to be negligible – the same assumption used for the concrete material model. From this assumption equilibrium in the radial direction leads to the relationship

$$\sigma=\frac{2tE\varepsilon_{\theta\theta}}{D_b} \tag{7.6-1}$$

where t and E are the thickness and Young's modulus of the steel ring, respectively, and $\varepsilon_{\theta\theta}$ is the hoop strain at point d.* As with the average bond stress estimate, this relationship explicitly assumes the normal stress is uniformly distributed.

* This is the relationship used to estimate the average normal stress in Figure 7.6-5.

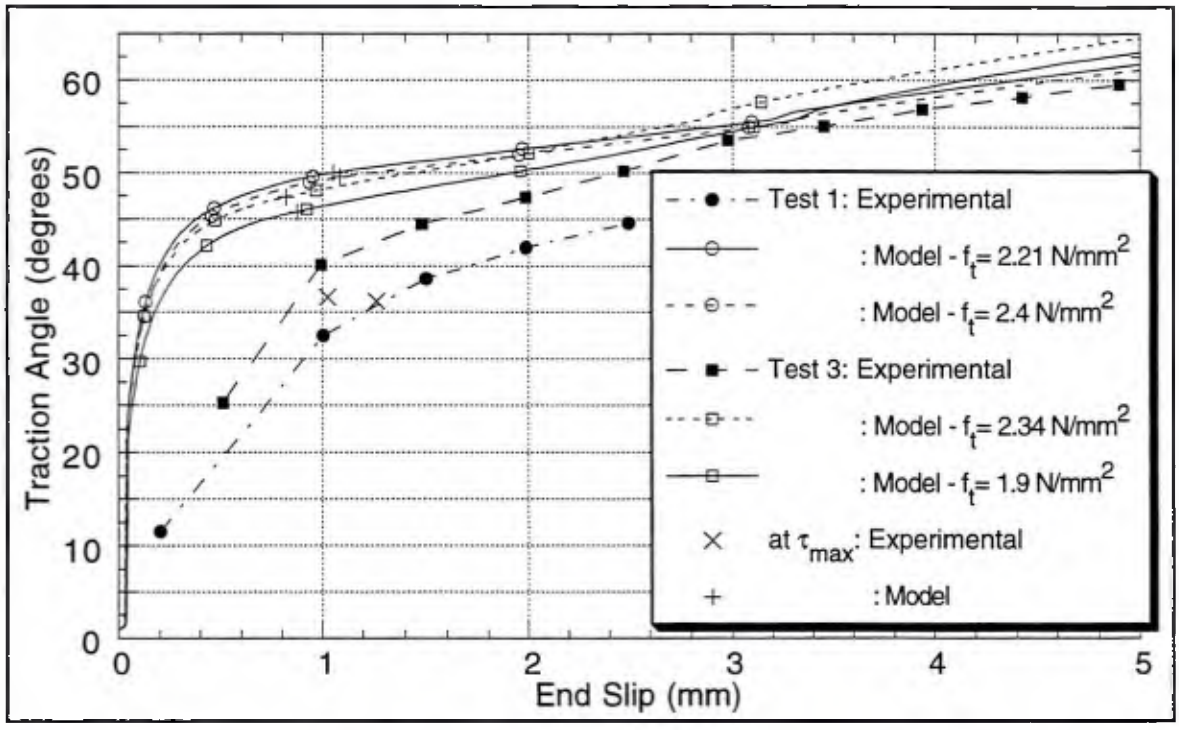

Figure 7.6-8 Traction angle versus end slip for the experiments and models – Tepfers and Olsson's tests 1 and 3.

With estimates of both traction components, the angle the traction makes with the axis of the reinforcing bar – the *traction angle* – can be determined. Figure 7.6-8 presents the traction angle versus end slip for the first two specimens and the corresponding model predictions. The values at the maximum bond stress are explicitly marked; for the experimental data the marked points were interpolated by the authors from representative curves fit to the data.

The various model results differ by less than 5 percent over most of the range. Prior to the maximum bond stress, the models exhibit a significantly greater traction angle than the experimental results (*i.e.*, the normal stress, relative to the bond stress, was disproportionately high). As the slip increases, the model results and experimental results (only test 3 applies) show better agreement.

Some of the previous validation problems indicate the confinement stress or corresponding radial dilation are under predicted; for the tests considered here the opposite seems true if we consider the traction angle alone. On the other hand, increasing the confinement stress would produce higher bond stresses since the yield surface monotonically increases with respect to this quantity. A possible explanation addresses an important assumption by the authors – that the number of radial cracks are numerous enough to produce uniform tractions with respect to θ. If the number of cracks that breach the edge of the specimen is small (*e.g.*, three or four was typical in the Malvar specimens), the current model omits a second bond response that could affect the results – the bond between the steel ring and the concrete. If the strain gages fall between longitudinal cracks, the normal stress calculated by Equation (7.6-1) would underestimate the actual normal stress until the steel is free to slip relative to the concrete. The feasibility of this explanation for the discrepancy has not been analytically examined; it certainly defies the assumption of axisymmetry.

Figure 7.6-9 shows the average bond stress versus end slip response of the model for the authors' series 4 tests. The intent of these tests was to show the experimental scatter of the results, but the scatter in traction angle versus end slip is not presented. The authors conclude that for a given slip the scatter in bond stress is approximately 20 percent (*i.e.*, ±10 percent), and the maximum bond stress occurs in the slip range of 1.0 to 2.5 mm.

Over all the bond-slip response seems to be predicted with reasonable accuracy. As with the previous two tests, the model over predicts the initial stiffness probably because these specimens are less confined than previous specimens considered. The bond stress is overestimated by the model. The average maximum bond stress of the tests is about 8.94 N/mm^2. Unlike the previous cases, here the "formula value" for tensile strength is higher than the cube splitting strength. Again using the latter produces more accurate bond strength results (about 11 percent different from the mean) than using the "formula value" (about 14 percent).

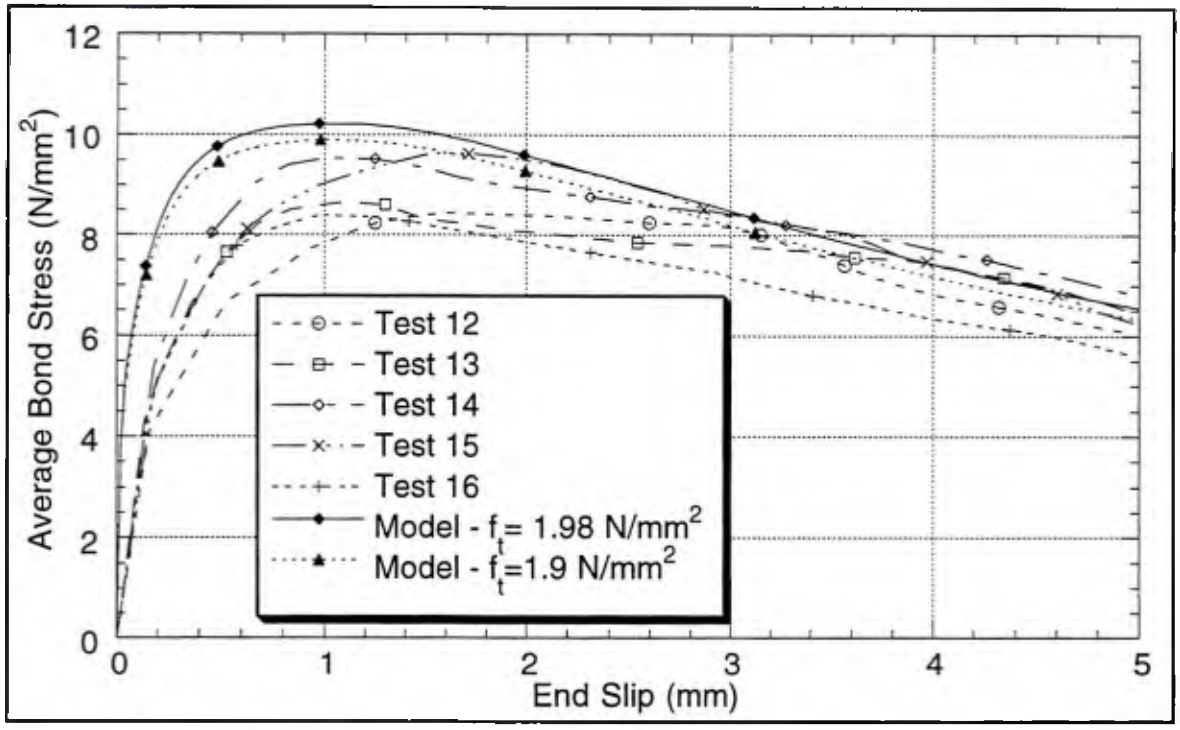

Figure 7.6-9 Average bond stress versus end slip for models with two different tensile strengths – Tepfers and Olsson's test series 4.

While the model falls within the accuracy goal of 20 percent, the bond strength falls outside of the experimental scatter for this series of tests. Note that for the first two tests considered the model under predicted the experimental results. These trends are consistent with the initial calibration to the data of Malvar (1991); the bond strength for bars with normal ribs is under predicted, and the bond strength for bars with skewed ribs (to the axis of the bar) is over predicted. These results again indicate that a refinement to the model to include the effect of rib angle on the bond strength might improve the model's overall accuracy. Considering that the rib angle of 45 degrees for the series 4 tests is a lower bound on all the validation problems, the apparent error in the current model is acceptable.

This chapter has presented a validation study examining the bond model's predictions of experimental results from six different research groups. The predictions of the model for each test have been discussed rather thoroughly. The next chapter concludes this study

presenting a summary of the model's development, strengths, and weaknesses, and recommendations for future work.

Chapter 8

Summary and Conclusions

This chapter provides a summary of the dissertation including key conclusions and observations. The chapter is organized into four sections. The first three sections summarize the dissertation in three divisions: 1) background, 2) model development and implementation, and 3) results. The last section presents recommendations for future work.

8.1 Background

The modeling of reinforced concrete requires models for the constituent materials, concrete and steel, and for their interaction. This study has focused on the latter in an attempt to provide a bond model with sufficient generality to reproduce the results of several experimental studies.

The earliest bond models were one-dimensional in nature relating bond stress to slip. Subsequent model development led to two-dimensional bond models that include normal stress and the conjugate relative displacement. These models are directly applicable at the bar-scale. The strength of the two-dimensional models is their potential generality; experiments have shown bond response to be dependent upon the stress state of the "adjacent concrete," and it was hypothesized that many "design parameters" (*e.g.*, cover thickness) might not be necessary for a model that is sensitive to this state. Furthermore, the mechanical interaction of the ribs can be more accurately represented and thus there is the potential to predict splitting failures. Many early two-dimensional models explicitly

modeled this interaction attempting to model the inclined compression strut contacting the ribs. While these models were usually limited in applicability, they were successfully used to model the response of many structural components and test specimens; the potential of bar-scale models was apparent.

Based upon experimental observations, a key premise to the model was that the normal stress (and the conjugate relative displacement) must be included to achieve a measure of generality and to predict different bond failure modes. Consistent with this premise, a bar-scale model was selected to meet the objective of developing a model that qualitatively reflected the micromechanics while having potential application at the member-scale. The model's initial application is limited to standard steel bars without coatings, subjected to monotonic loading with approximately an axisymmetric state near the bar.

Based upon experimental results that exhibited classical elastoplastic response, the theory of plasticity was selected as a framework in which to develop a model. While elastoplastic coupling had been observed, it was excluded from the initial model since insufficient data existed to quantify the effect; additionally, model simplicity promoted potential member-scale application. The plasticity model development required the definition of generalized stresses and strains, a yield surface, a flow rule, and elastic moduli.

8.2 Model Development and Implementation

The generalized stresses and strains are defined as unit cell averages of interface tractions, and the corresponding conjugate relative displacements nondimensionalized by the bar diameter, respectively. Conceptually the unit cell has the length of one rib pattern and a radius sufficient to bound the transverse cracks. The description of the bond phenomena in terms of interface quantities is a necessary compromise for this project's goals; details of the micromechanics are lost, but application of the model to member-scale application is a possibility.

Simplifying assumptions about the evolution of bond and the behavior of the Malvar (1991) specimens allowed yield surface and flow rule data to be extracted directly from his experimental data. While subsequent validation efforts indicated assumptions related to the flow rule might be inaccurate, the model still met the accuracy goals (bond stress estimates within 20 percent of measured values) for these tests.

The yield criterion expressed the bond stress as a linear combination of a power and exponential function of the normal stress. The former characterized the response when crushing and transverse cracking were dominant mechanisms, and the latter characterized the response when friction became the dominant mechanism. In addition to the transition of form, the yield surface evolution was characterized by kinematic softening and isotropic hardening and softening. Each component of the yield criterion was explained in terms of hypotheses on the underlying mechanics. The form of the evolution and shape of the yield surface were combined to provide increased "ductility" with higher confinement stress. The design and calibration of the yield surface produced a smooth bond response ($Q \in C^1(\underline{q})$).

The form of the flow rule is such that it is completely defined by the rate of plastic radial dilation with respect to plastic slip, g. The experimental data show numerous trends that are reflected in the analytical model, but the amount of experimental data is very sparse. For bars with ribs normal to the axis of the bar, the flow rule exhibits four states of observed response: 1) radial dilation, 2) constant radius, 3) radial contraction, and 4) sliding.

The proposed mechanics of each observed response stage was discussed. A particular example was the explanation for characteristically low values of the *effective coefficient of friction*; it appears the radial contraction (relatively small compared with the dilation) could be constrained by damaged material, both due to material dilation and deposition into cracks, thus reducing the actual normal stress at the bar surface.

At the bar-scale a nonassociative flow rule is essential for an accurate model. During the radial dilation state the form of the model reflects the geometric instability associated with the wedging action of the ribs and its dependency upon the normal stress.

Since a nonassociative flow rule was used, it could be developed somewhat independently from the yield surface. Nonetheless, thermodynamics constrained the combination. For the current calibration, the model was found to satisfy the second law of thermodynamics (*i.e.*, positive incremental plastic work). Simple analysis showed that except for special cases (of which Coulomb's law is an example), the radial dilation of the model must be dependent on the normal stress to maintain positive incremental plastic work.

Material stability is also an issue for laws with a nonassociative flow rule. In the case of the bond model, localization around the bar is explicitly included in the model, so analyses which provide the orientation of the plane of localization are unnecessary. With a nonassociative flow rule there is the potential for an instability under stress control even during hardening. That is, there potentially exists a stress path (the so-called wedge path) where the second order work remains negative during plastic loading; thus, the path cannot be followed under stress control. Apparently, this type of stress path has not been experimentally investigated in bond tests. So in the context of bond, it is not known if this instability has a physical basis or if its existence would simply be a mathematical quirk.

A model for the elastic response was significantly complicated by the concrete-rib contact problem. A hypothetical Cauchy elasticity law exhibited many traits of the contact problem, but "incremental elastic moduli" were adopted for simplicity. The moduli are "essentially" linear elastic. The off-diagonal terms are zero for zero slip, and their sign depends upon the direction of loading. The concrete-rib contact is recognized in the description of the simplified moduli but to a lesser extent than the hypothetical Cauchy elasticity law.

With a simple form for the elastic moduli adopted, the individual moduli were determined from experimental data. Thick-walled cylinder solutions suggested D_{22}^{e} should be relatively large with a significant bond zone thickness dependence (*i.e.*, depending on the assumed radius of the bond zone). These analyses also demonstrate the ambiguity of using a traction for the generalized stress while visualizing a relatively thick bond zone. Experimental data suggested elastic moduli two orders of magnitude smaller (for bond zones of thickness D_b) than the simple analyses; suggesting the response is localized near the ribs. A localized response was assumed, and the elastic moduli were defined to be proportional to the elastic modulus of concrete. Assuming the off-diagonal terms were small, the diagonal moduli were determined from experimental data. Several experimental studies were used to determine D_{11}^{e}. Examination of Malvar's (1991) data did not suggest D_{11}^{e} was a function of the normal stress. Data for determining D_{22}^{e} appeared to be nearly non-existent. A few tests of Malvar (1991) with a normal stress unload-reload gave a weak estimate of the order of magnitude of D_{22}^{e}. A flexibility interpretation of the Malvar (1991) radial dilation graphs gave order of magnitude estimates of the off-diagonal terms (two orders of magnitude smaller than the diagonal terms). As such, it appears that subsequent versions of the model could be simplified by eliminating the off-diagonal terms. The small magnitude of these terms is consistent with the accepted understanding of the mechanics; significant wedging effects (alias coupling) do not occur until crushed material near the rib face increases the effective angle of contact.

The weakest components of the model are related to its radial response – the flow rule and D_{22}^{e}. The experimental data available for both of these components were very limited. With this perspective, the effect of possible refinements of the model or its calibration was discussed for several validation problems.

Most of the mechanisms related to bond have been discussed in the literature, however, their relative importance has been controversial. The experimental data on which the model

is based do not usually allow one to distinguish the effects of the various mechanisms. Discussion of the mechanics 1) provided insight to the interrelation of some mechanisms (*e.g.*, the deposition of damaged material into open cracks), 2) gave a more rational basis for the form of the model, and 3) suggested limitations of the model.

The forms of the model's components suggest that for a model designed to reflect the mechanics, the scale of the ribs is still a liability. The kinematic softening, isotropic hardening, and radial dilation stage of the flow rule all reflect the size of the rib and the related instability which occurs during bond failure. To partially alleviate this problem, the evolution of the yield surface is expressed in closed form. However, this approach must be abandoned when extending the model to cyclic loading, and accurate integration of the flow rule is still a difficult task.

The bond model was implemented in the context of a general, nonlinear, implicit finite element system (Geneseos). A full Newton-Raphson method was used to solve the global system of nonlinear equations. The bond model can be easily incorporated in any system that has interface elements which allow for two-dimensional constitutive relations (*i.e.*, both normal stress and relative displacement must be included). For this study, the cutting-plane algorithm was selected for stress point calculations. The principal motivation for using this algorithm was its explicit form in the update of internal variables and plastic strains. The explicit form only required first order derivatives to be calculated of constitutive relations, and thus lessened the implementation burden during the model development cycle. The algorithm's simplicity comes at the following costs: 1) first order accuracy, 2) lack of algorithmically consistent elastoplastic moduli, and 3) a stability proof that does not appear to apply to the bond model during radial contraction (when the plastic potential function is nonconvex). While the algorithm was excellent for model development, an algorithm which overcomes the listed "costs" should be used in future implementation efforts. Second order accuracy would help alleviate the difficulty in

integrating a model which characterizes mechanics at the rib-scale. Algorithmically consistent elastoplastic moduli permit the global Newton-Raphson algorithm to attain quadratic convergence thus facilitating the model's application to large problems.

8.3 Results

Experimental data from six different research groups were considered in the calibration and validation effort. The specimens used by these groups varied significantly in both geometry and material properties. For example, bar diameters varied from 14 to 30.7 mm; specimen diameters varied from 7.6 to 50 cm; and concrete compressive strengths varied from 18.5 to 40.2 MPa. Only pull-out type specimens were considered.

The overall accuracy goal was to achieve a bond stress-slip response that was accurate to about 20 percent over the full-range of slip, for all the experiments. Many experiments have exhibited experimental scatter of this magnitude, and most of the experiments considered in this study have little or no measure of scatter.

In the calibration and validation analyses, two types of specimen models were used: point models and two-dimensional FEM models. The point models incorporated closed form solutions to represent the behavior of the specimen; they were implemented discretely and thus required no spacial approximation – thus their name. For most of the specimens, two-dimensional FEM models better approximated the specimen response; even these models incorporated many simplifying assumptions. For example, the concrete was modeled with an elastic brittle law which allowed splitting cracks to develop when a maximum hoop stress was attained. It did not include tension softening in its response.

The calibration, as discussed in the chapters on model development, focused on the data of Malvar (1991). There was no direct measure of experimental scatter and in some instances

the variation in the bar rib pattern appeared to significantly affect the response (especially the radial dilation). No distinction was made between bars having different rib patterns.

The calibration results accurately reproduced the experimental results of Malvar (1991) using a point model. The effects of the kinematic softening and shape evolution of the yield surface were only significant at very low confinement stress, where the experimental results showed similar irregularities. In particular, the kinematic softening appeared to qualitatively reflect the geometric dilation which is most significant at low confinement stress. The combination of isotropic hardening and kinematic softening successfully produced the increased "ductility" with higher confinement stress, that has been observed in experimental results such as Malvar's (1991).

All subsequent analyses used the same calibration. For a given validation test, the bond model only required the specification of four physical parameters; the parameters consisted of two geometric properties of the bar (diameter and rib spacing) and two material properties of the concrete (elastic modulus and tensile strength). Generally the concrete material properties were obtained from empirical relationships with the concrete compressive strength (Appendix B).

The two-dimensional analyses of the Malvar (1991) specimen were among the last analyses conducted. These analyses were validating to some extent. The slip at maximum bond stress showed better agreement with the experimental data than the point model. However, the omission of hoop stress in the point model produced a different stress history for the bond zone. This resulted in a reduction of the normal stress, radial dilation and bond stress for the two-dimensional model. This effect was most pronounced at higher normal stresses (*e.g.*, at σ=–31.0 N/mm^2 the bond stress was underestimated by 13 percent). The reduction in radial dilation was much more significant.

The two-dimensional analyses indicate that simplifying assumptions made for developing the flow rule were not accurate, yet the results are within the 20 percent accuracy goal for bond stress versus slip. While the form of the model appears to be good, a parameter study varying D_{22}^{e} indicates the calibration could be refined. Additional experiments with the Malvar (1991) specimen to study scatter and the effect of rib patterns would make additional refinements in the calibration more meaningful.

The simple Malvar (1991) point model was used to study the bond model instability. The model is inherently unstable by design (*i.e.*, it has softening) since its response includes a potential localization of the bond zone. This potential instability under stress control has a physical basis and is thus desirable. The other potential instability occurs during hardening when the stress path traverses the wedge region where the second order plastic work is negative. Very limited numerical studies of the wedge path exhibited second order elastic work sufficiently large to maintain stability (*i.e.*, the total work remained positive). While this is not a proof, these analyses suggested instability during hardening might not occur for the current calibration.

Examination of the spectrum of the elastoplastic moduli gave insight to how the individual moduli are related to the model components. Furthermore, it indicated that increasing the elastic moduli (particularly the diagonal terms) in calibration refinements would increase the likelihood of instability during hardening, since the second order elastic work would be reduced.

Gambarova *et al.* (1989) performed experiments where a fabricated crack opening was controlled. The constraining transverse forces gave "a measure" of the normal force on the bar. Both point and plane stress models of the Gambarova *et al.* (1989) specimen were developed. The various specimen models behaved nearly identically. Though sufficiently accurate, the initial stiffness was overestimated. The slip at τ_{max} and bond stress-slip softening response showed excellent agreement with experimental results. The maximum

bond stress was underestimated by about 9 percent. The confinement stress was underestimated by about 18 percent, and the experiment exhibited a more distinct maximum. The normal response was similar to that of other studies (*e.g.*, Malvar, 1991, series 3) with "angled ribs," but the model's flow rule is based more directly upon bars with "normal ribs." Again, including the effect of the rib pattern could improve the results.

The model exhibited what Gambarova *et al.* (1989) refer to as *confinement lag*. Physically this phenomenon is consistent with the accepted explanation of bond mechanics; that is, the wedging action of the ribs increases after local crushing at the face of the ribs. They observed this in their experiments but subtracted the effect when presenting their results. The model exhibited this response because the coupling elastic moduli were small.

Eligehausen *et al.* (1983) conducted an extensive set of bond tests with specimens which characterized the highly confined state in a beam-column connection. Unlike most validation problems, this one had an indication of experimental scatter. The specimen included a secondary reinforcement cage the effect of which was grossly accounted for in different point models. The model was rather insensitive to the exact model of the reinforcement; this was consistent with the authors' experimental observation that increasing the secondary reinforcement stiffness had a negligible effect on the bond response.

The model's behavior was very accurate over the full range of slip for the Eligehausen *et al.* (1983) test. Compared to the average response of the series, the early stiffness remained somewhat high producing failure at a smaller slip. However, the model response was still within the scatter, and the maximum bond stress was very accurate.

Rehm and Eligehausen (1979) studied the effect on bond of cyclic loading under stress control. Compared to the previous two validation problems, the specimen was significantly simpler to model. An axisymmetric finite element model of the specimen was

developed using the simple elastic-brittle model for the concrete. (The basic form of the model is shared by the two remaining validation studies.) The authors provided the compressive cube strength of the concrete. This compressive strength and the "equivalent cylinder strength" were employed in analyses.

Since the experiments of Rehm and Eligehausen (1979) were under stress control the range of slip was limited to the slip at failure, about 0.7 mm. The model's behavior showed very good agreement with the experimental results over this whole range. Using the cube strength, the model appears to have been fit to the experimental results; using the cylinder strength, the maximum bond stress was underestimated by about 16.5 percent.

The stress field in the specimen reflected a very localized response. This gives some support for the use of a simple concrete model assuming the bond model captures most of the nonlinear behavior.

As observed in the experiments, the model exhibited a pull-out failure. The radial response of the bond model produced longitudinal cracks in the specimen, but they remained stable and did not fail the specimen.

Shima *et al.* (1987) performed many monotonic pull-out tests some of which were loaded beyond the original yield point of the bar. To prevent splitting failures, the cylindrical specimens were designed with a diameter of 50 cm. The bars were heat-treated to increase their yield strength, thus allowing longer embedment length tests. Unlike previous tests considered in this study, these did include some bar strain measurements.

The model estimated the pull-out force of bars with embedment lengths ranging from 5 to 15 D_b. For the bar with an embedment length of 20 D_b, the model overestimated the pull-out force by about 20 percent. Below the initial yield strength of the bar, both the experimental and model results indicated the pull-out force was linear in embedment length. Above this level of force, the experiments exhibited less change in the pull-out force with

increased embedment. It was not clear if the unknown bar properties or bond behavior was responsible for the discrepancy.

The local bond stress was difficult to estimate near the unloaded end of the bar, but the authors' interpretation of the data gave bond stresses nearly 28 percent higher here than the remainder of the specimen. The model predicts these higher values accurately but appears to overestimate the internal values.

Stresses and relative displacements were examined for the Shima *et al.* (1987) specimen with a $20D_b$ embedment length. These results are representative of the model's response for long embedment. Short embedment specimens do not exhibit as much variation but are qualitatively very similar in response. The response up to the maximum bar force can be summarized as:

1. Bond stresses had high gradients during the elastic response, locally reduced in gradient during the plastic transition, and then became nearly uniform at the maximum bond stress.
2. Normal stresses were nearly zero during the elastic response, showed significant gradients during the plastic transition, and then became nearly uniform at the maximum bond stress.
3. Slips were nearly zero during the elastic response, and then continued to increase in magnitude and gradient.
4. Radial dilations were nearly zero during the elastic response, increased significantly near the loaded end of the member during plastic transition, and then evolved to almost a linear variation along the length of the bar. There was a noticeable reduction in normal stress near both ends of the specimen.

Unless the specimen causes a significant variation in normal stress along the length of the bar, the bond model will tend to predict uniform stress distributions (bond and normal). This is partially due to the following two factors: 1) a relatively simple measure of the

internal state of the material (d), and 2) an elastic modulus (D^e_{22}) that is not sensitive to the radial dilation. The last factor is made apparent by the radial dilation response near the free end of the specimen. As with all the axisymmetric models, there was a tendency for the specimen to rotate "like a ring subjected to a moment." This caused the free end to rotate toward the bar and cause a slightly higher normal stress. If D^e_{22} was sensitive to the radial dilation (*e.g.*, through elastoplastic coupling), then an increased modulus would produce significantly higher normal and thus bond stresses near the end of the beam. This would correspond to the behavior observed in the experiments, but would probably increase the predicted bar force at failure.

Two additional possible weaknesses of the model are a simple concrete model which might be unable to adequately represent the change of state in the concrete near the bond zone, and the lack of sensitivity of the model to the longitudinal normal stress in the bond zone. Further consideration of these various issues could change the model's tendency to estimate a linear variation of pull-out force with embedment length.

A study of the model sensitivity to bond zone thickness showed no mesh sensitivity in the bond model. This was due to the use of 1) interface integration with a finite thickness interface element (*i.e.*, integration at the bar surface), 2) relatively small bond zone thicknesses as compared with the specimen diameter, and 3) a "nearly linear" concrete model.

As with the last validation problem, longitudinal cracks developed within the specimen but remained stable and did not fail the specimen.

The last set of validation problems was a set of unique tests performed by Tepfers and Olsson (1992). Their intent was to measure the splitting tendency of different rib shapes. Their small cylindrical specimen was cast in a steel ring, so strain measurements on the ring gave a measure of the normal forces developed by the bar. Unlike all other specimens

considered, this specimen did not have an unbonded region at the loaded end. Confinement in the longitudinal direction was only provided by a relatively flexible teflon bearing ring.

The initial model results suggested that the strain measurements at the middle of the steel ring gave a good indication of the average normal stress after splitting. However, comparisons of model and experimental results indicated that the model had a higher traction angle for small slips (*i.e.*, the model's normal component of traction was too large in magnitude relative to its bond stress). Earlier validation problems suggested the opposite – that the normal stress produced by the model should be larger in magnitude. One explanation questions the modeling assumption of axisymmetry. It could be that the bond between the steel ring and concrete initially reduced the strain in the ring (except near cracks) thus under predicting the magnitude of normal stress in the experiments. The feasibility of this explanation has not been investigated.

Tepfers and Olsson (1992) used bars with rib angles that bounded (45 to 90 degrees) the rib angles of all the validation specimens. Consistent with the calibration, bond stresses for bars with small rib angles (*e.g.*, 45 degrees) were overestimated, and bond stresses for bars with normal ribs were underestimated. In contrast to this trend, the specimens of Gambarova *et al.* (1989) used bars with rib angles of 52 degrees and the model underestimated the bond stress.

Two tensile strengths were considered, the cube splitting strength and the tensile strength attained from Equation (B-1). (The "equivalent cylinder compression strength" was first calculated before using Equation (B-1) to estimate the tensile strength.) Comparisons were made to three tests or series of tests – test 1, test 3 and series 4. Using the cube splitting strength, the model results differed from the experiments by approximately -13, -7 and +11 percent, respectively. Using the tensile strength estimate from Equation (B-1), the model results differed from the experiments by approximately -19, -22 and +14 percent,

respectively. In all cases, better accuracy was attained using the cube splitting strength. The best measure of tensile strength for the bond model deserves additional investigation.

Overall the model showed good agreement, in bond stress versus slip response, with experimental results. The agreement was acceptable over the full range (*i.e.*, approaching the spacing of the ribs) -- from initial stiffness, to maximum bond stress, through softening.

The initial accuracy objective of limiting the difference between experimental and model responses to 20 percent was generally met. The largest differences were observed in the Shima *et al.* (1987) specimen 4 test and the Tepfers and Olsson's (1992) test 3. As just discussed, when using the cube splitting strength the difference in this later test reduced from -22 percent to -7 percent. The accuracy objective was attained with a variety of specimens. They differed significantly in properties (see Tables 7-1 and -2) and configuration (see Figure 7-1) indicating that this model has *a measure of generality.*

The normal or radial response of the model is novel, but it could also be improved. For example, it appears the model failed to accurately predict the normal stresses near the free end of some specimens. This is mainly attributed to the assumption of constant elastic moduli. Clearly the elastic modulus D_{22}^{e} should become significantly larger when the radial dilation approaches zero. While the model could be improved with a nonlinear elastic law, the added complexity could reduce its usefulness.

The model appears to qualitatively reflect the micromechanics (*i.e.*, the mechanical interaction of the ribs with the concrete). The apparent change in "bond ductility" with confinement stress was reproduced. The development of splitting cracks was consistent with experimental results; generally this verification was limited to the observed mode of failure, but additionally the predicted permanent slip at splitting, for the Malvar (1991) specimen, was within experimental scatter. The model also predicted the confinement lag

phenomenon which can be associated with the initial crushing necessary to develop significant wedging action with the ribs.

8.4 Recommendations

The recommendations listed below outline additional work that could be undertaken (*i.e.*, if funding were available) to facilitate the use of and improve the monotonic bond model. Extension of the model to cyclic loading is discussed in Herrmann and Cox (1994), and thus related recommendations will not be included here. The recommendations are divided into three lists; the first list addresses proposed modifications of the model and additional validation problems, the second list addresses additional experimental studies that would aid further model development, and the third list addresses implementation efforts that would facilitate use of the model.

The following modifications to the bond model (or its current calibration) should be considered if further development efforts occur:

1. Recalibrate the bond model to increase radial response in the two-dimensional models of the Malvar tests, while maintaining or improving the prediction of the other tests. A combination of reducing the elastic radial contraction and increasing the plastic radial dilation should be pursued. Ideally this should be completed simultaneously with the next recommendation.
2. Incorporate elastoplastic coupling or nonlinear elasticity to vary the radial stiffness with deformation.
3. Simplify the description of the flow rule while retaining its basic behavior. One approach might be to define the flow rule in terms of the yield surface while retaining its nonassociative form; a special inner product definition, in which the plastic strain increments are associative, could give a simple description without over predicting the radial dilations.

4. Modify the yield surface and the flow rule to reflect different rib geometries.
5. Modify the yield surface to eliminate tensile normal stresses, as suggested in Chapter 5.
6. Simplify elastic moduli to a diagonal form.
7. Attempt to further validate the model with tensile bond tests.
8. Attempt to further validate the model with additional "long embedment specimens." In particular, additional comparisons to measured bond stress distributions are needed.
9. Compare the model predictions to the tests results of Eligehausen *et al.* (1983) using #2 secondary reinforcing bars. Experimental results showed a reduction in bond strength with the more flexible cage.
10. Extend the model validation to three-dimensional analyses, so problems with non-axisymmetric states in the bond zone can be more accurately examined.
11. Attempt to validate the model using the current calibration but a more sophisticated concrete model. In particular, sensitivity of the specimen model predictions to alternative concrete models and bond zone thickness is of particular interest.

Some of the above mentioned modifications require extensive validation tests. The use of constrained optimization for material parameter identification might be the most cost effective approach. Since the function evaluations (of the constrained optimization approach) would be a weighted measure of the model's error relative to several experimental studies, they could require significant computer time.

The following experiments would promote additional model development efforts:

1. Test the Malvar specimen to study scatter and the effect of rib patterns.
2. Test the Tepfers and Olsson specimen with additional strain gages on the steel ring. A better understanding of the specimen behavior would clarify the radial response of the actual specimen.
3. Test the Malvar specimen with various normal stress histories so the radial response can be clarified. As suggested in Chapter 5, for different values of plastic slip a confinement

stress increase followed by a decrease to the "initial" stress state would provide valuable information about the normal response. In addition, tests with continuously varying confinement stresses would allow further validation.

5. Consider a long embedment length, ring-test specimen. A long specimen bound by many strain-gauged rings might provide additional validation data on the distribution of the normal response.
6. At a more basic level, a nondestructive high-resolution method of examining the damage in the bond zone (like an "MRI for bond") would greatly advance our understanding and characterization of bond.
7. Additional investigations of size effects on the bond of ribbed-bars are needed. Use of the Malvar specimen would provide additional data on the effect of confinement stress.

To meet the objective of applying the bond model in member-scale problems, the following implementation efforts will be needed:

1. After additional model development is complete, apply the closest-point-projection algorithm to the integration of the bond law. Also implement the consistent elastoplastic moduli and investigate modifications of the integration algorithm that would yield second order accuracy.
2. Investigate various "local models" to represent the region adjacent to the bond zone. This approach could help bridge the gap between the member-scale and bar-scale by providing the bar-scale model with a reasonable estimate of the state of the adjacent concrete.
3. Investigate means of incorporating the bond model (and possibly a local model) into member-scale FE analyses. In particular, the embedded element approach could yield a powerful analysis tool; the mesh would not be constrained by the reinforcement schedule and the anisotropy of the composite is determined directly by the analysis program.

The topics of these last two recommendations were addressed in this project (see *e.g.*, McMichael [1993]). The bond model fulfilled the objective of exhibiting a "measure of generality." Thus, while it has potential application to member-scale analyses, this potential can only be realized with efficient implementations of the bond and reinforcement models.

Bibliography

The bibliography is divided into two sections. The first section contains studies directly related to bond, some of which the text referenced. The second section contains the remaining references (*e.g.*, references related to material stability or stress-point algorithms).

Bond

ACI Committee 408, "Abstract of: State-of-the-art-report: Bond under cyclic loads," *ACI Materials Journal*, vol 88, no. 6, 1991, pp 669-673.

ASCE Task Committee on Finite Element Analysis of Reinforced Concrete Structures, "State-of-the-art report on finite element analysis of reinforced concrete," ASCE special publications, 1982.

Abrams, D.A., "Tests of bond between concrete and steel," University of Illinois Engineering Experiment Station, Bulletin 71, 1913.

Al-Mahaidi, R.S.H. and A.H. Nilson, "Non-linear finite element analysis of reinforced concrete deep members," Report No. 79-1, Dept. of Structural Engineering, Cornell University, Ithaca, NY, January 1979.

Altowaiji, W.A.K., D. Darwin, and R.C. Dohaney, "Bond of reinforcement to revibrated concrete," *ACI Journal*, vol 83, no. 6, 1986, pp 1035-1042.

Balaazs, G.L., "Bond behavior under repeated loads," *Studi e Ricerche - Corso Flli.* Pesenti, Politecnico di Milano, vol 8, 1986, pp 395-430.

Bangash, Y., and M. Ahmed, "Bond strength history in prestressed concrete reactor vessels," SMIRT 8, Eighth International Conference on Structural Mechanics in Reactor Technology, Brussels, Belgium, August 1985, Elsevier Science Publishers, pp 35-40.

Bergan, P.G., and I. Holand, "Nonlinear finite element analysis of concrete structures," *Computer Methods in Applied Mechanics and Engineering*, vol 17/18, 1979, pp 443-467.

Bertero, V.V., and E.P. Popov, "Seismic behavior of ductile moment-resisting reinforced concrete frames," ACI Special Publication SP-53, Detroit, 1977, pp 247-292.

Bertero, V.V., "Seismic behavior of structural concrete linear elements (beams and columns) and their connections," Comité Euro-International due Béton, Bulletin D`Information no. 131, Paris, April 1979.

Bresler, B., and V.V. Bertero, "Influence of load history on cracking in reinforced concrete," Report to California Division of Highways, Department of Civil Engineering, Division of Structural Engineering and Structural Mechanics, University of California, Berkeley, 1966, 20 pp.

Bresler, B., and V.V. Bertero, "Behavior of Reinforced Concrete Under Repeated Load," *Journal of the Structures Division*, ASCE, vol 94, no. ST6, June 1968, pp 1567-1590.

Bresler, B., Reinforced Concrete Engineering, Wiley Interscience, New York, NY, 1974, pp 42-64.

Broms, B.B., "Stress Distribution in Reinforced Concrete Members with Tension Cracks," *ACI Journal*, vol 62, no. 9, September 1965, pp 1095-1108.

Broms, B.B., "Crack Width and Crack Spacing in Reinforced Concrete Members," *ACI Journal*, vol 62, no. 10, October 1965, pp 1237-1255.

CEB (Comité Euro International du Béton), Bond in Concrete, Proceedings of the International Conference, Riga, Latvia, 3 volumes, 1992.

Cervenka, V., "Inelastic finite element analysis of reinforced concrete panels under in-plane loads," Ph.D. Thesis, Department of Civil Engineering, University of Colorado, 1970.

Cervenka, V., and Gerstle, K.H., "Inelastic analysis of reinforced concrete panels, part 1: theory," *International Associate of Bridge and Structural Engineers Publication*, vol 31-11, 1971.

Cervenka, V., and Gerstle, K.H., "Inelastic analysis of reinforced concrete panels, part 1: experimental verification and application," *International Associate of Bridge and Structural Engineers Publication*, vol 32-11, 1971.

Chamberlin, S.J., "Spacing of spliced bars in tension pull-out specimens," *ACI Journal*, vol 49, November 1952, pp 261-274.

Chang, Ko-Tao, "A one dimensional finite element model of bond behavior in reinforced concrete," M.S. Thesis, Department of Civil Engineering, University of California, Davis, 1992.

Ciampi, V., R. Eligehausen, V.V. Bertero and E.P. Popov, "Analytical model for deformed bar bond under generalized excitations," Transactions of IABSE Colloquium on Advanced Mechanics of Reinforced Concrete, Delft, Netherlands, 1981.

Ciampi, V., R. Eligehausen, V.V. Bertero and E.P. Popov, "Analytical model for concrete anchorages of reinforcing bars under generalized excitations," Report No. UCB/EERC 82-23, University of California, Berkeley, 1982.

Clark, A.P., "Comparative bond efficiency of deformed concrete reinforcing bars," *ACI Journal*, vol 18, no.4, December 1946.

Cowell, A.D., E.P. Popov, and V.V. Bertero, "Effects of concrete types and loading conditions on local bond-slip relationships," Earthquake Engineering Research Center, Report No. UCB/EERC 82/17, University of California, Berkeley, 1982.

Cowell, A.D., E.P. Popov and V.V. Bertero, "Effects of concrete types and loading conditions on local bond-slip relations," Earthquake Engineering Research Center, Report No. UCB/EERC 82/17, University of California, Berkeley, 1982a.

Cowell, A.D., V.V. Bertero and E.P. Popov, "An investigation of local bond slip under variation of specimen parameters," Earthquake Engineering Research Center, Report No. UCB/EERC 82/23, University of California, Berkeley, 1982b.

Cox, James V., and Leonard R. Herrmann, "A plasticity model for the bond between matrix and reinforcement," Proceedings of the Sixth Japan-U.S. Conference on Composite Materials, Orlando, Florida, 22-24 June 1992a.

Cox, James V., and Leonard R. Herrmann, "Confinement stress dependent bond behavior, part II: A two degree of freedom plasticity model," Bond in Concrete, Proceedings of the International Conference, Riga, Latvia, CEB, vol 3, 1992b, pp 11.11-11.20.

Darwin, David, and Ebenezer K. Graham, "Effect of deformation height and spacing on bond strength of reinforcing bars," *ACI Structural Journal*, vol 9, no.6, November-December, 1993, pp 646-657.

Davis, R.E., E.H. Brown and J.W. Kelly, "Some factors influencing the bond between concrete and reinforcing steel," *Proceedings of ASTM*, vol 38, Part II, 1938, pp 394-409.

De Groot, A.K., G.M.A. Kusters and T. Monnier, "Numerical modeling of bond-slip behavior," Heron, vol 26-1b, I.B.B.C. Institute TNO, Delft, Netherlands, 1981.

Diederichs, U., and U. Schneider, "Bond strength at high temperatures," *Magazine of Concrete Research*, vol 33, no.115, June 1981, pp 75-84.

Dohaney, R.C., and D. Darwin, "Bond on top cast bars in bridge decks," *ACI Journal*, vol 82, no.1, 1985, pp 40-45.

Dörr, Karlfried, "Bond behavior of ribbed reinforcement under transversal pressure," Proc. IASS Symposium on Nonlinear Behavior of Reinforced Concrete Structures, vol 1, Preliminary Report, Werner Verlag, Dusseldorf, Germany, July 1978.

Dörr, Karlfried, "Ein Beitrag zur Berechnung von Stahlbetonscheiben unter besonderer Berücksichtigung des Verbundverhaltens," Ph.D. Dissertation, Technischeltoch Schale, in Darmstadt, Germany, 1980.

Dragosavic, M., "Modeling of bond," IABSE Colloquim, Delft, 1987, pp 131-138.

Edwards, A.D., and P.J. Yannopoulos, "Local bond-stress to slip relationships for hot-rolled deformed bars and mild steel plain bars, *ACI Journal*, 1979, pp 405-420.

Edwards, A.D., and P.J. Yannopoulos, "Local bond-stress to slip relationships under repeated loading," *Magazine of concrete research*, vol 30, no. 103, June 1978, pp 62-72.

Eligehausen, R., "Bond in tensile lapped splices of ribbed bars with straight anchorages," Publication 301, German Institute for Reinforced Concrete, Berlin, 1970, 118 pp (in German).

Eligehausen, R., E.P. Popov, and V.V. Bertero, "Local bond stress-slip relations of deformed bars under generalized excitations," Report UCB/EERC-83/23, University of California, Berkeley, CA, October 1983.

Ferguson, P.M., and J.N. Thompson, "Development length of high strength reinforcing bars in bond," *ACI Journal*, vol 59, no. 9, July 1962, pp 887-992.

Ferguson, P.M., and J.N. Thompson, "Development length for large high strength reinforcing bars," *ACI Journal*, vol 62, no. 1, January 1965, pp 71-94.

Ferguson, P.M., R.D. Turpin and J.N. Thompson, "Minimum bar spacing as a function of bond and shear strength," *ACI Journal*, vol 50, no. 10, June 1954, pp 869-888.

Filippou, F.C., E.P. Popov and V.V. Bertero, "Effect of bond deterioration on histeretic behavior of reinforced concrete joints," Report No. UCB/EERC 93-19, University of California, Berkeley, California, 1983a.

Filippou, F.C., E.P. Popov and V.V. Bertero, "Modeling of reinforced concrete joints under cyclic excitations," *Journal of Structural Engineering*, ASCE, vol 109, no.11, 1983b, pp 2666-2684.

Filippou, F.C., "A simple model for reinforcing bar anchorages under cyclic excitations," Report No. UCB/EERC 85-5, University of California, Berkeley, California, 1985.

Filippou, F.C., "A simple model for reinforcing bar anchorages under cyclic excitations," *Journal of Structural Engineering*, ASCE, vol 112, no.7, 1988, pp 1639-1659.

Gambarova, Pietro G., and Cengiz Karakog, "Shear-confinement interaction at the bar-to-concrete interface," Proceedings of the international conference on bond in concrete, Peisley College of Technology, Scotland, P. Bartos, editor, Applied Science Publishers, 1982, pp 151-161.

Gambarova, Pietro G., Gian P. Rosati and Sharif Omar Sharif, "Bond and splitting in reinforced concrete," Bond in Concrete, Proceedings of the International Conference, Riga, Latvia, CEB, vol 1, 1992, pp 1.48-1.57.

Gambarova, Pietro G., Gian P. Rosati and Barbara Zasso, "Steel-to-concrete bond after concrete splitting: test results," *Materials and Structures*, International Association of Testing and Research, vol 22, no. 127, January 1989, pp 35-47.

Gambarova, Pietro G., Gian P. Rosati and Barbara Zasso, "Steel-to-concrete bond after concrete splitting: constitutive laws and interface deterioration," *Materials and Structures*, International Association of Testing and Research, vol 22, 1989, pp 347-356.

Gambarova, Pietro G., Gian P. Rosati and C. Schumm, "An elasto-cohesive model for steel-concrete bond," Fracture and Damage in Quasibrittle Structures: Experiment, Modeling and Computer Analysis, Europe-U.S. Workshop, Prague, September 21-24, 1994.

Gergely, P., "Splitting cracks along the main reinforcement in concrete members," Department of Structural Engineering, Report, Cornell University, 1969.

Gerstle, Walter H., and Anthony R. Ingraffea, "Does Bond-Slip Exist?" Micromechanics of Failure of Quasi-Brittle Materials, Proceedings of the International Conference, Albuquerque, NM, S.P. Shah, S.E. Swantz, and M.L. Wang eds., June 1990.

Gilkey, H.J., S.J. Chamberlin and R.W. Beal. "Bond between concrete and steel," Iowa Engineering Experiment Station, Bulletin 147, 1940.

Giuriani, E., G. Plizzari and C. Schumm, "Role of stirrups and residual tensile strength of cracked concrete on bond," *Journal of Structural Engineering*, ASCE, vol 117, no. 1, January 1991.

Goto, Y., and K. Otsuka, "Experimental studies on cracks formed in concrete around deformed tension bars," The Technology Reports of the Tohoku University, vol 44, no. 1, June 1979, pp 49-83.

Goto, Y., Cracks formed in concrete around tension bars," *ACI Journal*, vol 68, no. 4 April 1971.

Hand, F.R., D.A. Pecknold and W.C.Schnobrich, "Nonlinear layered analysis of r.c. plates and shells," *Journal of the Structural Division*, ASCE, vol 99, no. ST7, July 1973, pp 1491-1505.

Hassan, F.M., and N.M. Hawkins, "Effect of post-yielding loading reversals on bond between reinforcing bars and concrete," Report SM73-2, Department of Civil Engineering, University of Washington, Seattle, Washington, March 1973.

Hawkins, N.M., and I.J. Lin, "Bond characteristics of reinforcing bars for seismic loadings," Proceedings of the third Canadian Earthquake Engineering Conference, McGill University, Montreal, June 1979, pp 1225-1252.

Hawkins, N.M., I.J. Lin and F.L. Jeang, "Local bond strength of concrete for cyclic reversed loadings," Bond in Concrete, Proceedings of the International Conference on Bond in Concrete, Applied Science Publishers, London, 1982, pp 151-161.

Herrmann, Leonard R., and James V. Cox, "Development of a plasticity bond model for reinforced concrete – Preliminary calibration and cyclic applications," Contract Report CR 94.001-SHR, Naval Facilities Engineering Service Center, Port Hueneme, CA, March 1994.

Herrmann, Leonard R., and Z. Al Yassin, "Numerical analysis of reinforced earth systems," Proc. ASCE Symposium on Reinforced Earth, Pittsburgh, 1978, pp 429-457.

Houde, J., "Study of Force-Displacement Relationships for the Finite Element Analysis of Reinforced Concrete," Report No. 73-2, Department of Civil Engineering and Applied Mechanics, McGill University, Montreal, Dec. 1973.

Houde, J., and M.S. Mirza, "A finite element analysis of shear strength of reinforced concrete beams," Shear in Reinforced Concrete, vol 1, Special Publication, SP-42, ACI, Detroit, Michigan, 1974.

Hsu, T.C., and F.O. Slate, "Tensile bond strength between coarse aggregate and cement paste or mortar," *ACI Journal*, vol 60, no. 4, April 1963, pp 465-486.

Hungspreug, Siripong, "Local bond between a steel bar and concrete under high intensity cyclic loading," Ph.D. Dissertation, Cornell University, Ithaca, NY, 1981.

Ingraffea, Anthony R., Walter H. Gerstle, Peter Gergely and Victor Saoma, "Fracture mechanics of bond in reinforced concrete," *Journal of Structural Engineering*, ASCE, vol 111, no. 5, April 1984 (paper 18751).

Ismail, M.A.F., and J.O. Jirsa, "Bond deterioration in reinforced concrete subject to low cycle loads," *ACI Journal*, vol 69, no. 6, June 1972, pp 334-343.

Jiminez, R., R.N. White and P. Gergely, "Bond and Dowel Capacities of Reinforced Concrete," *ACI Journal*, vol 76, no. 1, January 1979, pp 73-92.

Johnston, B., and K.C. Cox, "The bond strength of rusted deformed bars," *ACI Journal*, vol 37, September 1940, pp 57-72.

Kemp, E.L., F.S. Brezny and J.A. Unterspan, "Effect of rust and scale on the bond characteristics of deformed reinforcing bars," *ACI Journal*, vol 65, September 1968, pp 743-756.

Kemp, E.L., and W.J. Wilhelm, "Investigation of the parameters influencing bond cracking," *ACI Journal*, vol 76, no. 1, January 1979, pp 47-71.

Kemp, E.L., W.J. Wilhelm and N.J. Chen, "An investigation of the parameters influencing bond behavior with a view towards establishing design criteria," Final Report, WVDOH Project No. 46, Report No. FHWA-WV-77-6, West Virginia University, November 1977.

Keuser, Manfred, and Gerhard Mehlhorn, "Finite element models for bond problems," *Journal of the Structural Division*, ASCE, vol 113, no. 10, Paper No. 21865, October 1987.

Keuser, Manfred, Gerhard Mehlhorn and V. Cornelius, "Bond between prestressed steel and concrete -- computer analysis using ADINA," *Computers and Structures*, vol 17, no. 5/6, 1983, pp 669-676.

Khouzam, M., "A finite element investigation of reinforced concrete beams," M. Eng. Thesis, McGill University, Montreal, Canada, October 1977.

Leonhardt, P., "On the need to consider the influence of lateral stresses on bond," RILEM-Symposium on bond and crack formation in reinforced concrete, Stockholm, vol 1, 1957, pp 29-33.

Losberg, Anders, and Per-Ake Olsson, "Bond failure of deformed reinforcing bars based on the longitudinal splitting effect of the bars," *ACI Journal*, vol 76, no. 1, January 1979, pp 5-18.

Lutz, Leroy A., "The mechanics of bond and slip of deformed reinforcing bars in concrete," Ph.D. Dissertation, Cornell University, Ithaca, NY, September 1966.

Lutz, Leroy A., "Analysis of stresses in concrete near a reinforcing bar due to bond and transverse cracking," *ACI Journal*, vol 67, no.10, October 1970, pg 778.

Lutz, Leroy A. and P. Gergely, "Mechanics of Bond and Slip of Deformed Bars in Concrete," *ACI Journal*, vol 64, November 1967, pp 711-721.

Lutz, Leroy A., P. Gergely and G. Winter, "The mechanics of bond and slip deformed reinforcing bars in concrete," Structural Engineering Report No. 324, Cornell University, August 1966.

Ma, S.M., V.V. Bertero and E.P. Popov, "Experimental and analytical studies on the hysteretic behavior of reinforced concrete rectangular and T-beams," Earthquake Engineering Research Center, Report No. EERC 76-2, University of California, Berkeley, May 1976.

Mains, R.M., "Measurement of the distribution of tensile and bond stresses along reinforcing bars," *ACI Journal*, vol 48, November 1951, pp.335-352.

Mainz, J., S. Stöckl, and H. Kupfer, "FE-Calculations concerning the bond behavior of deformed bars in concrete, Bond in Concrete, Proceedings of the International Conference, Riga, Latvia, CEB, vol 1, October 1992, pp 12.17-12.26

Malvar, L. Javier, "Bond of reinforcement under controlled confinement," Technical Note 1833, Naval Civil Engineering Laboratory, Port Hueneme, CA, June 1991.

Malvar, L. Javier, "Confinement stress dependent bond behavior, part I: Experimental investigation," Bond in Concrete, Proceedings of the International Conference, Riga, Latvia, CEB, vol 1, October 1992a, pp 1.79-1.99.

Malvar, L. Javier, "Bond of reinforcement under controlled confinement," ACI Materials Journal, vol 89, no. 6, November-December, 1992b, pp 593-601.

Martin, H., "Zusammenhang zwischen Oberflächenbesehaffenheit, Verbund und Sprengwirkung von Bewehrungsstählen unter Kurzzeitbelastung," (Relationship between deformation pattern, bond and splitting of reinforcing bars under short time loading), Deutscher Ausschuss Für Stahlbeton, Heft 228, Berlin, 1973 (in German).

Mathey, R.G., and D. Watstein, "Investigation of bond in beam and pull-out specimens with high-yield-strength deformed bars," *ACI Journal*, vol 57, no. 9, March 1961, pp 1071-1090 (discussion pp 1823-1826).

McMichael, Larry D., "A composite finite element model for reinforced concrete," M.S. Thesis, Department of Civil Engineering, University of California, Davis, 1993.

Mehlhorn, Gerhard, and Manfred Keuser, "Isoparametric contact elements for analysis of reinforced concrete structures," Finite Element Analysis of Reinforced Concrete Structures, ASCE, Proceedings of a Seminar Sponsored by Japan Society for the Promotion of Science and USNF, Tokyo, Japan, 1985, pp 329-347.

Menzel, C.A., "Some factors influencing results of pull-out bond tests," *ACI Journal*, vol 35, June 1939, pp 517-544.

Menzel, G.A., "A proposed standard deformed bar for reinforced concrete," presented at the 17'th semiannual meeting, Concrete Reinforcing Steel Institute, Colorado Springs, Colorado, September 1941.

Mirza, S.A., and J. Houde, "Study of Bond Stress-Slip Relations in Reinforced Concrete," *ACI Journal*, vol 76, no. 1, January 1979, pp 19-46.

Mirza, S.A., and J.G. MacGregor, "Variability of Mechanical Properties of Reinforcing Bars," ASCE, vol 105, no. ST5, May 1979, pp 921-937.

Modena, C., T. Coltro and G.P. Rossaro, "Study of bond between steel and concrete in presence of longitudinal splitting cracks: tests under prescribed confinements," *Studi E. Ricerche*, vol 10-1988, Politecnico di Milano, 1989, pp 179-218 (in Italian).

Morley, P.D., and R. Royles, "Response of bond in reinforced concrete to high temperatures," *Magazine of Concrete Research*, vol 35, no.123, June 1983, pp 67-74.

Morita, Shiro, and Shigeru Fujii, "Bond-slip models in finite element analysis, "Proceedings of the Japan-US Seminar on Finite Element Analysis of Reinforced Concrete Structures, Tokyo, May 1985, ASCE, pp 348-363.

Morita, Shiro, and Tetsuzo Kaku, "Local bond stress-slip relationship under repeated loading," Prel. Report, I.A.B.S.E. Symposium, Lisbon, 1973, pp 221-227.

Morita, Shiro, and Tetsuzo Kaku, "Splitting bond failures of large deformed reinforcing bars," *ACI Journal*, vol 76, no. 1, January 1979, pp 93-110.

Muguruma, H., and S. Morita, "Fundamental study on bond between steel and concrete (II. Deformation of reinforced concrete tension member)" *Transactions of AIJ*, vol 134, 1967, pp 1-8 (in Japanese).

Muguruma, H., and S. Morita, "Fundamental study on bond between steel and concrete (III. Pull-out tests)" *Transactions of AIJ*, vol 139, 1967, pp 1-10 (in Japanese).

Muguruma, H., S. Morita and K. Tomita, "Fundamental study on bond between steel and concrete (Bond stress distribution I)," *Transactions of AIJ*, vol 131, 1967, pp 1-8 (in Japanese).

Muguruma, H., S. Morita and K. Tomita, "Fundamental study on bond between steel and concrete (Bond stress distribution II)," *Transactions of AIJ*, vol 132, 1967, pp 1-6 (in Japanese).

Muhlenbruch, C.W., "The effect of repeated loading on bond strength of concrete," *Proceedings of the American Society for Testing and Materials*, vol 45, 1945, pp 824-845.

Muhlenbruch, C.W., "The effect of repeated loading on bond strength of concrete," *Proceedings of the American Society for Testing and Materials*, vol 48, 1948, pp 977-987.

Mylrea, T.D., "Bond and anchorage," *ACI Journal*, vol 44, March 1948, pp 521-552.

Navaratnarajah, V., "Variation of transfer bond in concrete under lateral restraint," Ph.D. Thesis, The City University, London, 1982, 265 pp.

Navaratnarajah, V., and P.R.S. Speare, "A theory of transfer bond resistance of deformed reinforcing bars in concrete under lateral pressure," *Magazine of Concrete Research*, vol 39, no. 140, September 1987, pp 161-168.

Naylor, D.J., and H. Richards, "Slipping strip analysis of reinforced earth," *International Journal for Num. Analy. Method in Geomechanics,* vol 2, no. 4, 1978.

Ngo, D., and A.C. Scordelis, "Finite Element Analysis of Reinforced Concrete Beams," *ACI Journal*, vol 64, no. 3, March 1967, pp 152-163.

Ngo, D. "A network-topological approach to the finite element analysis of progressive crack growth in concrete members," Ph.D. Thesis, University of California, Berkeley, CA, June 1975.

Nies, W., "A new method for the measurement of local slip between steel and concrete," Ph.D. Dissertation, Technical University, Darmstadt, 1979.

Nilson, A.H., "Nonlinear Analysis of Reinforced Concrete by the Finite Element Method," *ACI Journal*, vol 65, no. 9, September 1968, pp 757-766.

Nilson, A.H., "Bond Stress-Slip Relations in Reinforced Concrete," Report 345, School of Civil and Environmental Engineering, Cornell University, Ithaca, N.Y., December 1971, 40 pp.

Nilson, A.H., "Internal Measurement of Bond Slip," *ACI Journal*, vol 69, no. 7, July 1972, pp 439-441.

Nilson, A.H., Design of Prestressed Concrete, John Wiley and Sons, New York, NY, 1978.

Okushima, Horiyuki, and Takakazu Ooi, "Looking over again ASTM test method for evaluating bond development of concrete with reinforcing steel," *Transactions of the Japan Concrete Institute*, vol 8, 1986.

Orangun, C.O., J.O. Jirsa, and J.E. Breen, "Re-evaluation of test data on development length and splices," *ACI Journal*, vol 74, no. 3, March 1977, pp 114-122.

Ozbolt, Josko, and Rolf Eligehausen, "Simulation of cycling bond behavior," Proceedings of the First International Conference on Fracture Mechanics of Concrete Structures, Breckenridge, CO, Elsevier Science Publishers LTD, Essex, England, Z.P. Bazant, editor., 1992a, pp 912-917.

Ozbolt, Josko, and Rolf Eligehausen, "Numerical simulation of cycling bond-slip behavior," Bond in Concrete, Proceedings of the International Conference, Riga, Latvia, CEB, vol 3, 1992b, pp 12.27-12.33.

Park, R., and Paulay, T., Reinforced concrete structures, John Wiley and Sons, New York, 1978.

Perry, E.S., and Jundi, N., "Pullout bond stress distribution under static and dynamic repeated loads," *ACI Journal*, vol 66, no. 5, May 1969, pp 377-380.

Popov, E.P., "Bond and anchorage of reinforcing bars under cyclic loading," *ACI Journal*, July-August 1984, pp 340-349.

Prestressed Concrete Institute, PCI Design Handbook -- Precast and Prestressed Concrete, Prestressed Concrete Institute, Chicago, Illinois, 1971.

Rehm, G., "The fundamental law of bond," Proceedings of the Symposium on Bond and Crack Formation in Reinforced Concrete, Stockholm, vol 2, 1957, RILEM, pp 491-498.

Rehm, G., "The basic principle of bond between steel and concrete," *Deutscher Ausschuss für Stahlbeton*, no. 138, Wilhelm Ernest and Sohn, Berlin, (C & CA Library Translation no. 134, 1968), 1961.

Rehm, G., and R. Eligehausen, "Bond of ribbed bars under repeated loads," Report 291, German Institute for Reinforced Concrete, Berlin, 1977, (in German).

Rehm, G., and R. Eligehausen, "Bond of ribbed bars under high cycle repeated loads," *ACI Journal*, vol 76, no. 2, February 1979, pp 297-309.

Reinhardt, H.W., J. Blaauwendraad and E. Vos, "Prediction of bond between steel and concrete by numerical analysis," *Material and Structures*, vol 17, no. 100, 1984, pp 311-320.

Richart, F.E., and V.P. Jensen, "Tests of plain and reinforced concrete made with haydite aggregates," Bulletin No. 237, Engineering Experiment Station, University of Illinois, 1931.

RILEM, *Dynamic Behavior of Concrete Structures*, Report of the RILEM 65 MDB Committee, G.P. Tilly, editor, Elsevier Science Publishers LTD, Amsterdam, 1986.

Robins, P.J., and S.A. Austin, "Bond of lightweight aggregate concrete incorporating condensed silica fume," Proceedings of the Second International Conference on Fly Ash, Silica Fume, Slag and Natural Pozzolans in Concrete, Madrid, Spain, 1986, pp 941-958.

Robins, P.J., and I.G. Standish, "Effect of lateral pressure on bond of reinforcing bars in concrete," Bond in Concrete, Proceedings of the International Conference held at Peisley College of Technology, Scotland, pp 262-272, Applied Science Publishers, P. Bartos, editor, Barking , Essex, 1982.

Robinson, J.R., "Influence of transverse reinforcement on shear and bond strength," *ACI Journal*, vol 62, no. 3, March 1965, pp 343-362.

Rosati, Gianpaolo, and Cristiano Schumm, "Modeling of local bar-to-concrete bond in r.c. beams," Bond in Concrete, Proceedings of the International Conference, Riga, Latvia, CEB, vol 3, 1992, pp 12.34-12.43.

Russo, Gaetano, Gertano Zingone and Filippo Romano, "Analytical solution for bond-slip of reinforcing bars in R. C. Joints," *Journal of Structural Engineering*, ASCE, vol 116, no. 2, February 1990, pp 336-355.

Saouma, V.E., "Iterative finite element analysis of reinforced concrete: a fracture mechanics approach," Ph.D. Thesis, Cornell University, Ithaca, NY, January 1981.

Scanlon, A., "Time-dependent deflections of reinforced concrete slabs," Structural Engineering Research Report No. 38, Dept. of Civil Engineering, Univ. of Alberta, Edmonton, Canada, Dec. 1971.

Schafer, H., "A contribution to the solution of contact problems with the aid of bond elements," *Computer Methods in Applied Mechanics and Engineering*, North Holland Publishing Company, vol 6, (1975), pp 335-354.

Schmidt-Thro, G., "Verbundverhalten vin Rippenstahlen im Beton unter besonderer Berucksichtigung einer einachsigen Qverpressung," Dissertation, Technische Universitat Munchen, 1987.

Scordelis, A.C., "Finite Element Analysis of Reinforced Concrete Structures," Proceedings of the McGill, Engineering Institute of Canada Specialty Conference on Finite Element Methods in Civil Engineering, McGill University, Montreal, June 1972, pp 71-114.

Sharma, N.K., "Splitting failures in reinforced concrete members," Ph.D. Thesis, Cornell University, Ithaca, NY, June 1969.

Sharma, S., M. Reich and T.Y. Chang, "Review of current methodology for reinforced concrete structural evaluations," NUREG/CR-3284, BNL-NUREG-51673, April 1983.

Shen, Wendu, and Youlin Xu, "The bearing numerical analysis of anchorage deformed bars," Bond in Concrete, Proceedings of the International Conference, Riga, Latvia, CEB, vol 3, 1992, pp 12.1-12.8.

Shih, T.S., G.C. Lee and K.C. Chang, "Local concrete-steel bond behavior at low temperatures," *Journal of Structural Engineering*, ASCE, vol 113, no.11, November 1986, pp 2278-2289.

Shih, T.S., G.C. Lee and K.C. Chang, "Effect of freezing cycles on bond strength of concrete," *Journal of Structural Engineering*, ASCE, vol 114, no.3, March 1988, pp 717-726.

Shima, Hiroshi, Lie-Liung Chou and Hajime Okamura, "Micro and Macro Models for bond in reinforced Concrete," *Journal of the Faculty of Engineering, The University of Tokyo (B)*, vol 39, no. 2. 1987, pp 133-194.

Shima, Hiroshi, Lie-Liung Chou and Hajime Okamura," Bond-slip-strain relationship of deformed bars," Bond in Concrete, Proceedings of the International Conference, Riga, Latvia, CEB, vol 3, 1992, pp 11.38-11.47.

Shipman, J.M., "A study of bond effects in reinforced concrete using finite elements," M.S. Thesis, Department of Civil and Environmental Engineering, University of Colorado, January 1974.

Shipman, J.M., and K.H. Gerstle, "Bond deterioration in concrete panels under load cycles," *ACI Journal*, vol 76, no. 2, February 1979, pp 311-325.

Shirai, N., and T. Sato, "Anisotropic constitutive model for cracked reinforced concrete element," Transactions of the eighth International Conference on Structural Mechanics in Reactor Technology, Brussels, Belgium, vol 8, August 19-23, 1985, pp 99-106.

Singh, A., K.H. Gerstle and L.G. Tulin, "The behavior of reinforcing steel under reversed loading," *Materials Research and Standards*, ASTM, vol 5, January 1965, pp 12-17.

Singh, H.N., K.H. Gerstle and L.G. Tulin, "Shear strength of concrete beams under cyclic loadings," Prel. Report, I.A.B.S.E. Symposium, Lisbon, 1973, pp 61-65.

Skorobogatov, S.M., and A.D. Edwards, "The influence of the geometry of deformed steel bars on their bond strength in concrete," Proc. Instn. Civil Engineers, Part 2, vol 67, June 1979, pp 327-339.

Soleimani, D., E.P. Popov and V.V. Bertero, "Hysteretic behavior of reinforced concrete beam-column subassemblages," *ACI Journal*, vol 76, no.11, November 1979.

Somayaji, S., and S.P. Shah, "Bond stress versus slip relationship and cracking response of tension members," *ACI Journal*, May-June 1981, 217-225.

Soretz, S., and H. Holzenbein, "Influence of rib dimensions of reinforcing bars on bond and bendability," *ACI Journal*, vol 76, no.1, January 1979, pp 111-125.

Soroushian, Parviz, and Ki-Bong Choi, "Local bond of deformed bars with different diameters in confined concrete," *ACI Structural Journal*, vol 86, no.2, March-April 1989, pp 217-222.

Swamy, R.N., and A.D. Andriopoulos, "Contribution of aggregate interlock and dowel forces to the shear resistance of reinforced beams with web reinforcement," *Journal of the Structural Division,* ASCE, vol 99, no. 2, 1973.

Tanner, J.A., "An experimental determination of bond slip in reinforced concrete," M.S. Thesis, Cornell University, Ithaca, NY, November 1971.

Tassios, T.P., "Properties of bond concrete and steel under load cycles idealizing seismic actions," Comite Euro-International Du Beton, Bulletin No. 131, Paris, April 1979a.

Tassios, T.P., "Theories of bond between concrete and steel under load cycles idealizing seismic actions," AICAP-CEB Symposium, Rome, May 1979b, pp 67-122.

Tassios, T.P., and P.J. Yannopoulos, "Analytical studies of reinforced concrete members and under cyclic loading based on bond stress-slip relationships," *ACI Journal*, May-June 1981, pp 206-216.

Taylor M.A., and B.B. Broms, "Shear bond strength between coarse aggregate and cement paste or Mortar," *ACI Journal*, vol 61, no. 8, August 1964, pp 939-958.

Teng, Zhiming, Hueizhong Lu , and Jinping Zhang, "A new bond model for finite element analysis of rc structures," Bond in Concrete, Proceedings of the International Conference, Riga, Latvia, CEB, vol 3, 1992, pp 12.9-12.16.

Teng, Zhiming, and Zhiman Ye, "Bond behavior of deformed bars in high strength concrete," Bond in Concrete, Proceedings of the International Conference, Riga, Latvia, CEB, vol 2, 1992, pp 4.11-4.18.

Tepfers, Ralejs, "A theory of bond applied to overlapped tensile reinforcement splices for deformed bars," Gothenberg, Chalmers University of Technology, Division of Concrete Structures, Publication no. 73:2, 1973.

Tepfers, Ralejs, "Cracking of concrete cover along anchored deformed reinforcing bars," *Magazine of Concrete Research*, vol 31, no. 106, March 1979, pp 3-12.

Tepfers, Ralejs, and Per-Åke Olsson, "Ring test for evaluation of bond properties of reinforcing bars," Bond in Concrete, Proceedings of the International Conference, Riga, Latvia, CEB, vol 1, 1992, pp 1.89-1.99.

Tilantera, T., and T. Rechardt, "Bond of reinforcement in lightweight aggregate concrete," Otaniemi, Division of Structural Engineering, Helsinki University of Technology, Technical report no. 17, 1977, pp 1-36.

Ueda, T., I. Lin and N.M. Hawkins, "Beam bar anchorage in exterior column-beam connections," *ACI Journal*, May-June 1986, pp 412-422.

Untrauer, Raymond E., and Robert L. Henry, "Influence of normal pressure on bond strength," *Journal of the American Concrete Institute*, May 1965, pp 577-586.

Untrauer, Raymond E., and George E. Warren, "Stress development of tension steel in beams," *ACI Journal*, vol 74, no. 8, August 1977, pp 577-586.

Van Mier, J., Onderzoek, naar het schuifspanningsslipgedrag van geprofileerd wapenihgsstaal en beton (Investigation of the shear slip behavior of deformed reinforcing steel and concrete), Graduation thesis, Eindhoven University of Technology, Department of Architecture, June 1978 (in Dutch).

Viwathanatepa, S., "Bond deterioration of reinforcing bars embedded in confined concrete blocks," Ph.D. Thesis, University of California, Berkeley, June 1979.

Viwathanatepa, S., E.P. Popov and V.V. Bertero, "Effects of generalized loadings on bond of reinforcing bars embedded in confined concrete blocks," Earthquake Engineering Research Center, Report no. UCB/EERC-79/22, University of California, Berkeley, August 1979.

Vos, E., "Influence of loading rate and radial pressure on bond in reinforced concrete: A numerical and experimental approach," Delft University Press, Delft, 1983.

Vos, E. and H.W. Reinhardt, "Influence of loading rate on bond behavior of reinforcing steel and prestressing strands," *Materiaux et Constructions*, vol 15, no. 85, 1982, pp 3-10.

Wahla, M.I., "Direct measurement of bond slip in reinforced concrete," Ph.D. Thesis, Cornell University, Ithaca, NY, January 1970.

Wahla, M.I., N.R. Scott, and A.H. Nilson, "Direct measurement of bond slip in reinforced concrete," *Trans. Amer. Soc. of Agr. Engineers*, vol 14, no. 4, April 1971, pp 762-767.

Wang, Naisong, "Nonlinear fracture analysis of bond strength," Ph.D. Dissertation, University of Calgary, Canada, 1993, 333 pp.

Watstein, D., "Bond stress in concrete pullout specimens," *ACI Journal*, vol 38, September 1941, pp 35-50.

Watstein D. and R.G. Mathey, "Width of cracks in concrete at the surface of reinforcing steel evaluated by means of tensile bond specimens," *ACI Journal*, vol 56, no. 1, July 1959, pp 47-56.

Watstein, D., and N.A. Seese, "Effect of type of bar on width of cracks in reinforced concrete subjected to tension," *ACI Journal*, vol 41, no. 4 Feb. 1945, pp 293-304.

Wilhelm, W.J., E.L. Kemp and Y.T. Lee, "Influence of deformation height and spacing on the bond characteristics of steel reinforcing bars," Civil Engineering Report No. 2013, West Virginia University, 1971.

Yamao, H., L. Chou and J. Niwa, "Experimental study on bond stress-slip relationship," *Proceedings of JSCE*, no. 343, 1984, pp 219-228 (in Japanese).

Yankelevsky, David Z., Moshe A. Adin, and Daniel N. Farhey, "Mathematical model for bond-slip behavior under cyclic loading," *ACI Structural Journal*, vol 89, no. 6, November-December 1992, pp 692-698.

Yannopoulos, P., "Fatigue bond and cracking characteristics of reinforced concrete tension members," Ph.D. Thesis, Imperial College, London, January 1976.

Yao, Budan, "Finite element analysis of distributed discrete concrete cracking," Ph.D. Dissertation, University of Alberta, Canada, 1992.

Yoneyama, Kouichi, Asuo Yonekura, Shingo Miyazawa and Takeshi Inoue, "Time-dependent bond characteristics of reinforcing bar," *Transactions of the Japan Concrete Institute*, vol 8, 1986.

Yoshikawa, Hiromichi, and Tada-aki Tanabe, "An analytical study of the tension stiffness of reinforced concrete members on the basis of bond-slip mechanism," *Transactions of the Japan Concrete Institute*, vol 8, 1986.

Other Related References

Bazant, Z.P., and P. Gambarova, "Rough cracks in reinforced concrete," *Journal of Structural Engineering*, ASCE, vol 106, no.ST4, April 1980, pp 819-843.

Bishop, J.F.W., and R. Hill, "A theory of the plastic distortion of a polycrystalline aggregate under combined stress," *The Philosophical Magazine*, vol 42, no. 327, 1951, pp 414-427

CEB (Comité Euro International du Béton) - FIP, Model code, Thomas Telford Services Ltd., London, 1991.

Cheney, E.W., and A.A. Goldsmith, "Newton's method of convex programming and Tchebycheff approximation," *Numer. Math.*, vol 1, 1959, pp 253-268.

Cox, James V., "Geneseos - A finite element program for algorithm prototyping and the development of custom analysis systems," Technical Report, Naval Facilities Engineering Service Center, Port Hueneme, CA 1995 (in publication).

Drucker, Daniel C., "Some implications of work hardening and ideal plasticity," *Quarterly of Applied Mathematics*, vol 7, no. 4, January 1950, pp 411-418.

Drucker, Daniel C., "A more fundamental approach to plastic stress-strain relations," Proceedings of the First U.S. National Congress of Applied Mechanics, ASME, 1951, pp 487-191.

Drucker, Daniel C., "On the postulate of stability of material in the mechanics of continua," *Journal de Mécanique*, vol 3, no. 2, June 1964, pp 235-249.

Drucker, Daniel C., "Discussion of the paper: Nonassociative flow and stability of granular materials, by Lade, Nelson, and Ito, *Journal of Engineering Mechanics*, ASCE, vol 115, no. 8, 1989, pp 1842-1845.

Drucker, Daniel C., and Ming Li, "Non-associated plastic deformation and genuine instability," *Acta Mechanica*, Supplement 3, D.E. Beskos and F. Zeigler, editors, 1992, pp 161-171.

Drucker, Daniel C., and Ming Li, "Triaxial test instability of a nonassociated flow-rule model," *Journal of Engineering Mechanics*, ASCE, vol 119, no. 6, June 1993, pp 1188-1204.

Goodman, R.E., R.L. Taylor and T.L. Brekke, "A model for the mechanics of jointed rock," *Journal of Soil Mechanics and Foundation Division*, ASCE, vol 94, no. SM3, May 1968, pp 637-659.

Hill, R., "A general theory of uniqueness and stability in elastic-plastic solids," *Journal of the Mechanics and Physics of Solids*, vol 6, 1958, pp 236-249.

Hughes, Thomas J.R., "Efficient and simple algorithms for the integration of general classes of inelastic constitutive equations including damage and rate effects: application to

the cap model for soils and concrete," Technical Report CR 87.004, Naval Civil Engineering Laboratory, Port Hueneme, CA, February 1987.

Hughes, Thomas J.R., "An assessment of modeling techniques for the finite element analysis of reinforced concrete plate and shell structures," Technical Report No. CR 88.008, Naval Civil Engineering Laboratory, Port Hueneme, CA, January 1988.

Hughes, Thomas J.R., "Three-dimensional and plane stress constitutive models and algorithms for reinforced concrete plate and shell structures incorporating anisotropic damage mechanisms and viscous regularization effects," Technical Report No. CR 91.010, Naval Civil Engineering Laboratory, Port Hueneme, CA, August 1991.

Jung, Joseph, "Discrete failure modeling of reinforced concrete systems," Ph.D. Dissertation, Department of Civil Engineering, University of California, Davis, 1989.

Kelly, J.E., "The cutting-plane method for solving convex programs," *J. Soc. Indust. Appl. Math*, vol 8, no. 4, December 1960, pp 703-712.

Lade, Poul V., Richard Nelson and Marvin Ito, "Nonassociated flow and stability of granular materials," *Journal of Engineering Mechanics*, ASCE, vol 113, no. 9, September 1987, pp 1302-1318.

Lade, Poul V., and Daniel Pradel, "Instability and plastic flow of soils. I: Experimental observations," *Journal of Engineering Mechanics*, ASCE, vol 116, no. 11, November 1990, pp 2532-2550.

Lade, Poul V., and Jerry A. Yamamuro, "Stability of granular materials in postpeak softening regime," *Journal of Engineering Mechanics*, ASCE, vol 119, no. 1, January 1993, pp 128-144.

Leroy, Y., and M. Ortiz, "Finite element analysis of strain localization in frictional materials," *International Journal for Numerical Methods in Engineering*, vol 13, 1989, pp 53-74.

L'Hermite, R. "Idées actuelles sur la technologie du béton," Documentation Technique du Bâtiment et des Travoux Publics, Paris, 1955.

Lubliner, Jacob, Plasticity theory, Macmillan Publishing Company, New York, NY, 1990.

Luenberger, David G., Linear and nonlinear programming, 2'nd edition, Addison-Wesley Publishing Company, Reading, MA, 1984.

Mandel, J., "Conditions de stabilité et postulat de Drucker," in Proceedings of the IUTAM Symposium on Rheology and Soil Mechanics, Springer-Verlag, Berlin, 1964, pp 58-68.

Marsden, J., "On the product formulas for nonlinear semigroups," *Journal of Functional Analysis*, vol 13, 1973, pp 51-72.

Melan, E., *Ing-Arch.*, vol 9, 1938, pp 116.

Mroz, Z., "A note on Non-associated flow laws in plasticity," *Journal de Mécanique*, vol 2, 1963, pp 21-42.

Needleman, A., "Non-normality and bifurcation in plane strain tension and compression," *Journal of the Mechanics and Physics of Solids*, vol 27, 1979, pp 231-254.

Ortiz, M., "Topics in constitutive theory for inelastic solids," Ph.D. Dissertation, Department of Civil Engineering, University of California, Berkeley, December 1981.

Ortiz, M., and E.P. Popov, "Accuracy and stability of integration algorithms for elastoplastic constitutive relations," *International Journal for Numerical Methods in Engineering*, vol 21, 1985, pp 1561-1576.

Ortiz, M., and J.C. Simo, "An analysis of a new class of integration algorithms for elastoplastic constitutive relations," *International Journal for Numerical Methods in Engineering*, vol 23, 1986, pp 353-366.

Perano, Kenneth J., "SKYLDU -- A General Purpose Simultaneous Linear Equation Solver Using Skyline Storage," Division 8241, Applied Mechanics Department, Sandia National Laboratories, Livermore, California, September 12, 1986.

Pradel, Daniel, and Poul V. Lade, "Instability and plastic flow of soils. II: Analytical investigation," *Journal of Engineering Mechanics*, ASCE, vol 116, no. 11, November 1990, pp 2551-2566.

Prager, W., "Recent developments in the mathematical theory of plasticity," *Journal of Applied Physics*, vol 20, pp 235-241, 1949.

Raniecki, B., *Bull. Acad. Pol. Sci. Ser. Sci. Tech.*, vol 27, 1979, pg 391.

Rice, J.R., "The localization of plastic deformation," in Theoretical and Applied Mechanics, W.T. Koiter, editor, Proceedings of the 14'th International Congress of Theoretical and Applied Mechanics, North-Holland, Amsterdam, 1976, pp 207-220.

Richtmyer, R.D., and K.W. Morton, Difference methods for initial value problems, John Wiley and Sons, New York, NY, 1967.

Rosinger, E.E., "Stability and convergence of non-linear difference schemes are equivalent, *J. Inst. Math. Applics.*, vol 26, 1980, pp 143-149.

Rudnicki, J.W., and J.R. Rice, "Conditions for the localization of deformation in pressure-sensitive dilatant materials," *Journal of the Mechanics and Physics of Solids*, vol 23, 1975, pp 371-394.

Runesson, K., and Z. Mroz, "A note on non-associated plastic flow rules," *International Journal of Plasticity*, vol 5, 1988, pp 639-659.

Runesson, K., and S. Sture, "Stability of frictional materials," *Journal of Engineering Mechanics*, ASCE, vol 115, no. 8, August 1989, pp 1828-1833.

Runesson, K., and S. Sture, "Discussion of the paper: Nonassociative flow and stability of granular materials," by Lade, Nelson, and Ito, *Journal of Engineering Mechanics*, ASCE, vol 115, no. 8, August 1989, pp 1845-1846.

Simo, J.C., and T.J.R. Hughes, "General return mapping algorithms for rate-independent plasticity," Constitutive Laws for Engineering Materials: Theory and Applications, C.S. Desai *et al.* editors, Elsevier Science, 1987.

Simo, J.C., and R.L. Taylor, "A return mapping algorithm for plane stress elastoplasticity," Computer Methods in Applied Mechanics and Engineering, vol 48, 1985, pp 101-118.

Simo, J.C., and R.L. Taylor, "Consistent tangent operators for rate-independent elastoplasticity," *International Journal for Numerical Methods in Engineering*, vol 22, 1986, pp 649-670.

Sokolnikoff, Ivan Stephen., Mathematical theory of elasticity, 2'nd edition, McGraw-Hill, New York, NY, 1956.

Wang, C.T., Applied elasticity, McGraw-Hill, New York, NY, 1953.

Zienkiewicz, O.C., The finite element method, 3'rd edition, McGraw-Hill, London, England, 1977.

Appendix A

Satisfaction of Drucker's Inequality Implies Stability of Path

Using the notation established in Section 2.6, the following briefly shows that satisfaction of Drucker's Inequality (2.6-1b) implies stability of path as defined by Mandel (1964):

$$\dot{\sigma}_{ij}\dot{\varepsilon}^{p}_{ij}\geq 0 \;\wedge\; \dot{\varepsilon}_{ij}=\dot{\varepsilon}^{e}_{ij}+\dot{\varepsilon}^{p}_{ij} \Rightarrow \dot{\sigma}_{ij}\dot{\varepsilon}_{ij}\geq\dot{\sigma}_{ij}\dot{\varepsilon}^{e}_{ij}$$

$$\dot{\sigma}_{ij}=D_{ijkl}\dot{\varepsilon}_{kl} \;\wedge\; \dot{\sigma}_{ij}=D^{e}_{ijkl}\dot{\varepsilon}^{e}_{kl} \Rightarrow \dot{\varepsilon}_{ab}D_{abcd}\dot{\varepsilon}_{cd}\geq\dot{\varepsilon}^{e}_{ij}D^{e}_{ijkl}\dot{\varepsilon}^{e}_{kl}$$

Since the total and corresponding elastic strains are arbitrary, the positive definiteness of the tangent elastic moduli implies positive definiteness of the elastoplastic moduli.* Now consider specific strain rate tensors of the form $\dot{\varepsilon}_{ij}=m_i m_j$ (*i.e.*, a uniaxial deformation in the $\underline{\mathrm{m}}$ direction):

$$\dot{\varepsilon}_{ij}D_{ijkl}\dot{\varepsilon}_{kl}>0 \;\wedge\; \dot{\varepsilon}_{ij}=m_i m_j \Rightarrow m_i m_j D_{ijkl} m_k m_l>0$$

$$A_{kl}(\underline{\mathrm{m}})\equiv m_i D_{ijkl} m_l \Rightarrow m_j A_{jk}(\underline{\mathrm{m}}) m_k>0$$

Since $\underline{\mathrm{m}}$ was arbitrary, positive definiteness of **D** is shown to imply positive definiteness of **A** – thus stability of path.

---

* Actually a stronger statement than this is proven but this is all we need. That is, satisfaction of Inequality (2.6-1b) implies satisfaction of Inequality (2.6-1a) (assuming positive definite tangent elastic moduli) so the former is more restrictive.

Appendix B

Empirical Relations Between Concrete Properties

This appendix presents empirical relationships for the concrete tensile strength and elastic modulus as a function of the compressive strength. These relationships are defined in units of the metric system.

The tensile strength is expressed in terms of the compressive strength as

$$f_t = 0.3(f_c)^{2/3} \tag{B-1}$$

where both f_t and f_c are expressed in N/mm^2. For this study, the relationship was initially adopted from the work of Eligehausen *et al.* (1983). (It is in common use in Europe since it was proposed in the Comité Euro International du Béton, CEB, model code.) This relationship was used for most of the validation problems to relate a measure of the concrete compressive strength to a measure of the tensile strength. The compressive strength of a cylinder was typically used.

Figure B-1 shows how concrete tensile and compressive strengths, for specimens addressed in this study, compare with the empirical relationship.* The CEB uses Equation (B-1) to relate compressive strength to the tensile strength and indicate that the tensile strength is assumed to be equal to only 60 percent of the splitting strength; they indicate the

---

* Generally, the squares denote cube strength values, and circles denote cylinder strength values. The exception to this convention is the "cylinder strength" values of Tepfers and Olsson (1992); in this case the "equivalent cylinder strength" is obtained by the formula from L'Hermite (1955) are combined with the cube splitting strengths.

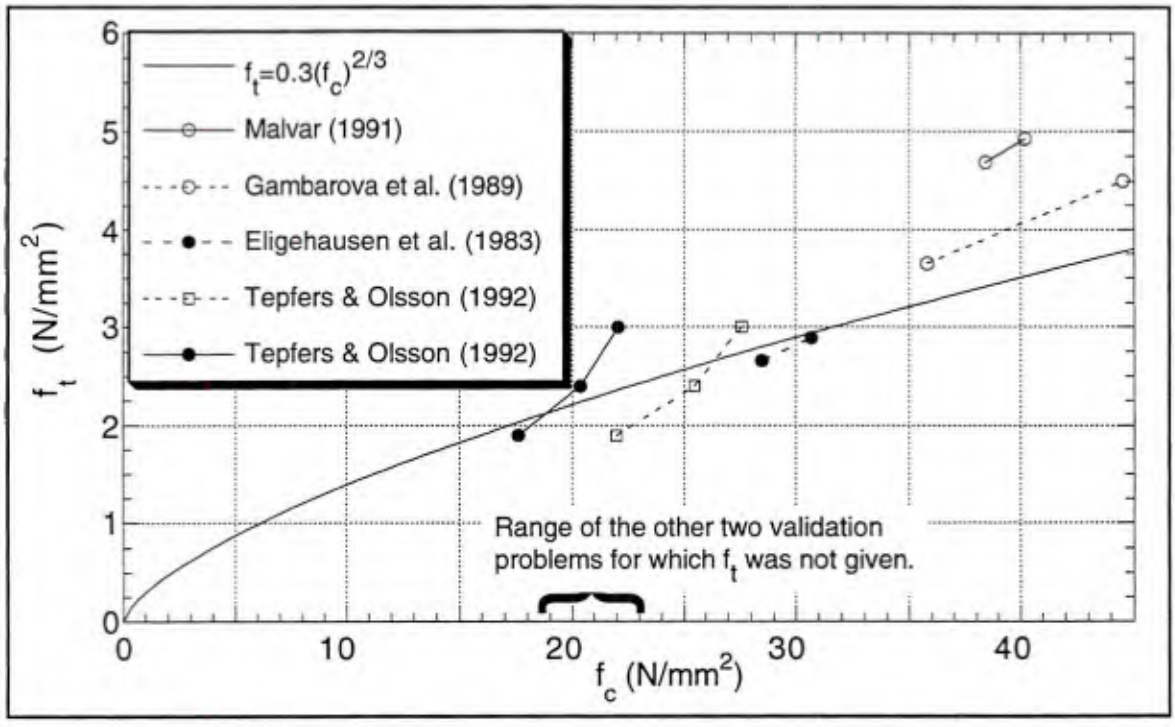

Figure B-1 Equation (B-1) for f_c versus f_t compared to experimental values of validation tests.

range of variability is ±30 percent. The most significant deviation from Equation (B-1) was by the concrete used in the Malvar (1991) specimens; this deviation could be due to the use of relatively small, coarse aggregates in the mix to accommodate the small specimen size. Mirza *et al.* (1979) studied the relationship between concrete compressive and tensile strengths; the scatter in the experimental data would bound that shown in Figure B-1.

The formula used in this study to relate the elastic modulus to the compression strength is given by

$$E_c=41{,}000[1-\exp(-0.075f_c)]. \qquad \text{(B-2)}$$

Appendix C

Proof of Nonnegative Incremental Plastic Work for the Current Calibration

For the current calibration of the bond model, the incremental plastic work can be shown to be nonnegative for all material states. Assuming plastic loading, the plastic work is nonnegative if and only if the rate of radial dilation (g) is less than or equal to the secant to the yield criterion for all corresponding states – Inequality (4.4-3). As noted in Section 4.4, the secant is referred to as the *dilation bound.* In this appendix the satisfaction of this inequality is considered in detail.

First let's obtain a lower bound, with respect to damage, on $-|\tau|/\sigma$ – a "weak" dilation bound. The transition from the power criterion to the exponential criterion occurs when $d\in(d_0,d_1)$ while dilation can occur for $d\in[0,Z_1)$. For this calibration $(d_0,d_1)=(0.38,0.53)$ and $Z_1\le Z_2=0.48$ so both components (power and exponential) of the yield criterion can participate during the radial dilation – a very annoying detail in this context.

Initially let's consider only the power component of the yield criterion (*i.e.*, as if $W_e\equiv 0$); that's all we would need to do if $Z_1\le d_0$ for all states of stress – not the case for this calibration. Based on Equation (3.3-2) it follows that

$$\frac{|\tau|}{-\sigma}=\frac{C(d)M\left|\frac{-\sigma}{f_t}+\hat{\alpha}(d)\right|^{\alpha_p}\operatorname{sgn}\left(\frac{-\sigma}{f_t}+\hat{\alpha}(d)\right)}{\left(\frac{-\sigma}{f_t}\right)}. \tag{C-1a}$$

Since the power component of the yield criterion monotonically increases in $\hat{\sigma}(d)$, it can be replaced by its minimum value – 0 (see Figure 3.3-3). Similarly $C(d)$ can be replaced by its minimum, $C(1)$, to obtain an even weaker *dilation bound* as

$$\frac{|q|}{-\sigma} \geq C(1)M\left(\frac{-\sigma}{f_t}\right)^{\alpha_p - 1}. \tag{C-1b}$$

This dilation bound is completely independent of d (*i.e.*, it holds for all d), but assumes W_e=0.

Now we seek to obtain an upper bound on dilation that is independent of d. Figure 4.3-1 shows the model function for g (for σ constant) and illustrates that we simply must determine $g_{max}(-\sigma/f_t)$ as outlined in Algorithm 4.3-1. In "scaled-space" g attains a maximum at a value of

$$\begin{aligned} d_s &= d_{gmax} H_{scale} \\ &= \langle a + b(-\sigma/f_t) + c(-\sigma/f_t)^2 \rangle \end{aligned} \tag{C-2}$$

where $a \cong -0.002394$, $b \cong 0.00265$, and $c \cong 0.001154$. Applying Equation (4.3-2b) and converting the result from "scaled-space" gives the maximum dilation as

$$g_{max}(-\sigma/f_t) = \frac{\dfrac{1}{1.1 + 50\langle a + b(-\sigma/f_t) + c(-\sigma/f_t)^2 \rangle} - \dfrac{1}{18.6}}{\hat{V}_{scale}(-\sigma/f_t)} \tag{C-3}$$

where $\hat{V}_{scale}(-\sigma/f_t)$ represents the value given by Equation (4.3-1b) with the dependence on confinement stress explicitly shown here.

Combining the results of Inequality (C-1b) and Equation (C-3), a sufficient condition for satisfying Inequality (4.4-3) (for the case W_e=0) is given by

$$g_{max}(-\sigma/f_t) \leq C(1)M\left(\frac{-\sigma}{f_t}\right)^{\alpha_p - 1} \tag{C-4}$$

for all stress states on the yield surface. Figure C-1 shows the graph of both sides of the inequality for $g_{max}(-\sigma/f_t) \geq 0$ with the current calibration. For confinement stresses greater

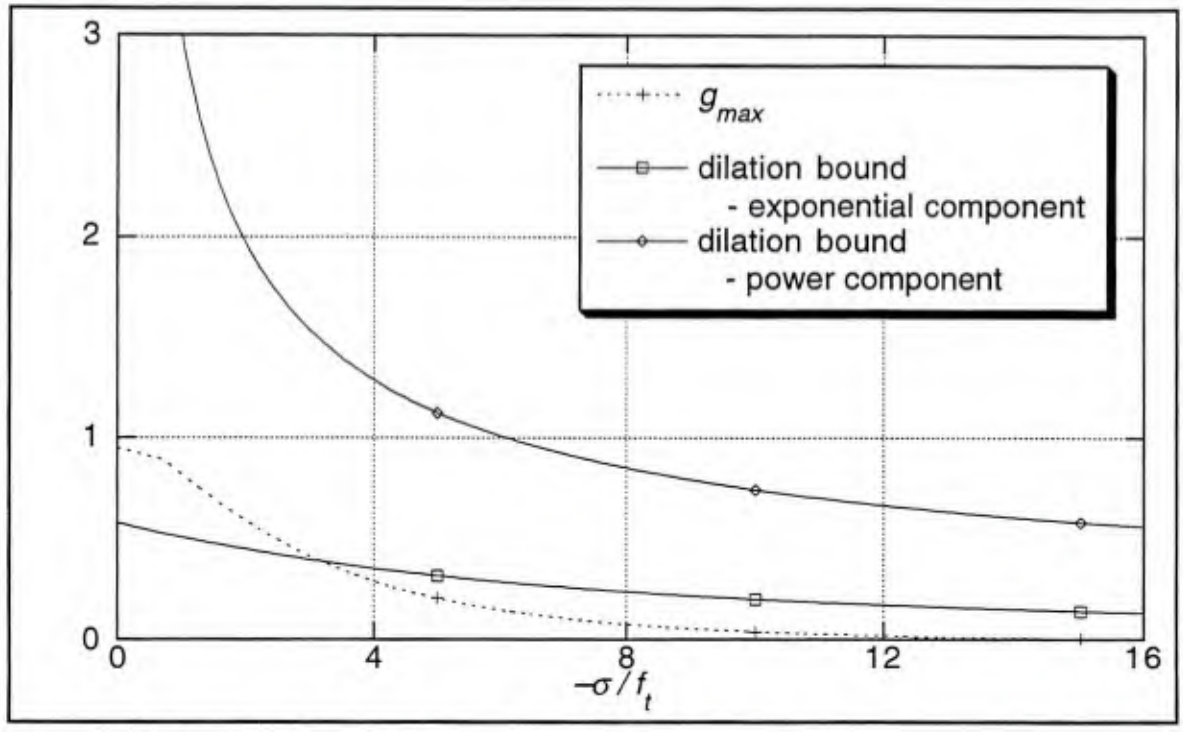

Figure C-1 Dilation bounds and g_{max} versus confinement stress.

than shown, the *dilation bound* and g_{max} asymptotically approach zero from above and below, respectively.

In addition to the dilation bound for the power component, a dilation bound for the exponential component is also shown. Using the same simplifications that led to Inequality (C-1b), the dilation bound for the exponential component is found to be

$$\frac{|\tau|}{-\sigma} \geq \frac{C(1)\left[1 - e^{-\alpha_e(-\sigma/f_t)}\right]}{\left(\frac{-\sigma}{f_t}\right)}. \tag{C-5}$$

For the current calibration, the transition to the exponential component is not complete when the radial dilation ends (*i.e.*, $Z_1 < d_1$ for all confinement stresses); in addition a positive g_{max} (as defined in Algorithm 4.3-1) is not attained when the exponential component contributes to the yield criterion (*i.e.*, for a $d_{gmax} > d_0$). Both of these points indicate that a sufficient condition analogous to Inequality (C-4) for the exponential

component though expedient might be excessively strict. Figure C-1 shows that for small confinement stresses this suggested sufficient condition would be violated for the current calibration. This does not necessarily imply that the incremental plastic work is negative, but at the very least it implies a more accurate bound is needed.

As discussed in the Chapter 3, the yield criterion is a linear combination of a power and exponential component where the respective weighting factors range between zero and one and have a sum of one. We've already shown that the power component satisfies Inequality (4.4-3) for all d, so if we can show that the exponential component satisfies it for $d>d_0$ the weighted combination of the components will satisfy it for $d>d_0$.

For $d>d_0$ when $g_{max}>0$ the maximum value of g is at d_0 (*i.e.*, if $g_{max}>0 \Rightarrow$ for a fixed σ $\max_{d\in[d_0,1]} g(\sigma,d) = g(\sigma,d_0)$ since g monotonically decreases in d for this subset of its domain). Thus instead of using g_{max}, as in Inequality (C-4), we can use the smaller upper bound on g given by

$$\begin{aligned}\max_{d\in[d_0,1]} g(\sigma,d) &= g(\sigma,d_0) \\ &= \frac{\dfrac{1}{1.1+50d_0[0.73+0.244(-\sigma/f_t)]}\dfrac{1}{18.6}}{\widehat{V}_{scale}(-\sigma/f_t)}.\end{aligned} \tag{C-6}$$

Figure C-2 shows that the dilation bound of Inequality (C-5) bounds the local maximum of g when the exponential component contributes to the yield criterion. Thus the incremental plastic work always remains nonnegative, and the second law of thermodynamics is satisfied.

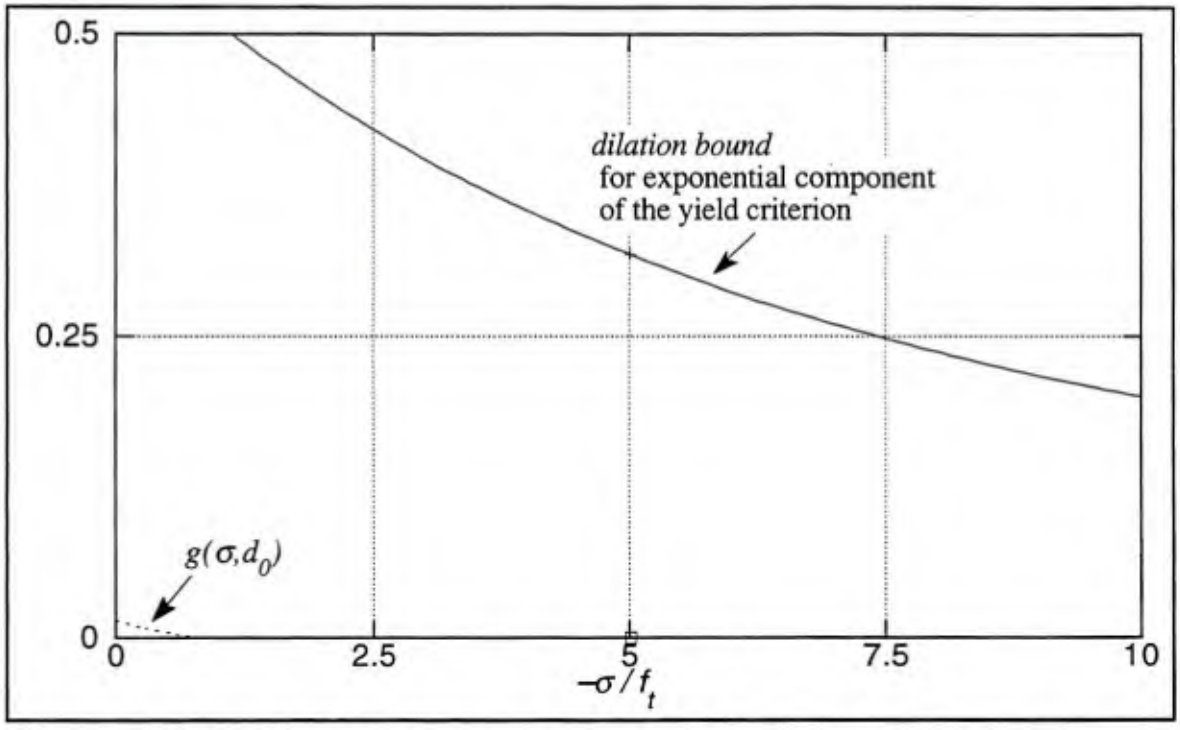

Figure C-2 Dilation bound for exponential component of yield criterion and $g(\sigma,d_0)$ versus confinement stress.

Appendix D

The Effect of the Rigid Bar Assumption in Determining Elastic Constants

Because of the difficulty in measuring local bond-slip behavior, experiments are often designed with relatively short embedment lengths; the underlying premise is that the bar will essentially behave as if it is rigid. If this is valid then: 1) the bond stress is approximately constant over the length of the bar and therefore the average bond stress is approximately equal to the local bond stress, and 2) the slip is approximately constant over the length of the bar and therefore any measurement of bar slip is approximately equal to the local slip. Though the predictions of the model developed in this study support these assumptions near ultimate load and during softening, they are not valid during the initial loading when elastic response plays a more critical role.

In this appendix we examine the effect of the rigid bar assumption on determining the elastic constant D_{11}^{e}. To do so we will invoke two simple uniaxial models and thus ignore the effects of normal displacement and confinement stress. Figure D-1 shows the first model – a continuous model that smears the effect of the ribs. The bar is modeled as linear elastic under a state of uniaxial tension. The effect of the concrete is treated as a localized effect, modeled as having a linear elastic shear resistance.

Consider equilibrium of an arbitrary, finite piece of the bar as shown in Figure D-2. Equilibrium is trivially given by Equation (D-1). Applying the fundamental theorem of calculus, noting that for the resulting integral to be zero requires the integrand to be zero, and since x_1 and x_2 are arbitrary, the governing differential equation is obtained as

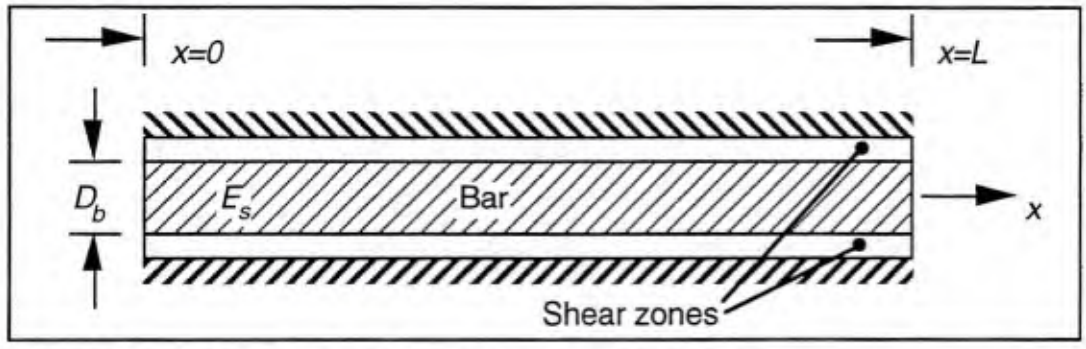

Figure D-1 Uniaxial bar model with continuous bond zone.

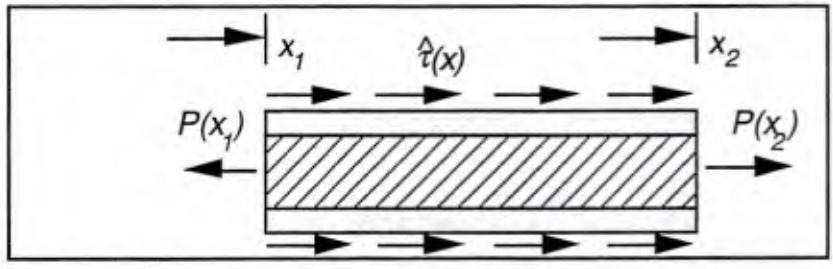

Figure D-2 Equilibrium forces on a finite piece of the bar.

$$\frac{dP}{dx} + \hat{\tau} = 0 \tag{D-1}$$

where P denotes the bar force and $\hat{\tau}$ denotes the axial force per unit length provided by the shear zone. Now introducing the constitutive laws for the shear zone and the rod gives the differential equation in terms of the displacement as

$$\frac{d^2u}{dx^2} - \Omega^2 u = 0 \tag{D-2}$$

where $\Omega = \frac{2}{D_b}\sqrt{\frac{D^e}{E_s}}$ and D^e denotes the shear stiffness of the bond zone. The latter term is equivalent to D_{11}^e of the bond model. Applying the boundary conditions of $P(0)$=0 and $u(L) = u_L$, the solutions for the axial displacement and force are found to be

$$u(x) = \frac{u_L}{\cosh(\Omega L)}\cosh(\Omega x) \text{ and } P(x) = \frac{\pi E_s D_b^2 u_L \Omega}{4\cosh(\Omega L)}\sinh(\Omega x), \tag{D-3a,b}$$

respectively.

Now let's consider the stiffness obtained with the "rigid bar assumption" given the slip at the free end and the bar force at the loaded end (used to calculate the average bond stress). The resulting stiffness is given by

$$\frac{\tau_{ave}}{u(0)/D_b} = \frac{\sqrt{E_s D^e} D_b}{2L} \sinh(\Omega L) \tag{D-4}$$

Now expanding the sinh term in a Taylor series about zero gives

$$\frac{\tau_{ave}}{u(0)/D_b} = D^e \left(1 + \frac{2D^e L^2}{3E_s D_b^2} + O\left((\Omega L)^5\right) \right). \tag{D-5}$$

By a similar analysis, if the slip is measured at the loaded end of the specimen one obtains a stiffness estimate of

$$\frac{\tau_{ave}}{u_L/D_b} = \frac{\sqrt{E_s D^e} D_b}{2L} \tanh(\Omega L) \tag{D-6}$$

and a Taylor series expansion gives

$$\frac{\tau_{ave}}{u_L/D_b} = D^e \left(1 - \frac{4D^e L^2}{3E_s D_b^2} + O\left((\Omega L)^5\right) \right). \tag{D-7}$$

The second term in each Taylor series, shown in full glory here, is proportional to $(\Omega L)^3$. Thus as the rod becomes rigid (*i.e.*, $\Omega L \rightarrow 0$) the actual stiffness of the bond zone, D^e, is obtained no matter where the slip is measured.

The calculation of the average bond stress is based upon the bar force and thus gives an accurate average value; by Equations (D-1) and (D-3a) the distribution of τ is proportional to u. In contrast the measurements used for end slips represent bounds on the displacement response, Figure D-3. When the free-end slip is used the "average slip" is under predicted, and thus Equation (D-5) indicates the stiffness is over predicted. When the loaded-end slip is used the "average slip" is over predicted, and thus Equation (D-7) indicates the stiffness is under predicted. The magnitude of the "second order" term in Equation (D-5) is twice that of Equation (D-7) which simply indicates that the lower bound on the displacement is more representative of the displacements on the average.

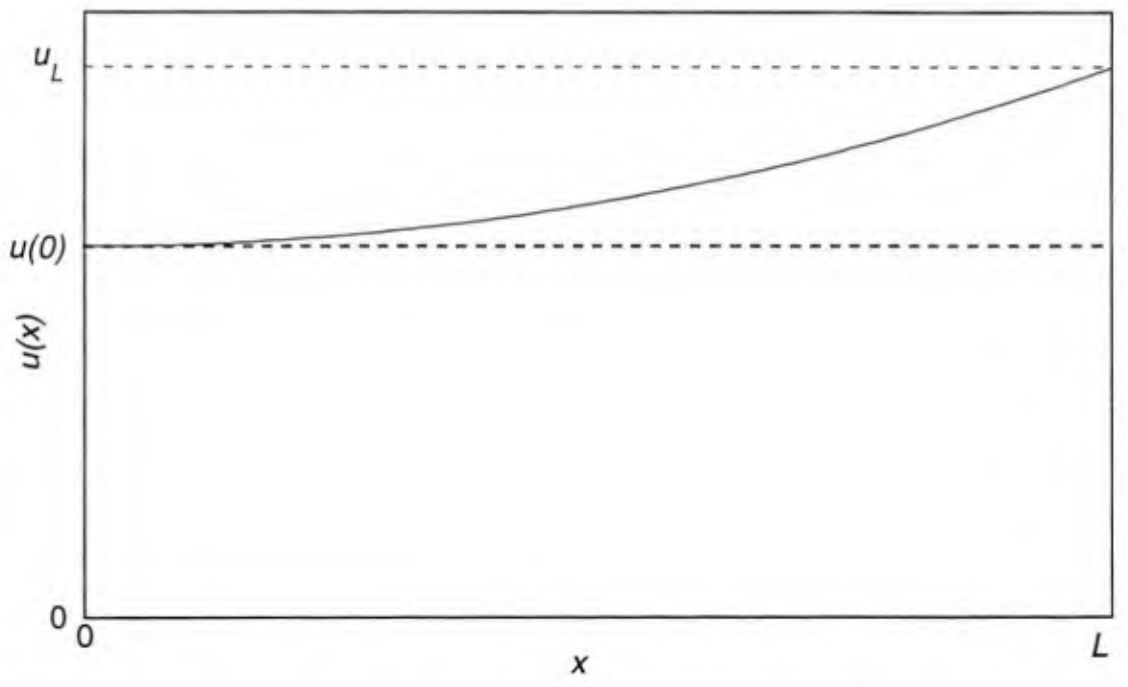

Figure D-3 Axial displacement for the bond model with a continuous shear zone.

Assuming this simple model has some merit, there are means to improve the estimate of the elastic stiffness. If an experiment includes slip measurements at both ends of the specimen and $\Omega L<1$, this simple model suggests the estimate of the elastic stiffness can be improved simply by using a weighted average of the stiffnesses based upon each displacement. A weighted average using two times Equation (D-5) and one times Equation (D-7) reduces the error to $O((\Omega L)^5)$. If only one end slip is measured, the typical situation, then the corresponding nonlinear Equation (D-4) or (D-6) can be 1) solved numerically for D^e or 2) approximated by a Taylor series to two terms (the first two terms of Equation [D-5] or [D-7]) and then solved by the quadratic equation for D^e.

If we assume that $\tau_{ave}/(u_L/D_b)=0.1E_c$ is measured, let's consider the magnitude of the error introduced by the rigid bar assumption. Table D-1 gives the numerical solution of Equation (D-4) for three experiments considered in the early stages of this study. For this table, E_c is calculated by Equation (B-2)..

Table D-1. "Errors" in the elastic stiffness due to the rigid bar assumption for three experiments addressed in this study. End slip is measured at the free end.

	Malvar (1991) series 3 Tests	**Gambarova *et al.* (1989)**	**Eligehausen *et al.* (1983)**
$\tau_{ave}/(u(0)/D_b)$	3870	3899	3668
D^e *from Equation (A-4)*	3395	3472	2851
"Error" in $\tau_{ave}/(u(0)/D_b)$	14%	12%	29%

For the experiments of Malvar (1991) the end slips at the loaded end provide the most reliable data. The errors in D^e numerically obtained from Equation (D-6) are 26 and 28 percent for test series 2 and 3, respectively. In this case the value of D^e is greater than $\tau_{ave}/(u_0/D_b)$ (the approximate value estimated directly from measurements). Now consider the converse case of a model value of D^e given by $0.1E_c$. The corresponding $\tau_{ave}/(u_0/D_b)$ value is 21 and 22 percent less than D^e for test series 2 and 3, respectively.

These errors can be significant relative to the simulation of a single elastic response, but they might not be significant relative to the amount of scatter in a given data set. The initial stiffness is one component of the response that we intended to model relatively accurately; thus the interpretation of the data must be well understood. In some of the early development efforts that made exclusive use of point models, the above analysis had not yet been considered. Subsequent two-dimensional analyses motivated the above analysis.

As a simple check on the validity of a continuous model, I also considered a discrete model that was based on the assumption that the bars only contact the concrete on the rib faces. For the Malvar tests where the adhesion is broken during precracking, this is a reasonable assumption. Figure D-4 shows a schematic of the model for n ribs. The discrete

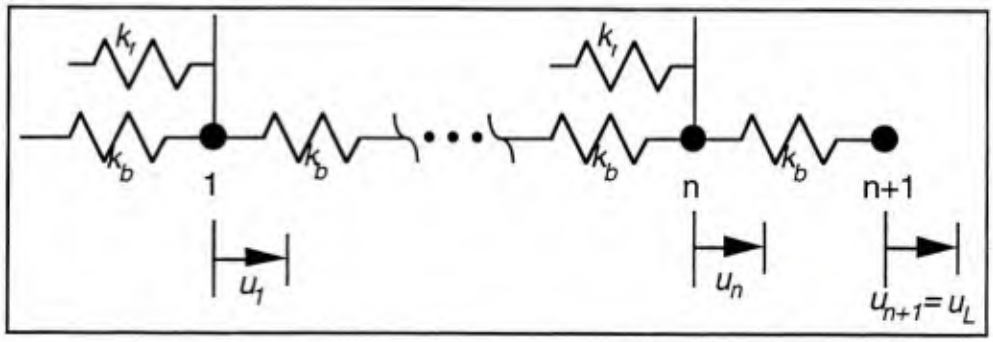

Figure D-4 Schematic of a discrete model for the bar and bond zone.

stiffnesses k_r and k_b denote the stiffness of bond zone at a rib and the bar between two adjacent ribs, respectively.

Equilibrium of the i'th node gives the difference equation

$$k_b(u_{i+1}-u_i) - k_b(u_i-u_{i-1}) - k_r u_i = 0 \tag{D-8}$$

Considering the equilibrium of n nodes and applying the boundary conditions $u_0=u_1$ and $u_{n+1}=u_L$ gives a tridiagonal system that is easily solved for the rib displacements. Figure D-5 compares the results of the discrete and continuous models for the Malvar specimen. The continuous model implicitly represents the homogenization over a unit cell of the more discrete problem. The good agreement of the results indicates that the homogenization gives a sufficiently accurate approximation for this simple discrete problem. Thus the effect of the rigid bar assumption will be nearly identical to that obtained for the continuous model.

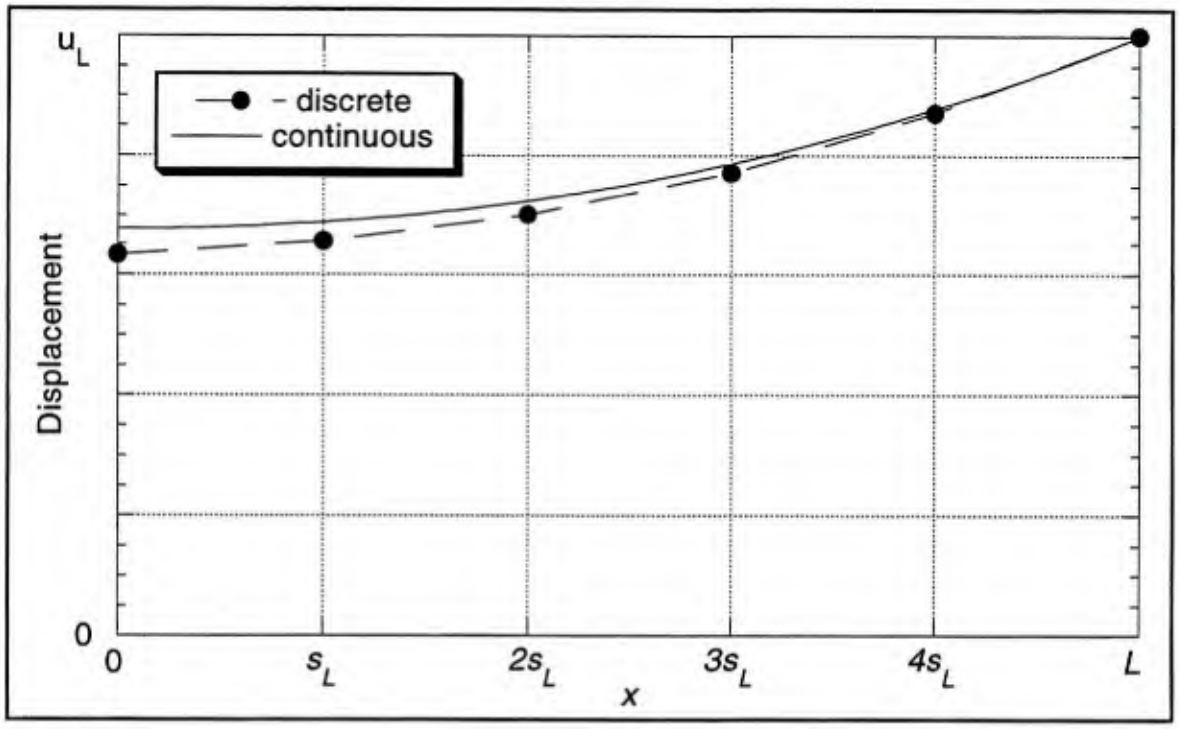

Figure D-5 Continuous versus discrete model results for the Malvar specimen.

Appendix E

Reinforcing Bar Point Model

This appendix presents a simple point model for the axisymmetric response of a reinforcing bar. For short embedment length specimens, a combination of link elements can be used to construct a discrete model of a bond specimen. The point model presented here can serve as the "constitutive law" for a link element that represents the response of the bar.

Figure E-1 shows a reinforcing bar, of embedment length L, in an axisymmetric state of stress. The 1-axis represents the axis of symmetry. The link element will relate the relative displacements between points *a* and *b* to normal and tangent components of traction on the face of the bar (*i.e.*, the "bond stresses"). In this case, it is assumed the displacements are measured at the loaded end.

Assume an axisymmetric state and that σ and τ are uniform. Equilibrium of an arbitrary section of the bar in the 1-direction allows us to express σ_{11} in terms of τ as

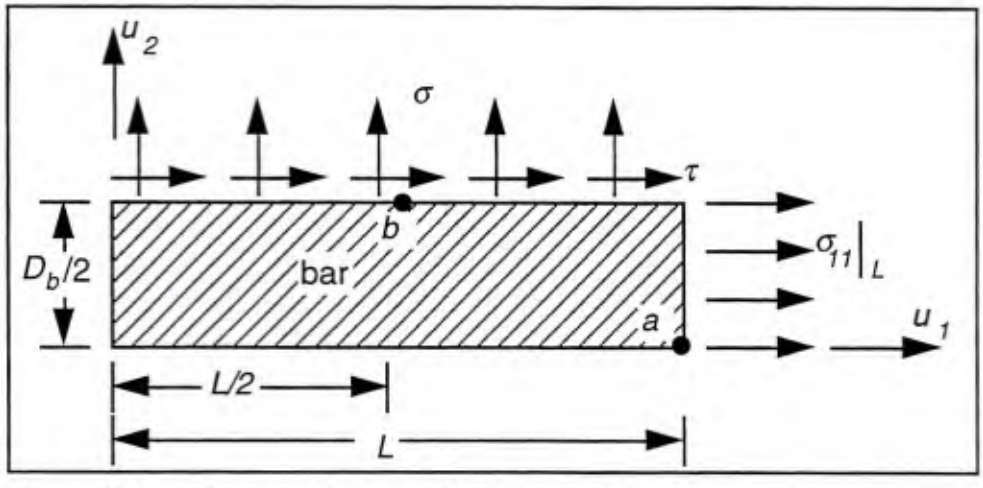

Figure E-1 Axisymmetric stress state of a short bar.

$$\sigma_{11}(x_1) = -\frac{4\tau x_1}{D_b}.$$

Now applying Hook's law gives the two normal strains as

$$\varepsilon_{11}(x_1) = -\frac{4\tau x_1}{ED_b} - \frac{2\nu\sigma}{E} \text{ and } \varepsilon_{22}(x_1) = (1-\nu)\frac{\sigma}{E} + \frac{\nu}{E}\frac{4\tau x_1}{D_b}$$

Now integrating the normal strains between the two points (*i.e.*, assuming the shear strain contributions are insignificant) gives the relative displaces as

$$\Delta u_1 = u_1^b - u_1^a = \left(\frac{3L^2}{2ED_b}\right)\tau + \left(\frac{\nu L}{E}\right)\sigma \text{ and } \Delta u_2 = u_2^b - u_2^a = \left(\frac{\nu L}{E}\right)\tau + \left(\frac{D_b(1-\nu)}{2E}\right)\sigma.$$

Expressing these relations in matrix form gives the compliance matrix as

$$\begin{Bmatrix} \Delta u_1 \\ \Delta u_2 \end{Bmatrix} = \begin{bmatrix} \frac{3L^2}{2ED_b} & \frac{\nu L}{E} \\ \frac{\nu L}{E} & \frac{D_b(1-\nu)}{2E} \end{bmatrix} \begin{Bmatrix} \tau \\ \sigma \end{Bmatrix}.$$

Inverting this matrix gives the stiffness matrix for the point model of the bar.

Appendix F

An Elastic-Brittle Constitutive Model with Longitudinal Cracking

This appendix presents a simple constitutive model that was used to model the concrete in axisymmetric bond specimens. This trivial model is the "two-dimensional implementation" of the "partly-cracked elastic" model presented by Tepfers (1979). Since bond failures are often associated with splitting, it is necessary to have a concrete model that includes longitudinal cracking so that splitting failures can be predicted.

The concrete model's simplicity certainly leads to questions about the accuracy of the specimen models, but the model's simplicity also makes the validation problems more relevant to member-scale problems; this is because for member-scale problems, the bond model is likely to be "connected to" a "local model" that captures the response of the concrete adjacent to the bond zone. This local model is intended to provide a transition between the member-scale and bar-scale, and will probably be based upon a simple model. In addition, many of the nonlinearities that occur near the bar are accounted for in the response of the bond model.

In the axisymmetric constitutive model, the material (concrete in this case) is treated as a homogeneous, isotropic elastic solid until the hoop stress reaches a limiting value, σ_t. Upon reaching the limiting value, the model releases all hoop stresses at the particular material point and enters a state of plane stress (*i.e.*, it behaves as a "radial deck of cards" which vary in thickness with the radius). The implicit assumption here is that when a bond

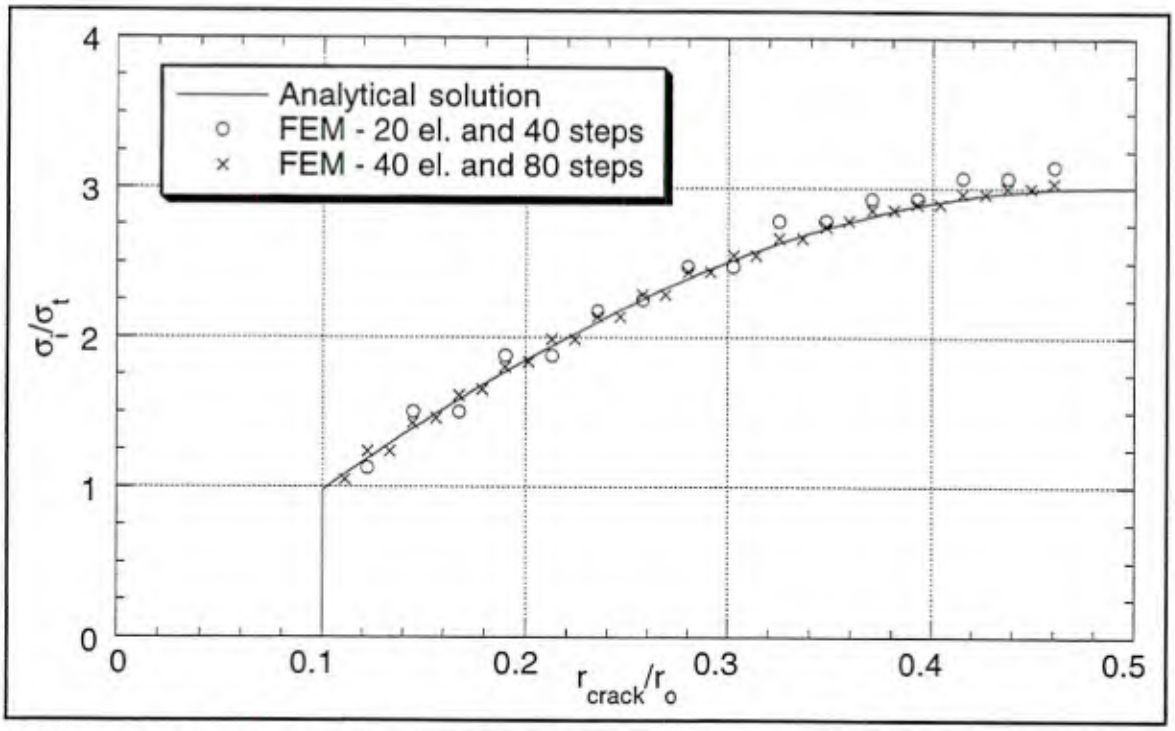

Figure F-1 Comparison of elastic-brittle constitutive model to the analytical, elastic partially-cracked solution of Tepfers.

specimen cracks longitudinally, there are numerous cracks around the circumference, and an axisymmetric analysis is still relevant.

Figure F-1 compares the elastic partially-cracked solution of Tepfers with a FE model incorporating the simple material model. The problem consists of a thick-walled cylinder subjected to an internal pressure, σ_i. The inner and outer (r_o) radius of the cylinder are 7 mm and 70 mm, respectively. The material properties are σ_t= 2.46 MPa and E=34,000 MPa. The figure shows the internal pressure versus the radius of the cracks, both in a nondimensional form. The analytical solution (see *e.g.*, Herrmann and Cox [1994]) becomes unstable at a radius of about 49 percent of r_o.

The FEM model used uniform length elements and uniform time steps. The spacial and temporal model refinement show convergence to the analytical solution. Because of the lack of material softening, there is no mesh sensitivity.

Appendix G

Comments on the Geneseos Interface Element

This appendix provides a brief discussion of the Geneseos (Cox [1995]) interface element used in the two-dimensional validation tests. The bond model is defined in terms of interface quantities (tractions and relative displacements). As such, for implementation it can serve as a two-stress law for interface elements.* There is a wealth of interface element derivations in the literature (see *e.g.*, Goodman *et al.*, [1968], and Keuser and Mehlhorn [1987]); this appendix will merely comment on a few aspects of the Geneseos element that might clarify the validation analyses.

Figure G-1 presents a schematic of the element. There are two sides of the element, 1-2 and 3-4. The Geneseos element integrates the "constitutive law" along the *master side*, side 3-4. Two integration rules are available, trapezoidal and Gaussian Quadrature. For the bond model application, only the Gaussian Quadrature rule was used.

The element is shown with separation between the two sides. This separation can be interpreted as a physical gap (*e.g.*, in a contact problem) or as a "finite thickness" for the interface element. In the latter case, the "finite thickness" is for modeling convenience; it does not suggest the element has a volume. That is, the integration is limited to the master

* It could also serve as a two-stress law for slide lines, but the simpler interface elements were considered to be adequate for the specimens considered.

side, irrespective of the thickness. As such, the equivalent nodal forces at nodes 1 and 2 are determined as if the element has no thickness.

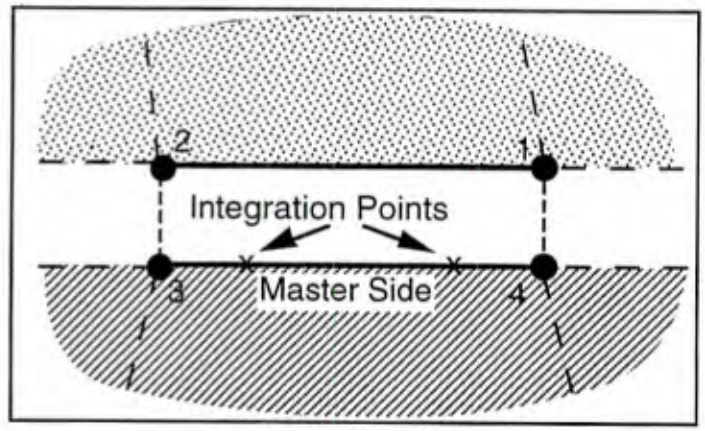

Figure G-1 Schematic of Geneseos interface element.

There are two subtle points to be made about these equivalent nodal forces when used with a finite thickness element: 1) the element is not in equilibrium due to the couple formed by the tangent nodal forces, and 2) for axisymmetric applications the normal stress is implicitly assumed to vary as 1/r. The first point could be overcome by balancing the "tangential couple" with a "vertical couple." However, for bond applications convergence studies indicated the effect is of second order. The second point implies the element acts as if it cannot carry hoop stress.

For some applications, the stiffness of the interface element is related to the element's finite thickness. For the Geneseos interface element this requires the material law to be adjusted by the user. This has not been done in the validation problems, and no apparent size effects have occurred. This behavior for the bond problems is discussed in Section 7.5.

AC ENGRG INC / BERRY, WEST LAFAYETTE, IN
ADINA ENGRG, INC / WALCZAK, WATERTOWN, MA
ADVENT ENGRG SVCS / DYRNESS, SAN RAMON, CA
AEWES / LIB, VICKSBURG, MS; PETERS, VICKSBURG, MS
AFOSR / NA (WU), WASHINGTON, DC
AFWL/NTE / BALADI, KIRTLAND AFB, NM
ALLIED BAR COATERS / HARTLEY, CARDIFF WALES
ANATECH APPLICATIONS / CASTRO, SAN DIEGO, CA
ANATECH RESEARCH CORP / RASHID, SAN DIEGO, CA
APPLIED PHYSICS TECH / SWANSON, MCLEAN, VA
APPLIED RSCH ASSOC, INC / HIGGINS, ALBUQUERQUE, NM
ARMY / R&D LAB, STRNC-UE, NATICK, MA
ARMY CORPS OF ENGRS / HQ, DAEN-ECE-D, WASHINGTON, DC
ARMY EWES / WES (NORMAN), VICKSBURG, MS; WESIM-C (N. RADHAKRISHNAN), VICKSBURG, MS
ASSOCIATED SCIENTISTS/ MCCOY, WOODS HOLE, MA
BING C YEN / IRVINE, CA
BRITISH EMBASSY / ELLIS, WASHINGTON, DC
BUREAU OF RECLAMATION / MCLEAN, DENVER, CO
BYU / ROLLINS, PROVO, UT
CALIF INST OF TECH / PASADENA, CA
CALTRANS / ZELINSKI, SACRAMENTO, CA; HOLLAND, SACRAMENTO, CA
CATALINA MARINE SCIENCE / AVALON, CA
CATHOLIC UNIV / CE DEPT (KIM) WASHINGTON, DC
CENTRIC ENGINEERING SYSTEMS INC / TAYLOR, PALO ALTO, CA
CHALMERS UNIVERSITY OF TECH / AKESSON, GOTEBORG SWEDEN; TEPFERS, 412 74 GOTEBORG, SWEDEN
CHEUNG AND ASSOCIATES / CHEUNG, IRVINE, CA
CHILDS ENGRG CORP / K.M. CHILDS, JR., MEDFIELD, MA
COLORADO SCHOOL OF MINES / GOLDEN, CO
COLORADO ST UNIV / FORT COLLINS, CO
COMPUTATIONAL MECHANICS / BREBBIA SOUTHAMPTON,
CONSEJO SUPERIOR DE INVESTIGACIONES CIENTIFICAS / TORROJA, 28080 MADRID, SPAIN
CORNELL UNIV / ITHACA, NY
COUNTY OF VENTURA / TAKAHASHI, VENTURA, CA
CRREL / KOVACS, HANOVER, NH
CSU CHICO / ARTHUR, CHICO, CA; MISH, CHICO, CA
CSU FULLERTON / RAMSAMOOJ, FULLERTON, CA
DAMES & MOORE / LOS ANGELES, CA
DET NORSKE VERITAS RESEARCH AS / BERGAN, VERITASVEIEN 1, N-1322 HOVIK, NORWAY
DOT / TRANSP SYS CEN (TONG), CAMBRIDGE, MA
DTIC / ALEXANDRIA, VA
ENVIROPLEX / AUDIBERT, HOUSTON, TX
FAU / REDDY, BOCA RATON, FL
FHWA / LANE, MCLEAN, VA
FORT F / VRETBLAD
GEOCISA / RODRIGUEZ, 28820 COSLADA MADRID, SPAIN
GEORGE WASHINGTON UNIV / ENGRG & APP SCI SCHL (FOX), WASHINGTON, DC
GEOTECHNICAL ENGRS, INC / MURDOCK, WINCHESTER, MA
GERWICK INC / SAN FRANCISCO, CA
HALEY & ALDRICH, INC. / CHET SEYDEMIR, CAMBRIDGE, MA
HERIOT-WATT UNIV / CAIRNS, UNITED KINGDOM
HEUZE / ALAMO, CA
HKS (WEST) INC / REBELO, NEWARK, CA
HKS INC / PAWTUCKET, RI
HQ AFESC / TYNDALL AFB, FL; RDC (DR. M. KATONA), TYNDALL AFB, FL
INSTITUTE OF MARINE SCIENCES / MOREHEAD CITY, NC
IOWA STATE UNIV / AMES, IA
JOHN HOPKINS UNIV / COX, BALTIMORE, MD; LADE, BALTIMORE, MD
KARAGOZIAN AND CASE / CRAWFORD, GLENDALE, CA
LABORATOIRE CENTRAL DES PONTS ET CHAUSSEES / ROSSI, PARIS CEDEX 15, FRANCE
LABORATOIRE DE MECANIQUE DES SOLIDES / LUONG, CEDEX, FRANCE
LABORATOIRE DE MECANIQUE ET TECHNOLOGIE / BERTHAUD, CACHAN, FRANCE

LANTNAVFACENGCOM / CODE 411, NORFOLK, VA
LAWRENCE LIVERMORE NATIONAL LAB / MAKER, LIVERMORE, CA; MCCALLEN, LIVERMORE, CA
LAWRENCE TECH UNIV / SOUTHFIELD, ME
LEHIGH UNIV / BETHLEHAM, PA; RICLES, BETHELEHEM, PA
LIN OFFSHORE ENGRG / SAN FRANCISCO, CA
LOCKHEED / RSCH LAB (M. JACOBY), PALO ALTO, CA; RSCH LAB (P UNDERWOOD), PALO ALTO, CA
MAINE MARITIME ACADEMY / LIB, CASTINE, ME
MARC ANALYSIS RSCH CORP / HSU, PALO ALTO, CA
MATERIALS SCIENCES CORP / CHATTERJEE, BLUE BELL, PA
MCCLELLAND ENGRS / HOUSTON, TX
MCDONNELL DOUGLAS / DORR, SAINT LOUIS, MO
MICHIGAN UNIV / HOUGHTON, MI
MINISTERIO DE DEFENSA / BRAVO, 47007 VALLADOLID, SPAIN
MIT / R.V. WHITMAN, CAMBRIDGE, MA
MOBILE R&D CORP / DALLAS, TX
MONTANA STATE UNIV / PERKINS, BOZEMAN, MT
NATIONAL TECHNICAL UNIVERSITY / TASSIOS, ATHENS
NATL ACADEMY OF SCIENCES / NRC, DR. CHUNG, WASHINGTON, DC
NAVFACENGCOM / CODE 04A3, ALEXANDRIA, VA
NCSC / PANAMA CITY, FL
NEW ENGLAND MARINE RESEARCH LAB / LIB, DUXBURY, MA
NFESC ECDET / WASHINGTON, DC; ESC61 (WU), WASHINGTON, DC; ESC61 CHAWLA, WASHINGTON, DC
NOAA / JOSEPH VADUS, ROCKVILLE, MD
NORDA / BENNETT, NSTL, MS
NORTH CAROLINA STATE UNIV / RAHMAN, RALEIGH, NC
NORTHWESTERN UNIVERSITY / BAZANT, EVANSTON, IL; CE DEPT (BELYTSCHKO), EVANSTON, IL; DOWDING, EVANSTON, IL; LIU, EVANSTON, IL
NRL / CODE 4430, WASHINGTON, DC; RATH, ARLINGTON, VA; VALENT, STENNIS SPACE CENTER, MS
NSF / ASTILL, ARLINGTON, VA; STRUC & BLDG SYSTEMS (KP CHONG), WASHINGTON, DC
NTH / LANGSETH, N-7034 TRONDHEIM; MALO, N-7034 TRONDHEIM, NORWAY
NY MARITIME COLLEGE / BRONX, NY
OCNR / CODE 10P4 (KOSTOFF), ARLINGTON, VA; CODE 1121 (EA SILVA), ARLINGTON, VA
ONR / CODE 1132SM, ARLINGTON, VA; RAMBERG, ARLINGTON, VA
OREGON STATE UNIV / CORVALLIS, OR; CE DEPT (YIM), CORVALLIS, OR; DEPT OF MECH ENGRG (SMITH), CORVALLIS, OR
PENN ST UNIV / KROUTHAMMER, UNIVERSITY PARK, PA; LAB, STATE COLLEGE, PA
PMB ENGRG / LUNDBERG, SAN FRANCISCO, CA
POLITECNICO DI MILANO / GAMBAROVA, 20133 MILANO, ITALY
PORTLAND STATE UNIV / MIGLIORI, PORTLAND, OR
PURDUE UNIVERSITY / WEST LAFAYETTE, IN; RAMIREZ, WEST LAFAYETTE, IN
RAMBOLL HANEMANN & HOJLUND A/S / ANDREASE, VIRUM, DENMARK
RIGAER TECHNISCHE UNIVERSITAT / BULAVS, RIGA 226355, LATVIA
SAN DIEGO STATE UNIV / SAN DIEGO, CA
SCHWER ENGR & CONSULTING SERVICES / SCHWER, WINDSOR, CA
SCOPUS TECHNOLOGY INC / (B NOUR-OMID), EMERYVILLE, CA
SEATTLE UNIV / SEATTLE, WA
SJSU / VUKAZICH, SAN JOSE, CA
SOUTH DAKOTA SCHOOL OF MINES AND TECH / BANG, RAPID CITY, SD
SRI INTL / ENGRG MECH DEPT (GRANT), MENLO PARK, CA; ENGRG MECH DEPT (SIMONS), MENLO PARK, CA
STANFORD UNIV / APP MECH DIV (HUGHES), STANFORD, CA; CE DEPT (PENSKY), STANFORD, CA; LAW, STANFORD, CA
STRUCTURAL ANALYSIS PROGRAMS INC / WILSON, EL CERRITO, CA
TEXAS A&M UNIV / ROSCHKE, COLLEGE STATION, TX
TU DELFT / DE BORST, 2600 GA DELFT, THE NETHERLANDS; VAN MIER, 2600 GA DELFT, THE NETHERLANDS
TUFTS UNIV / SANAYEI, MEDFORD, MA
UCLA / JU, LOS ANGELES, CA
UCSB / MECH ENGRG DEPT (BAYO), SANTA BARBARA, CA; MECH ENGRG DEPT (JANSSON), SANTA BARBARA, CA; MECH ENGRG DEPT (LECKIE), SANTA BARBARA, CA; MECH ENGRG DEPT (MCMEEKING), SANTA BARBARA, CA; MECH ENGRG DEPT (TULIN), SANTA BARBARA, CA
UCSD / SEIBLE, LA JOLLA, CA
UNIV OF ARIZONA / EHSANI, TUCSON, AZ
UNIV OF CAL BERKELEY / FILIPPOU, BERKELEY, CA; GOVINDJEE, BERKELEY, CA
UNIV OF CALIFORNIA / CE DEPT (ROMSTAD), DAVIS, CA; SELMA, LOS ANGELES, CA
UNIV OF CALIFORNIA DAVIS / CE DEPT (HERRMANN), DAVIS, CA; CE DEPT (KUTTER), DAVIS, CA; CE DEPT (RAMEY), DAVIS, CA
UNIV OF COLORADO / MECH ENGRG DEPT (PARK), BOULDER, CO

UNIV OF CONN / LEONARD, STORRS, CT
UNIV OF DELAWARE / NEWARK, DC
UNIV OF HAWAII / HONOLULU, HI
UNIV OF ILLINOIS / CE LAB (ABRAMS), URBANA, IL; CE LAB (PECKNOLD), URBANA, IL
UNIV OF KANSAS / DARWIN, LAWRENCE, KS
UNIV OF MICH / ANN ARBOR, ME
UNIV OF N CAROLINA / CE DEPT (GUPTA), RALEIGH, NC; CE DEPT (TUNG), RALEIGH, NC
UNIV OF NEVADA / SIDDHARTAN, RENO, NV
UNIV OF NY / BUFFALO, NY
UNIV OF RHODE ISLAND / KOVACS, KINGSTON, RI; VEYERA, KINGSTON, RI
UNIV OF STUTTGART / ELIGEHAUSE
UNIV OF TENNESSEE / KNOXVILLE, TN
UNIV OF TEXAS / AUSTIN, TX; TASSOULAS, AUSTIN, TX
UNIV OF WASHINGTON / MATTOCK, SEATTLE, WA
UNIV OF WYOMING / CIVIL ENGRG DEPT, LARAMIE, WY
UNIVERSIDAD POLITECNICA DE MADRID / ELICES, 28040 MADRID; PLANAS, 28040 MADRID, SPAIN
UNIVERSITAT POLITECNICA DE CATALUNYA / GETTU, 08034 BARCELONA, SPAIN
US MERCHANT MARINE ACADEMY / KINGS POINT, NY
USA BELVOIR / FORT BELVOIR, VA
USAMMRC / DRXMR-SM, WATERTOWN, MA
WEIDLINGER ASSOCIATES / LEVINE, LOS ALTOS, CA
WEST VIRGINIA UNIV / BARBERO, MORGANTOWN, WV; KIGER, MORGANTOWN, WV; PRUCZ, MORGANTOWN, WV
WOODWARD CLYDE CONSULTANTS / OAKLAND, CA
WORCHESTER POLYTECH / SULLIVAN, WORCESTER, MA